Université de Lille

Université de Lille

Doctoral School **ED 104 - Sciences de la Matière, du Rayonnement et de l'Environnement**

University Department **Laboratoire PhLAM**

Thesis defended by **Maxime Infuso**

Defended on **June 8, 2023**

In order to become Doctor from Université de Lille

Academic Field **Physics**

Speciality **Theoretical chemical physics**

Unravelling the atmospheric iodine chemistry using molecular simulations

Committee members

Referees	Manuel Ruiz-Lopez	Directeur de recherche CNRS – LPCT, Université de Lorraine	
	Carine Clavaguéra	Directrice de recherche CNRS – ICP, Université Paris-Saclay	
Examiners	Jean-François Paul	Professeur – UCCS, Université de Lille	Committee President
	Aude Simon	Chargée de recherche CNRS – LCPQ, Université de Toulouse	
	Stéphane Coussan	Chargé de recherche CNRS – PIIM, Université Aix-Marseille	
Supervisors	Denis Duflot	Maître de conférences HDR – PhLAM, Université de Lille	
	Florent Louis	Maître de conférences HDR – PC2A, Université de Lille	
	Céline Toubin	Professeure – PhLAM, Université de Lille	

UNIVERSITÉ DE LILLE

Doctoral School **ED 104 - Sciences de la Matière, du Rayonnement et de l'Environnement**

University Department **Laboratoire PhLAM**

Thesis defended by **Maxime INFUSO**

Defended on **June 8, 2023**

In order to become Doctor from Université de Lille

Academic Field **Physics**

Speciality **Theoretical chemical physics**

Unravelling the atmospheric iodine chemistry using molecular simulations

Committee members

Referees	Manuel RUIZ-LOPEZ	Directeur de recherche CNRS – LPCT, Université de Lorraine	
	Carine CLAVAGUÉRA	Directrice de recherche CNRS – ICP, Université Paris-Saclay	
Examiners	Jean-François PAUL	Professeur – UCCS, Université de Lille	Committee President
	Aude SIMON	Chargée de recherche CNRS – LCPQ, Université de Toulouse	
	Stéphane COUSSAN	Chargé de recherche CNRS – PIIM, Université Aix-Marseille	
Supervisors	Denis DUFLOT	Maître de conférences HDR – PhLAM, Université de Lille	
	Florent LOUIS	Maître de conférences HDR – PC2A, Université de Lille	
	Céline TOUBIN	Professeure – PhLAM, Université de Lille	

Thèse présentée par **Maxime INFUSO**

Soutenue le **8 juin 2023**

En vue de l'obtention du grade de docteur de l'Université de Lille

Discipline **Physique**

Spécialité **Physico-Chimie Théorique**

Étude de la chimie atmosphérique de l'iode avec des aérosols par simulations moléculaires

Composition du jury

Rapporteurs	Manuel RUIZ-LOPEZ	Directeur de recherche CNRS au LPCT, Université de Lorraine	
	Carine CLAVAGUÉRA	Directrice de recherche CNRS à l'ICP, Université Paris-Saclay	
Examinateurs	Jean-François PAUL	Professeur à l'UCCS, Université de Lille	président du jury
	Aude SIMON	Chargée de recherche CNRS au LCPQ, Université de Toulouse	
	Stéphane COUSSAN	Chargé de recherche CNRS au PIIM, Université Aix-Marseille	
Directeurs de thèse	Denis DUFLOT	Maître de conférences HDR au PhLAM, Université de Lille	
	Florent LOUIS	Maître de conférences HDR au PC2A, Université de Lille	
	Céline TOUBIN	Professeure au PhLAM, Université de Lille	

This thesis has been prepared at the following research units.

Laboratoire PhLAM

Laboratoire PhLAM
CNRS UMR 8523
Université de Lille
Bâtiment P5
59655 Villeneuve d'Ascq
France

☎   (33)(0)3 20 33 60 37

✉   `cristian.focsa@univ-lille.fr`

Web Site   `http://phlam.univ-lille.fr`

Laboratoire PC2A

Laboratoire PC2A
CNRS UMR 8522
Université de Lille
Bâtiment C11
59655 Villeneuve d'Ascq
France

☎   (33)(0)3 20 43 40 67

✉   `benjamin.hanoune@univ-lille.fr`

Web Site   `https://pc2a.univ-lille.fr`

To my grand-father

To my family

To my friends

Unravelling the atmospheric iodine chemistry using molecular simulations

Abstract

Oceans, through algae and phytoplankton activities, are the main source of iodine, including organic compounds as CH_3I. In the recent past, iodine has played a critical role in health issues through historical events such as the Fukushima nuclear crisis or open-air bomb testing. Iodine, among other halogens, also participates in the catalytic destruction of ozone. The details of the interactions between iodinated compounds and aerosols in the troposphere remain largely unknown. In particular, the modification of the chemical speciation or effects of the environing molecules/aerosols on the iodine chemistry have consequences on its reactivity. Therefore, the knowledge of iodine atmospheric chemistry is essential to better understand general atmospheric phenomena. In this context, this thesis aims to improve the iodine atmospheric chemistry state of knowledge using theoretical simulations, focusing on interactions/chemical reactions between methyl iodide (CH_3I) and its surrounding.

In a first part, the adsorption of gaseous iodomethane (CH_3I) on model sea-salt aerosols (NaCl) at various humidities is investigated. We performed periodic density functional theory (DFT) as well as classical molecular dynamics (MD) calculations to investigate the influence of water coverage. To this aim, we parametrized a flexible non-polarizable force field for iodomethane. This force field shows good performances in describing the interactions with water and sea-salt surfaces. Simulations show that the presence of water tends to stabilize CH_3I at the salt surface. The lifetime of CH_3I in the atmosphere (in gas phase or adsorbed on aerosols) may also be altered by its reaction with gas phase radicals. The reaction of CH_3I with OH is thus investigated both in gas phase and in presence of water by means of quantum mechanical calculations. The presence of an additional water molecule favors the hydrogen abstraction by OH radical under atmospheric conditions. In other words, H_2O plays the role of a catalyst in this atmospheric chemical reaction. Finally, through cooperation with the laboratory "Physics of the Interactions of Ions and Molecules (PIIM)", we investigated the adsorption of methyl iodide on amorphous solid water (ASW) surfaces. In agreement with previous studies, we highlighted the importance of configuration sampling when dealing with amorphous interfaces. Using classical MD and quantum mechanical calculations, we have computed theoretical spectra for ASW surfaces with and without adsorbed CH_3I, which could be directly compared with experimental ones. Adsorption of CH_3I induces a redshift of about $20\,cm^{-1}$ of the dangling OH stretching mode.

This thesis combines several theoretical methods to study the reactivity and capture of molecules by surfaces of atmospheric interest. The approaches applied in this work can be extended to other systems providing valuable interpretation of the spectra and experimental data.

Keywords: iodine, methyl iodide, sea-atmosphere interactions, atmospheric chemistry, marine aerosols, amorphous solid water, molecular dynamics, density functional theory

Étude de la chimie atmosphérique de l'iode avec des aérosols par simulations moléculaires

Résumé

Les océans, par le biais de l'activité des algues et du phytoplancton, sont la principale source d'iode, y compris de composés organiques tels que l'iodométhane (CH$_3$I). Dans un passé récent, l'iode a joué un rôle essentiel dans les questions de santé, en raison d'événements historiques tels que la crise nucléaire de Fukushima ou les essais de bombes en plein air. L'iode, parmi d'autres halogènes, participe également à la destruction catalytique de l'ozone. Les détails des interactions entre les composés iodés et les aérosols dans la troposphère restent encore peu connus. En particulier, la modification de la spéciation chimique ou les effets des molécules/aérosols environnants sur la chimie de l'iode ont des conséquences sur sa réactivité. Par conséquent, la connaissance de la chimie atmosphérique de l'iode est essentielle pour mieux comprendre les phénomènes atmosphériques généraux. Dans ce contexte, cette thèse vise à améliorer l'état des connaissances sur la chimie atmosphérique de l'iode par le biais de simulations théoriques, en se concentrant sur les interactions/réactions chimiques entre l'iodométhane (CH$_3$I) et son environnement.

Dans une première partie, l'adsorption de l'iodométhane gazeux (CH$_3$I) sur des aérosols modèles de sel marin (NaCl) à différentes humidités est étudiée. Nous avons effectué des calculs périodiques de théorie fonctionnelle de la densité (DFT) ainsi que des calculs classiques de dynamique moléculaire (MD) pour étudier l'influence de la couverture d'eau. À cette fin, nous avons paramétré un champ de force flexible non polarisable pour l'iodométhane. Ce champ de force montre de bonnes performances dans la description des interactions avec l'eau et les surfaces de sel marin. Les simulations montrent que la présence d'eau tend à stabiliser CH$_3$I à la surface du sel.

La durée de vie du CH$_3$I dans l'atmosphère (en phase gazeuse ou adsorbé sur des aérosols) peut également être modifiée par sa réaction avec des radicaux en phase gazeuse. La réaction de CH$_3$I avec OH est donc étudiée à la fois en phase gazeuse et en présence d'eau au moyen de calculs de mécanique quantique. La présence d'une molécule d'eau supplémentaire favorise l'abstraction d'hydrogène par le radical OH dans les conditions atmosphériques. En d'autres termes, H$_2$O joue le rôle de catalyseur dans cette réaction chimique atmosphérique.

Enfin, en collaboration avec le laboratoire "Physics of the Interactions of Ions and Molecules (PIIM)", nous avons étudié l'adsorption de l'iodure de méthyle sur des surfaces d'eau solide amorphe (ASW). En accord avec des études antérieures, nous avons mis en évidence l'importance de l'échantillonnage de configuration dans le cas d'interfaces amorphes. En utilisant des calculs classiques de MD et de structure électronique, nous avons calculé des spectres théoriques pour les surfaces ASW avec et sans CH$_3$I adsorbé, qui peuvent être directement comparés aux spectres expérimentaux. L'adsorption de CH$_3$I induit un décalage d'environ $20\,\mathrm{cm}^{-1}$ du mode d'étirement des OH pendants de la surface.

Cette thèse combine plusieurs méthodes théoriques pour étudier la réactivité et la capture de molécules par des surfaces d'intérêt atmosphérique. Les approches suivies dans ces travaux peuvent être étendues à d'autres systèmes dans le but d'interpréter des spectres ou mieux comprendre des données expérimentales.

Mots clés : iode, iodométhane, interactions mer-atmosphère, chimie de l'atmosphère, aérosols marins, eau solide amorphe, dynamique moléculaire, théorie de la fonctionnelle de densité

Contents

Atmospheric Iodine

Outline of the current chapter

1.1 Generalities

Iodine is the fourth heaviest stable halogen element, with an atomic number $Z = 53$, and its ground state electronic configuration is $[Kr]4d^{10}5s^25p^5$. There are 25 known isotopes of iodine. Their molar mass starts from 117 to $141\,\text{g}\,\text{mol}^{-1}$, but the most stable one is ^{127}I. Among all the unstable isotopes, thirteen come from fission processes, and two of them, ^{129}I and ^{131}I, have a half-life of 1.57×10^7 years and 8 days, respectively. During a severe nuclear incident, the most radiotoxic isotopes are ^{131}I, ^{132}I (half-life of 2 hours), and ^{133}I (half-life of 20 hours). Due to its longer half-life decay, ^{133}I has time to spread into the atmosphere and can be assimilated by living organisms.

1

Indeed, in the past, ^{133}I was an essential contributor to health issues from historical events: open-air bomb testing in the 1950s, the Chernobyl disaster in 1986, and the Fukushima nuclear crisis in 2011. Via its β^- decay mode, ^{133}I is known to induce mutations or to kill living cells. In human beings, it is assimilated mainly by the thyroid gland and can be the cause of cancers of the latter [1]. However, iodine is an essential nutrient for mammals, and its concentration in food is usually insufficient for optimal nutrition [2, 3].

Additionally, volatile iodide contributes to the oxidizing capacity of the atmosphere through the catalytic destruction of ozone [4, 5]. It was one of the reasons why it was removed as a fumigant in 2001 [6, 7]. Indeed, iodine and its various component forms can be easily photodissociated in the near-UV and visible range of the electromagnetic spectrum [8]. It is also the case for CH_3I, as discussed in the next section. Furthermore, Vogt et al. have shown that ozone destruction depends on the amount of reactive iodine in the troposphere, with an additional ozone loss of 0.6 nmol/mol/days [9]. This relatively small value makes it difficult to measure through experimental setups. Moreover, iodine chemistry can influence the atmospheric oxidizing species concentration, particularly hydroxyl radicals (OH) [4].

This chapter will begin by discussing the different natural sources and forms of atmospheric iodine. Then the atmospheric reactivity is approached, with a focus on iodine. The following section will discuss aerosol role in atmospheric chemistry. Then, the effect of environing water molecules is introduced, followed by the introduction of amorphous solid water systems. Finally, the Thesis outlines will be presented.

1.2   Sources

Anthropogenic releases (except those from nuclear accidents) of iodinated compounds appear negligible compared to natural emissions [10]. Measurements of the latter [11–17] show that oceans are the primary source through emissions of iodinated organic compounds such as methyl iodide (CH_3I), ethyl iodide (C_2H_5I), and propyl iodide (1- and 2-C_3H_7), also by emissions of polyhalogenated compounds such as chloroiodomethane (CH_2ICl), bromoiodomethane (CH_2IBr), and diiodomethane (CH_2I_2), and finally by emitting molecular iodine (I_2) [4].

Oceans cover more than 70 % of the surface of the Earth, making them a significant source of halocarbons [18]. The mechanisms contributing to the emission of organic iodide compounds in this marine boundary layer still need to be fully understood. Two different pathways are proposed in the literature to explain measurements made in the marine boundary layer. On the one hand, the biological pathway: microalgae, macroalgae, phytoplanktons, and bacteria can be responsible

for the emission of organic iodine from oceans to the atmosphere. On the other hand, the chemical pathway: halomethane compounds can be produced by a photochemical reaction at the sea surface, depending on the irradiation light. These two pathways will be detailed in the following paragraphs.

Much data are available in the literature concerning the biological pathway. According to them, marine algae are the primary source of organic iodide compounds from oceans, releasing it through a halide ion methyl transferase enzyme [10]. A field campaign at Mace Head (Ireland) [19] has correlated emissions of iodinated compounds with the production of marine algae. Carpenter et al. have also calculated that the total flux of iodine atoms from organic precursors is dominated by the photolysis of CH_2I_2, whereas this process contributes less than 3 % for CH_3I. Further laboratory works have pointed out that the significant organic iodine species emitted by brown algae is CH_2I_2 [20]. The latter being a short-lived compound, it might be transformed through photolysis processes in the upper water column, explaining its low concentration level at the surface of oceans. Furthermore, marine phytoplanktons [21] and sponges [22] are also partially responsible for this emission through the same mechanism.

Moreover, with a lower contribution, some land-based microorganisms also emit organic iodide compounds proportionally to the concentration of the latter in soil [23]. Many plants can emit methyl iodide through methyl transferase reactions [24, 25]. Also, rice paddies and marshland are significant sources of iodine [26–28]. The leaves of rice plants participate in its emission, with a global emission of 64 Gg(I)/year [29]. Duborská et al. [30] have estimated annual emissions of CH_3I in the range of 0.1 Gg(I)/year to 11.4 Gg(I)/year from peatland. In addition, several fungi are also well-known methyl iodide sources [25, 30–32].

Concerning the photochemical pathway, some information is available in the literature. Stemmler et al. hypothesized, through modeling experiments, that the photochemical pathway for emission explains better surface CH_3I concentration than emissions from phytoplanktons [33]. Experiments also show a production dependence of methyl iodide molecules depending on sunlight, suggesting a recombination between methyl radicals and iodine atoms at the sea-water surface [34, 35].

Nuclear weapon testing and nuclear facilities operations [36, 37] also released ^{129}I into the environment. In the literature, a high concentration of this element was found in the USA [38, 39], Europe [39–41], and Japan [39]. Because this element has a long life, it is distributed globally. It is expected to behave like stable iodine over a long period [39, 42, 43]. The United Nations Scientific Committee on the Effects of Atomic Radiation (UNSCEAR) evaluates the levels and effects of exposure to ionizing radiation. This Committee is also responsible for evaluating the risks and international protection standards. In the UNSCEAR-2000 report [44], ^{129}I was

considered one of the most critical radioactive species. Indeed, due to its complex behavior and the lack of data for this compound, its life cycle and chemistry are not sufficiently known.

1.2.1 Atmospheric measurements

Atmospheric mixing ratios from measurements of CH_3I and CH_2I_2 are shown respectively in Table 1.1 and 1.2 from Saiz-Lopez et al. [4] work. Regarding these values, we can see that the mixing ratio of CH_3I is higher than CH_2I_2 in both coastal and open oceans. It can be related to photodissociation processes, which are quicker for CH_2I_2 than CH_3I [10]. In addition, coastal areas show a higher mixing ratio of both species, which is correlated to the algae density in each area [20].

In addition, it has been shown that there are seasonality effects in the production of CH_3I in a given area [53, 56]. Regarding literature, those effects impact the photochemical production more than biological ones. In summer, the higher methyl iodide concentration was around the equator. Due to the lack of photolysis in winter, a higher quantity of CH_3I can be transported from midlatitudes to poles [16]. Furthermore, global atmospheric CH_3I is uniformly distributed during wintertime. In addition, another study suggests that the local oceanic emission of CH_3I is 2.2 to 3.6 times faster in summer than in winter [57]. The same effect was observed for terrestrial biomass emissions [49].

1.2.2 Emission rates and mechanisms

Studies available in the literature have tried to quantify the emissions of CH_3I and CH_2I_2. They also attempted to identify the sources and the sink of these molecules. Table 1.3 summarizes these results. Moore et al. [61] have done measurements in NW Atlantic, NE Atlantic, and Pacific Oceans. They estimated flux from the ocean to the atmosphere of $114\,Gg(I)/year$ to $317\,Gg(I)/year$. More recently, Bell et al. [6] have done simulations of this transfer. They obtained a net oceanic emission of CH_3I to the atmosphere of $190\,Gg(I)/year$. Their result lies in the range of the ones of Moore et al. [61]. Nevertheless, Butler et al. [14] have measured a total oceanic emission rate of $546\,Gg(I)/year$ through seven field campaigns. It is twice the maximum range of Moore et al. [61].

Concerning terrestrial emissions, Sive et al. [49] have measured slightly lower emission rates. Allard et al. [63] have shown that manganese oxides participate in the global terrestrial methyl iodide emission through the oxidation of natural organic matter. In addition, Keppler et al. [64] have shown that in the presence of humic acid, ferric oxides release CH_3I in the atmosphere through the same process. Plants also play an essential role in terrestrial emissions [65]. Muramatsu et al. [66] have studied the emission of iodinated components from rice plants. They measured

a higher emission from rice than other plants. They hypothesized that the action of the roots or microorganisms did the methylation of iodine. Landini et al. [67] showed that the *harmless to ozone layer* (HOL) gene was responsible for iodine methylation, as the plant does not need iodine to grow [68].

Furthermore, iodine volatilization is enhanced in the presence of carbonyl compounds and alkyl chlorides [69]. Recent studies have been done at the Hanford Site sediments and revealed that methyl iodide is the only iodinated compound to be released in the atmosphere, solely by microcosms [70]. Within a minor impact on the total methyl iodine emissions, fungi are also known to emit iodine into the atmosphere [65].

Table 1.1: Atmospheric mixing ratios of CH$_3$I organoiodines in the marine boundary layer[1] [4]

Species	Region	Mixing ratio/pptv		Ref
		Mean	Range	
CH$_3$I	**Coastal**			
	Spitzbergen, Norway	1.04	<0.004-2.12	Schall and Heumann [45]
	Mace Head, Ireland (spring)	0.43	0.12-1.47	Carpenter et al. [19]
	Mace Head, Ireland (summer)	3.4	1.9-8.7	Bassford et al. [46]
	Mace Head, Ireland (summer)	3.78	1.3-12.0	Carpenter et al. [10]
	Cape Grim, Australia	2.6	1.0-7.3	Carpenter et al. [10]
	Cape Grim, Australia	1.2		Krummel et al. [47]
	Cape Grim, Australia	0.53	0.14-0.9	Yokouchi et al. [16]
	Okinawa, Japan	1.2	0.5-2.0	Li et al. [48]
	Pacific and Atlantic Coast	0.8	0.4-1.6[2]	Butler et al [14]
	Appledore Island, United States	1.39	1.3–1.5	Sive et al. [49]
	NW Pacific Islands[3]	0.86	0.1–4.5	Yokouchi et al. [16]
	San Cristobal Island, Ecuador	1.13	0.53–2.55	Yokouchi et al.[16]
	Antarctic Peninsular	2.4	0.6–7.9	Reifenhäuser and Heuman [50]
	East China and Southern Yellow Sea	2.0	0.7-4.5	Li et al. [51]
	mean	**1.6**	**0.7–4.4**[4]	
	median	**1.2**		
	Open ocean			
	Western Pacific	1.07	0.6–1.8	Atlas et al. [52]
	Western Pacific	0.6	0.12–1.15	Blake et al. [53]
	Western Pacific	1.2	0.5–1.9	Yokouchi et al. [54]
	Asian Seas	0.63	0.24–2.0	Yokouchi et al. [54]
	Western Pacific	0.7	0.6–0.8	Li et al. [55]
	Pacific	0.7	0.4–1.6	Butler et al. [14]
	Western Pacific[5]	0.7	0.25–1.7	Yokouchi et al. [16]
	Northern Pacific[6]	0.68	0.19–2.09	Yokouchi et al. [16]
	Atlantic	0.8	0.4–1.2	Butler et al. [14]
	Eastern Atlantic	1.63	0.4–2.24	Chuck et al. [15]
	mean	**0.87**	**0.37–1.58**[4]	
	median	**0.70**		

[1] Mean and median values given where $\geq$ 5 locations/studies.
[2] On the basis of 90% confidence limits.
[3] Mean value of data from Cape Ochiishi (43.2°N), Tsukuba (36.0°N), Happo Ridge (36.7°N), and Hateruma Island (24.1°N).
[4] Mean values of minima and maxima.
[5] Mean of 2 latitudinal bands
[6] Mean of 6 latitudinal bands

Table 1.2: Atmospheric mixing ratios of CH_2I_2 in the marine boundary layer[1] [4]

| | | Mixing ratio/pptv | | |
Species	Region	Mean	Range	Ref
CH_2I_2	**Coastal**			
	Mace Head, Ireland (spring)	0.05	<0.02–0.36	Carpenter et al. [19]
	Mace Head, Ireland (summer)	0.10	<0.02–0.46	Carpenter et al. [10]
	Spitzbergen, Norway	0.46	<0.08–1.02	Schall and Heumann [45]
	Roscoff, France	0.03	0.01–0.07	Jones et al. [58]
	Outer Hebrides, United Kingdom, kelp beds	0.10	0.02–0.18	Jones et al. [59]
	mean	**0.15**	**0.012–0.42**[2]	
	median	**0.10**		
	Open ocean			
	Northern Atlantic (15–60°N)	**0.01**	**<0.01–0.02**	Jones et al. [59]

[1] Mean and median values given where ≥ 5 locations/studies.
[2] Mean values of minima and maxima.

Table 1.3: Estimated local lifetimes in the sunlit marine boundary layer and global emission rates for CH_3I and CH_2I_2 compounds [4]

Species	Lifetime	emission rate / Gg (I) year^{-1}	Reference
CH_3I			
	5 days [60]	114–317 total ocean	Moore and Groszko [61]
	6 days [6]	190 total ocean	Bell et al.[6]
		546 total ocean	Butler et al. [14]
		80–110 terrestrial	Bell et al. [6], Sive et al.[49]
CH_2I_2			
	2–10 min [62]	223 total ocean	Jones et al. [59]

1.3   Atmospheric reactivity

The chemistry of iodine has a significant impact on the biogeochemical cycle and on the atmosphere composition. Many studies and reviews have treated halogen reactivity in the atmosphere [4, 5, 71–76]. To our knowledge, the most recent review on this topic was done by Simpson et al. [77]. In this context, understanding the mechanisms and kinetics of iodine reactions in the atmosphere is crucial for predicting and mitigating the potential impacts of iodine chemistry on the Earth's atmosphere.

1.3.1   Iodine radical

Most of the emitted iodinated compounds face photolysis during the day because of the sunlight. It leads to the formation of highly reactive radicals. A non-exhaustive list of possible photolysis reactions is shown below:

$$CH_3I \xrightarrow{h\nu} CH_3 + I \tag{R1}$$

$$C_2H_5I \xrightarrow{h\nu} C_2H_5 + I \tag{R2}$$

$$CH_2ICl \xrightarrow{h\nu} CH_2ICl + I \tag{R3}$$

$$CH_2I_2 \xrightarrow{h\nu} CH_2I + I \tag{R4}$$

$$I_2 \xrightarrow{h\nu} 2\,I \tag{R5}$$

$$HOI \xrightarrow{h\nu} OH + I \tag{R6}$$

The previous step is often called the *initiation* step. Indeed, it "activates" the iodine atom to react with other species. Then, the previously formed radicals can then react with non-radical species in the atmosphere. It is the *propagation* step. However, two radicals can also react together to form a non-radical specie. In this case, this step is called *termination*. Indeed, we do not have any radical to continue the reaction propagation, ending the whole process.

1.3.2   Impact on ozone depletion

Radicals have a very short lifetime (from seconds to some minutes). Thus, gaseous iodinated compounds can be seen as a reservoir forming radicals during the day continuously.

Iodine radicals react primarily with ozone compared to other halogen radicals [77]. It leads to the formation of iodine monoxide:

$$I + O_3 \longrightarrow IO + O_2 \tag{R7}$$

The formed product, through photolysis, can lead back to radical iodine:

$$IO \xrightarrow{h\nu} I + O \tag{R8}$$

Iodine monoxide can react with another halogen monoxide, like BrO, leading to the formation of iodine dioxide (80 %) or halogen radicals and dioxygen (20 %) [78, 79]:

$$IO + BrO \longrightarrow OIO + Br \tag{R9}$$
$$IO + BrO \longrightarrow I + Br + O_2 \tag{R10}$$
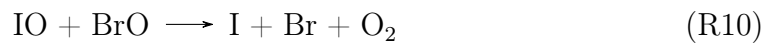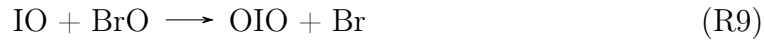
Furthermore, iodine monoxide can also self-react to form OIO and I_2O_2 with a high reaction rate [4, 79]. In addition, the IOI self-reaction can lead to the formation of higher iodine oxides:

$$IO + IO \longrightarrow OIO + I \tag{R11}$$
$$IO + IO \longrightarrow I_2O_2 \tag{R12}$$
$$IO + OIO \longrightarrow I_2O_3 \tag{R13}$$
$$OIO + OIO \longrightarrow I_2O_4 \tag{R14}$$

Iodine dioxide can also lead to the formation of iodine monoxide or dioxygen through photolysis:

$$OIO \xrightarrow{h\nu} IO + O \tag{R15}$$

$$OIO \xrightarrow{h\nu} I + O_2 \tag{R16}$$

At low IO and BrO mixing ratio, the reaction between iodine monoxide and hydroperoxyl radical (HO_2) becomes non-negligible [75]:

$$IO + HO_2 \longrightarrow HOI + O_2 \tag{R17}$$

$$HOI \xrightarrow{\text{h}\nu} I + OH \tag{R18}$$
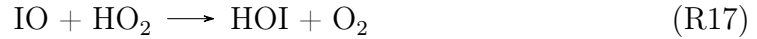
In semipolluted atmospheres, iodine monoxide reacts with NO_2 to form $IONO_2$. The latter, through photolysis, leads to different products [4]:

$$IO + NO_2 \longrightarrow IONO_2 \tag{R19}$$

$$IONO_2 \xrightarrow{\text{h}\nu} IO + NO_2 \tag{R20}$$

$$IONO_2 \xrightarrow{\text{h}\nu} I + NO_3 \tag{R21}$$

$$NO_3 \xrightarrow{\text{h}\nu} NO + O_2 \tag{R22}$$

$$NO + O_3 \xrightarrow{\text{h}\nu} NO_2 + O_2 \tag{R23}$$
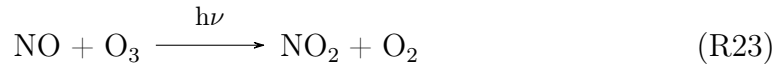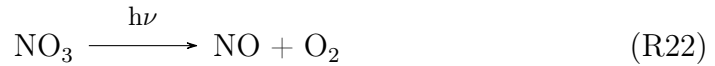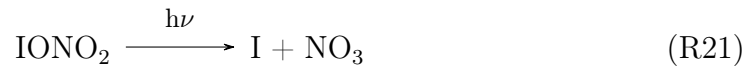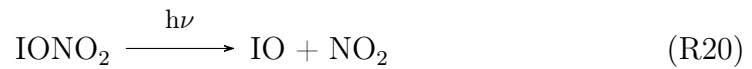
Using all the previous reactions, we can see three ozone depletion cycles, represented in Table 1.4. Furthermore, iodine radicals can be combined with other halogen radicals. For example, reaction R11 can be replaced by reaction R9. In addition, the higher iodine oxides can also react with ozone [80–82]:

$$I_2O_2 + O_3 \longrightarrow I_2O_3 + O_2 \tag{R24}$$
$$I_2O_3 + O_3 \longrightarrow I_2O_4 + O_2 \tag{R25}$$
$$I_2O_4 + O_3 \longrightarrow I_2O_5 + O_3 \tag{R26}$$
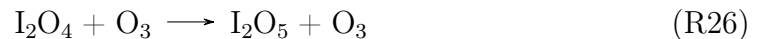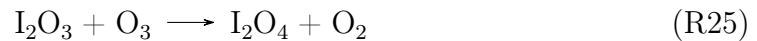
The ensemble of reactions is schematically represented in Fig 1.1. It is essential to highlight that some reactions occur during the day and others during the night [75]. For example, reactions involving NO_3 or HOI can occur during the night. They form iodine oxides that are decomposed during the daytime through photolysis.

Even if Saiz-Lopez et al. [4] have reviewed only the photolysis reaction for methyl iodide in the troposphere, it has been shown that CH_3I reacts with the hydroxyl radical (OH) through the reactions [83]:

$$CH_3I + OH \longrightarrow CH_2I + OH \tag{R27}$$
$$CH_3I + OH \longrightarrow CH_3 + HOI \tag{R28}$$

Table 1.4: Definition of the different ozone depletion cycles induced by iodine radical.

Cycle 1

$(I + O_3 \longrightarrow IO + O_2)\ \times 2$	R7
$IO + IO \longrightarrow OIO + I$	R11
$OIO \xrightarrow{h\nu} I + O_2$	R16
$2\,O_3 \longrightarrow 3\,O_2$	

Cycle 2

$I + O_3 \longrightarrow IO + O_2$	R7
$IO + HO_2 \longrightarrow HOI + O_2$	R17
$HOI \xrightarrow{h\nu} I + OH$	R18
$HO_2 + O_3 \longrightarrow OH + 2\,O_2$	

Cycle 3

$I + O_3 \longrightarrow IO + O_2$	R7
$IO + NO_2 \longrightarrow IONO_2$	R19
$IONO_2 \xrightarrow{h\nu} I + NO_3$	R21
$NO_3 \xrightarrow{h\nu} NO + O_2$	R22
$NO + O_3 \xrightarrow{h\nu} NO_2 + O_2$	R23
$2\,O_3 \longrightarrow 3\,O_2$	

Despite the exhaustive literature studies carried out over the years on iodine chemistry, the role of water vapor on the iodine cycle has yet to be investigated. Nevertheless, it is one of the essential atmospheric compounds. In addition, methyl iodide can be transported and react with tropospheric aerosols. The later processes
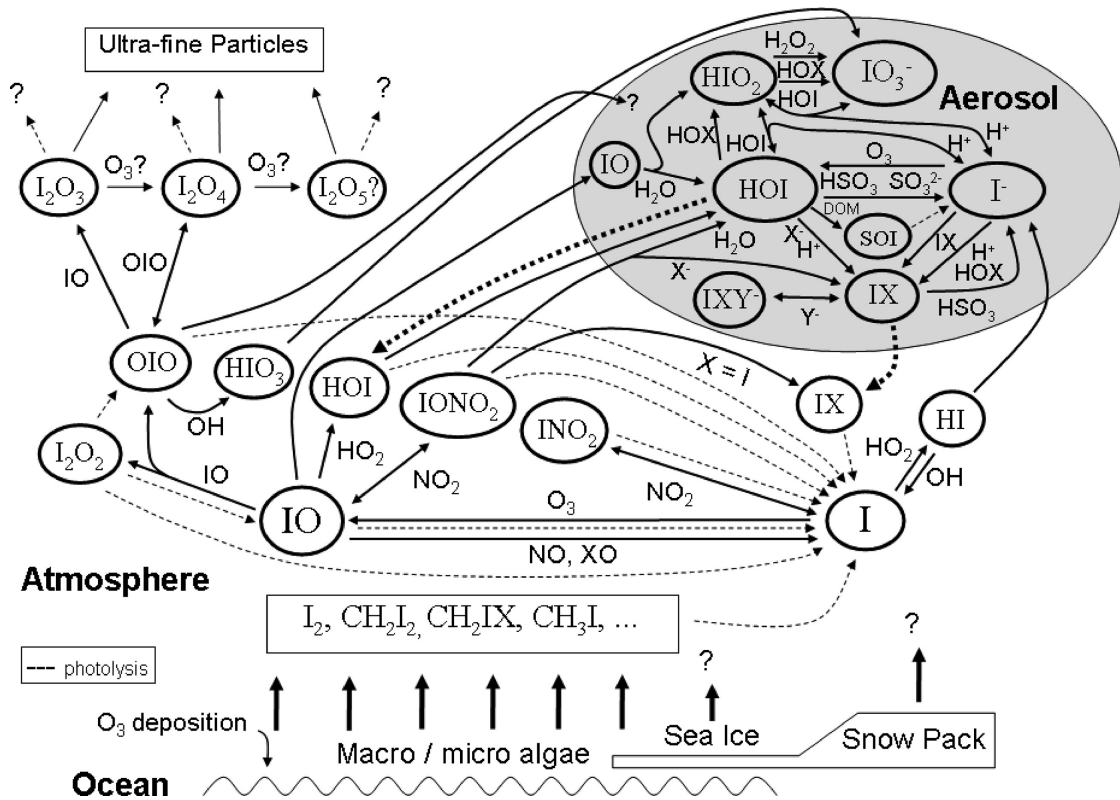
Figure 1.1: Schematic representation of the overall iodine reactivity in the atmosphere. X and Y are halogen atoms, DOM is dissolved organic matter, and SOI is soluble organic iodine. Figure taken from Saiz-Lopez et al. [4]

being less characterized, it appears essential to better understand how iodine reactivity is affected by the presence of aerosols.

1.4   Role of tropospheric aerosols

According to Agranovski [84], an aerosol collection is defined by a suspension of particles (liquid, solid, or heterogeneous). Two essential features can discriminate them from other objects suspended in the gas phase. First, aerosol particles can exist beyond their collection for a long time. Secondly, it can be defined by its concentration of aerosol particles [84]. For example, using this definition, clouds are not considered as aerosols, as if we isolate a small part of a cloud, it will evaporate. In atmospheric science, clouds are generally not considered as aerosols but as a separate phenomenon [85].

Furthermore, aerosols can be characterized by different criteria. Looking at their formation mechanisms, we can divide them into *primary* and *secondary* aerosols [86]. Primary aerosols result from particles introduced directly into the gas phase. Sources include biomass burning, incomplete combustion of fossil fuels, volcanic eruptions, traffic-related suspension of roads, soil, mineral dust, sea salt, and biological materials [87]. Secondary aerosols are formed through *gas-to-particle conversion* or aging from primary ones. In other words, it refers to forming new particles by nucleation and condensation of precursors in the atmosphere [87].

Two secondary aerosol classes exist depending on their chemical compositions. Secondary inorganic aerosols (SIAs), composed of inorganic matter, are generally formed by a series of chemical reactions and physical processes involving sulfur dioxide (SO_2), nitrogen oxides (NOx), ammonia (NH_3) and several volatile organic compounds (VOCs) [88]. Secondary organic aerosols (SOAs), composed of organic matter are more complex. Indeed, they can be formed from thousands of compounds. As for SIAs, SOAs are mainly formed from chemical reactions from VOCs [89].

The characterization of aerosols can be done through different essential criteria. The particle size is one of the most critical parameters, as most of the properties are size-dependent [86]. Even if aerosols are not perfect spherical particles, the size usually refers to the particle diameter. The specific case of non-spherical particles refers to *equivalent volume diameter*. It is the diameter of the sphere that has the same volume as the non-spherical particle [86].

Laj et al. [90] estimated (Table 1.5) the particle quantities emitted in the atmosphere per year, discriminating between natural and anthropogenic sources. We observe large variations between the minimum and maximum value of aerosol emissions for both source types. Indeed, the variation for sea salt aerosols is about one order of magnitude, with the average closer to the minimum than the maximum value. Nevertheless, they are one of the most emitted aerosol types in the troposphere.

After being released into the atmosphere, sea salt aerosols can be divided into two groups. First, the fresh sea salt aerosols. They are mainly composed of NaCl particles coated by $MgCl_2$ and $CaSO_4$. The second group, aged sea salt aerosols, comprises NaCl particles coated by $NaNO_3$, Na_2SO_4, $Mg(NO_3)_2$, and $MgSO_4$ [91]. These aerosols can thus play an important role in atmospheric chemistry, transporting species or participating in chemical reactions [91]. For example, NO_2 can react with wet sea salt aerosol particles to form NO_3^- and ClNO through the following reaction [92]:

$$2\,NO_2 + Cl^- \longrightarrow NO_3^- + ClNO \qquad (R29)$$

At this stage, it is important to recall the general concepts about the gas-aerosols interactions and their impacts on atmospheric chemistry. According to George
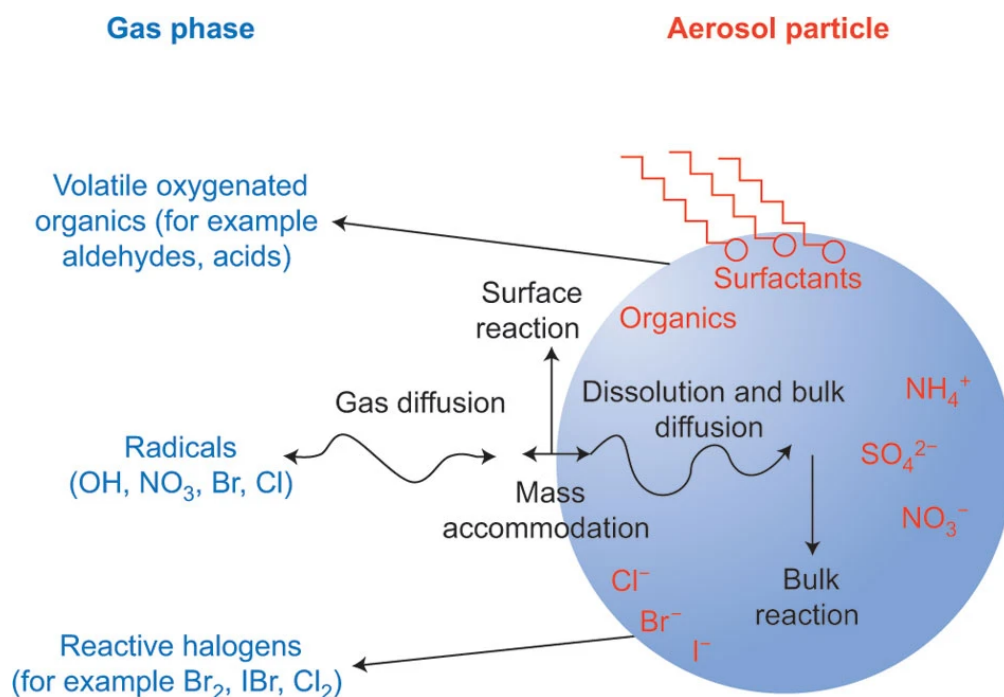
Figure 1.2: Schematic representation of the overall gas-aerosols interactions. Figure taken from George et al. [93].

et al. [93], different processes are occuring at the gas-aerosol surface or in the bulk, as schematized in Fig. 1.2. They can be grouped into eight categories.

Collision

Assuming a constant gas concentration, gas kinetic theory can describe collisions between gas and aerosol particles.

Gas diffusion

The gas around an aerosol particle can diffuse through the aerosol surface and the reverse. This process is directly related to the amount of colliding particles. We can compute a diffusion factor depending on the concentration of gas close and far from the aerosol surface.

Adsorption

Once a gas molecule is close to the surface, it can stick to it briefly. This process is called adsorption. Two types of adsorption exist: physisorption, when the molecule is bonded to the surface through weak intermolecular interactions, and chemisorption is when the molecule is chemically bonded to the surface. The latter has higher adsorption energy (energy needed to

desorb the molecule) than the former. This thesis will more specifically deal
with these adsorption phenomena.

Desorption

It is the adsorption reverse process. The molecule can return to the gas phase,
after being adsorbed, due to thermal effects.

Surface reaction

Once the molecule is adsorbed on the surface, it can react with the surface or
environing species. It can lead to chemisorption processes or the generation
of new molecules.

Bulk accommodation/diffusion

This phenomenon mainly happens when the aerosol is a liquid one. The
adsorbed molecule can diffuse through the bulk. An essential parameter
describing this phenomenon is the diffusion coefficient.

Bulk reaction

Reactions may also append in bulk if diffusion is not the limiting process.

Dissolution

The last process is dissolving the gas phase molecule into the aerosol. This
process occurs in the absence of reactivity between gas phase molecules and
the aerosol.

All these processes are included in one parameter: the uptake coefficient. It is
calculated as the number of gas molecules taken by the aerosol particle divided by
the number of those impacting onto the particle surface [87].

Several experimental methods have been used to characterize gas-aerosols in-
teractions. Among them, we can cite flow tube and flow tube-like techniques [94],
Knudsen cell [95], Diffuse Reflectance Fourier Transform Spectroscopy (DRIFT)
cell [96], and the atmospheric simulation chamber [97]. Nonetheless, these interac-
tions can also be investigated theoretically, as shown by the work of Roose et al.,
Lovrić et al. [98, 99] using classical molecular dynamics (MD) calculations.

Water is also omnipresent in the atmosphere in the form of droplets, mixed
particles or at the surface of the aerosols. They indeed play an essential role in the
gas-aerosols processes. Then, the next section will highlight these effects and how
they influence the chemistry in the atmosphere.

Table 1.5: Quantities of particles emitted in the atmosphere, expressed in Mt/year. Table taken from Laj et al. [90].

	Source	Annual global emission (Mt/year)		
		Average	**Minimum**	**Maximum**
90 %	**Natural**			
	Primary			
	Mineral dust	1500	1000	3000
	Sea salt aerosols	1300	1000	10 000
	Biological debris	50	26	80
	Volcanic ash	33	4	10 000
	Secondary			
	Biological sulfate	90	80	150
	Volcanic sulfate	12	5	60
	SOA	55	40	200
	Nitrates	22	15	50
	Total	3060	2170	23 540
10 %	**Anthropogenic**			
	Primary			
	Soot	20	5	20
	Industrial dust	100	40	130
	Secondary			
	Vegetation fires	80	60	160
	Organic aerosols	10	5	52
	Sulfates	140	120	250
	Nitrates	36	25	65
	Total	390	300	710

1.5   Role of the environing water molecules

Depending on the area, temperature, and altitude, the water vapor amount of the atmosphere can drastically differ. These water molecules interact with aerosols and environing gas phase molecules. In the former case, we talk about the hygroscopic properties of atmospheric aerosol particles [100, 101]. It has been shown that these properties are critical in aerosol aging and interactions with other species and human health [101]. In addition, it has been shown that the presence of a single water molecule can have decisive influences on gas phase chemistry [102, 103]. Furthermore, Aloisio et al. [104] have evidenced that water-containing clusters show distinct photochemistry from isolated systems. It has been demonstrated theoretically and experimentally that water highly affects atmospheric chemistry and is a crucial element to consider when dealing with atmospheric chemical reactions ([105] and references therein).

Micro-hydration studies have been carried out on several iodinated compounds. Taamalli et al. [106] have studied the micro-hydration reaction of iodous acid (HOIO) by adding up to four water molecules around an isolated HOIO molecule. They show that such systems can exist under tropospheric conditions. Moreover, Sobanska et al. [107] have studied the micro-hydration processes of iodomethane experimentally and using density functional theory (DFT) theoretical calculations. They have shown that CH_3I and H_2O may form stable hetero-aggregates (dimers, trimers...).

Concerning chemical reactions, water can also have a catalytic role [103]. Anglada et al. [108] have studied the effect of water vapor on the atmospheric oxidation of CH_3OOH by OH. They concluded that water highly increases the kinetic rate constants of both hydrogen abstraction (terminal hydrogen or the one bonded to the methyl group). Other reactions have been studied, like OH + HOCl [109]. In this case, they concluded that water vapor reduces the kinetic rate constant, keeping the reaction favorable. More recently, Ali et al. [110] have seen no relevant effect of water vapor on the kinetic of the OH + CH_4 reaction under atmospheric conditions.

Water vapor can affect atmospheric chemistry, but it is not systematic. Nevertheless, neglecting the effect of H_2O on atmospheric chemical reactions can lead to biased results compared to laboratory experiments and real conditions. To conclude, it is essential to deeply study the effect of water vapor on gas uptake or reactivity.

Among iodine-water systems, the case of the ice surface will be discussed in the next section.

1.6   Interactions with ice

Ice is present at the earth surface under the form of snowpack or in the stratosphere. It is assumed to be polycristalline with some irregularities. Amorphous solid water (ASW), mostly present in the interstellar medium, but still its existence is postulated in the Earth's upper atmosphere (polar clouds) [111, 112]. Thus, it is one of the universe's most abundant forms of water [113]. ASW is widely used in cryogenic experiments [114–118].

It presents some particular properties. Increasing the system pressure leads to a denser ASW [119–121]. This process is called the amorphous-amorphous transition. They also show that, when releasing the pressure, the system has different paths depending on the temperature. Below 76 K, the system keeps its dense form. We call this system high-density ASW. However, above 110 K, the system shows another amorphous-amorphous transition, recovering its original form. We call the latter low-density ASW.

Ice systems present dangling bonds (dOH), unsaturated atoms directed toward the interface, presenting a small adsorption peak around $3700 \, \text{cm}^{-1}$ on bare ASW surfaces [122]. Experimental and theoretical studies have demonstrated that the adsorption of different species induced a quantifiable red shifts of these dOHs [114–118, 123, 124]. This effect can help identifying adsorbed molecules on ice. ASWs systems are also known to have a catalytic behavior towards chemical reactions. In the interstellar medium, small molecules such as H_2 [125, 126], O_2 [127], NH_3 [128], CO_2 [129, 130], and CO [131] can be adsorbed on the ASW surface and then react to form complex molecules, such as CH_3OH [118, 132].

Manca et al. [124] have carried out periodic Hartree-Fock coupled to DFT calculations of adsorbates on the surface of a two bilayers slab of water molecules presenting dOHs. They have studied the adsorption of several molecules on the ice surface. They could isolate dOH vibrational modes and give vibrational frequency shifts upon adsorption. They conclude that the electric field induced by the adsorbate plays a crucial role in the adsorption process or reaction ones. However, their systems do not represent a true ASW surface. In this direction, Michoulier et al. [133] have calculated the vibrational shift induced by polycyclic aromatic hydrocarbons by coupling MD and DFT-B calculations. They show that it was necessary to probe a reasonable number of adsorption sites to get an accurate estimation of the vibrational shift induced upon adsorption.

The adsorption of iodinated compounds on ASW is a subject of interest in the literature. DeSimone et al. [134] have studied the adsorption of methyl iodide on ASW and low-density porous amorphous solid water (PASW). PASW contains more surface defects (increasing surface reactivity) than ASW because of its preparation method [135]. They were motivated by photodissociation experiments in the

gas [136–145] and adsorbed phases on different substrates [146–156]. They found a better photodissociation yield when CH$_3$I was adsorbed on ASW than PASW. The main reason involves porosity that increases methyl iodide trapping (PASW) when pore-free surfaces (ASW) favor adsorption and formation of two-dimensional methyl iodide clusters leading to I$_2$ formation. In addition, iodinated compound interactions with ice have studied, focused on atmospheric interests. Allanic et al. [157] have studied the adsorption of HOI on ice, and highlighted that a reasonable proportion of HOI was transformed into I$_2$. Furthermore, iodinated coumpounds adsorption on ice films was also investigated for several species as IH [158, 159], I$_2$ (doped ice) [160] and CH$_3$I [161, 162].

In conclusion, ASW is a common form of water in the universe and its properties have been extensively studied. The adsorption of iodinated compounds on ASW has also been studied, revealing that the surface defects of PASW can affect the photodissociation yield of methyl iodide. Within a collaboration with Stéphane Coussan (Laboratoire PIIM, Marseille), Sophie Sobanska and Joëlle Mascetti (Laboratoire ISM, Bordeaux), the adsorption CH$_3$I on a ASW will be investigated theoretically to quantify the dOH shift and to compare with experiments.

1.7   Outline

We have seen large sea-salt aerosols emissions in the atmosphere. In addition, the photodissociation of methyl iodide or its reaction with hydroxyl radicals are major sources of activated iodine that plays a role in the ozone depletion. We have also highlighted that aerosols and water can enhance or change drastically the reactivity of gas phase molecules in the atmosphere. Following the work done by Houjeij et al. [96], we propose to study the adsorption of CH$_3$I on a model sea-salt surface, the NaCl(001) surface. The aim is to compute the IR spectrum of the system and in addition to investigate the effect of humidity on the adsorption process. This work is presented in chapter 4.

Because we were dealing with large molecular systems, we had to parametrize a force field to pursue our studies. This is described in chapter 3.

We are also interested into quantifying the effect of water vapor on reactions containing iodinated compounds related to atmospheric chemistry. We picked the reaction of methyl iodide with the hydroxyl radical and search for a possible catalytic effect upon addition of a water molecule. All the discussion is done in chapter 6.

Furthermore, we take interest of the interaction of iodinated compounds on ASW and the systematic red-shift of dOH upon the adsorption of a molecule. Indeed, using our force field and coupling the results with quantum calculations,

we aim to compute the dOH red-shift upon adsorption of methyl iodide, as detailed in chapter 5.

To numerically compute all these properties, we use a variety of numerical methods (quantum and classic ones) and combine them to obtain optimal results given their respective limitations. All the information necessary to understand the basics of these methods are developed in chapter 2.

Finally, all the results and perspectives are sum up in the last part, in chapter 7.

Methodology

Outline of the current chapter

2.1   The adiabatic approximation

The system of interest in the present Thesis consists in N_n nuclei and n_e electrons. The corresponding time-independent Hamiltonian comprises the kinetic energy of the electrons (T_e), the kinetic energy of the nuclei (T_n), and the potential energy between the particles. The latter is decomposed into electron-electron interactions (V_{ee}), nucleus-nucleus interactions (V_{nn}), and nucleus-electron interactions (V_{ne}). It leads to the following equations:

$$H = T_e + V_{ee} + V_{ne} + V_{nn} + T_n$$

$$= -\sum_j^{n_e} \frac{\hbar^2}{2m_e} \nabla_{\mathbf{r}_j}^2 + \frac{1}{2} \sum_{j \neq j'}^{n_e} \frac{e^2}{|\mathbf{r}_j - \mathbf{r}_{j'}|} - \sum_{j,i}^{n_e, N_n} \frac{Z_i e^2}{|\mathbf{R}_i - \mathbf{r}_j|} \qquad (2.1)$$

$$+ \frac{1}{2} \sum_{i \neq i'}^{N_n} \frac{Z_i Z_{i'} e^2}{|\mathbf{R}_i - \mathbf{R}_{i'}|} - \sum_i^{N_n} \frac{\hbar^2}{2M_i} \nabla_{\mathbf{R}_i}^2 \;,$$

where m_e and M_i are the electron mass and the mass of the ith nucleus, respectively, $\hbar$ is the reduced Planck constant, $\mathbf{r}_j$ and $\mathbf{R}_i$ are the position vectors of the jth electron and the ith nucleus, Z_i is the atomic number of the ith nucleus, e is the elementary charge, and $\nabla_{\mathbf{r}_j}^2$ and $\nabla_{\mathbf{R}_i}^2$ are respectively the Laplace operator along the electron and nucleus position vectors.

The stationary states of the system fulfill the time-independent Schrödinger equation, which is:[1]

$$H\Psi(\{\mathbf{R}\}, \{\mathbf{r}\}) = E\Psi(\{\mathbf{R}\}, \{\mathbf{r}\}) \;, \qquad (2.2)$$

where $\{\mathbf{R}\}$ and $\{\mathbf{r}\}$ denote the total set of coordinates of the nuclei and the electrons, respectively, and $\Psi(\{\mathbf{R}\}, \{\mathbf{r}\})$ is the stationary many-body wave function. The time-independent Schrödinger equation for the n_e electrons where $\{\mathbf{R}\}$ is held fixed is chosen to construct a set of basis states where Ψ can be expanded [163]. It is written as:

$$H_e \Phi_\nu(\{\mathbf{R}\}, \{\mathbf{r}\}) = E_\nu^e(\{\mathbf{R}\})\Phi_\nu(\{\mathbf{R}\}, \{\mathbf{r}\}) \;, \qquad (2.3)$$

where H_e is the electronic Hamiltonian which is expressed as:

$$H_e = T_e + V_{ee} + V_{ne} + V_{nn} \;. \qquad (2.4)$$

Equation (2.3) is called the *electronic wave equation* where the eigenvalues E_ν^e and the electronic wave functions $\Phi_\nu(\{\mathbf{R}\}, \{\mathbf{r}\})$ for each electronic state ν depend on $\{\mathbf{R}\}$ [163]. For each value of $\{\mathbf{R}\}$, the electronic wave functions $\Phi_\nu(\{\mathbf{R}\}, \{\mathbf{r}\})$ form a complete orthonormal basis set. Then, the total wave function Ψ can be expanded using this basis set as [163]:

$$\Psi(\{\mathbf{R}\}, \{\mathbf{r}\}) = \sum_\nu \Lambda_\nu(\{\mathbf{R}\})\Phi_\nu(\{\mathbf{R}\}, \{\mathbf{r}\}) \;, \qquad (2.5)$$

where the Λ_ν are the expansion coefficients depending on the nucleus coordinates $\{\mathbf{R}\}$. To solve equation (2.2), we first note that the Hamiltonian of the complete

---

[1]To simplify the notation, the dependence of Ψ on the spin variable will not be displayed.

system can be written as:

$$H = H_e + T_n \ , \tag{2.6}$$

which, according to the expansion (2.5), leads to the following:

$$(T_n + H_e) \sum_\nu \Lambda_\nu(\{\mathbf{R}\}) \Phi_\nu(\{\mathbf{R}\}\}, \{\mathbf{r}\}) = E \sum_\nu \Lambda_\nu(\{\mathbf{R}\}) \Phi_\nu(\{\mathbf{R}\}, \{\mathbf{r}\}) \ . \tag{2.7}$$

As detailed in Appendix A, by projecting equation (2.7) successively on the functions Φ_μ ($\mu = 0, 1, 2, \ldots$), the following equations are obtained [163–166]:

$$\left[E_\mu^e(\{\mathbf{R}\}) + T_n \right] \Lambda_\mu(\{\mathbf{R}\}) + \sum_\nu (\mathcal{A}_{\mu\nu} + \mathcal{B}_{\mu\nu}) \Lambda_\mu(\{\mathbf{R}\}) = E \Lambda_\mu(\{\mathbf{R}\}) \ , \tag{2.8}$$

where $\mathcal{A}_{\mu\nu}$ and $\mathcal{B}_{\mu\nu}$ are defined as:

$$\mathcal{A}_{\mu\nu} = -\sum_i^{N_n} \frac{\hbar^2}{2M_i} \langle \Phi_\mu | \nabla_{\mathbf{R}_i^2} | \Phi_\nu \rangle \ , \tag{2.9}$$

$$\mathcal{B}_{\mu\nu} = -\sum_i^{N_n} \frac{\hbar^2}{M_i} \langle \Phi_\mu | \nabla_{\mathbf{R}_i} | \Phi_\nu \rangle \nabla_{\mathbf{R}_i} \ . \tag{2.10}$$

The set of coupled equations (2.8) is an exact solution of the total time-independent Schrödinger equation (2.2). The Born-Oppenheimer approximation will then be introduced because the nuclear motion is slow compared to the electron one. Then, the electronic wave functions $\Phi_\nu(\{\mathbf{R}\}, \{\mathbf{r}\})$ in $\mathcal{A}_{\mu\nu}$ and $\mathcal{B}_{\mu\nu}$ varies slowly according to $\{\mathbf{R}\}$, which means that $\nabla_{\mathbf{R}_i} \Phi_\nu$ can be neglected compared to $\nabla_{\mathbf{R}_i} \Lambda_\nu$. In other words, $\mathcal{A}_{\mu\nu}$ and $\mathcal{B}_{\mu\nu}$ can be considered to vanish in the Born-Oppenheimer approximation. It leads to the following equation for each electronic state μ:

$$\left[E_\mu^e(\{\mathbf{R}\}) + T_n \right] \Lambda_\mu(\{\mathbf{R}\}) = E \Lambda_\mu(\{\mathbf{R}\}) \ , \tag{2.11}$$

which is an eigenvalue equation for the nuclei. At this point, the coefficients $\Lambda_\mu(\{\mathbf{R}\})$ can be identified as nuclear wave functions. In the Born-Oppenheimer approximation, the electronic wave equation (2.3) is solved at different values of $\{\mathbf{R}\}$ to obtain $E_\mu^e(\{\mathbf{R}\})$. The nuclear wave functions can be solved using $E_\mu^e(\{\mathbf{R}\})$ as the potential energy. The hypersurface $E_0^e(\{\mathbf{R}\})$ associated with the ground state $\Phi_0(\{\mathbf{R}\}, \{\mathbf{r}\})$ is commonly known as the adiabatic potential energy surface (PES), and it will be denoted as $V(\{\mathbf{R}\})$ in the rest of the manuscript.

2.2   Electronic structure

This section will use the Born-Oppenheimer (BO) approximation to write the wave function defining many-electron systems. First, we will discuss wave functions for a mono-electronic system before discussing the multi-electron case. Then, we will define the multi-fermionic wave functions through Slater determinants, which satisfies the antisymmetry property required by the Pauli exclusion principle.

2.2.1   Spin-orbitals

A one-electron wave function is called a *spin-orbital*. Such functions are usually divided into two parts: one describing the spatial distribution of the electron, called the *spatial orbitals*, and the other one specifying the spin component of the electron, the *spin function*.

Let $\phi(\mathbf{r})$ be a spatial orbital for one electron. It describes the electron probability distribution according to the electronic position vector $\mathbf{r}$ such that $|\phi(\mathbf{r})|^2 \, d\mathbf{r}$ is the probability of finding the electron in the small volume $d\mathbf{r}$. Generally, we use orthonormal basis sets such as:

$$\int d\mathbf{r} \ \phi_i^*(\mathbf{r})\phi_j(\mathbf{r}) = \delta_{ij} \ , \tag{2.12}$$

where δ_{ij} is the Kronecker symbol, defined as:

$$\delta_{ij} = \begin{cases} 0 & \text{if } i \neq j \ , \\ 1 & \text{if } i = j \ . \end{cases} \tag{2.13a}$$
$$\tag{2.13b}$$

The previous set of spatial orbitals can be expanded through a function of the form:

$$\phi(\mathbf{r}) = \sum_{i=1}^{\infty} a_i \phi_i(\mathbf{r}) \ , \tag{2.14}$$

where a_i are the expansion coefficients. Without any approximations, the previous sum is over infinity. To have numerical values, summing over infinity is not possible. Then, we usually sum over a finite number of orbitals. This number has to be sufficiently large to represent the system and not too large to make the calculation possible.

There are needs to enhance the definition of an electron. Indeed, an electron has a spin of 1/2. The spin projection quantum number over the z-axis, written s_z, can take only two possible values for a single particle: $\pm 1/2$. The positive value is referred to as *spin-up* ($\uparrow$), and the negative one as *spin-down* ($\downarrow$). The spin function defines one of these two states for a spin at coordinates ω_i, where $\alpha(\omega_i)$

represents the spin-up function, and $\beta(\omega_i)$ is the spin-down one. Combining the spin functions with the spatial orbitals, we obtain the *spin-orbital* function defined as:

$$\chi_i(\mathbf{r}) = \begin{cases} \phi_i(\mathbf{r}_i)\alpha_i(\omega_i) \ , & (2.15a) \\ \text{or} \\ \phi_i(\mathbf{r}_i)\beta_i(\omega_i) \ , & (2.15b) \end{cases}$$

where $\chi_i(\mathbf{r}_i)$ is the spin-orbital function. If the spatial orbitals are orthonormal, the spin-orbital functions will also be orthonormal.

2.2.2   Slater determinant

In the last part, we have seen the properties and definitions of a one-electron wave function. Nevertheless, multi-electronic wave functions have to be defined. One way to define them is the *Hartree product* [167], defined for a two-electrons wave function as:

$$\phi(\mathbf{r}_i, \mathbf{r}_j) = \chi_i(\mathbf{r}_i)\chi_j(\mathbf{r}_j) \ . \tag{2.16}$$

Nevertheless, this expression shows deficiency by not meeting two essential properties of the wave function:

- The electrons are not indistinguishable

- The resulting wave function does not satisfy the Pauli's principle.

Pauli's principle states that two electrons cannot have the same quantum numbers. One method to obtain a correct wave function (i.e., satisfying Pauli's principle) is using a *Slater determinant* [168]. More rigorously, the wave function has to be antisymmetric, as the following for a two-electron wave function:

$$\phi(\mathbf{r}_i, \mathbf{r}_j) = -\phi(\mathbf{r}_j, \mathbf{r}_i) \ . \tag{2.17}$$

Pauli's principle states that the wave function vanishes if two electrons occupy the same spin-orbital. It verifies both antisymmetry and exclusion principles. For a n_e-electron system, the Slater determinant is defined as:

$$\phi(\mathbf{r}_i, \mathbf{r}_j, \ldots, \mathbf{r}_{n_e}) = \frac{1}{\sqrt{n_e!}} \begin{vmatrix} \chi_i(\mathbf{r}_i) & \chi_j(\mathbf{r}_i) & \ldots & \chi_{n_e}(\mathbf{r}_i) \\ \chi_i(\mathbf{r}_j) & \chi_j(\mathbf{r}_j) & \ldots & \chi_{n_e}(\mathbf{r}_j) \\ \vdots & \vdots & \ddots & \vdots \\ \chi_i(\mathbf{r}_{n_e}) & \chi_j(\mathbf{r}_{n_e}) & \ldots & \chi_{n_e}(\mathbf{r}_{n_e}) \end{vmatrix} \ , \tag{2.18}$$

where $1/\sqrt{n_e!}$ is the normalization factor. For convenience, a diagonal notation for the normalized Slater determinant is used:

$$|\phi(\mathbf{r}_i, \mathbf{r}_j, \ldots, \mathbf{r}_{n_e})\rangle = |\chi_i(\mathbf{r}_i)\chi_j(\mathbf{r}_j) \ldots \chi_{n_e}(\mathbf{r}_{n_e})\rangle \ . \tag{2.19}$$

We highlight that antisymmetrizing the wave function using a single Slater determinant induces invariance of $|\phi(\mathbf{r})^2|\, d\mathbf{r}$ when exchanging two electrons in the space orbital and the spin function. Furthermore, we can use atomic orbitals (AOs) as a basis to build molecular orbitals (MOs) using the linear combination of atomic orbitals (LCAO) method. It assumes that the number of atomic and MOs are the same. Then, we can define the ith MO as:

$$\phi_i^{\text{MO}} = \sum_j c_{ji} \phi_j^{\text{AO}} \ , \tag{2.20}$$

where ϕ_i^{MO} is the MO defined as the sum of the j atomic orbitals ϕ_j^{AO} associated to a coefficient c_{ji}. We need to use methods such as the Hartree-Fock one to obtain the coefficients, detailed in the next section.

2.3   The Hartree-Fock method

Computational chemists must handle many-electrons problems except for the most straightforward cases. In the previous section, we have seen that the many-body wave function can be approximated using a single Slater determinant composed of molecular spin-orbitals. This section will present the *Hartree-Fock* method, which is the root of wave functions based methods.

We start by using the variation principle [169]. It states that the best wave function is the one that gives the lowest possible energy. It gives:

$$E_0 = \langle \chi_0 \,|\, H_e \,|\, \chi_0 \rangle \ , \tag{2.21}$$

where E_0 is the ground state energy and χ_0 the ground state wave function. One can derive the Hartree-Fock equations to minimize E_0 according to the choice of the set of spin-orbitals contained in χ_0. It determines the optimal choice for the set of spin-orbitals.

2.3.1 Hartree-Fock equations

We start the Hartree-Fock equations by introducing the kinetic and potential energy operator of an electron j interacting only with the nuclei:

$$h_j = T_e + V_{ne} = -\sum_j^{n_e} \frac{\hbar^2}{2m_e} \nabla^2_{\mathbf{r}_j} - \sum_{j,i}^{n_e, N_n} \frac{Z_i e^2}{|\mathbf{R}_i - \mathbf{r}_j|} \ , \tag{2.22}$$

$$h = \sum_j h_j \ . \tag{2.23}$$

We need to minimize $E_0 \{\chi_i\}$ with respect to the spin-orbitals under the orthonormalization constraint. We can define:

$$\int d\mathbf{r}_1 \chi_j^*(\mathbf{r}_1) \chi_i(\mathbf{r}_1) = \langle j \, | \, i \rangle = \delta_{ji} \ . \tag{2.24}$$

We can now demonstrate that an approximated expression of the ground state energy is of the form:

$$E_0 = \sum_i^{n_e} \langle i \, | \, h \, | \, i \rangle + \frac{1}{2} \sum_i^{n_e} \sum_{j \neq i}^{n_e} \left([jj|ii] - [ji|ij] \right) + V_{nn} \ . \tag{2.25}$$

2.3.2 The Coulomb and Exchange integrals

We have seen in Eq. (2.25) an expression of the ground state energy. To better understand each term of the equation, we have to decompose our spin-orbitals into spin and space parts:

$$
\begin{aligned}
[jj|ii] &= \int d\mathbf{r}_1 d\mathbf{r}_2 \ \chi_j^*(\mathbf{r}_1) \chi_j(\mathbf{r}_1) \frac{e^2}{|\mathbf{r}_j - \mathbf{r}_i|} \chi_i^*(\mathbf{r}_2) \chi_i(\mathbf{r}_2) & (2.26) \\
&= \int d\omega_1 \ \sigma_j^*(\omega_1) \sigma_j(\omega_1) \int d\omega_2 \ \sigma_i^*(\omega_2) \sigma_i(\omega_2) & (2.27) \\
&\quad \int d\mathbf{r}_1 d\mathbf{r}_2 \ \phi_j^*(\mathbf{r}_1) \phi_j(\mathbf{r}_1) \frac{e^2}{|\mathbf{r}_j - \mathbf{r}_i|} \phi_i^*(\mathbf{r}_2) \phi_i(\mathbf{r}_2) \ ,
\end{aligned}
$$

where ω_i refers to spin coordinates and σ_i to the spin of the electron (can be α_i or β_i). For the spin integration, the rules are the following:

$$
\begin{cases}
\displaystyle\int d\omega_k \; \alpha_i^*(\omega_k)\alpha_i(\omega_k) = 1 \; , & \text{(2.28a)} \\[2ex]
\displaystyle\int d\omega_k \; \beta_i^*(\omega_k)\beta_i(\omega_k) = 1 \; , & \text{(2.28b)} \\[2ex]
\displaystyle\int d\omega_k \; \alpha_i^*(\omega_k)\beta_i(\omega_k) = 0 \; , & \text{(2.28c)} \\[2ex]
\displaystyle\int d\omega_k \; \beta_i^*(\omega_k)\alpha_i(\omega_k) = 0 \; . & \text{(2.28d)}
\end{cases}
$$

In other words, the integral is 1 when integrating two similar spins and 0 when integrating two different spins.

Regarding the spin-integration of Eq. (2.27), we can see that it never cancels because both spins in the same integral are always the same. Then, if we analyze Eq. (2.27), we can see that it represents the Coulomb repulsion between electron 1 in orbital j and electron 2 in orbital i. It is usually called the *Coulomb integral* and can be further simplified as follows:

$$
J_{ij} = [ii|jj] \; . \tag{2.29}
$$

At this step, we can also analyze the second two electrons integral of Eq. (2.25) which is:

$$
\begin{aligned}
[ji|ij] &= \int d\mathbf{r}_1 d\mathbf{r}_2 \; \chi_j^*(\mathbf{r}_1)\chi_i(\mathbf{r}_1)\frac{e^2}{|\mathbf{r}_j - \mathbf{r}_i|}\chi_i^*(\mathbf{r}_2)\chi_j(\mathbf{r}_2) & \text{(2.30)} \\[2ex]
&= \int d\omega_1 \; \sigma_j^*(\omega_1)\sigma_i(\omega_1) \int d\omega_2 \; \sigma_i^*(\omega_2)\sigma_j(\omega_2) & \text{(2.31)} \\[2ex]
&\quad \int d\mathbf{r}_1 d\mathbf{r}_2 \; \phi_j^*(\mathbf{r}_1)\phi_i(\mathbf{r}_1)\frac{e^2}{|\mathbf{r}_j - \mathbf{r}_i|}\phi_i^*(\mathbf{r}_1)\phi_j(\mathbf{r}_1) \; .
\end{aligned}
$$

The spin-integration can be 0 if the spins of electron i and j are different and 1 if the spins are the same. For this term, the spin integration differs from the previous case. In opposition to Eq. (2.27), Eq. (2.32) has no classical meaning and is a direct consequence of using a Slater determinant. It is usually called *Exchange integral* and can be written as follows:

$$
K_{ij} = [ij|ji] \; . \tag{2.32}
$$

Within the same logic, we can simplify the first term of Eq. (2.25) as:

$$h_i = \langle i \,|\, h \,|\, i \rangle \ .$$

(2.33)

Finally, the Hartree-Fock energy can be written as:

$$E_{\mathrm{HF}} = \sum_i \epsilon_i - \frac{1}{2} \sum_{i,j} (J_{i,j} - K_{i,j}) \ .$$

(2.34)

2.3.3 The Fock operator

Up to this point, the Hartree-Fock equations are written as follows:

$$\left[h_i + \sum_j^{n_e} (J_{ij} - K_{ij}) \right] \chi_i = \epsilon_i \chi_i \ ,$$

(2.35)

where the Coulomb and exchange operators act here only for one electron i.

The next step is to define operators from the previous equation. The first one is called the *one-electron potential operator* v^{HF}, which is:

$$v_i^{\mathrm{HF}} = \sum_j^{n_e} (J_{ij} - K_{ij}) \ .$$

(2.36)

Therefore, we can build the Fock operator (f) as [170] :

$$f_i = h_i + v_i^{\mathrm{HF}} \ .$$

(2.37)

2.3.4 The Roothaan Equations

At this point, the Hartree-Fock equations can be written in the eigenvalue form:

$$f_i(\mathbf{r}_1)\chi_i(\mathbf{r}_1) = \epsilon_i \chi_i(\mathbf{r}_1)$$

(2.38)

This equation can be solved numerically for atoms. However, there is no practical procedure for solving this equation directly. It comes from the fact that f depends on the orbitals, which are expanded in some known basis functions $\tilde{\chi}_\mu$ as:

$$\chi_i = \sum_{\mu=1}^{N_{\mathrm{basis}}} C_{\mu i} \tilde{\chi}_\mu \ ,$$

(2.39)

where N_{basis} is the number of basis functions and $C_{\mu i}$ the expansion coefficients. It was first introduced by Roothaan [171, 172] that standard matrix techniques can

solve the previous differential equations. We also want to highlight the importance of the choice of the basis set $\{\tilde{\chi}_\mu\}$, into which will be expanded the molecular orbitals $\{\chi_i\}$, particularly for the molecular orbitals which are occupied in the groud state. For practical reasons, the sum in Eq. (2.39) is always truncated, with a finite number of known basis functions $\tilde{\chi}_\mu$. A later section will discuss constructing such basis sets and their limits.

From Eq. (2.39), we can see that the eigenvalue problem can be reduced to the problem of minimizing the total energy for a given basis set. By substituting Eq .(2.39) into Eq. (2.38), it gives:

$$f(\mathbf{r}_1) \sum_{\mu=1}^{N_{\text{basis}}} C_{\mu i} \tilde{\chi}_\mu(\mathbf{r}_1) = \epsilon_i \sum_{\mu=1}^{N_{\text{basis}}} C_{\mu i} \tilde{\chi}_\mu(\mathbf{r}_1) \ . \tag{2.40}$$

Then, by multiplying by $\tilde{\chi}_\nu^*$ and integrating, we obtain:

$$\sum_{\mu=1}^{N_{\text{basis}}} C_{\mu i} \int d\mathbf{r}_1 \ \tilde{\chi}_\nu^*(\mathbf{r}_1) f(\mathbf{r}_1) \tilde{\chi}_\mu(\mathbf{r}_1) = \epsilon_i \sum_{\mu=1}^{N_{\text{basis}}} C_{\mu i} \int d\mathbf{r}_1 \ \tilde{\chi}_\nu^*(\mathbf{r}_1) \tilde{\chi}_\mu(\mathbf{r}_1) \ . \tag{2.41}$$

We can now define the matrices involved in this equation. We first define the *Fock matrix* $\mathbf{F}_{\mu\nu}$ as:

$$\mathbf{F}_{\mu\nu} = \int d\mathbf{r}_1 \ \tilde{\chi}_\nu^*(\mathbf{r}_1) f(\mathbf{r}_1) \tilde{\chi}_\mu(\mathbf{r}_1) \ . \tag{2.42}$$

Then, the second matrix is called the *overlap matrix* $(\mathbf{S}_{\mu\nu})$ and is defined as:

$$\mathbf{S}_{\mu\nu} = \int d\mathbf{r}_1 \ \tilde{\chi}_\nu^*(\mathbf{r}_1) \tilde{\chi}_\mu(\mathbf{r}_1) \ . \tag{2.43}$$

The name of the last matrix comes from the fact that the basis set functions $\{\tilde{\chi}_\nu\}$ are generally not entirely orthogonal and overlap to a small magnitude.

With the definition of the matrices $\mathbf{F}$ and $\mathbf{S}$, we can now write Eq. (2.41) as:

$$\sum_{\mu=1}^{N_{\text{basis}}} \mathbf{F}_{\mu\nu} C_{\mu i} = \epsilon_i \sum_{\mu=1}^{N_{\text{basis}}} \mathbf{S}_{\mu\nu} C_{\mu i} \ . \tag{2.44}$$

The previous equation can also be written in a single matrix form by defining the expansion coefficient matrix as a $N_{\text{basis}} \times N_{\text{basis}}$ matrix of the form:

$$\mathbf{C} = \begin{pmatrix} C_{11} & C_{12} & \ldots & C_{1K} \\ C_{21} & C_{22} & \ldots & C_{2K} \\ \vdots & \vdots & \ddots & \vdots \\ C_{K1} & C_{K2} & \ldots & C_{KK} \end{pmatrix} . \tag{2.45}$$

In the same way, we can define orbital energy matrix $\boldsymbol{\epsilon}$ as a diagonal matrix of the form:

$$\boldsymbol{\epsilon} = \begin{pmatrix} \epsilon_1 & 0 & \ldots & 0 \\ 0 & \epsilon_2 & \ldots & 0 \\ \vdots & \vdots & \ddots & \vdots \\ 0 & 0 & \ldots & \epsilon_K \end{pmatrix} . \tag{2.46}$$

Combining all the matrix definitions in Eq. (2.44), we obtain the Roothaan equations [171, 172], which are:

$$\mathbf{FC} = \mathbf{SC}\boldsymbol{\epsilon} . \tag{2.47}$$

Finally, determining the Hartree-Fock molecular orbitals and energies involves solving the Roothaan equations self-consistently (called SCF) following this process:

1. Specify the geometry, basis set, electronic state, total spin, and charge of the molecular system

2. Compute the overlap matrix $\mathbf{S}$

3. Guess initial molecular expansion coefficients $\mathbf{C}$

4. Compute the Fock matrix $\mathbf{F}$

5. Solve the Roothaan equations

6. Use the new coefficients from the newest matrix $\mathbf{C}$ to compute a new Fock matrix $\mathbf{F}$

7. Repeat until $\mathbf{C}$ variations are under a chosen threshold value

2.3.5   Limitations

The Hartree-Fock method is the basis of numerous others methods. Nevertheless, it presents some significant limitations. Hypothetically, one can reach the Hartree-Fock limit using an infinite basis set for building molecular orbitals, which is impossible for practical reasons. Indeed, if we take, for example, N_{basis} basis set functions to compute our molecular orbitals, the number of two-electron integrals will be N_{basis}^4. This number can be very high when using many basis functions. Optimizing in a finite basis set, we reach energy higher than the exact ground state energy. The missing energy contributions come from the basis set limitation, *correlation*, and *relativistic* effects, which are neglected. They highly impact the results and lead to substantial deviations from experimental results. It can be corrected using *post-Hartree-Fock* methods, which will be developed later in the manuscript. Using alternative methods, such as density functional theory, can also lead to better results or even allow hybrid methods, i.e., treating a part of the exchange energy using the Hartree-Fock method.

2.4   Basis sets

In section (2.3.4), we have seen that the molecular spin-orbitals χ_i are expanded as a linear combination of functions, which are the basis set. Then the full HF wave function is then expressed as a single Slater determinant of occupied molecular orbitals. We have also seen that the molecular orbitals are perfectly described using an infinite basis set. However, it is not possible for practical reasons (numerical).

The main idea is to find a finite set of basis functions that efficiently approaches the Hartree-Fock limit. Nevertheless, this number of functions should be as small as possible, regarding the computational cost evocated earlier in this section. In addition, it is helpful to pick basis set functions that are computationally friendly with the calculation of the two-electron integrals. Indeed, if the latter is computed easily, we can increase the number of basis set functions without increasing too much computational time. Finally, building basis functions with some physical meaning are better. For example, they must have a large amplitude associated with high electron probability density and the reverse. They are usually developed and optimized for individual atoms. In this case, we can call them atomic orbitals. Then, the molecular orbitals can be obtained as a LCAO. Optimizing functions within these three constraints (small number of functions, computationally friendly, and having a physical meaning) is essential to finding optimal basis set functions.

2.4.1 Slater-type orbitals and Gaussian-type orbitals

As said in the previous paragraph, basis functions are usually atomic orbitals. As the standard for atomic orbitals, we separate the function into a radial part and a spherical harmonic part:

$$\tilde{\chi}_{nmla}(r_a, \theta_a, \phi_a) = f_n(r_a) Y_l^m(\theta_a, \phi_a) \ , \tag{2.48}$$

where n, l, and m are respectively the principal, azimuthal, and magnetic quantum numbers, a is the index of the concerned atom, and r_a, θ_a, ϕ_a are the spherical system coordinates with the nucleus a at his origin.

It was historically valuable to compute diatomic molecules, but it is not easy to solve numerically for larger molecules due to their computational cost [173, 174]. We first introduce Slater-type orbitals (STOs) [175], where the radial part is defined as:

$$f_n^{\text{STO}}(r_a) = r_a^{n-1} e^{-\zeta r_a} \ , \tag{2.49}$$

where ζ is a screening constant.

A second developed type of atomic orbitals is Gaussian-type orbitals (GTOs) [176]. The main idea is to use Gaussian functions to describe the atomic orbitals. The general form of the radial part is defined as:

$$f_l^{\text{GTO}}(r_a) = r_a^l e^{-\alpha r_a^2} \ , \tag{2.50}$$

where α is the exponent controlling the width of the Gaussian function. Nevertheless, using a single Gaussian function to describe an atomic orbital is insufficient and is a bad approximation to the atomic orbitals. For example, all hydrogenic atomic orbitals have an exponential decay in r_a, and GTOs have an exponential decay in r_a^2, resulting in a rapid diminution of the GTOs amplitude according to the nucleus distance [173].

One good combination is to have the efficiency of the STOs to describe atomic orbitals and the low computational cost of GTOs. A way to do it is to combine several GTOs linearly to reproduce as accurately as possible STOs. In addition, it has been shown that the deficiency of GTOs could be highly reduced when we combine them linearly [177]. These kinds of orbitals are called contracted Gaussian-type orbitals (CGTOs) and are defined as:

$$f_l^{\text{CGTO}}(r_a) = r_a^l \sum_i^M d_i e^{-\alpha_i r_a^2} \ , \tag{2.51}$$

where M is the number of GTO used in the linear combination. The coefficients d_i are set to optimize the shape of the CGTO and normalize them. The GTOs used

in the sum are called primitive Gaussian-type orbital (PGTO). They can also be tuned by optimizing α_i for each PGTO.

Hehre et al. [178] have built different CGTOs for atoms, that mimic STOs. They called them STO-MG series, where M is the number of PGTOs used to construct the CGTO.

2.4.2   Single-ζ, Multiple-ζ, and split-valence basis sets

STO-MG basis sets are called single-ζ or minimal basis sets. It comes from the fact that there is only one basis function to describe the atomic orbital [173]. Nevertheless, combining linearly different CGTOs to describe one atomic orbital is possible. It is expressed as:

$$\tilde{\chi}_{nmla}(r_a, \theta_a, \phi_a) = \sum_{m=1}^{M} z_m \, \tilde{\chi}^{\mathrm{STO}}(r_a, \zeta_m) \, , \tag{2.52}$$

where $\tilde{\chi}^{\mathrm{STO}}$ is the STO-like function, z_m is the expansion coefficient, and M is the number of functions that describe the atomic orbital. We have a M-ζ basis function from the previous equation, where M usually ranges from 1 to 6. For example, taking $M = 2$ leads to a double-ζ basis set.

Usually, core orbitals are slightly affected by chemical bonding. Consequently, the resulting molecular orbital will be similar to the corresponding atomic orbital. However, valence orbitals vary widely with chemical bonding. Then, it is more interesting to have more flexibility on valence orbitals rather than for core ones. This observation leads to the development of *split-valence* basis sets [173]. The main idea is to use a single CGTO to describe core orbitals, whereas the valence ones are split into several basis functions.

2.4.3   Polarization and diffuse functions

Some systems, like anions or supermolecular complexes, have more spatially diffuse molecular orbitals. We can increase this flexibility by adding basis functions corresponding to a higher principal quantum number than the valence orbital. Such functions are called *polarization* functions [173]. For example, we can add one p orbital to the basis set describing H atoms and d orbitals for C atoms. Adding such functions will induce valence orbitals deformation, increasing its mathematical flexibility in describing molecular orbitals.

Systems with more diffuse orbitals show to have weakly bounded electrons that can be localized far from the other electron densities. To describe those cases well, we can increase the number of basis functions with small expansion coefficients.

These basis sets are called *augmented* or *diffused* basis sets, whereas the added functions are called *diffusion* functions.

Both methods can be used separately or at the same time. We can know the basis set we use by its nomenclature. The following section will introduce two basis set families and discuss their nomenclatures.

2.4.4 Pople and Dunning basis sets

This section will introduce two basis set families, among the most used in the literature. We start with the ones adopted by Pople and coworkers [179]. They are split-valenced basis sets with a specific nomenclature of the form X-YZG for a double-ζ one and is encoded as:

X: Number of PGTO composing the core-shell

Y: Number of PGTO composing the first valence shell

Z: Number of PGTO composing the second valence shell

In the same way, triple-ζ basis sets are encoded as X-YZWG. In other words, the number of digits after the hyphen corresponds to the ζ number.

Polarization is included using the symbol *. However, an alternative encoding is preferred, and the polarization functions are encoded between parenthesis. The first number corresponds to the number of polarization functions used on heavy atoms and the second one for hydrogen atoms. If there is only one number, it refers to heavy atom polarization functions. For example, a 6-311G(2df,2p) basis set implies heavy atoms polarized by two sets of d functions and one set of f functions, and hydrogen atoms are polarized by two sets of p functions.

Regarding diffusion functions, they are indicated by the symbol "+". Only one "+" indicates diffusion functions on heavy atoms, and two "+" corresponds to diffusion functions on heavy atoms and hydrogen ones. Respectively, two examples are 6-311+G(3df,2p) and 3-21++G.

The next basis sets we will present were optimized by Dunning [180], also called *correlation-consistent* (written cc) basis sets. This family uses a "general" contraction of the core-shell. In other words, a single set of PGTO is used in *all* basis functions but with different expansion coefficients for each atom. It indicates if the basis sets have polarization functions through the letter "p" and diffusion functions through the letters "aug" for augmented. Then, it is possible to have double (D), triple (T), quadruple (Q), quintuple-ζ (5) basis sets, even a ninefold-ζ (9) basis set. For example, the basis set aug-cc-pVTZ stands for an augmented correlation consistent polarized valence-only (general contraction) triple-ζ basis set. It is also possible to double the number of diffusion functions. In this case,

it is indicated by the letters "d-aug" present in the d-aug-cc-pVQZ basis set, for example.

2.4.5 Plane waves basis sets

Theoretical calculations are also done for a non-isolated system, such as for solids or surfaces for example. For the latter case, periodic boundary conditions are necessary to describe an infinite system. We will discuss this later in the manuscript. An alternative way to build basis sets is the use of plane waves. They are intuitive to periodic conditions, and fulfill the Bloch condition [181].

In a perfect crystal, the potential energy $E_e(\mathbf{R})$ is periodic, with a periodicity of $\boldsymbol{\mathcal{R}}$, which leads to:

$$E_e(\mathbf{R}) = E_e(\mathbf{R} + \boldsymbol{\mathcal{R}}) \ . \tag{2.53}$$

Then, the Bloch conditions state that the Schrödinger equation can be solved by a basis set of solutions which must be of the form:

$$\psi(\mathbf{R}) = e^{i\mathbf{k}\cdot\mathbf{R}} u(\mathbf{R}) \ , \tag{2.54}$$

where $\mathbf{k}$ is the wave vector and $u(\mathbf{R})$ is the plane wave extension, having the same periodicity as the potential energy:

$$u(\mathbf{R}) = u(\mathbf{R} + \boldsymbol{\mathcal{R}}) \ . \tag{2.55}$$

Using a plane wave basis set, the crystalline orbitals can be expressed as:

$$\phi(\mathbf{R}, \mathbf{K}) = \sum_{\mathbf{K}} c_{\mathbf{k}.\mathbf{K}} e^{-i(\mathbf{k}+\mathbf{K})\cdot\mathbf{R}} \ , \tag{2.56}$$

where $\mathbf{K}$ are the reciprocal lattice vectors. Because we can only sum over a finite number, $\mathbf{K}$ is truncated according to the cutoff energy E_{cutoff}, which has to be set before the calculation. The condition is the following [174]:

$$\frac{\hbar^2}{2m_e}(\mathbf{k} + \mathbf{K})^2 \leq E_{\text{cutoff}} \ . \tag{2.57}$$

Regarding core electrons, we need to have a very high value for the cutoff energy if we want to describe them using plane waves. This value implies many plane waves, increasing the computational cost.

2.4.6 Basis set superposition error

The basis set superposition error (BSSE) is a common problem in quantum chemistry calculations. It arises from using finite basis sets to represent the electron density of a molecule, leading to an overestimation of the interaction energy between subsystems. The BSSE can significantly impact the accuracy of molecular properties predicted from quantum chemical calculations, such as bond lengths, reaction energetics, and reaction pathways.

The BSSE occurs because using finite basis sets leads to an incomplete representation of the electron density. When subsystems are treated separately, they occupy their own basis set, leading to overcounting of the electron-electron repulsion energy between them [182]. The BSSE can be corrected by various methods, including counterpoise correction [182], which aim to remove the overcounting of electron-electron repulsion energy and improve the accuracy of the calculated interaction energy.

2.5 Post-Hartree-Fock methods

As we have introduced previously in this manuscript, one disadvantage of the Hartree-Fock method is the lack of correlation energy. Post-Hartree-Fock methods were developed, to include the electronic correlation in the total energy calculations. In this manuscript, we will describe two methods, which are the Møller-Plesset perturbation theory (MPPT), particularly the second order expansion (MP2) [183], and finally, the Coupled Cluster (CC) method.

2.5.1 Møller-Plesset perturbation theory

The idea behind MPPT is to include correlation energy by slightly perturbating the original one. It can be done by adding a perturbated Hamiltonian to the unperturbed one. If the perturbation is small enough, quantities obtained by the perturbed Hamiltonian can be seen as corrections to the unperturbed one. To fully describe how MPPT works, we will describe the time-independent perturbation theory, also known as the Rayleigh-Schrödinger perturbation theory (RSPT) [184, 185]. This method has several levels of corrections. We will describe the first, then second order correction, to end with the general case of the nth order correction.

To start with RSPT, we must pick an unperturbed Hamiltonian, written $H^{(0)}$, where the superscript defines the correction order. We assume that the latter has no time dependency, known energy levels, and known eigenstates. Then, a perturbation is introduced through a perturbative Hamiltonian, written V. The latter is weighted by a dimensionless parameter, λ, varying between 0 (no perturbation) to 1 ("full"

Table 2.1: Rayleigh-Schrödinger perturbation theory corrections according to the powers of λ for the first 3rd rows

λ order	Terms from Eq. (2.59)
λ^0	$H^{(0)}\left|\chi_i^{(0)}\right\rangle = E_i^{(0)}\left|\chi_i^{(0)}\right\rangle$
λ^1	$H^{(0)}\left|\chi_i^{(1)}\right\rangle + V\left|\chi_i^{(0)}\right\rangle = E_i^{(0)}\left|\chi_i^{(1)}\right\rangle + E_i^{(1)}\left|\chi_i^{(0)}\right\rangle$
λ^2	$H^{(0)}\left|\chi_i^{(2)}\right\rangle + V\left|\chi_i^{(1)}\right\rangle = E_i^{(0)}\left|\chi_i^{(2)}\right\rangle + E_i^{(1)}\left|\chi_i^{(1)}\right\rangle + E_i^{(2)}\left|\chi_i^{(0)}\right\rangle$

perturbation). In this case, our final Hamiltonian, H, is defined as:

$$H = H^{(0)} + \lambda V \ . \tag{2.58}$$

We can now apply this Hamiltonian to spin-orbitals, which gives:

$$(H^{(0)} + \lambda V)\left|\chi_i\right\rangle = E_i\left|\chi_i\right\rangle \ . \tag{2.59}$$

Within this formalism, the wave function and the energy can be expressed as a power series of λ, as:

$$\begin{cases} \left|\chi_i\right\rangle = \sum_j \lambda^j \left|\chi_i^{(j)}\right\rangle \ , & \text{(2.60a)} \\ \\ E_i = \sum_j \lambda^j E_i^{(j)} \ . & \text{(2.60b)} \end{cases}$$

By plugging Eqs. (2.60) into Eq. (2.59) and grouping terms according to the powers of λ, we obtain the results shown in Table 2.1. Multiplying the first-order correction by the unperturbed wave-function $\left\langle\chi_i^{(0)}\right|$, we can obtain the first-order correction to the energy, which is:

$$\left\langle\chi_i^{(0)}\left|V\right|\chi_i^{(0)}\right\rangle = E_i^{(1)} \ . \tag{2.61}$$

This result shows that the first-order correction to the unperturbed system is the expectation value of the perturbative Hamiltonian over the unperturbed wave function.

Going to the second order correction and using the same methodology as before, we then have:

$$\left\langle\chi_i^{(0)}\left|V\right|\chi_i^{(1)}\right\rangle = E_i^{(2)} \ . \tag{2.62}$$

In a general way, we can obtain the nth-order correction energy as:

$$\left\langle \chi_i^{(0)} \middle| V \middle| \chi_i^{(n-1)} \right\rangle = E_i^{(n)} \ . \tag{2.63}$$

As written before, we must define an unperturbed Hamiltonian $H^{(0)}$. MPPT is typically a particular case of the RSPT. In this case, we will write the unperturbed Hamiltonian as the sum of the Fock operators, leading to:

$$H^{(0)} = \sum_i f_i = \sum_i \left[h_i + v_i^{\text{HF}} \right] \ . \tag{2.64}$$

Then, we can define the perturbative Hamiltonian as the difference between $H^{(0)}$ and H, leading to:

$$V = H^{(0)} - H = \frac{1}{2} \sum_{i,j} \left(J_{ij} - K_{ij} \right) - \sum_i v_i^{\text{HF}} \ . \tag{2.65}$$

Within this scheme, the first-order correction to the energy is given by:

$$E_0^{(1)} = -\frac{1}{2} \sum_{i,j} \left(J_{ij} - K_{ij} \right) \ , \tag{2.66}$$

leading to a total energy of :

$$E_0^{(0)} + E_0^{(1)} = \sum_i \epsilon_i - \frac{1}{2} \sum_{i,j} \left(J_{ij} - K_{ij} \right) = E_{\text{HF}} \ . \tag{2.67}$$

From the previous equation, we can see that the first-order corrected energy is the Hartree-Fock energy. Then, we must to go to the second-order correction to improve this energy. Using Eq. (2.62) and Eq. (2.39), it can be proved that the ground state MP2 energy can be expressed as [186]:

$$E_0^{(2)} = \sum_{\mu \neq 0} \frac{\left| \left\langle \chi_0^{(0)} \middle| V \middle| \chi_\mu^{(0)} \right\rangle \right|^2}{E_0^{(0)} - E_\mu^{(0)}} \ . \tag{2.68}$$

MP2 is the least costly *ab initio* method for correcting Hartree-Fock results by including correlation energy. It scales as $O(M^5)$, with M being the number of orbitals in the total basis set. Nevertheless, one main disadvantage of MPPT is that it computes correlation effects from Hartree-Fock orbitals, which are mean-field orbitals. It can lead to symmetry breaking and spin contaminations in some specific cases [187].

2.5.2   Coupled Cluster theory

Another important post-Hartree-Fock method is the CC theory. The idea behind this is to express the wave function as an exponential *ansatz*:

$$|\phi_{\text{CC}}\rangle = e^T |\phi_0\rangle \ , \tag{2.69}$$

where $|\phi_{\text{CC}}\rangle$ is the CC wave function, and T is the cluster operator that acts on the reference wave function $|\phi_0\rangle$. The cluster operator can be expressed as:

$$T = \sum_l T_l \ , \tag{2.70}$$

where T_l operators generate all possible determinants with l excitations from the reference [173].

Then, using the definition of T in Eq. (2.70) and using it to expand the exponential in Eq (2.69) as power series, we can obtain the following:

$$e^T = 1 + T + \frac{T^2}{2!} + \frac{T^3}{3!} + \cdots \ . \tag{2.71}$$

Within this scheme, we can define the one-particle excitation operator T_1 and the two-particle excitation operator T_2 as [188]:

$$T_1 |\phi_0\rangle = \sum_{a=n_e+1}^{M} \sum_{i=1}^{n_e} t_i^a |\phi_i^a\rangle \ , \tag{2.72}$$

$$T_2 |\phi_0\rangle = \sum_{b=a+1}^{M} \sum_{a=n_e+1}^{M} \sum_{j=i+1}^{n_e} \sum_{i=1}^{n_e-1} t_{ij}^{ab} |\phi_{ij}^{ab}\rangle \ , \tag{2.73}$$

where $|\phi_i^a\rangle$ is a single Slater determinant, in which we have replaced the spin-orbital χ_i with the virtual one χ_a, and t_i^a is a coefficient depending on i and a. A virtual orbital is a type of molecular orbital in quantum chemistry that is not occupied in the ground state. For the two-particle excitation operator, the same process happens, but we replace two spin-orbitals χ_i and χ_j, with two virtual ones, which are respectively χ_a and χ_b. In other words, e^T in Eq. (2.69) expresses the $|\phi_0\rangle$ as a linear combination of Slater determinants including ϕ_0 and all possible electron excitations from occupied to virtual states [188]. This electronic mixing into the wave function allows electrons to keep away from one another and then provides electronic correlation.

The objective in CC calculations is to find the *amplitudes t* from Eq. (2.73) for all the possible configurations. Once done, the CC wave function ϕ_{CC} from

Eq. (2.69) is known. Considering the CC singles and doubles, written CCSD, we can obtain the CC energy by solving the following:

$$\left\langle \phi_0 \left| e^{-(T_1+T_2)} H e^{(T_1+T_2)} \right| \phi_0 \right\rangle = E_{\text{CCSD}} \ , \tag{2.74}$$

$$\left\langle \phi_i^a \left| e^{-(T_1+T_2)} H e^{(T_1+T_2)} \right| \phi_0 \right\rangle = 0 \ , \tag{2.75}$$

$$\left\langle \phi_{ij}^{ab} \left| e^{-(T_1+T_2)} H e^{(T_1+T_2)} \right| \phi_0 \right\rangle = 0 \ . \tag{2.76}$$

To further improve the resulting CCSD energy, ones can define the CC singles, doubles, and triples (CCSDT) by defining a cluster operator of the form $T = T_1 + T_2 + T_3$. It gives accurate correlation energy and molecular properties results but at a high computational cost. An alternative is to include the triple excitations using a perturbative method. In this case, we write it as CCSD(T) method [189], one of the most popular and successful extensions of the CC theory.

2.6   Density functional theory

Even if equation (2.3) goes from the $3n_e + 3N_n$ degrees of freedom of the potential energy surface to only $3n_e$ using the Born-Oppenheimer approximation, it is still hard to tackle. The theorems made by *Hohenberg and Kohn* [190] allows overcoming this issue by using the electronic density $n(\mathbf{r})$.

2.6.1   One body density

Considering a system composed of n_e indistinguishable electrons with $\mathbf{r}_1, \mathbf{r}_2, \ldots, \mathbf{r}_{n_e}$ their corresponding positions, then $\left|\phi(\mathbf{r}_1, \ldots, \mathbf{r}_{n_e})\right|^2$ is the probability density of the coincidence measurement of the positions of those n_e electrons. Since $\mathbf{r}_1$ is the position vector of electron 1, $p(\mathbf{r}_1)d\mathbf{r}_1$ is the probability of finding electron 1 in a volume $d\mathbf{r}_1$ around $\mathbf{r}_1$, whatever the positions of the other electrons. Since electrons are indistinguishable particles, $\mathbf{r}_1$ can be written $\mathbf{r}$, then the probability density $p(\mathbf{r})$ is given by [163]:

$$p(\mathbf{r}) = \int d\mathbf{r}_2 d\mathbf{r}_3 \ldots d\mathbf{r}_{n_e} \left|\phi(\mathbf{r}, \ldots, \mathbf{r}_{n_e})\right|^2 \ . \tag{2.77}$$

In order to have the mean number of electrons in a volume $d\mathbf{r}$ around $\mathbf{r}$, the probability density has to be multiplied by the number of electrons n_e and by $d\mathbf{r}$. It is, therefore, $n_e p(\mathbf{r})d\mathbf{r}$ to give the density at $\mathbf{r}$, which is $n(\mathbf{r}) = n_e p(\mathbf{r})$. Then, the total expression for the electronic density is:

$$n(\mathbf{r}) = n_e \int d\mathbf{r}_2 \ldots d\mathbf{r}_{n_e} \left|\phi(\mathbf{r}, \ldots, \mathbf{r}_{n_e})\right|^2 \ . \tag{2.78}$$

2.6.2   The Hohenberg and Kohn theorems

For any system consisting of electrons moving under the influence of an external potential $v_{ext}(\mathbf{r})$, the Hohenberg and Kohn theorems state [190]:

Theorem 1. The external potential $v_{ext}(\mathbf{r})$ is determined, within a trivial additive constant, by the electron density $n(\mathbf{r})$.

Theorem 2. The exact ground state electron density $n(\mathbf{r})$ minimizes the electron energy functional $E_e[n(\mathbf{r})]$.

The electronic Hamiltonian can be written as a function of the electron density. With the use of equation (2.78), the electron-nucleus interaction is:

$$
\begin{aligned}
E_{ne}[n(\mathbf{r})] &= \langle \phi | \widehat{V}_{ne} | \phi \rangle = -\sum_i^{N_n} Z_i e^2 \int d\mathbf{r} \ldots \, d\mathbf{r}_{n_e} \frac{\left| \phi(\mathbf{r}, \ldots, \mathbf{r}_{n_e}) \right|^2}{|\mathbf{R}_i - \mathbf{r}|} \\
&= -\sum_i^{N_n} Z_i e^2 \int d\mathbf{r} \frac{n(\mathbf{r})}{|\mathbf{R}_i - \mathbf{r}|} = \int d\mathbf{r} \; n(\mathbf{r}) v_{ext}(\mathbf{r}) \;,
\end{aligned} \tag{2.79}
$$

where $v_{ext}(\mathbf{r})$ is defined as the external potential created by the nuclei. The electron-electron interaction term is decomposed into two terms because of the two-electron problem.

$$
E_{ee}[n(\mathbf{r})] = \frac{e^2}{2} \iint d\mathbf{r} \; d\mathbf{r}' \; \frac{n(\mathbf{r})n(\mathbf{r}')}{|\mathbf{r} - \mathbf{r}'|} + E_{xc}[n(\mathbf{r})] \;. \tag{2.80}
$$

The first term,

$$
E_H[n(\mathbf{r})] = \frac{e}{2} \iint d\mathbf{r} \; d\mathbf{r}' \; \frac{n(\mathbf{r})n(\mathbf{r}')}{|\mathbf{r} - \mathbf{r}'|} \;, \tag{2.81}
$$

is the Hartree energy, coming from the classical electron-electron electrostatic interaction, and $E_{xc}[n(\mathbf{r})]$ is the exchange-correlation energy. The latter lowers the energy, which makes the Hartree energy higher than the real one. Those terms and kinetic energy are usually summarized in a new functional $F[n(\mathbf{r})]$.

Finally, with equations (2.79) and (2.80), the total electron energy functional is written as:

$$
E_e[n(\mathbf{r})] = E_{ne}[n(\mathbf{r})] + F[n(\mathbf{r})] \;. \tag{2.82}
$$

Using the Hohenberg and Kohn theorems [190], the ground state can be described by minimizing the electron energy functional $E_e[n(\mathbf{r})]$, and it is a unique solution. However, the exact analytical expression for $E_{xc}[n(\mathbf{r})]$ and the kinetic energy term are unknown. Thus approximations are required.

2.6.3   Kohn-Sham equations

In order to overcome the issues from the kinetic energy functional calculation and the interactions between electrons, Kohn and Sham [191] proposed to build a fictitious system of non-interacting electrons that produces the exact ground state electronic density as the original interacting electrons system.

For an interacting electron system, the electronic energy functional can be written as:

$$E_e[n(\mathbf{r})] = T_s[n(\mathbf{r})] + \frac{e}{2} \iint d\mathbf{r}d\mathbf{r}' \, \frac{n(\mathbf{r})n(\mathbf{r}')}{|\mathbf{r} - \mathbf{r}'|} + E_{xc}[n(\mathbf{r})] + \int d\mathbf{r} \, v_{ext}(\mathbf{r})n(\mathbf{r}) \, , \quad (2.83)$$

with $T_s[n(\mathbf{r})]$, the kinetic energy functional of non-interacting electrons. The variation of the previous electronic energy functional subject to the conservation of the number of electrons in the system ($\int d\mathbf{r} \, n(\mathbf{r}) = n_e$) gives[2] [192]:

$$\partial \Big[E_e[n(\mathbf{r})] - \mu \Big(\int d\mathbf{r} \, n(\mathbf{r}) - n_e \Big) \Big] = 0 \, , \quad (2.84)$$

$$\mu = \frac{\partial E_e[n(\mathbf{r})]}{\partial n(\mathbf{r})} = \frac{\partial T_s[n(\mathbf{r})]}{\partial n(\mathbf{r})} + e \int d\mathbf{r}' \frac{n(\mathbf{r}')}{|\mathbf{r} - \mathbf{r}'|} + \frac{\partial E_{xc}[n(\mathbf{r})]}{\partial n(\mathbf{r})} + v_{ext}(\mathbf{r}) \, , \quad (2.85)$$

with μ the chemical potential.

If the same calculation is done considering non-interacting electrons moving under an effective potential v_{eff}, equations (2.83) and (2.85) become:

$$E_e[n(\mathbf{r})] = T_s[n(\mathbf{r})] + \int d\mathbf{r} \, v_{eff}(\mathbf{r})n(\mathbf{r}) \, , \quad (2.86)$$

$$\mu = \frac{\partial T_s[n(\mathbf{r})]}{\partial n(\mathbf{r})} + v_{eff}(\mathbf{r}) \, . \quad (2.87)$$

By identification between equation (2.85) and (2.87), $v_{eff}(\mathbf{r})$ is defined as:

$$v_{eff}(\mathbf{r}) = v_{ext}(\mathbf{r}) + e \int d\mathbf{r}' \frac{n(\mathbf{r}')}{|\mathbf{r} - \mathbf{r}'|} + v_{xc}(\mathbf{r}) \, , \quad (2.88)$$

with

$$v_{xc}(\mathbf{r}) = \frac{\partial E_{xc}[n(\mathbf{r})]}{\partial n(\mathbf{r})} \, . \quad (2.89)$$

---

[2] $\partial E_e[n(\mathbf{r})]/\partial n(\mathbf{r})$ is the functional derivative of $E_e[n(\mathbf{r})]$ with respect to $n(\mathbf{r})$

The effective potential $v_{eff}(\mathbf{r})$ changes the many-particle problem into a fictitious single-particle problem, and the corresponding Hamiltonian $h_{eff}(\mathbf{r})$ is:

$$h_{eff}(\mathbf{r}) = -\frac{\hbar^2}{2m_e}\nabla^2_{\mathbf{r}} + v_{eff}(\mathbf{r}) \ , \qquad (2.90)$$

which leads to a set of coupled single-particle Schrödinger-like equations called Kohn-Sham equations

$$h_{eff}(\mathbf{r})\phi_i^{KS}(\mathbf{r}) = \left[-\frac{\hbar^2}{2m_e}\nabla^2_{\mathbf{r}} + v_{eff}(\mathbf{r})\right]\phi_i^{KS}(\mathbf{r}) = \epsilon_i\phi_i^{KS}(\mathbf{r}) \ . \qquad (2.91)$$

The ground state density for closed-shell systems only is given by:

$$n(\mathbf{r}) = 2\sum_{i=1}^{n_e/2} |\phi_i^{KS}(\mathbf{r})|^2 \ , \qquad (2.92)$$

where the sum is over the n_e lowest occupied orbitals. The kinetic energy functional of non-interacting electrons, $T_s[n(\mathbf{r})]$, can be exactly computed at this step and is:

$$T_s[n(\mathbf{r})] = \sum_{i=1}^{n_e} \langle\phi_i^{KS}| -\frac{\hbar^2}{2m_e}\nabla^2_{\mathbf{r}}|\phi_i^{KS}\rangle = \sum_{i=1}^{n_e} \epsilon_i - \int d\mathbf{r} \ v_{eff}(\mathbf{r})n(\mathbf{r}) \ . \qquad (2.93)$$

Finally, combining equations (2.86), (2.88), (2.89), and (2.93), the total energy can be written as

$$E_e[n(\mathbf{r})] = \sum_{i=1}^{n_e} \epsilon_i - \frac{e^2}{2}\iint d\mathbf{r}d\mathbf{r'} \ \frac{n(\mathbf{r})n(\mathbf{r'})}{|\mathbf{r}-\mathbf{r'}|} + E_{xc}[n(\mathbf{r})] - \int d\mathbf{r} \ v_{xc}(\mathbf{r})n(\mathbf{r}) \ . \quad (2.94)$$

Finally, the Kohn-Sham equations are solved self-consistently[3] by repeating the following procedure until the desired convergence threshold is achieved:[4]

$$n^{(i)}(\mathbf{r}) \to v_{eff}^{(i)}(\mathbf{r}) \to \texttt{KS equations} \to [\phi_j^{KS}(\mathbf{r})]^{(i+1)} \to n^{(i+1)}(\mathbf{r}) \ . \qquad (2.95)$$

The exchange-correlation functional $E_{xc}[n(\mathbf{r})]$ is approximated, and an appropriate expression has to be found. Using the Born-Oppenheimer approximation (which does not consider the non-adiabatic terms), the Hohenberg and Kohn theorems, and the Kohn-Sham equations, the electronic energy can be computed by approximate density functional theory (DFT) calculations.

---

[3] As in Hartree-Fock theory
[4] The superscript (i) refers here to the iteration number

2.7 Phonons and harmonic vibrational frequencies from density functional perturbation theory

In modern solid-state physics, the theory of lattice vibrations is one of the best established. Many physical properties can be computed, such as specific heat, heat conduction, and electron-phonon interactions. Others can be compared to experiments using infrared (IR), Raman spectroscopy, and elastic neutron scattering methods. Computing such properties are evidence that our quantum picture of the system is correct [193]. Density functional perturbation theory (DFPT) is a way to describe the vibrational properties through the linear response of the electron density from the perturbation of the external potential. Because crystal structures are central in periodic DFT codes, we will describe such systems and how to find the minimum energy geometry.

2.7.1 Lattice dynamics

All the ions are assumed to be at their equilibrium positions, following the Born-Oppenheimer approximation, with all the forces at their minimum (the latter will be defined later in the manuscript). Of course, ions are quantum objects and can not be in an absolute well-defined position without moving because it breaks Heisenberg's uncertainty principle. Then here, it is assumed that the system's temperature is well below the melting point of the crystal. It allows the ions to move and perform oscillations around their equilibrium positions without breaking the crystal.

In the first part, all the electrons will be forgotten to simplify equations. They will be treated later in this section. The studied system is a 3D supercell composed of $N = N_1 N_2 N_3$ unit cells and periodic boundary conditions. Respectively, N_1, N_2, and N_3 are the number of unit cells that compose the crystal supercell in the $\mathbf{a_1}$, $\mathbf{a_2}$, and $\mathbf{a_3}$ directions. The unit cells are indexed by $n = (n_1, n_2, n_3)$, where each n_i are integers starting from 1 to N_i. Then, we can define the volume of the supercell, which is $N_1 a_1 \times N_2 a_2 \times N_3 a_3$, and the location of each unit cell, set by $\boldsymbol{\mathcal{R}}_n$, which is:

$$\boldsymbol{\mathcal{R}}_n = \sum_{i=1}^{3} n_i \mathbf{a}_i \ . \tag{2.96}$$

Let us consider that there are N_n atoms per unit cell, labeled i, with a corresponding mass M_i, at their equilibrium position $\mathbf{R}_i$. Then, within the frozen approximation, atom i is at position $\boldsymbol{\mathcal{R}}_{n,i}^{\mathrm{frozen}}$ which is:

$$\boldsymbol{\mathcal{R}}_{n,i}^{\mathrm{frozen}} = \boldsymbol{\mathcal{R}}_n + \mathbf{R}_i \ . \tag{2.97}$$
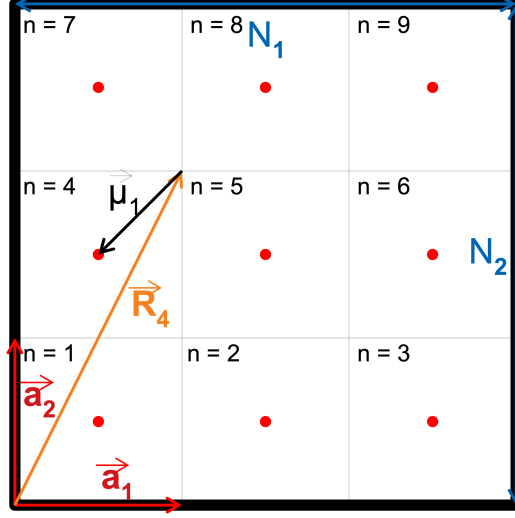
Figure 2.1: *Schematic representation of a system in 2 dimensions composed by 1 supercell, 9 atoms, and 9 unit cells*. *The supercell is in bold black. Unit cells are represented in black dotted line. Atoms are in red. Here, $r = 1$ and α can only take the value 1.*

If ions are allowed to oscillate around their equilibrium positions, then equation (2.97) becomes:

$$\boldsymbol{\mathcal{R}}_{n,i} = \boldsymbol{\mathcal{R}}_n + \mathbf{R}_i + \boldsymbol{\mu}_{n,i}(t) \; , \tag{2.98}$$

where $\boldsymbol{\mu}_{n,i}(t)$ is the displacement from the equilibrium position of ion i in the unit cell labeled n. A schematic 2D representation of this system is presented in Figure 2.1. From now on, the labelled unit cell will not be written for clarity.

Within the Born-Oppenheimer approximation, nuclei move on a potential energy surface given by the total electronic energy $E_e(\mathbf{R}, \boldsymbol{\mu}_i)$. If $\|\boldsymbol{\mu}_i\|$ is small, we can expand $E_e(\mathbf{R}, \boldsymbol{\mu}_i)$ in a Taylor series according to $\boldsymbol{\mu}_i$. Within the harmonic approximation (i.e., limited to second order), we get:

$$
\begin{aligned}
E_e(\mathbf{R}, \boldsymbol{\mu}_i) = E_e(\mathbf{R}) + \sum_{i,\alpha} \nabla_{\boldsymbol{\mu}_{i,\alpha}} E_e(\mathbf{R}) \boldsymbol{\mu}_{i,\alpha} \\
+ \frac{1}{2} \sum_{i\alpha, i'\beta} \nabla_{\boldsymbol{\mu}_{i,\alpha}} \nabla_{\boldsymbol{\mu}_{i',\beta}} E_e(\mathbf{R}) \boldsymbol{\mu}_{i,\alpha} \boldsymbol{\mu}_{i',\beta} \; ,
\end{aligned}
\tag{2.99}
$$

where the gradients are calculated at $\boldsymbol{\mu}_i = \mathbf{0}$, and α and β represent the three Cartesian coordinates. Regarding the second term in Eq. (2.99), we can identify the interatomic forces ($\mathbf{F}_I$).

The Hellman-Feynman theorem [194, 195] links the partial derivative of the system total energy $(E\{\mathbf{R}\})$ according to a parameter λ to the expectation value of the derivative of the Hamiltonian with respect to λ. It is a fundamental tool to compute the equilibrium geometry and the vibrational properties of the system, as it allows the computation of the first and second derivatives of the potential energy surface. It is expressed as:

$$\frac{\partial E_\lambda}{\partial \lambda} = \left\langle \Psi_\lambda \left| \frac{\partial H_\lambda}{\partial \lambda} \right| \Psi_\lambda \right\rangle . \tag{2.100}$$

Using it, we can now express the interatomic forces as:

$$\mathbf{F}_I \equiv -\nabla_{\mathbf{R}} E_e = \mathbf{0} . \tag{2.101}$$

The forces here are zero because we assumed all the ions were at equilibrium. Consequently, the second term of the right hand in Eq. (2.99) vanishes. The second-order derivatives correspond to a symmetric matrix called the Hessian matrix [196, 197]. All the eigenvalues must be positive if the system is at a local or global minimum energy. The Hessian matrix is also called the force-constant matrix $(\mathcal{C}_{i',\beta}^{i,\alpha})$, and is defined as the following:

$$\mathcal{C}_{i',\beta}^{i,\alpha} = \nabla_{\boldsymbol{\mu}_{i,\alpha}} \nabla_{\boldsymbol{\mu}_{i',\beta}} E_e(\mathbf{R}) . \tag{2.102}$$

Therefore, Eq (2.99) can be written as:

$$E_e(\mathbf{R}, \boldsymbol{\mu}_i) = E_e(\mathbf{R}) + \frac{1}{2} \sum_{i\alpha, i'\beta} \mathcal{C}_{i',\beta}^{i,\alpha} \, \boldsymbol{\mu}_{i,\alpha} \boldsymbol{\mu}_{i',\beta} . \tag{2.103}$$

When an ion is displaced from its equilibrium position, a force appears. The latter follows the principle of virtual work. Applying this to the displacement $\boldsymbol{\mu}_{i,\alpha}$ of Eq. (2.103), we have:

$$\mathbf{F}_I(i, \alpha) = -\nabla_{\boldsymbol{\mu}_{i,\alpha}} E_e(\mathbf{R}, \boldsymbol{\mu}_i) = -\frac{1}{2} \sum_{i\alpha, i'\beta} \mathcal{C}_{i',\beta}^{i,\alpha} \, \boldsymbol{\mu}_{i',\beta} . \tag{2.104}$$

Then, the classical Lagrangian for the ions is:

$$\mathcal{L} = \frac{1}{2} \sum_{i,\alpha} M_i \dot{\boldsymbol{\mu}}_{i,\alpha}^2 - \frac{1}{2} \sum_{i\alpha, i'\beta} \mathcal{C}_{i',\beta}^{i,\alpha} \, \boldsymbol{\mu}_{i,\alpha} \boldsymbol{\mu}_{i',\beta} . \tag{2.105}$$

The corresponding Euler-Lagrange equation is then:

$$M_i \ddot{\boldsymbol{\mu}}_{i,\alpha} = -\sum_{i'\beta} \boldsymbol{\mathcal{C}}^{i,\alpha}_{i',\beta} \, \boldsymbol{\mu}_{i',\beta} \ , \tag{2.106}$$

where $\dot{\boldsymbol{\mu}}_{i,\alpha}$ and $\ddot{\boldsymbol{\mu}}_{i,\alpha}$ are, respectively, the first and second time derivatives of $\boldsymbol{\mu}_{i,\alpha}$. The next step is to find an expression for $\boldsymbol{\mu}_{i,\alpha}$. Since it is a set of coupled harmonic oscillators, using the *Born-von Kármán* periodic boundary conditions as well as Bloch's theorem [181], a reasonable ansatz is to use plane-waves as solutions:

$$\boldsymbol{\mu}_{n,i,\alpha}(t) = \frac{\mathbf{A}_\alpha(i,\mathbf{q})}{\sqrt{M_i}} e^{i(\mathbf{q}\cdot\mathbf{R}_n - \omega t)} \ , \tag{2.107}$$

where $\mathbf{q}$ is the wave vector, ω the vibrational pulsation, and $\mathbf{A}_\alpha(i,\mathbf{q})$ is the plane wave amplitude. Inserting Eq. (2.107) into Eq. (2.106), we obtain the following result:

$$\omega^2 \mathbf{A}_\alpha(i,\mathbf{q}) = \sum_{i'\beta m} \frac{\boldsymbol{\mathcal{C}}^{i,\alpha}_{i',\beta}}{\sqrt{M_i M_{i'}}} \mathbf{A}_\beta(i',\mathbf{q}) e^{i\mathbf{q}\cdot(\mathbf{R}_m - \mathbf{R}_n)} \ . \tag{2.108}$$

In periodic calculations, all the unit cells are symmetric with respect to translation. Therefore, the force constants do not depend on the value of m and n but on the difference $\mathbf{R}_m - \mathbf{R}_n$. As a consequence, we can set $\mathbf{R}_n = \vec{0}$, and the previous equation becomes:

$$\omega^2 \mathbf{A}_\alpha(i,\mathbf{q}) = \sum_{i'\beta m} \frac{\boldsymbol{\mathcal{C}}^{i,\alpha}_{i',\beta}}{\sqrt{M_i M_{i'}}} \mathbf{A}_\beta(i',\mathbf{q}) e^{i\mathbf{q}\cdot(\mathbf{R}_m)} \ . \tag{2.109}$$

By introducing the dynamical matrix (also called the mass-weighted Hessian matrix) as:

$$D^{i,\alpha}_{i',\beta}(\mathbf{q}) = \frac{1}{\sqrt{M_i M_{i'}}} \sum_m \boldsymbol{\mathcal{C}}^{i,\alpha}_{i',\beta} e^{i\mathbf{q}\cdot(\mathbf{R}_m)} \ , \tag{2.110}$$

Eq. (2.109) can be rewritten as:

$$0 = \sum_{i'\beta} \left[D^{i,\alpha}_{i',\beta}(\mathbf{q}) - \omega^2 \delta_{\alpha\beta}\delta_{ii'} \right] \mathbf{A}_\beta(i',\mathbf{q}) \ , \tag{2.111}$$

and non-trivial solutions can exist only if:

$$\det \left[D^{i,\alpha}_{i',\beta}(\mathbf{q}) - \omega^2 \delta_{\alpha\beta}\delta_{ii'} \right] = 0 \ . \tag{2.112}$$

The previous equation provides the system's harmonic solutions $\omega^2(\mathbf{q})$ and the band structure. The lowest first three values correspond to acoustical phonons

with the limit of $\omega(\mathbf{q})$ as $\mathbf{q}$ approaches zero is zero. All the other modes are optical and approach finite frequencies at the gamma point (the center of the Brillouin zone). One can also determine the corresponding atomic displacements for each harmonic vibration using the eigenvectors from Eq. (2.112).

2.7.2 Linear response

In the previous section, using the Hellman-Feynman theorem, we have seen that interatomic forces ($\mathbf{F}_I$) can be defined as the first partial derivative of the total energy according to atomic displacement. In the Born–Oppenheimer approximation, it can also be defined as:

$$\mathbf{F}_I = -\nabla_{\mathbf{R}_i} E_e(\mathbf{R}, \mathbf{r}) \tag{2.113}$$

Starting from Eq. (2.1) and using Eq. (2.79) and Eq. (2.113), we can write:

$$\mathbf{F}_I = -\int d\mathbf{r}\, n(\mathbf{r})\nabla_{\mathbf{R}_i} v_{ext}(\mathbf{R}, \mathbf{r}) - \nabla_{\mathbf{R}_i} V_{nn}(\mathbf{R}) \ . \tag{2.114}$$

Using the previous equation, we can express the force-constant matrix (Eq. (2.102)) as:

$$\begin{aligned}
\nabla_{\mathbf{R}_i}\nabla_{\mathbf{R}_j} E_e(\mathbf{R}, \mathbf{r}) = & -\nabla_{\mathbf{R}_j}\mathbf{F}_I \\
= & \int d\mathbf{r}\, \left(\nabla_{\mathbf{R}_j} n(\mathbf{r})\right)\left(\nabla_{\mathbf{R}_i} v_{ext}(\mathbf{R}, \mathbf{r})\right) \\
& + \int d\mathbf{r}\, n(\mathbf{r})\nabla_{\mathbf{R}_i}\nabla_{\mathbf{R}_j} v_{ext}(\mathbf{R}, \mathbf{r}) + \nabla_{\mathbf{R}_i}\nabla_{\mathbf{R}_j} V_{nn}(\mathbf{R}) \ .
\end{aligned} \tag{2.115}$$

Eq. (2.114) shows that the forces depend only on the ground state electronic density. In contrast, the interatomic force constants depend on the ground state electronic density and its linear response to an atomic displacement, $\nabla_{\mathbf{R}_j} n(\mathbf{r})$ [198, 199].

2.7.3 Density functional perturbation theory

We have seen that the energy $E_e(\mathbf{R}, \mathbf{r})$ gradients with respect to nuclear coordinates $\mathbf{R}_i$ and $\mathbf{R}_j$ can be computed using only the electron density distribution and its linear response to an atomic displacement. The next step is to compute this response, starting from Eq. (2.92), which leads, for closed-shell systems, to [193]:

$$\Delta^{\mathbf{R}_j} n(\mathbf{r}) = 4\mathrm{Re}\sum_{n=1}^{n_e/2} \phi_n^*(\mathbf{R}, \mathbf{r})\Delta^{\mathbf{R}_j}\phi_n(\mathbf{R}, \mathbf{r}) \ , \tag{2.116}$$

where $\Delta^{\boldsymbol{\lambda}}$ is the finite-difference operator with respect to $\boldsymbol{\lambda}$ and $\phi_n(\mathbf{R}, \mathbf{r})$ are Kohn-Sham spin-orbitals. Applying it to a function F, it states:

$$\Delta^{\boldsymbol{\lambda}} F = \sum_i \frac{\partial F_{\boldsymbol{\lambda}}}{\partial \lambda_i} \Delta \lambda_i \; . \qquad (2.117)$$

Equation (2.117) represents the variation of a quantity F with respect to $\boldsymbol{\lambda}$. The symbol Δ represents here quantity's difference. In other words, this equation describes how the change in the quantity F depends on the changes in the parameters $\boldsymbol{\lambda}$.

The first order correction to a Kohn-Sham spin-orbital $\Delta^{\mathbf{R}_j} \phi_n(\mathbf{R}, \mathbf{r})$[5], expressed as a sum over all the possible eigenvalues of the Hamiltonian H is given by [200]:

$$\Delta \phi_n(\mathbf{R}, \mathbf{r}) = \sum_{m \neq n} \phi_m(\mathbf{R}, \mathbf{r}) \frac{\langle \phi_m(\mathbf{R}, \mathbf{r}) \, | \, \Delta v_{eff}(\mathbf{r}) \, | \, \phi_n(\mathbf{R}, \mathbf{r}) \rangle}{\epsilon_n - \epsilon_m} \; . \qquad (2.118)$$

It is essential to note that this correction can lead to divergence issues when it is applied to degenerated states. Then, the electron density response becomes:

$$\Delta n(\mathbf{r}) = 4 \mathrm{Re} \sum_{n=1}^{n_e/2} \sum_{m \neq n} \phi_n^*(\mathbf{R}, \mathbf{r}) \phi_m(\mathbf{R}, \mathbf{r}) \frac{\langle \phi_m(\mathbf{R}, \mathbf{r}) \, | \, \Delta v_{eff}(\mathbf{r}) \, | \, \phi_n(\mathbf{R}, \mathbf{r}) \rangle}{\epsilon_n - \epsilon_m} \; . \qquad (2.119)$$

In Eq. (2.119), we can see that the part relative to occupied states cancels by separating the sum over all the states into occupied and non-occupied ones. Consequently, the index m only runs along non-occupied (or conduction) states. We need to know all the possible eigenvalues of the Hamiltonian to solve Eq. (2.119), leading to a high computational cost calculation. Baroni et al.[193] have shown that, using the previous equations, we can express the Kohn-Sham equations (Eq. 2.91) for a perturbed system using a projection over the occupied states. It is done via a projector $\mathbf{P}_c$ defined as:

$$\mathbf{P}_c = 1 - \sum_m^{\neq/2} |\phi_m(\mathbf{R}, \mathbf{r})\rangle \, \langle \phi_m(\mathbf{R}, \mathbf{r})| \; , \qquad (2.120)$$

---

[5]The superscript $\mathbf{R}_j$ will be omitted in the following for readability, as it will not give rise to ambiguities

where the right-hand part is the projector on the valence bonds. The Kohn-Sham equations for a perturbed system become:

$$\left[-\frac{\hbar^2}{2m}\nabla_{\mathbf{r}}^2 + v_{eff}(\mathbf{r}) - \epsilon_m \right] \mathbf{P}_c \Delta\phi_m(\mathbf{R}, \mathbf{r}) = -\mathbf{P}_c \Delta v_{eff}(\mathbf{r})\phi_m(\mathbf{R}, \mathbf{r}) , \qquad (2.121)$$

As in DFT, we can solve the self-consistent equations by repeating the following procedure until the desired convergence threshold is achieved:

$$n^m(\mathbf{r}) \rightarrow \Delta v_{eff}^m(\mathbf{r}) \rightarrow \text{DFPT equations} \rightarrow n^{m+1}(\mathbf{r}) . \qquad (2.122)$$

2.8 Thermochemistry

In this work, we are also interested in characterizing the energetics of some chemical reactions, which can absorb or release energy through heat with its surrounding. Knowledge of such quantities is essential, as it influences the kinetics of reactions and the chemical composition of the atmosphere. When doing some simulations, one needs these thermodynamic properties (also kinetics ones) of a system's possible reactions to simulate the species concentrations according to time.

In this section, we will see how we can define enthalpy and Gibbs free energies for a chemical reaction using theoretical calculations from partition functions q. We will also introduce the zero-point energies (ZPEs) correction to the energy and its impact on thermochemistry.

2.8.1   Partition functions and energy contributions

In a molecular system in the gas phase, the electronic energy computed from theoretical methods is not sufficient to fully describe its thermodynamic properties. Indeed, we need to consider the energy contributions from the system's entropy, translational, rotational, and vibrational motions. To include the latter contributions, we need to build a *partition function* q, which is defined by the sum of the partition functions of all the contributions as [201]:

$$q = q_t + q_e + q_r + q_v , \qquad (2.123)$$

where q_t, q_e, q_r, and q_v are, respectively, the translational, electronic, rotational, and vibrational partition functions.

Once we know each partition function, we can determine the entropy contribution S_i from the corresponding component, using [201]:

$$S = Nk_B + Nk_B \ln(\frac{q}{N}) + Nk_B \left(\frac{\partial \ln q}{\partial T} \right)_V \; , \qquad (2.124)$$

where N is the number of particles, k_B is the Boltzmann constant, and V is the volume. We can also compute the internal thermal energy E_T as [201]:

$$E_T = Nk_B T^2 \ln \left(\frac{\partial q}{\partial T} \right)_V \; . \qquad (2.125)$$

The notion of mole and volume are undefined in gas phase calculations. Regarding the mole number, we can divide N by the Avogadro number (N_A) to obtain a number of moles. To overcome the volume issue, we need to make an important assumption: assuming that particles are non-interacting, then behaving as an ideal gas. In this approximation, we can express the volume V using the ideal gas law as:

$$V = \frac{k_B T}{P} \; . \qquad (2.126)$$

Then, using the fact that the ideal gas constant R is related to N_A and k_B as $R = N_A \times k_B$, we can rewrite Eq. (2.124) as:

$$S = R \left(\ln(q) + 1 + T \left(\frac{\partial \ln q}{\partial T} \right)_V \right) \; , \qquad (2.127)$$

Since we have expressed e in this entropic contribution, it will not appears to other's entropic contributions.

In the following parts, we will focus on each contribution to the energy, more specifically, by determining the partition functions and the corresponding entropy terms, ending with the corresponding contribution to the energy.

2.8.2 Translational contribution

Starting for translation, McQuarrie et al. [201] give the partition function as:

$$q_t = \left(\frac{2\pi M_{\text{mol}} k_B T}{h^2} \right)^{\frac{3}{2}} \frac{k_B T}{P} \; , \qquad (2.128)$$

where M_{mol} is the molecular mass, and h is Planck's constant. The next step is to compute the last term in Eq. (2.127):

$$\left(\frac{\partial \ln q_t}{\partial T} \right)_V = \frac{3}{2} T \; . \tag{2.129}$$

Finally we can compute the translational contribution to the entropy (S_t) and internal energy (E_T^t):

$$\begin{cases} S_t = R \left(\ln(q_t) + 1 + \frac{3}{2} \right) & \text{(2.130a)} \\[2ex] E_T^t = \frac{3}{2} RT & \text{(2.130b)} \end{cases}$$

2.8.3 Rotational contribution

For the general case, the rotational partition function given by McQuarrie et al. [201] is:

$$q_r = \frac{\pi^{1/2}}{\sigma_r} \left(\frac{T^{3/2}}{(\Theta_{r,x} \Theta_{r,y} \Theta_{r,z})^{1/2}} \right) \; , \tag{2.131}$$

where σ_r is the symmetry number of rotations, and $\Theta_{r,i}$ is the characteristic temperature for rotation in the i plane. The latter, using the rigid rotor approximation, can be expressed as:

$$\Theta_{r,i} = \frac{h^2}{8\pi^2 I_i k_B} \; , \tag{2.132}$$

where I_i is the moment of inertia according to the axis i. The latter can be computed through the moment of inertia tensor, which we will not detail. Then, plugging Eq. (2.132) into Eq. (2.131), we can obtain the following expression:

$$q_r = \frac{8\pi^2 (2\pi k_B T)^{3/2} (I_x I_y I_z)^2}{\sigma_r h^3} \; . \tag{2.133}$$

Then, we can compute the following quantity:

$$\left(\frac{\partial \ln q_r}{\partial T} \right)_V = \frac{3}{2T} \; . \tag{2.134}$$

Finally, we can compute its contribution to entropy and internal energy as:

$$
\begin{cases}
S_t = R \left(\ln(q_r) + \dfrac{3}{2} \right) & \text{(2.135a)} \\[2ex]
E_T^r = \dfrac{3}{2} RT & \text{(2.135b)}
\end{cases}
$$

2.8.4 Vibrational contribution

Concerning vibrational contributions, we want to highlight that the latter is composed of the product of the contribution for each vibrational mode. This number will be written N_v. In this scheme, imaginary modes are not taken into account. For each mode, we can define a characteristic vibrational temperature of the form:

$$
\Theta_{v,N_v} = \frac{hc\bar{\nu}_n}{k_B} \; , \tag{2.136}
$$

where c is the speed of light, and $\bar{\nu}$ is the wave number.

The vibrational energy is expressed relative to the computed electronic energy from theoretical calculations. This reference is called "bottom of the well". This scheme defines the vibrational partition function as [201]:

$$
q_v = \prod_{N_v} \frac{e^{-\Theta_{v,N_v}/2T}}{1 - e^{-\Theta_{v,N_v}/T}} \; . \tag{2.137}
$$

Defining the zero point (vibrational) energy as:

$$
E_{\text{ZPE}} = \sum_{N_v} \frac{hc\bar{\nu}_n}{2} \; , \tag{2.138}
$$

we can rewrite Eq. (2.137) as:

$$
q_v = e^{-E_{ZPE}/k_B T} \prod_{N_v} \frac{1}{1 - e^{-\Theta_{v,N_v}/T}} \; . \tag{2.139}
$$

Within some development detailed in Appendix B, we can compute the following quantity:

$$
\left(\frac{\partial \ln q_v}{\partial T} \right)_V = \frac{E_{\text{ZPE}}}{k_B T^2} + \sum_{N_v} \frac{\Theta_{v,N_v}/T^2}{e^{\Theta_{v,N_v}/T} - 1} \; . \tag{2.140}
$$

Therefore, the vibrational entropic and internal energy contribution is:

$$
\begin{cases}
S_v = R \sum_{N_v} \dfrac{\Theta_{v,N_v}/T}{e^{\Theta_{v,N_v}/T} - 1} - \ln\left(1 - e^{-\Theta_{v,N_v}/T}\right) \ , & \text{(2.141a)} \\[2em]
E_T^v = R \left[\dfrac{E_{\text{ZPE}}}{k_B} + \sum_{N_v} \dfrac{\Theta_{v,N_v}}{e^{\Theta_{v,N_v}/T} - 1} \right] \ . & \text{(2.141b)}
\end{cases}
$$

We see that the ZPE contribution appears only in the calculations of the internal vibrational energy. Indeed as seen in Appendix B, the ZPE energy contribution cancels calculating the vibrational entropic contribution.

2.8.5 Electronic motion contribution

As for translations, the ground and excited states impact the thermodynamic properties of molecular systems. The partition function regarding the electronic motions is defined as [201]:

$$
q_e = \sum_i c_i e^{E_i/(k_B T)}, \tag{2.142}
$$

where E_i is the electronic energy of the ith states, and c_i are the degeneracy levels. Generally, we assume that the difference in energy between the ground state and the first excited state is much lower than $k_B T$. It implies that only the ground state is accessible, and then transform the previous equation into a much simpler one, which is:

$$
q_e = c_0 = 1 \ . \tag{2.143}
$$

The previous equation shows no dependence on temperature, making the equivalence in electronic motion of Eq. (2.129) equal to zero. Then, the entropic contribution within these conditions is:

$$
S_e = R(\ln(q_e)) = 0 \ . \tag{2.144}
$$

2.8.6 Total contribution

We have seen how to compute all the different contributions to the internal thermal energy and entropy at constant volume. Then, we can compute the total contribution to those two values. First, the total thermal internal energy is expressed as the sum of the internal thermal energy contributions, then we can write:

$$
E_T = E_T^t + E_T^r + E_T^v \ . \tag{2.145}
$$

Within the same scheme, the total contribution to the entropy can be expressed as the sum of all the entropic contributions:

$$S = S_t + S_e + S_r + S_v \ . \tag{2.146}$$

The last values that we must define are the internal energy, enthalpy, and Gibbs free energy.

2.8.7 Internal energy, enthalpy, entropy, and Gibbs free energy

We have seen how to compute all the different contributions to the internal energy and entropy terms from previous sections. The next step is to define and compute the total internal energy (U), the enthalpy (H), and the Gibbs free energy (G).

From theoretical calculations, we obtain the electronic energy of the ground state, E_0. From this value, we can compute the internal energy of the molecular system as follows:

$$U = E_0 + E_T \ , \tag{2.147}$$

where E_T also contains the ZPE energy contribution, as seen in the previous section. Then, the enthalpy at a given temperature is defined as:

$$H = U + PV = U + k_B T \ , \tag{2.148}$$

where the left-handed part of the equation works only in the ideal gas approximation. Its value is often seen as a thermal correction to the enthalpy. In this case, the correction (taken into account in the previous expression) is defined as:

$$H_{\mathrm{corr}} = E_T + k_B T. \tag{2.149}$$

The last value to define is Gibbs free energy. It is computed as:

$$G = H - TS \ . \tag{2.150}$$

Within the same scheme, we can also define the thermal correction to the Gibbs free energy as:

$$G_{\mathrm{corr}} = H_{\mathrm{corr}} - TS \ . \tag{2.151}$$

Within the corrections, we can define the enthalpy and the Gibbs free energy as:

$$\begin{cases} H = E_0 + H_{\mathrm{corr}} \ , & \text{(2.152a)} \\ G = E_0 + G_{\mathrm{corr}} \ . & \text{(2.152b)} \end{cases}$$

In the previous sections, we have seen so far how we can describe molecular systems using quantum mechanics. Even if these methods are sufficiently accurate to obtain the target observables, their complexity makes them impossible for large molecular systems (> 1000 atoms). Then, other methods with more approximations are needed to compute such systems. In section 2.9, we will discuss the force field approach combined with classical MD as one answer to this problem.

2.9   Force Field and classical molecular dynamics

A force field is a mathematical expression, taking the form of a functional, that describes the potential energy of a system of molecules or atoms. It is based on parameters using classical mechanics that need to be determined. The latter can be fitted from experiments, quantum calculations, or both. The only variable in the force field is the set of atomic positions, $\{\mathbf{R}\}$. Regarding electrons, they are implicitly treated through different parameters. Regarding molecules, they are defined as an ensemble of atoms linked by intramolecular forces. They interact via intermolecular and intramolecular forces, generally composed of the Coulombic and Van der Waals interactions (repulsion, dispersion).

Compared to DFT, the approximations made in force fields considerably reduce the computational time. Combined with MD, it allows the possibility to sample larger systems at a larger time scale than *ab initio* molecular dynamics. Nevertheless, force fields show some limitations, like the use of atomic partial charges and the impossibility of having chemical reactions[6]. A direct consequence of the latter is that we can not do simulations on systems that present charge transfer phenomena (i.e., the transfer of one or more electrons from one atom or molecule to another in a chemical reaction or interaction).

In the following, we shall start by introducing force field mathematical expressions. Then, we will treat the parameter fitting methods, and discuss the limitations of such methods, ending by introducing MD.

2.9.1   Mathematical expression

Usually, the basic functional form of a force field includes intramolecular and intermolecular terms. Even if the decomposition of each term depends on the force field, we can write a general form which is:

$$V = V_{\text{bonded}} + V_{\text{nonbonded}} \ , \tag{2.153}$$

---

[6]Some force fields allow chemical reactions, and are called *reactive force fields*. Nevertheless, they are more complex than in this manuscript.

where V_{bonded} and $V_{\text{nonbonded}}$ are, respectively, the intramolecular and intermolecular potential energies. We will detail each term decomposition in the following sections.

2.9.2 Intramolecular terms

Intramolecular potentials are functions which compute potential energies between atoms in one molecule. In our case, it includes bond stretching and angle bending as the following:

$$V_{\text{bonded}} = V_{\text{bond}} + V_{\text{angle}} \; , \tag{2.154}$$

where V_{bond} and V_{angle} are, respectively, the potential energy for bond stretching and angle bending contributions to the intramolecular potential.

We represent them with a quadratic function. The bond stretching potential energy (V_{bond}) is defined in Eq. (2.155):

$$V_{\text{bond}} = \sum_{\text{bonds}} K_b (r - r_{\text{eq}})^2 \; , \tag{2.155}$$

and the angle bending potential V_{angle}, also known as the Urey-Bradley potential [202], is defined as:

$$V_{\text{angle}} = \sum_{\text{angles}} K_a (\theta - \theta_{\text{eq}})^2 \; , \tag{2.156}$$

where K_b and K_a are respectively the bond stretching and the angle bending spring constants, r and r_{eq} the distance and the equilibrium distance between atoms, and θ and θ_{eq} are respectively the angle and the equilibrium angle between atoms. To fully describe a molecule, we must sum these two expressions over all the different pairs of atoms and angles.

We highlight that Eq. (2.155 and 2.156) use the harmonic approximation. We describe such interaction using a quadratic evolution of the potential energy according to atomic distance or the angle bending. Such a description is valid only if the variable does not significantly deviate from the equilibrium value. In practice, the high spring constant value keeps it close to the equilibrium ones, making the harmonic approximation valid for the target simulations. The second consequence of the approximation is the impossibility of having chemical reactions. Indeed, such definitions show that the potential energy tends to infinity when the variable evolves in both directions. We do not expect reactivity in the target simulation, which makes the approximation correct for our purpose. In addition, we set the minimum potential energy to zero to have only positive values for bond stretching and angle bending. Indeed, molecular distortions increase the molecule's potential energy, represented here by a positive value. A molecule has no contribution to the total energy when in its minimal energy geometry.

2.9.3   Intermolecular forces

Intermolecular potentials are functions that describe interactions between molecules. They are composed of Coulombic and Van der Waals interactions. Even if they are usually weaker than intramolecular ones, they are essential to a good description of the molecular system. For example, they define species' boiling and melting points, density, and enthalpies (fusion and vaporization).

Intermolecular potentials comprise four elements: Van der Waals, Coulombic, proper, and improper angle contributions. Proper and improper torsions describe the energy associated with rotations and out-of-plane bending. Consequently, they are only defined if the molecule has four-atom groups that could be in a "cis" or "trans" configuration. We will not detail these terms in this Thesis because we deal only with molecules without proper and improper torsions. Finally, we can decompose the intermolecular potentials as:

$$V_{\mathrm{nonbonded}} = V_{\mathrm{LJ}} + V_{\mathrm{elec}} \;, \tag{2.157}$$

where V_{LJ} and V_{elec} are the Van der Waals and the Coulombic contibution to the intermolecular potential energy.

The first term, Van der Waals interaction, includes repulsive and attractive force depending on the distance between two objects. The fluctuations of the polarization of nearby particles cause them. The 12-6 Lennard-Jones (LJ) potential is often used to describe such interactions and is defined as:

$$V_{\mathrm{LJ}} = \sum_{i<j} 4\epsilon_{ij} \left[\left(\frac{\sigma_{ij}}{R_{ij}}\right)^{12} - \left(\frac{\sigma_{ij}}{R_{ij}}\right)^{6} \right] \;, \tag{2.158}$$

where R_{ij} is the distance between atoms labeled i and j, ϵ_{ij} is the depth of the potential well between atoms i and j, and σ_{ij} is the distance at which the inter-particle potential is zero between atoms i and j. Usually, force fields give individual atomic parameters of σ and ϵ and combine them through some rules. To obtain the depth of the potential well ϵ_{ij}, most of the force fields use the geometric mean, $\epsilon_{ij} = (\epsilon_i \epsilon_j)^{1/2}$. However, for the distance σ_{ij}, it can be given instead by the geometric, $\sigma_{ij} = (\sigma_i \sigma_j)^{1/2}$, or by the arithmetic mean, $\frac{1}{2}(\sigma_i + \sigma_j)^7$, depending on the force field.

As previously seen, electronic density can be obtained by using quantum calculations, such as DFT. Nevertheless, using such methods is impossible when dealing with large molecular systems, due to their expensive computational time. The last term of intermolecular interactions, the Coulombic or electrostatic one, is introduced to describe the electronic density in a force field and is defined by the

---

[7]The arithmetic mean definition of σ_{ij}, together with the geometric mean definition of ϵ_{ij}, are called the Lorentz-Berthelot combination rules.

Coulomb law:

$$V_{\text{elec}} = \sum_{i<j} \frac{q_i q_j}{\epsilon_r R_{ij}} \ , \tag{2.159}$$

where $q_{i/j}$ are the fixed atomic partial charges, ϵ_r the relative dielectric constant of the medium, and R_{ij} the distance between atoms labeled i and j. Such a description implies the introduction of atomic partial charges. We will discuss these charges in the next part of the Thesis. Using fixed charges implies that polarization effects can not be implemented as crucial as they are. Then, the resulting dipole moments are kept fixed, regardless of the nature, number, and positions of surrounding molecules. As will be discussed in the section 2.9.6, there are methods to consider the inherent polarization of the molecules, dependent on their environment.

2.9.4   Atomic partial charges

Atomic partial charges are used to compute the electrostatic interaction in a force field, one of the most dominant contributions to the total potential energy, especially for polar molecules. Because they rule interatomic interactions, they are fundamental, for examples, for determining minimum energy cluster geometries, interaction/adsorption energies, melting, and boiling points. They are also bringing helpful information for qualitative understanding of chemical phenomena.

Nevertheless, their definitions are ambiguous from a physical point of view. Indeed, they can not be measured by experiments. Because they are used in different ways within the context of qualitative or quantitative models, no single process is optimal for all possible purposes. According to Cramer [203], we can divide atomic partial charges into four classes which are:

Class 1. Charges not derived from quantum mechanics. They are based on intuitive and arbitrary approaches. They can be computed quickly, making them efficient when we compute many. One of the most used method is the partial equalization of orbital electronegativity (PEOE) one [204].

Class 2. Charges are computed by partitioning the molecular wave function into atomic contributions. Even if these partial charges are easily computed, they are basis-set dependent [203]. They are still helpful for qualitative analysis. The most famous method for this class is the Mulliken analysis [205].

Class 3. Charges are computed from the analysis of physical observables calculated from the wave function. The most used methods are the Bader (based on electronic density) and the ESP/RESP [206–210] (based on the electrostatic potential). Those methods are interesting for building force fields because they aim to reproduce the molecule's external electrostatic potential, which is essential in molecular simulations.

Class 4. Charges derived from the semi-empirical mapping of a precursor charge (from Class 2 or 3, for example) to reproduce an experimentally determined observable. For example, Charge Model 1 (CM1) [211] was one of this class's first methods.

A second point to discuss is that partial charges are not limited to atomic positions. In this case, charges may be carried out by dummy atoms. One good example is the TIP4P water model [212], in which a dummy atom is inserted with negative partial charge to better describe the H_2O dipole moment in the liquid phase.

2.9.5   ESP/RESP atomic partial charges

In the case of a classical force field, ESP/RESP charges are widely used. Indeed, they are built to mimic the electrostatic potential evaluated quantum mechanically. ESP charges were first introduced by Momany [206], then improved by Cox et al. [207], and finally applied to a large number of systems by Singh et al. [208] and Weiner et al. [209, 210]. To compute them, we use a thin grid around the molecule where, for each intersection, we compute the electrostatic potential at a given level of theory. Then, we optimize atomic partial charges in the force field's parameters $(V_{\mathbf{R},i})$ that fit all the previously computed energies $(\hat{V}_{\mathbf{R}})$. The force field's atomic partial charges at point $\mathbf{R}$ are computed as:

$$V_{\mathbf{R},i} = \sum_j \frac{q_j}{|\|\mathbf{R} - \mathbf{R}_j\||} \ , \qquad (2.160)$$

where q_j is the ESP partial charge of atom j and $\mathbf{R}_j$ its position. We can now define a figure-of-merit function χ_{ESP}, which has to be minimized and is defined as:

$$\chi_{\mathrm{ESP}}^2 = \sum_i \left(V_{\mathbf{R},i} - \hat{V}_{\mathbf{R},i} \right)^2 \ . \qquad (2.161)$$

A more detailed process is given by Besler et al. [213].

To better understand ESP charges weakness, Bayly et al. [214] have represented the figure-of-merit evolution according to the computed atomic partial charges in methanol (see Fig. 2.2). For each atom positioned at the extremity of the molecule, we can see that a slight variation of the partial atomic charge leads to a hight evolution of χ_{ESP}^2. However, the figure-of-merit square evolution according to the carbon partial charge differs. Indeed, it evolves slower than other atoms. It can be explained by the fact that charges are coefficients, and the ones for buried atoms are statistically poorly determined compared to the other ones.
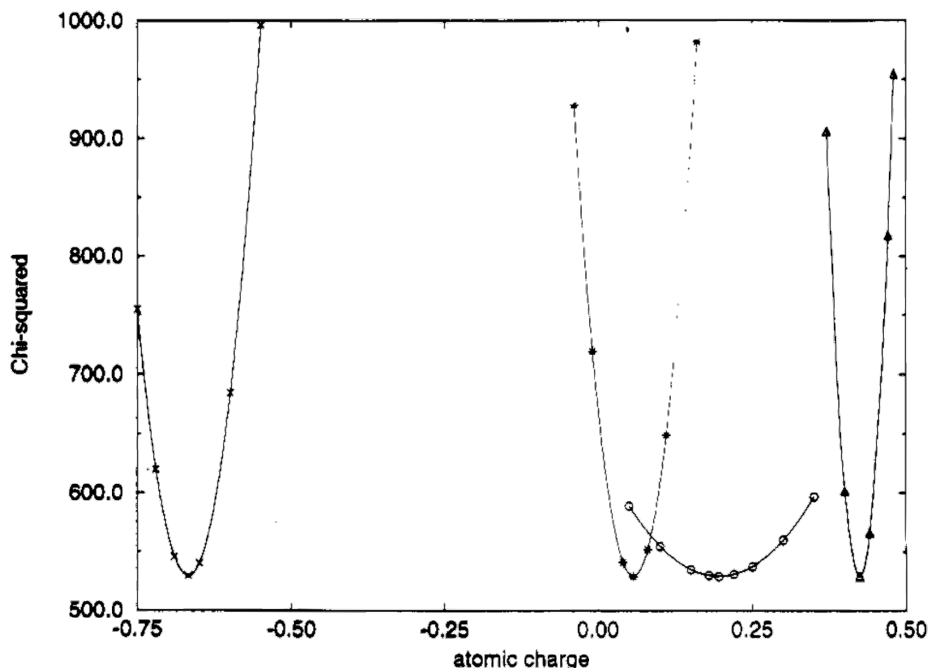
Figure 2.2: Dependence of the quality of fit in terms of the merit function χ^2_{ESP} on each atomic charge in methanol: (X) oxygen; ($\triangle$) hydroxyl hydrogen; ($\bigcirc$) methyl carbon; (*) methyl hydrogen. Figure taken from Bayly et al. [214].

This issue can be solved using a penalty function to the procedure [214]. The figure-of-merit to be minimized is now:

$$\chi^2 = \chi^2_{\text{ESP}} + \chi^2_{\text{rstr}} \ , \tag{2.162}$$

where χ^2_{rstr} is the penalty function. The latter increases the weight of buried partial atomic charge contributions to the total figure-of-merit. This method is called RESP [214].

2.9.6   Inherent polarization

During simulations, one needs to take care of polarization effects. They are defined as the deformation of the electronic density around atoms in response to the induced electric field from other atoms. It has been shown that using only fixed partial atomic point charges (neglecting polarization effects) leads to some errors [215–218]. There are methods to account for polarization, such as the fluctuating charge model [219], the Drude model [220], and the induced dipole one [221–223].

Nevertheless, there are other ways to correctly describe the system than directly accounting for polarization. Leontyev et al. [224] showed that if the system involves structurally similar configurations, then we can describe inherent polarization with an equivalent fixed-charge model by scaling atomic charges [215, 225]. The main drawback of this method is that the scaling factor has to be recomputed and optimized when molecular systems change. Then, it highly impacts the transferability of a force field, even if the scaling factor does not necessarily differ much between two similar systems.

2.9.7 Molecular dynamics

In a molecular system, once we know all the forces acting on each atom, we can produce dynamical trajectories integrating Newton's equations of motion. We need a force field describing the potential and thus the forces, initial conditions as starting point, and periodic boundary conditions to perform classical molecular dynamics. We need to solve the classical equations of motions for each atom i, which are:

$$M_i \frac{\partial^2 \mathbf{R}_i}{\partial t^2} = -\nabla_{\mathbf{R}_i} V(\mathbf{R}) \ , \tag{2.163}$$

where t is the time variable, and the left-handed term of the equation is the sum of the forces present in the system. Eq. (2.163) has to be numerically solved step by step using an algorithm.

One of the most used integration algorithms is called leapfrog [226]. It is a second-order method defined by the following equations based on a Taylor's expansion:

$$\begin{cases} \mathbf{v}_i \left(t + \frac{1}{2}\Delta t \right) = \mathbf{v}_i \left(t - \frac{1}{2}\Delta t \right) + \mathbf{a}_i \Delta t & \text{(2.164a)} \\[2ex] \mathbf{R}_i \left(t + \Delta t \right) = \mathbf{R}_i(t) + \mathbf{v}_i \left(t + \frac{1}{2}\Delta t \right) & \text{(2.164b)} \end{cases}$$

where Δt is the simulation time step, $\mathbf{v}_i$ is the velocity vector, and $\mathbf{a}_i$ is the acceleration vector. In summary, the leapfrog algorithm updates the position $\mathbf{R}_i$ and the velocity $\mathbf{v}_i$ of atom i at interleaved time points. We can illustrate this in Fig (2.3). This algorithm has the advantages of being time-reversible and correctly describes the long-term small changes in the properties of a nearly periodic orbit [227], which are the main reasons of its popularity.

Sometimes, the studied systems require costly and long simulations. To speed up MD simulations, one can increase the time step. Consequently, the simulation has fewer steps, speeding up the calculation. However, the time step must always be smaller than the fastest motion in the system. In molecules, the fastest motion is usually vibrations. Then, if these values are constrained to be at the equilibrium
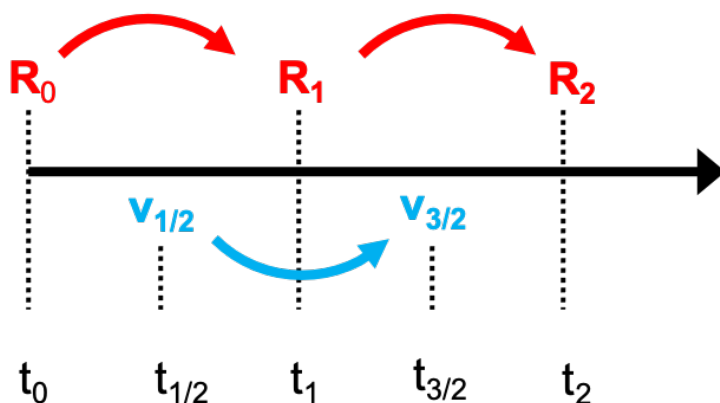
Figure 2.3: Scheme showing the leapfrog algorithm. In red is represented the evolution of the positions and in blue the evolution of the velocities according to the time step.

distance, suppressing molecular vibrations in the dynamics, we can increase the time step significantly. One of the most used constraints method is the SHAKE algorithm, proposed by Ryckaert et al. [228].
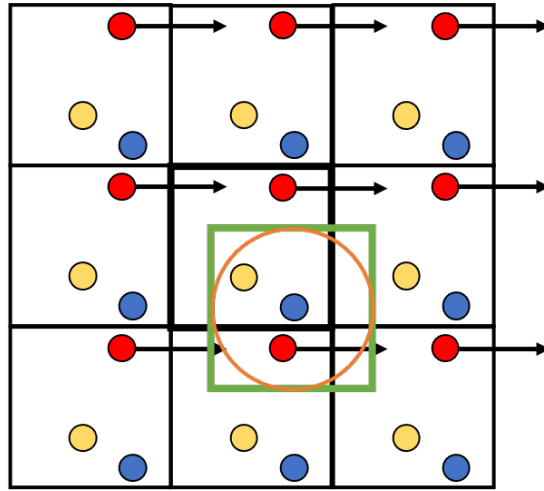
2.9.8   Boundary conditions

Taking our molecular system, we can simulate it in a vacuum by directly solving the classical equations of motion. However, in most cases, we want simulations to determine/predict liquid, gas, bulk, or interface properties. It is possible to model quasi infinite systems without increasing the number of molecules and consequently the computational cost by introducing periodic boundary conditions.

Therefore, the actual simulation box is surrounded by an infinite number of replicas, making any particles crossing the boundary of the simulation emerge back to the opposite side of the box, as shown in Fig. 2.4 for the red particle. Consequently, the number of atoms N in the simulation box remains constant.

Periodic boundary conditions allow us to simulate a continuous system with a finite number of particles. Because we want simulations representative of experiments, we need to set a reasonable number of atoms reproducing the target properties regarding the computational cost. With these conditions verified, we can compute properties for gas, bulk, liquid, or even interfaces. We can see the corresponding scheme in Fig. (2.4).

A system with an infinite number of replicas has an infinite number of interactions between atoms. The minimum image convention is used to compute short-range interactions, restraining the latter's number. In other words, only the

Figure 2.4: Scheme of the main simulation box (bold black) and its replicas. The red particle illustrates the periodic boundary conditions, the green square the minimum image convention on the blue particle, and the orange circle the cut-off sphere.

interactions with the nearest image are considered. To make all the maximum distances equal within this truncation, we usually use a cutoff sphere with a maximum radius equal to the dimension of the box divided by two ($L_x/2$, where L_x is the cubic box length).

Regarding Eq. (2.159), the electrostatic potential energy does not decay rapidly according to interatomic distances. Then, truncating such interactions might be a rude approximation during the simulation. One solution is to compute the Coulombic interactions using the Ewald summation scheme [229]. It consists in splitting Eq. (2.159) into two series: short-range and long-range ones. The first is fully computed in the real space, whereas the long-range interactions are computed in the reciprocal space.

2.9.9 Controlling temperature

Looking at Eq. (2.163), we can see that the number of particles, the total energy, and the volume are kept constant. In statistical physics, it means that we are using the NVE microcanonical ensemble. Controlling the temperature is an essential feature in comparing simulations to experiments. Thermostats are used to control the temperature in a simulation. The temperature of the system is given by the equipartition theorem [230]:

$$\langle T_n \rangle = \frac{3}{2} N_n k_B T \ , \tag{2.165}$$

where T_n is the total kinetic energy, N_n is the number of atoms, k_B is Boltzmann's constant, and T the temperature of the system. Then, we can do simulations in the canonical ensemble NVT. We can define the kinetic energy at a given time t of the simulation through:

$$T_n(t) = \frac{1}{2} \sum_i^{N_n} M_i v_i^2(t) \; , \tag{2.166}$$

where $v_i(t)$ is the velocity of atom i at a time t. The previous equation allows us to define the instantaneous temperature $\mathcal{T}$ at any time t by:

$$\mathcal{T}(t) = \frac{\sum_i^{N_n} M_i v_i^2(t)}{3 N_n k_B} \; . \tag{2.167}$$

One has to modify the velocities to control and act on the system's temperature. The average of the instantaneous temperature $\langle \mathcal{T} \rangle$ must be equal to the macroscopic temperature T. In other words, the instantaneous temperature oscillates around the macroscopic one. In the canonical ensemble, the resulting instantaneous temperature distribution must obey a Boltzmann distribution. Dimelow et al. [231] have theoretically shown that for a system containing N_n atoms at a temperature T, the probability distribution of the system's kinetic energy T_n denoted $P_{N_n}(T_n)$ is:

$$P_{N_n}(T_n) = \frac{1/(k_B T)^{\frac{3N_n}{2}}}{\Gamma(\frac{3N_n}{2})} (T_n)^{\frac{3N_n}{2}-1} e^{T_n/(k_B T)} \; , \tag{2.168}$$

where Γ is the gamma function. This expression can also be written to express the probability distribution of the system's instantaneous temperature denoted $P_{N_n}(\mathcal{T})$ as:

$$P_{N_n}(\mathcal{T}) = \frac{1/(k_B T)^{\frac{3N_n}{2}}}{\Gamma(\frac{3N_n}{2})} \left(\frac{3N_n}{2} k_B \mathcal{T} \right)^{\frac{3N_n}{2}-1} e^{(3N_n \mathcal{T})/(2T)} \; . \tag{2.169}$$

Thus, according to the canonical ensemble, the method has to allow temperature fluctuation. There are numerous thermostats that has been proposed, nonetheless, we will only present two thermostats used in our studies: the Berendsen and the Nosé-Hoover ones.

2.9.9.1 Berendsen thermostat

The main idea behind the Berendsen thermostat [232] is to couple the system to a heat bath at the target temperature of T_0. It can be accomplished by scaling the velocity at time $t + \Delta t$ as:

$$v_i(t + \Delta t) = v_i \left(1 + \frac{\Delta t}{\tau} \left(\frac{T_0}{\mathcal{T}} - 1 \right) \right) \; , \tag{2.170}$$

where τ is the damping constant, determining the coupling strength between the system and the heat bath. We can have two specific cases from Eq. (2.170). When $\mathcal{T} > T_0$, the last term of the equation is negative, leading to a decrease in the velocity of atom i, decreasing the system's temperature. On the opposite, when $\mathcal{T} < T_0$, the last term is positive, leading to an increase in the velocity of atom i.

Berendsen's thermostat is efficient in quickly reaching the target temperature. Nevertheless, the kinetic energy then converges to a constant that does not fluctuate during the simulation. Thus, this property does not sample the phase space correctly and does not represent a strictly correct canonical ensemble.

2.9.9.2 Nosé-Hoover thermostat

The main idea of the Nosé-Hoover thermostat [233–235] is to couple the system to an additional heating bath by adding a virtual degree of freedom. The latter can exchange heat with the system. As for the Berendsen thermostat, we can insert a friction coefficient in the equations of motion. It leads to the following equation:

$$M_i \frac{\partial^2 \mathbf{R}_i}{\partial t^2} = -\nabla_{\mathbf{R}_i} V(\mathbf{R}_i) - \gamma \mathbf{v}_i \ , \tag{2.171}$$

where the time derivative of the damping parameter γ is defined as:

$$\dot{\gamma} = \frac{1}{Q} \left[\sum_i^{N_n} M_i v_i^2 - 3N_n k_B T_0 \right] \ , \tag{2.172}$$

where Q is the strength of the coupling constant. It determines the response time of the thermostat to a target temperature deviation. The value of Q should be chosen to be consistent with the time step used in the simulation[8]. Then we must select a value of Q for this thermostat that combines well with the simulation.

Dividing Eq. (2.172) by a factor of $3N_n k_B$, we can write it as a function of the instantaneous temperature:

$$\dot{\gamma} = \frac{1}{Q} \left[\mathcal{T} - T_0 \right] \ . \tag{2.173}$$

The main advantage of this thermostat is that it allows kinetic energy fluctuations, leading to a correct canonical distribution of the latter. However, it depends on its coupling frequency, which can lead to non-canonical oscillations if care is not taken. It is usually the most used thermostat in recent studies.

Both thermostat can be used sequentially to optimize molecular simulations. The first step of the later is the equilibration one, where we equilibrate the system at

---

[8]The Nosé-Hoover thermostat can become unstable when using a too large value of Q. However, a too low value can lead to insufficient temperature control, resulting in temperature fluctuations.

the target temperature. We can use the Berendsen thermostat during equilibration because it reaches quickly the target temperature. However, during the production phase, Nosé-Hoover thermostat has to be preferred because of its correct canonical distribution of the kinetic energy.

Having introduced the methods used in this work, we move to the results, starting by the force field optimization for CH_3I molecule.

CH$_3$I Force field parametrization

Outline of the current chapter

3.1   Introduction

An important aspect of classical force fields is the fitting of intramolecular and intermolecular parameters values, used in the equations to represent interactions between atoms within the molecule. To the best of our knowledge, the only existing non-polarizable methyl iodide force field available in the literature was proposed by Crone-Münzebrock et al. [236] in 1990. Thus, building a new force field starting from their parameters is essential to have a good description of molecular interactions. To start, reproducing and fitting/benchmarking parameters from *ab initio* CH$_3$I-containing molecular structures will be a first step in building the force field.

The methyl iodide dimer has already been extensively studied theoretically. Futami et al. [237] and Ito [238] have made calculations at the MP2/LanL2DZ+fdp level of theory on the isolated CH$_3$I dimer, where Ramasami et al. [239] have done the same calculations at the MP2/aug-cc-pVTZ(-PP) level of theory. Two isomers are stable according to the literature, for all level of theories [237–240]: the head-to-tail (HtT) and head-to-head (HtH) structures. The former is a global minimum, and the latter is local [240]. They are shown in Fig. 3.2.

Moreover, CH$_3$I will interact with other species in our simulations, such as NaCl and H$_2$O. Regarding the adsorbed phase (interactions with NaCl), benchmarks are realized using optimized geometries from periodic DFT calculations that will be detailed in chapter 4. Concerning the gas phase and its interactions with water molecules, we need to look at the micro hydration processes of methyl iodide. This subject has been studied recently, as it impacts the halide cycle [107, 241]. Sobanska et al. [107] have performed both experimental (matrix isolation experiments) and theoretical calculations (at the ωB97X-D/aug-cc-pVTZ(-PP) level of theory) on the methyl iodide micro hydration process. Within atmospheric conditions, they show experimentally that CH$_3$I and H$_2$O tend to form homogeneous aggregates rather than heterogeneous clusters. Habartová et al. [241] have studied the partial hydration of alkyl halides at the water-vapor interface. They did MD simulations using polarizable force fields, adsorbing alkyl halides on a liquid water surface at 300 K. Once adsorbed, they show that methyl iodide tends to be localized at the interface without diffusing inside the bulk.

Regarding the atomic LJ parameters for C and H, we have used the ones provided by Habartová et al. [242], and for I, the ones provided by Freitas et al. [243]. They are presented in Table 3.14 at the end of the chapter. Calculated RESP atomic partial charges are used at the MP2/aug-cc-pVTZ(-PP) level of theory using the GAUSSIAN 16 code [244] and the ANTECHAMBER package [245]. All this part is detailed in section 3.2.

Furthermore, we must pay attention to the effects of polarization on CH$_3$I. Because developing a polarizable force field was beyond the scope of this Thesis work, we used the inherent polarization approximation described in section 2.9.6 to approximate it. We need *ab initio* data to compute the resulting scaling factors (SFs). Then, we optimize CH$_3$I-containing molecular clusters at the MP2/aug-cc-pVTZ(-PP) level of theory. From these calculations, we fit the SFs to obtain their optimized values. All the force field calculations are made using the GROMACS package version 5.1.4 [246]. The whole process will be described in sections 3.4.1 and 3.4.3.

3.2 *Ab initio* gas phase calculations

In order to provide *ab initio* data for fitting and benchmarking the force field parameters, we have optimized the isolated CH_3I molecule geometry at the MP2/aug-cc-pVTZ(-PP) level of theory [180, 247, 248] using the GAUSSIAN 16 code [244]. In this calculation, the 28 inner electrons of the iodine atom were described using the fully relativistic effective core potential (ECP) of Peterson et al. [249]. The resulting geometry is displayed in Fig 3.1, and the geometric parameters are given in Tab. 3.1. Our calculations agree well with experimental values. Then, it is possible to use *ab initio* calculations at the MP2/aug-cc-pVTZ(-PP) level of theory to fit intramolecular parameters. By varying the bond lengths and the angles,

Figure 3.1: (left) CH_3I optimized geometry at the MP2/aug-cc-pVTZ(-PP) level of theory; (right) CRAM representation of the CH_3I molecule with atom numbering.

Table 3.1: Geometric parameters of CH_3I geometry optimized at different levels of theory compared to experimental values. Distances are in Å, angles are in degrees.

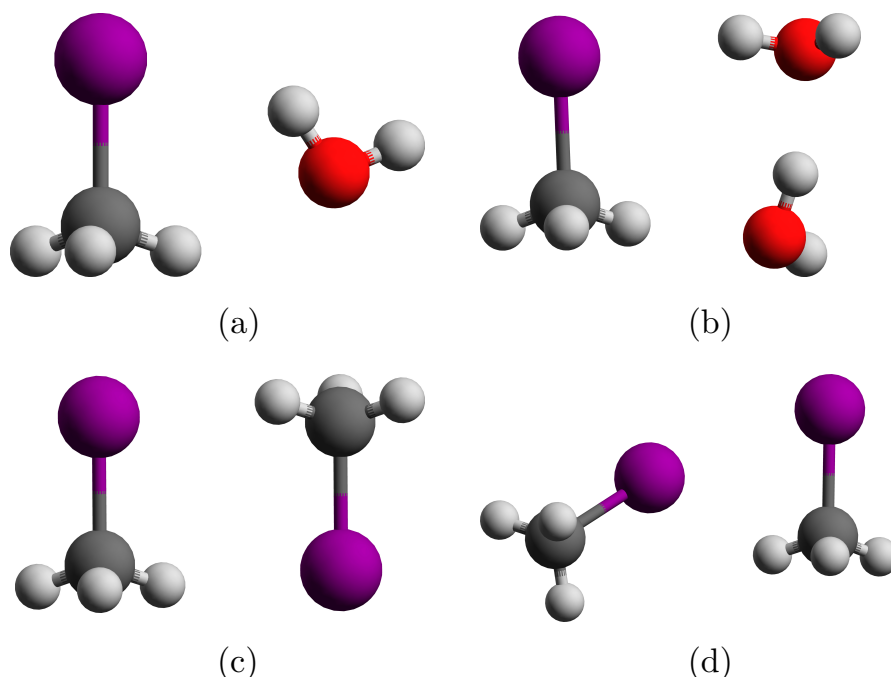|	Theo.[a]	Theo.[b]	Exp.[c]	Exp.[d]
r C−I	2.123	2.136	2.136	2.146
r C−H	1.083	1.082	1.084	—
∡ HCI	107.7	107.8	107.5	106.8
∡ HCH	111.2	111.1	111.4[e]	111.6

[a] MP2/aug-cc-pVTZ-PP (This work)
[b] M06-2X/6-311+G(2df,2p) (This work)
[c] IR spectroscopy [250, 251]
[d] Neutron powder diffraction (crystal structure) [252]
[e] Calculated from the previous geometric parameters

Figure 3.2: Geometry samples used to benchmark methyl iodide force field. All geometries are calculated at the MP2/aug-cc-pVTZ-(PP) level of theory. The samples consist in CH$_3$I + H$_2$O (a), CH$_3$I + 2 H$_2$O (b), 2 CH$_3$I in the head-to-tail (HtT) configuration (c), and 2 CH$_3$I in the head-to-head (HtH) configuration (d).

we can determine, using a nonlinear fit, the parameters for each distortion. The applied methodology will be developed in section 3.3.

Regarding the SF fitting and benchmarks in the gas phase, we optimized four molecular clusters of CH$_3$I with and without H$_2$O molecules at the MP2/aug-cc-pVTZ(-PP) level of theory. We have picked the most stable structure for each clusters, in agreement with previous calculations [107, 240, 253]. They are represented in Fig. 3.2, whereas the structural parameters are shown in Table 3.3.

The 2 CH$_3$I HtT dimer results differ between the literature and our calculations. Indeed, Sobanska et al. [107][1] have found a global minimum structure where there is only one (H$\cdots$I) intermolecular bond, whereas Ito [238][2] has found a global minimum without intermolecular hydrogen bonds. In addition, Ramasami et al. [239] have also found that the non-hydrogen-bonded structure is the most stable one. Nevertheless, within our calculations at the MP2/aug-cc-pVTZ(-PP) level of theory, we have found that the doubly-hydrogen-bonded structure is the

---

[1] Calculations done at the ωB97X-D/aug-cc-pVTZ(-PP) level of theory, ZPE corrected.

[2] Calculations done at the B971/LanL2DZ+fdp, MP2/aug-cc-pVTZ, and MP2/LanL2DZ+fdp level of theory, ZPE and BSSE corrected.

Table 3.2: Various relative energies of the $2\,CH_3I$ HtT optimized geometries at the MP2/aug-cc-pVTZ(-PP) level of theory. The doubly-hydrogend bonded structure is picked as the reference. Energies are in $kJ\,mol^{-1}$.

	E_0	ZPE	E_0 + ZPE	BSSE	E_0 + BSSE + ZPE
Difference	0.4	−0.2	0.2	−1.2	−1.0

global minimum, with an energy difference of $0.4\,kJ\,mol^{-1}$ with respect to the non-hydrogen-bonded structure, without the ZPE correction. Adding the latter, we ended with a difference of $0.2\,kJ\,mol^{-1}$, where the doubly-hydrogen-bonded structure is still the global minimum. The only remaining difference between our methods and the work done by Ramasami et al. [239] is that they corrected the energy using the BSSE. After including ZPE and BSSE corrections in our calculations, we obtained the same results, with a non-hydrogen-bonded structure more stable by $1.0\,kJ\,mol^{-1}$ than the hydrogen-bonded structure. Results are summarized in Table 3.2.

Nevertheless, such energy differences indicate that both structures are nearly degenerate, and we have chosen to keep the hydrogen-bonded structure as a reference to parametrize the force field. Consequently, we do not have any structural values to compare our results for this cluster with the literature in Table 3.3. Our values are in excellent agreement with the literature for all the other clusters. Those geometries and energies will be used to fit the atomic partial charges SFs. It can be done by looking at the variation of the interaction energy according to the SF value.

Table 3.3: Comparison of the structures obtained in this work, at the MP2/aug-cc-pVTZ(-PP) level of theory, with reported values. Distances are in Å.

Cluster	Observable	Value	Observable	Value
CH$_3$I + H$_2$O				
	r (I$\cdots$H)	2.76[a]	r (O$\cdots$H)	2.42[a]
		2.97[b]		2.51[b]
		3.09[c]		2.37[c]
		2.82[d]		2.41[d]
		2.99[e]		2.45[e]
CH$_3$I + 2 H$_2$O				
	r (I$\cdots$H)	2.65[a]	r (CH$\cdots$O)	2.25[a]
		2.79[b]		2.26[b]
	r (OH$\cdots$H)	1.88[a]		
		1.87[b]		
2 CH$_3$I HtH				
	r (I$\cdots$I)	3.76[a]	r (I$\cdots$H)	3.42[a]
		3.96[c]		3.64[c]
		3.84[d]		3.53[d]
		4.07[e]		3.38[e]

[a] MP2/aug-cc-pVTZ(-PP) (This work)   [d] MP2/aug-cc-pVTZ [238]
[b] ωB97X-D/aug-cc-pVTZ(-PP) [107]   [e] B971/LanL2DZ+fdp [238]
[c] MP2/LanL2DZ+fdp [238]

3.3 Intramolecular parameters fitting

The goal of fitting intramolecular parameters is to obtain a force field that can accurately mimic the interaction of the molecule with others at the quantum level. This process involves adjusting them so that the energy of the molecule predicted

by the force field matches the energy obtained from experimental measurements or quantum calculations. In this thesis, we only used the second option.

This process can be challenging because the energy of a molecule depends on many factors, including the molecule's geometry, the type and strength of the bonds between atoms, and the method used for quantum calculations. To model intramolecular interactions, we are using the harmonic approximation to describe molecular distortions. In this context, we will present the methods and the results obtained by matching the parameters with calculations made at the MP2/aug-cc-pVTZ(-PP) level of theory. We will start by developing the part related to bond stretching first, before describing the angle bending.
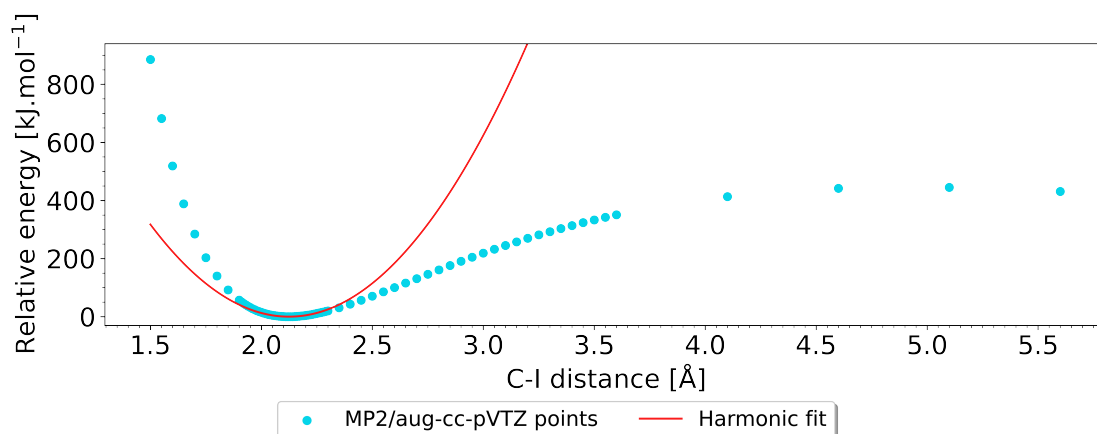
3.3.1   C−I bond stretching

Within the harmonic approximation, bond stretching parameters are constant values that describe the energy of a bond distortion according to atomic distance, as previously discussed. In Eq. (2.155), it is represented by K_b.

The first step in fitting these parameters starts with the optimized geometry. After picking an intramolecular bond, we made a rigid scan along the bond. It consists in freezing all the atoms not involved in the chemical bond (i.e., making them a rigid structure) and varying the bond length. As a result, we obtain a series of geometries with the corresponding energies. With this information, we can represent the energy according to the bond length. Then, we can fit them by optimizing K_b and r_{eq} from Eq. (2.155) using a least squares method. After convergence, we obtain the corresponding values of the constants at the MP2/aug-cc-pVTZ(-PP) level of theory, represented in Fig. 3.3, for the C−I bond stretching from CH$_3$I.

First, we recognize the characteristic shape of the curve associated with bond stretching. Indeed, we observe the equilibrium value associated with a minimum for a bond length at $r_{eq} = 2.125$ Å. The molecular energy increases as the bond length increases or decreases from the equilibrium value. In the first case, the energy increases quickly because of the strong repulsion between nuclei. When the bond length increases, the energy converges at some point when the two nuclei are too far to interact with each other (dissociation limit).

In addition, we highlight that a quadratic function can not approximate the whole curve for all the bond lengths, as presented in Fig 3.3. Indeed, the quadratic fit values match with the *ab initio* ones in the vicinity of the well only. Furthermore, the energy keeps increasing when the bond distance increases or decreases, leading to an unbreakable bond description. Then, to fit the *ab initio* values, we must select some points close to the equilibrium bond distance. The next step is to evaluate the quality of the fit according to the number of points we have selected. There are several ways to do it, like looking at the residual value or evaluating it

Figure 3.3: Evolution of the potential energy according to the C−I bond stretching from the optimized geometry at the MP2/aug-cc-pVTZ(-PP) level of theory. Dots represent the quantum calculations and the continuous line represents the bottom well fitting using the harmonic approximation.
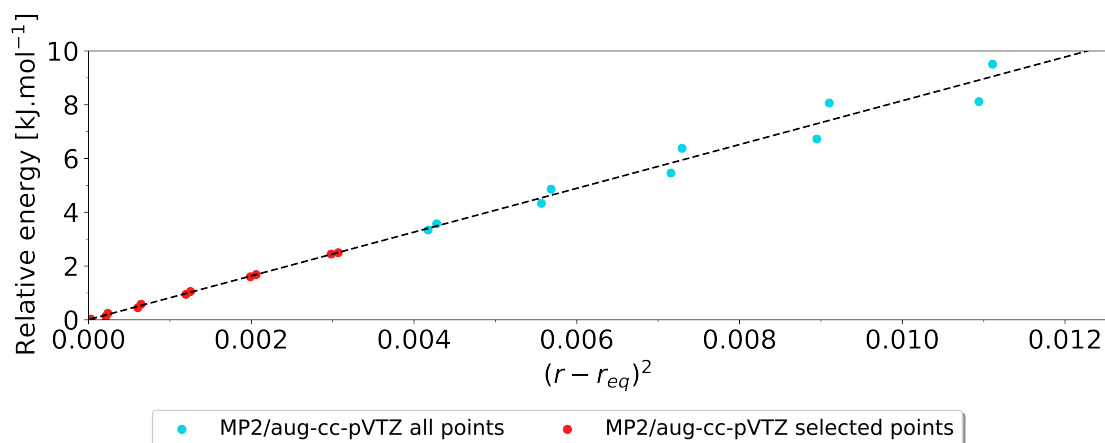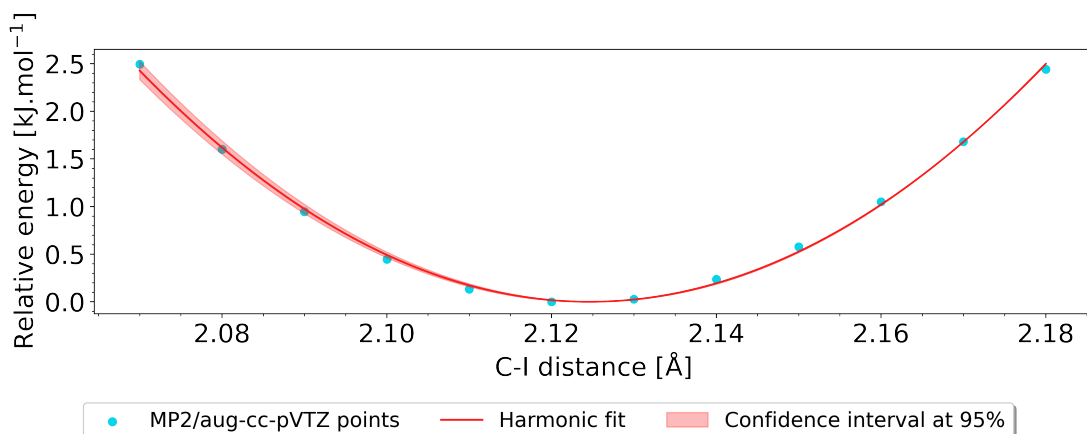

Figure 3.4: Evolution of the potential energy according to $(r-r_{\mathrm{eq}})^2$ with respect to the C−I bond stretching from the optimized geometry at the MP2/aug-cc-pVTZ(-PP) level of theory. Dots represent the quantum calculations and the dashed line represents the fit using the harmonic approximation. Red dots represent selected point for the fit and blue dots the ones not selected for the fit.

visually. Furthermore, we can plot the energy according to $(r - r_{\mathrm{eq}})^2$, which should be linear in the domain where the harmonic approximation is correct. This last point is shown in Fig 3.4.

The first twelve points (represented in red) are well aligned. The same observation can be made for the two first blue dots. Then, the harmonic approximation

Figure 3.5: Evolution of the potential energy according to the C−I bond stretching from the optimized geometry at the MP2/aug-cc-pVTZ(-PP) level of theory. Dots represent the quantum calculations, and the red line represents the fit using the harmonic approximation. The red area represents the 95 % confidence interval of the fit.

matches the *ab initio* values for the first 14 points closer to the equilibrium bond distance. The following points spread to higher or lower energies than the dashed line, meaning that the harmonic approximation begins to be insufficient to describe this behavior because of the anharmonicity of the potential energy surface. In addition, selecting the first 12 or 14 points to make the harmonic fit is equivalent. Indeed, even if the 13th and 14th points slightly deviate from the dashed line, it might not impact the calculated value of K_b highly.

We know how many and which points we must select for the harmonic fit and the bond distance range for which this approximation is correct. Then, we can determine the parameters by fitting the potential energy curve directly or by computing the slope of the dashed line in Fig. 3.4. The first method allows us also to compute a fitted r_{eq} value, resulting in a better description of the energy in this area.

The fit is done using the CURVE_FIT function from the OPTIMIZE package included in the SCIPY software [254]. This function uses nonlinear least squares analysis to optimize the parameters that better fit the reference points. More specifically, we have used the trust region reflective algorithm, one of the best optimization methods to solve nonlinear problems [255]. To quantify the quality of the fit, we calculated the adjusted R^2 and the root mean squared error (RMSD). In addition, we computed the standard error for each parameter (K_b and r_{eq}) as the confidence interval at 95 %. The results are displayed in Tab. 3.4 and Fig. 3.5.

Table 3.4: Results and measurements fitting using a harmonic function of the C−I from the optimized geometry at the MP2/aug-cc-pVTZ(-PP) level of theory. The uncertainty on the parameters corresponds to the one for a confidence interval equal to 95 %.

Name	Value
PARAMETERS OF THE FITTED FUNCTION	
r_{eq} (Å)	2.125
Δr_{eq} (Å)	0.001
K_b (kJ/mol/Å^2)	814.2
ΔK_b (kJ/mol/Å^2)	17.5
QUALITY OF THE FIT MEASUREMENTS	
Adjusted R^2	0.997
RMSD (kJ/mol)	0.039

Fitted values of r_{eq} and K_b are respectively 2.125 ± 0.001 Å and 814.2 ± 17.5 kJ/mol/Å^2 in a 95 % confidence interval. The accuracy on r_{eq} is close to 0. Nevertheless, the one obtained on K_b is slightly higher. This accuracy on the parameter is acceptable, representing around 2 % of the current value. Regarding the adjusted R^2 and the RMSD values, they both indicate a high-quality fit. Looking at the accuracy of describing the potential energy according to the bond length, we can see that it depends on r. If we use the propagation of error formula, we can see that the error in the potential energy should be symmetric according to r_{eq}. Nonetheless, plotting the confidence interval using the maximum and minimum possible values, we see that the error increases only when we decrease the bond length from its equilibrium value. Indeed, error compensations appear when we increase the bond length from its equilibrium value. In the simulations, the bonds will only vary substantially from equilibrium values because of the high value of the spring constant K_b.

To conclude, the methodology employed to fit the C−I bond stretching parameters give accurate results for all the parameters. We can employ the same process to compute the others parameters, as discussed in the following.
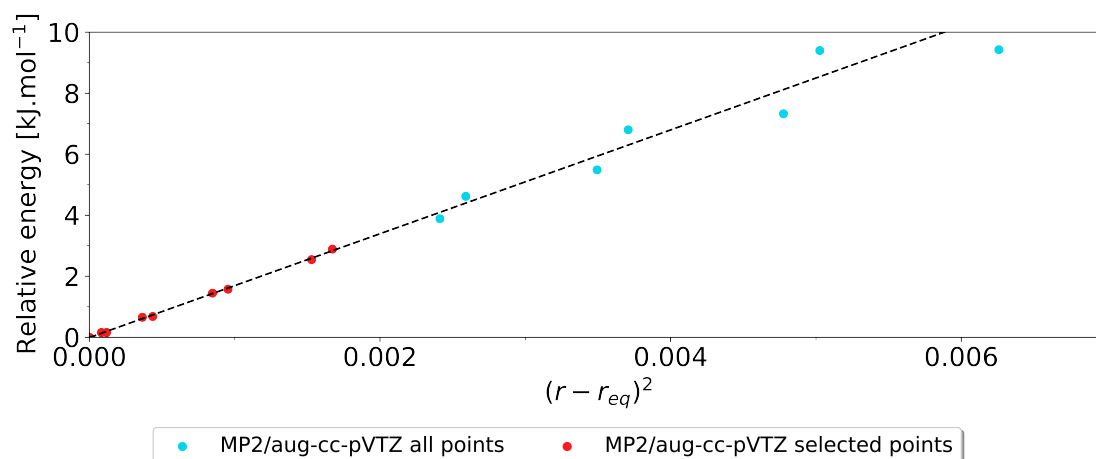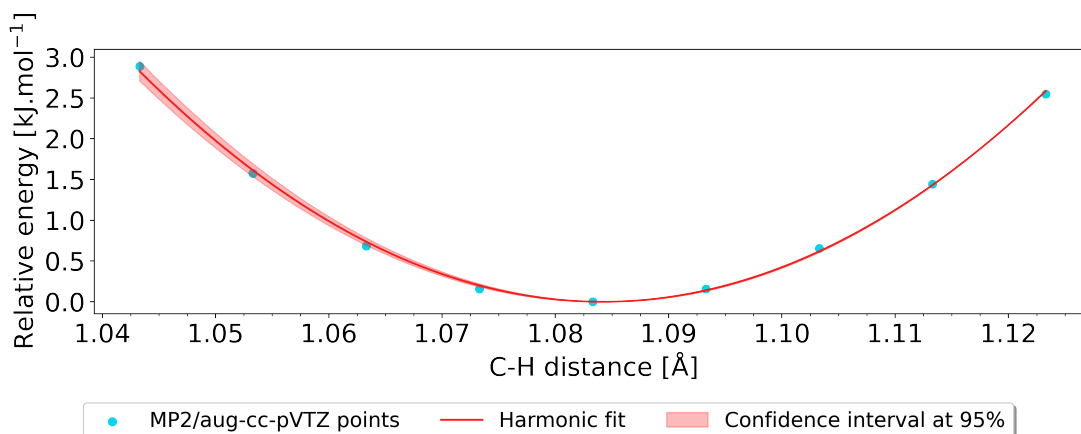
Figure 3.6: Evolution of the potential energy according to $(r-r_{\mathrm{eq}})^2$ with respect to the C$-$H bond stretching from the optimized geometry at the MP2/aug-cc-pVTZ(-PP) level of theory. Dots represent the quantum calculations and the dashed line represents the fit using the harmonic approximation. Red dots represent selected point for the fit and blue dots the ones not selected for the fit.

3.3.2 C$-$H bond stretching

The same method from section 3.3.1 is applied for the C$-$H bond stretching fitting. After having computed the corresponding rigid scan, we can plot the energy according to $(r - r_{\mathrm{eq}})^2$, as shown in Fig. 3.6. In this case, we have picked the nine closest points to the equilibrium geometry. From the 10th one, it started to deviate slightly from the linear fit, meaning that anharmonic effects are becoming high. The next step is to do a nonlinear fit using the same tools as in section 3.3.1. All the results are shown in Fig. 3.7 and Table 3.5.

Fitted values of r_{eq} and K_b are respectively $1.084\,\text{Å}$ and $1690.0 \pm 39.2\,\text{kJ/mol/Å}^2$ in a $95\,\%$ confidence interval. The R^2 and the RMSD values are respectively close to 1.0 and 0.0. As for the C$-$I bond stretching, the values have low uncertainties, where ΔK_b represents around $2\,\%$ of K_b. In this case, we have a bond stretching spring constant higher than the one for C$-$I. It indicates that the potential energy increases quicker according to r. A comparison with OPLS or AMBER force field values is presented in Table 3.6. We observe that our values are in agreement with the ones reported in the literature.

Concerning uncertainties on the potential energy prediction, we observe the same effect as for C$-$I bond stretch fitting (Fig 3.5). Indeed, the $95\,\%$ confidence interval increases only when decreasing the bond length. It agrees with the highest deviation from the harmonic approximation of the *ab initio* points in this direction of the PES. Nevertheless, we will not investigate such a hypothesis in this thesis.

Figure 3.7: Evolution of the potential energy according to the C−H bond stretching from the optimized geometry at the MP2/aug-cc-pVTZ(-PP) level of theory. Dots represent the quantum calculations, and the red line represents the fit using the harmonic approximation. The red area represents the 95 % confidence interval of the fit.

Table 3.5: Results and measurements fitting using a harmonic function of the C−H from the optimized geometry at the MP2/aug-cc-pVTZ(-PP) level of theory. The uncertainty on the parameters corresponds to the one for a confidence interval equal to 95 %.

Name	Value
PARAMETERS OF THE FITTED FUNCTION	
r_{eq} (Å)	1.084
Δr_{eq} (Å)	$<$ 0.001
K_b (kJ/mol/Å^2)	1691.0
ΔK_b (kJ/mol/Å^2)	39.2
QUALITY OF THE FIT MEASUREMENTS	
Adjusted R^2	0.998
RMSD (kJ/mol)	0.039

Table 3.6: C−H bond stretching parameters previously obtained compared with values reported in the literature.

Parameter	This work	OPLS[a]	AMBER[b]
r_{eq} (Å)	1.084	1.080	1.090
K_b (kJ/mol/Å^2)	1691.0	1422.6	2097.0

[a] Doherty et al. [256]
[b] Wang et al. [257]

3.3.3   Bending angle

In this section, we will present the results of fitting the angle-bending parameters of our classical force field. We will describe the methods used to obtain these parameters. The quality of the fits will be evaluated, and any notable features or discrepancies will be discussed. We will also compare the angle bending parameters to those from other classical force fields and to *ab initio* calculations to provide insight into the accuracy of the force field for these types of interactions.

For angle bending, Eq. (2.156) is used to fit parameters. Mathematically, it has the same form as Eq. (2.155). Only the parameter names are different. Then, the same method is used to fit the angle bending parameters. Because we now analyze angles, the rigid scan is done by moving three atoms simultaneously. The variable is then an angle, as stated in Eq. (2.156).

Starting with the HCI angle, the next step is determining how many points we need to fit within the harmonic approximation. As before, we plot the potential energy according to $(\theta - \theta_{\text{eq}})^2$, where the *ab initio* points are aligned when correctly approximated within the harmonic approximation. Results are shown in Fig. 3.8 with 22 *ab initio* points. We can see that they are all aligned, meaning they are all well described using the harmonic approximation. Then, we can apply a nonlinear fit where results are shown in Fig. 3.9 and Table. 3.7.   Fitted values of θ_{eq} and K_{a} are respectively 107.8° and 0.0783 ± 0.0002 kJ/mol/°^{2} in a 95 % confidence interval. Both uncertainties are much lower than the parameters, leading to an accurate fitting. This is confirmed by the values of the adjusted R^2 (1.0) and the RMSD (0.025 kJ mol^{-1}) of the corresponding fit. According to previous results, the confidence interval at 95 % displayed in Fig 3.9 is small.

Then, we treat the HCH angle bending parameters. Results from plotting $(\theta - \theta_{\text{eq}})^2$ are presented in Fig. 3.10. As for the HCI parameters fitting, all the points are aligned, leading to a valid approximation for all 22 points. Then, we apply the nonlinear fit to determine the parameters. The results are shown in Fig 3.11 and Table 3.8.   Fitted values of θ_{eq} and K_{a} are respectively 111.2° and
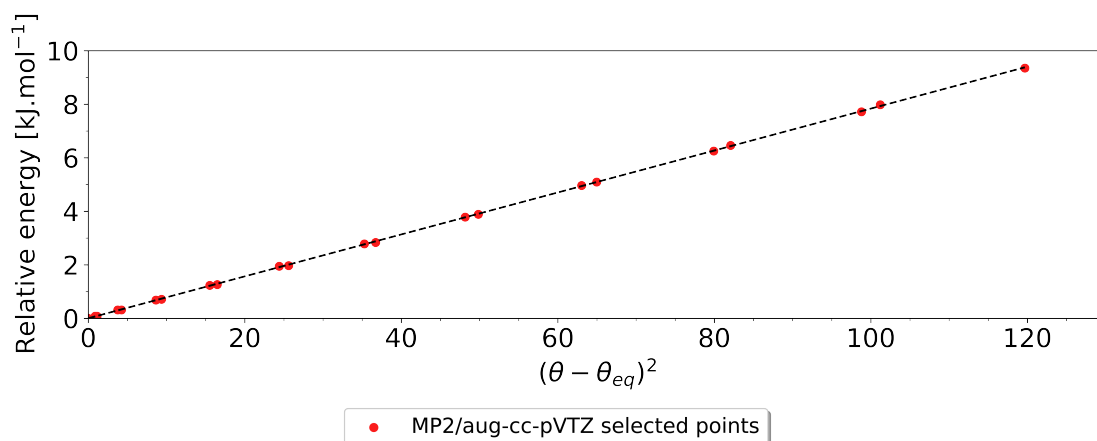
Figure 3.8: Evolution of the potential energy according to $(\theta - \theta_{\mathrm{eq}})^2$ from the optimized geometry at the MP2/aug-cc-pVTZ(-PP) level of theory for the HCI angle bending. Dots represent the quantum calculations and the dashed line represents the fit using the harmonic approximation. Red dots represent selected points for the fit.
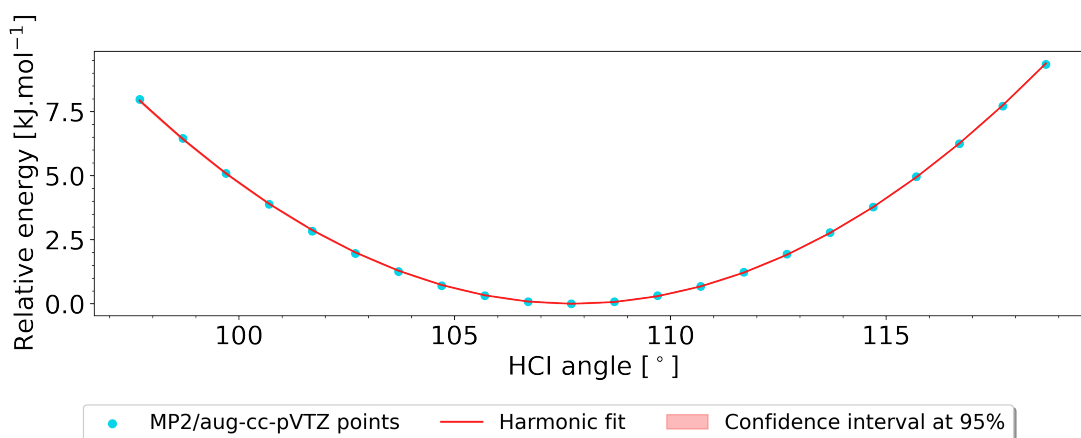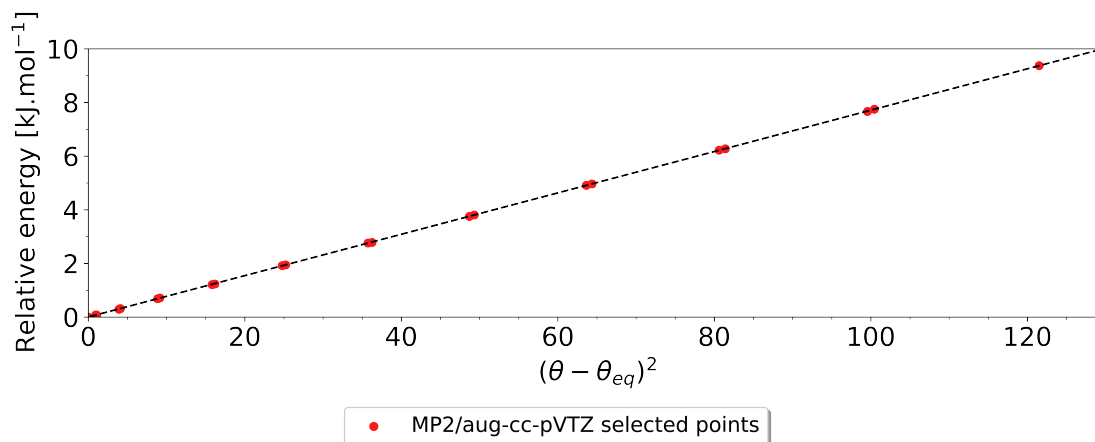

Figure 3.9: Evolution of the potential energy according to the HCI angle bending from the optimized geometry at the MP2/aug-cc-pVTZ(-PP) level of theory. Dots represent the quantum calculations, and the red line represents the fit using the harmonic approximation. The red area represents the 95 % confidence interval of the fit.

$0.0771 \pm 0.0001 \, \mathrm{kJ/mol/°^2}$ in a 95 % confidence interval. Measuring the quality of the fit, we obtain adjusted R^2 and RMSD values of 1.0 and $0.001 \, \mathrm{kJ \, mol^{-1}}$, leading to a high-quality fit. As for the HCI angle bending, uncertainties on fitted
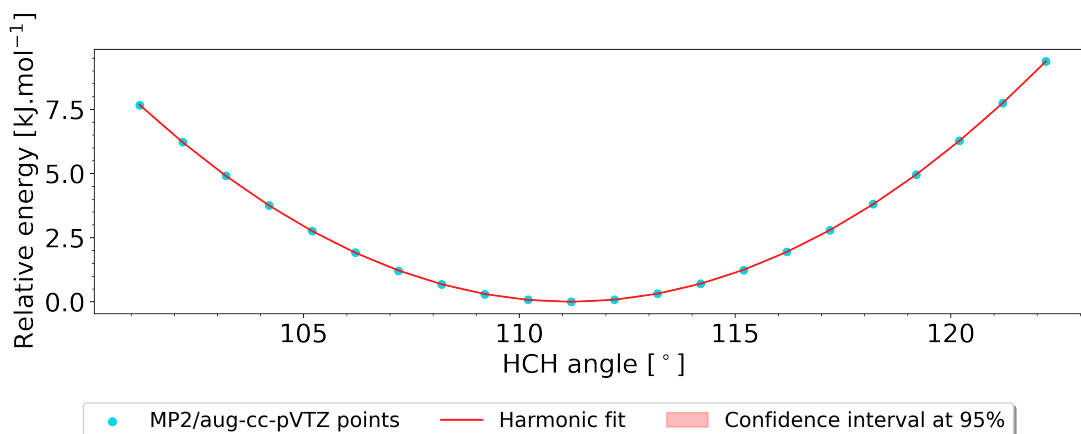
Table 3.7: Results and measurements fitting using a harmonic function of the HCl angle from the optimized geometry at the MP2/aug-cc-pVTZ(-PP) level of theory. The uncertainty on the parameters corresponds to the one for a confidence interval equal to 95 %.

Name	Value
PARAMETERS OF THE FITTED FUNCTION	
θ_{eq} (°)	107.8
$\Delta\theta_{\text{eq}}$ (°)	< 0.1
K_a (kJ/mol/°^{2})	0.0783
ΔK_a (kJ/mol/°^{2})	0.0002
QUALITY OF THE FIT MEASUREMENTS	
Adjusted R^2	1.0
RMSD (kJ mol^{-1})	0.025

Figure 3.10: Evolution of the potential energy according to $(\theta - \theta_{\text{eq}})^2$ from the optimized geometry at the MP2/aug-cc-pVTZ(-PP) level of theory for the HCH angle bending. Dots represent the quantum calculations and the dashed line represents the fit using the harmonic approximation. Red dots represent selected points for the fit.

parameters are low. The confidence interval is also small, as shown in Fig 3.11. A

Figure 3.11: Evolution of the potential energy according to the HCH angle bending from the optimized geometry at the MP2/aug-cc-pVTZ(-PP) level of theory. Dots represent the quantum calculations, and the red line represents the fit using the harmonic approximation. The red area represents the 95 % confidence interval of the fit.

Table 3.8: Results and measurements fitting using a harmonic function of the HCH angle from the optimized geometry at the MP2/aug-cc-pVTZ(-PP) level of theory. The uncertainty on the parameters corresponds to the one for a confidence interval equal to 95 %.

Name	Value
PARAMETERS OF THE FITTED FUNCTION	
θ_{eq} (°)	111.2
$\Delta\theta_{\mathrm{eq}}$ (°)	< 0.1
K_a (kJ mol^{-1} °$^{-2}$)	0.0771
ΔK_a (kJ mol^{-1} °$^{-2}$)	0.0001
QUALITY OF THE FIT MEASUREMENTS	
Adjusted R^2	1.0
RMSD (kJ mol^{-1})	0.007

Table 3.9: HCH bending angle parameters previously obtained compared with values reported in the literature.

Parameter	This work	OPLS[a]
θ_{eq} (°)	111.2	109.8
K_a (kJ mol^{-1} °$^{-2}$)	0.0771	0.0421

[a] Doherty et al. [256]

comparison with the parameters of the OPLS force field reported in the literature is presented in Table 3.9. We see that our results agree with the literature.

3.4 Intermolecular parameters fitting

Intermolecular parameters describe the interactions between different molecules in a system. These interactions can include van der Waals forces and electrostatic interactions, as described in section 2.9.3. In a classical force field, these parameters are used to calculate the potential energy of a system of molecules, which can then be used to predict the behavior of the molecules under various conditions. The process of intermolecular parameter fitting involves adjusting the values of these parameters so that the energy of the system predicted by the force field matches the energy obtained from experimental measurements or quantum mechanical calculations. The fitting of intermolecular parameters can be challenging because the energy of a system of molecules depends on many factors, including the geometry of the molecules and the type and strength of the interactions between them.

First, we will describe how we computed the atomic partial charges used in the classical force field. Then, we will discuss several parameters in the literature about methyl iodide. Finally, the inherent polarization will be introduced to finalize the results.

3.4.1 Atomic partial charges

Another important aspect of classical force fields is the fitting of atomic partial charges, which represent the distribution of electrical charge on the atoms of a molecule. One method for fitting atomic partial charges is RESP, as defined in section 2.9.5. It uses quantum mechanical calculations to obtain an electrostatic potential for a molecule and then fits the atomic partial charges to reproduce this potential using a classical force field. All those calculations are done using the GAUSSIAN 16 code [244] and the ANTECHAMBER package [245].

Table 3.10: Calculated RESP atomic partial charges for methyl iodide at the MP2/aug-cc-pVTZ(-PP) level of theory. Results are compared with values found in the literature. Charges are fractions of the elementary charge e.

	C	H	I	Cl	Br
CH$_3$I[a]	−0.63	0.24	−0.09	—	—
CH$_3$I[b]	−0.52	0.20	−0.09	—	—
CH$_3$Cl[b]	−0.37	0.18	—	−0.16	—
CH$_3$Cl[c]	−0.26	0.14	—	−0.16	—
CH$_3$Br[b]	−0.47	0.20	—	—	−0.14
CH$_3$Br[c]	−0.49	0.20	—	—	−0.11

[a] This work
[b] Habartová et al. [241], at the MP2/cc-pVDZ level of theory
[c] Habartová et al. [225], at the B3LYP/cc-pVTZ level of theory

The fitting of atomic partial charges using the RESP method is a crucial step in developing a classical force field because the distribution of charge on a molecule's atoms significantly impacts the molecule's behavior. Inexact partial charges can lead to errors in a molecule's calculated energy and structural properties. The RESP fit allows to obtaining a reliable estimation of the atomic partial charges by considering the electrostatic potential generated by the molecule's electron density. It can be used as a starting point for other methods of charge fitting and can help to model intermolecular interactions, such as hydrogen bonding and electrostatic interactions.

In this context, the RESP fit was done at the MP2/aug-cc-pVTZ(-PP) level of theory on the optimized CH$_3$I molecule represented in Fig. 3.1. The results and comparisons to the literature are shown in Tab. 3.10. Habartová et al. [241] have computed RESP atomic partial charges for halomethanes at the MP2/cc-pVDZ level of theory. Our calculated charges are slightly higher than the ones reported for methyl iodide. Nevertheless, we are in significant agreement with the results of this study. One year before, they had provided charges for halomethanes [225]. Comparing the evolution of the partial charges on the halogen, it decreases when the halogen atomic number increases. Our calculated values on methyl iodide follow this tendency, with a RESP partial atomic charge on iodine of $-0.09\,e$.

3.4.2 Lennard-Jones parameters

In classical force fields, LJ parameters describe the Van der Waals interactions between atoms or molecules. These interactions are essential in describing the behavior of molecular systems, as they contribute to the system's overall stability and govern the behavior of the molecules at short distances.

LJ parameters are taken from the work of Habartová et al. [242, 258]. The Lorentz-Berthelot combination rule is used to combine atomic LJ parameters. We have tested several parameters for iodine from the literature. They are shown in Table 3.11. The parameters can be divided into three groups regarding the ϵ_i value. Group 2 contains parameter 7, with a high value of ϵ_i computed from liquid CH_3I. We have Group 1 (parameters from 1 to 3) with intermediate values and Group 3 (parameters from 5 to 7) with low values. The aim is to test the whole bench of parameters by comparing the minimum geometry structures and the interaction energies with the MP2/aug-cc-pVTZ(-PP) level of theory. The interaction energy is defined as:

$$E_{\text{int}} = E_{\text{cluster}} - \sum_{\text{molecules}} E_{\text{isolated}} \ , \tag{3.1}$$

where E_{cluster} is the cluster's total potential energy, and E_{isolated} is the potential energy of a single isolated molecule. Within this method, the global minimum energy of the isolated molecule is zero.

The first calculations are done on the $2\,CH_3I$ HtT cluster presented in Fig. 3.2. We used the parameters computed in all the previous sections. Because of their low ϵ_i values, the parameters from Group 3 give structures very different from the *ab initio* resulting ones. Thus, for clarity, we will not display their results. We allowed molecular distortion using the parameters calculated in the previous sections. The

Table 3.11: Lennard-Jones parameters for the iodine atom taken from the litterature

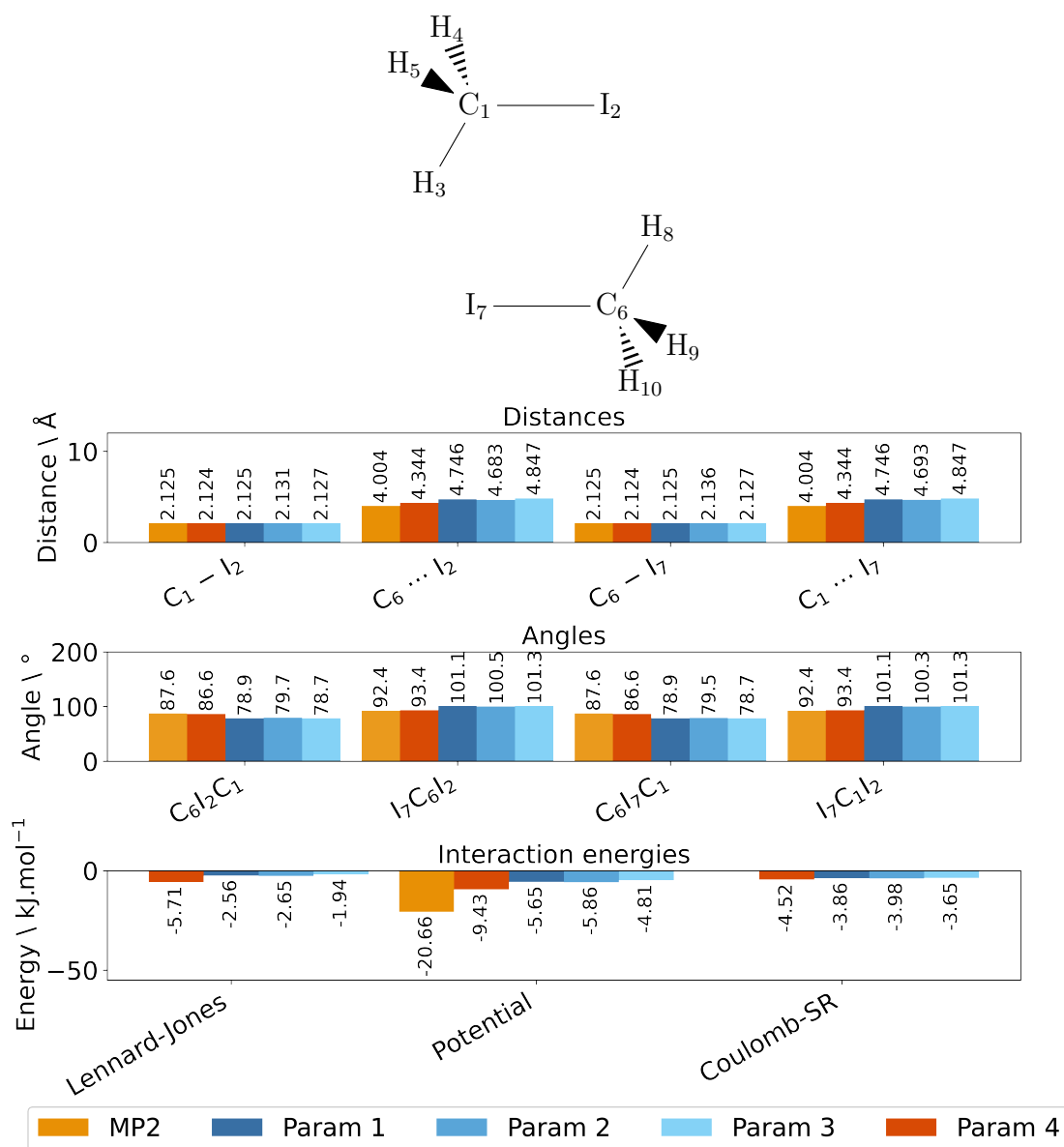|	Group 1			Group 2	Group 3		
	Param 1[a]	Param 2[b]	Param 3[c]	Param 4[d]	Param 5[e]	Param 6[e]	Param 7[e]
σ_i (nm)	0.49	0.48	0.52	0.41	0.70	0.74	0.72
ϵ_i (kJ mol^{-1})	0.67	0.71	0.42	2.69	0.08	0.04	0.05
Original pair	$I-I$	$I-I$	$I-O$	$I-I$	$I-O$	$I-O$	$I-O$
Water model	SWN4-NDP	TIP4P	SPC	Liquid CH_3I	TIP3P	TIP4Pew	SPC/E

[a] Lamoureux et al. [259]
[b] Jensen et al. [260]
[c] Rajamani et al. [261]

[d] Crone-Münzebrock et al. [236]
[e] Joung et al. [262]

Figure 3.12: 2 CH$_3$I HtT structural parameters calculated at the MP2/aug-cc-pVTZ(-PP) level of theory and using a classical force field. Parameters from 1 to 4 are compared.

structure and interaction energies comparison between each parameter and the *ab initio* results are shown in Fig. 3.12.

For all the parameters, as expected, the intramolecular C$-$I bond length agrees with the MP2 calculations. However, the intermolecular C$-$I bond distance in CH$_3$I dimers differs slightly from the reference. Indeed, parameter 4 has the

closest value to the MP2 reference calculations. Nevertheless, all the force field calculations tend to overestimate the intermolecular C−I distance between the two methyl iodide molecules. Regarding the angles, parameter 4 best matches the MP2 calculations, with angles that are in excellent agreement with the MP2 values. Again, the other parameters overestimate the ICI angle and underestimate the CIC one. Then, we see that the dihedral angle formed by the two intramolecular C−I bonds is perfectly planar for all the calculations. Finally, all the parameters highly underestimate the potential interaction energy between both molecules. We observe an underestimation by a factor of 10 for Group 1 parameters and a factor of 2 for parameter 4, that gives the best results in terms of geometry.

3.4.3   Inherent polarization

To accurately describe the molecular interactions, it is crucial to consider the polarization effects. As discussed in section 2.9.6, the lack of polarization induces an underestimation of the interaction energies. Classical molecular dynamics simulations achieve this by introducing inherent polarization through scaling atomic partial charges using a SF. This process adjusts the charges on the atoms to account for their polarizability and allows for a more accurate representation of the molecular interactions. By incorporating inherent polarization, the force field used in the calculations can more accurately predict the interaction energy between molecules.

In the literature, Habartová et al. [225] have scaled halomethane atomic partial charges to fit the experimental hydration free energy better, using one SF by halomethane molecule. We tested four different values to find the correct SF and made the comparisons as in the previous section. Among all the tested SFs, we have found that the one that best matches MP2 calculations is a SF of 1.7. It leads to the atomic charges presented in Table 3.12. We observe that the atomic charges on the halogen still decrease as the atomic number increase. Within the same tendency, we observe an increase in the atomic charge of the carbon and the hydrogen atom when the halogen atomic number increases. Our results follow the same tendency as the ones computed by Habartová et al. [225] in their study.

The next step is to measure the impact of the SF on the optimized structures calculated with our force field. The structural parameters and interaction energies comparisons are shown in Fig. 3.13. As expected, scaling the atomic partial charges does not modify the intramolecular CI bond length. However, the structure optimized by force field is slightly modified for parameters 1 to 3, with higher modification for parameter 4. We also note that the interaction energies are now more in agreement with MP2 values, even if they still underestimate the latter. Scaling the atomic charges induces an increase in the Coulombic interaction energy and a decrease in the LJ ones. It modifies slightly the optimized structures compared to MP2 geometries. We observe that the higher the SF value is, the more

Table 3.12: Calculated RESP atomic partial charges for methyl iodine at the MP2/aug-cc-pVTZ(-PP) level of theory with a scaling factor value of 1.7. Results are compared with values found in the literature.

	C	H	I	Cl	Br
CH$_3$I[a]	−1.07	0.41	−0.16	—	—
CH$_3$Cl[b]	−0.44	0.24	—	−0.26	—
CH$_3$Br[b]	−0.96	0.39	—	—	−0.22

[a] This work
[b] Habartová et al. [225], at the B3LYP/cc-pVTZ level of theory with a SF value of 1.7 for CH$_3$Cl and 1.95 for CH$_3$Br
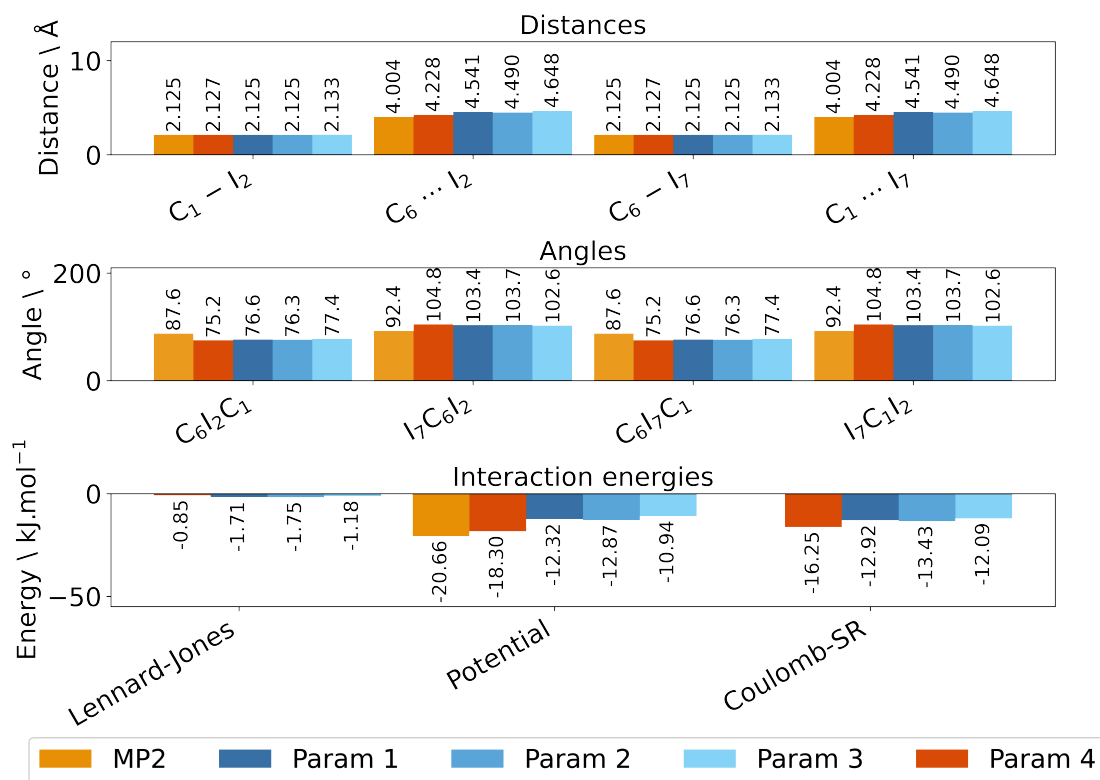

Figure 3.13: 2 CH$_3$I HtT structural parameters calculated at the MP2/aug-cc-pVTZ(-PP) level of theory and using different sets of parameters and a scaling factor of 1.7. Parameters from 1 to 4 are compared.
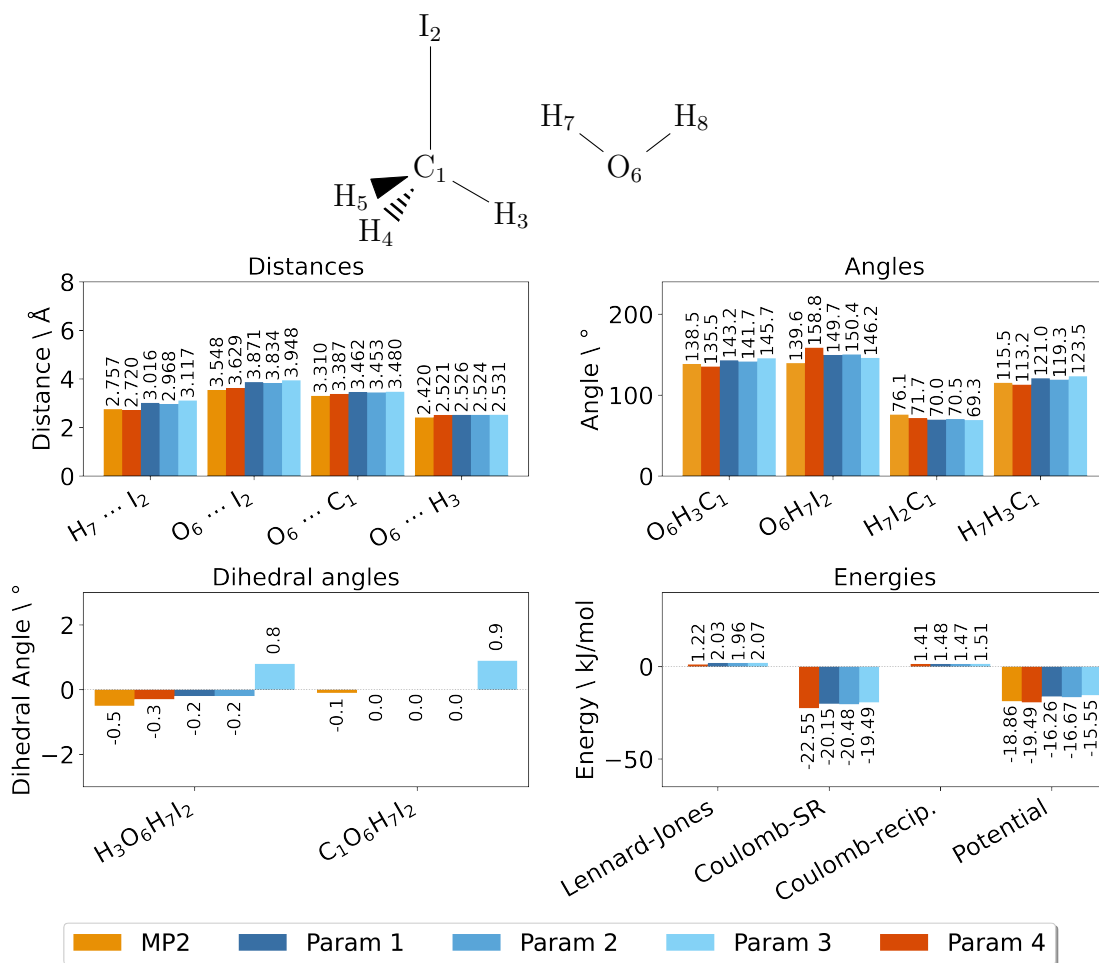
Figure 3.14: CH$_3$I + H$_2$O structural parameters calculated at the MP2/aug-cc-pVTZ(-PP) level of theory and using different sets of parameters with a scaling factor of 1.7. Water is described using the SPC/E model. Parameters from 1 to 4 are compared.

distortion we induce. A good balance between a good interaction energy value and a good structure is found when the SF equals 1.7.

An important feature is that our force field must also describe correctly the CH$_3$I − H$_2$O interaction. We tested also our sets of parameters in combination with the SPC/E model [263, 264] for the CH$_3$I − H$_2$O dimer. Results are shown in Fig. 3.14. For all the parameters, we observe that intermolecular atomic distances are excellently reproduced by the force field, where parameter 4 gives the best results. Angles computed by the force field also agree with MP2 calculations, as well as dihedral ones. Regarding the interaction energies, we observe that overall, the total interaction energy is in excellent agreement with the MP2 values.
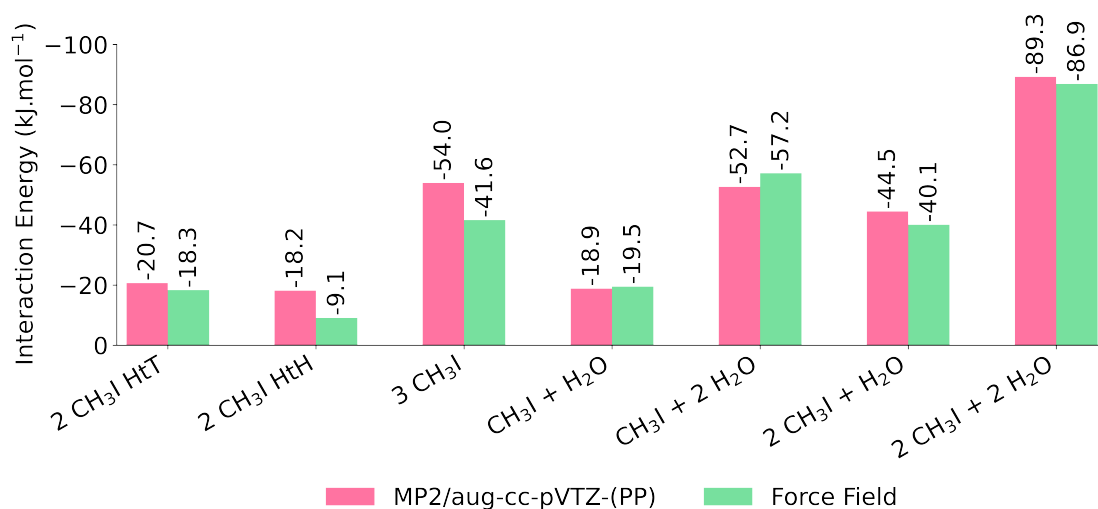
Figure 3.15: Comparison of the force field interaction energies obtained with parameter 4 with quantum results at the MP2/aug-cc-pVTZ(-PP) level of theory. Water is described with SPC/E model.

To conclude, our force field describes well the interactions between 2 CH$_3$I HtT and CH$_3$I + H$_2$O clusters, with suitable structural parameters and interaction energies. The last step in this process is to benchmark our force field further. In the next section, we will benchmark our force field in bulk environment. We will also test its transferability to describe CH$_3$I interacting in clusters and with NaCl.

3.5 Benchmarks

3.5.1 Gas phase clusters

In the previous section, we benchmarked the results of the force field using different parameters. We have shown that the parameters labeled 4 give the best results on CH$_3$I + H$_2$O and 2 CH$_3$I HtT clusters. Then, we have also benchmarked our force field performances to other gas phase clusters optimized at the MP2/aug-cc-pVTZ(-PP) level of theory, as presented in Fig. 3.15. Nevertheless, including clusters of larger sizes for evaluating the force field performances is crucial.

For almost all the tested gas phase clusters, we observe that the interaction energies obtained by our force field agree with MP2 values. For these configurations, our force field describes the intermolecular interactions between molecules well. However, for the 2 CH$_3$I HtH and 3 CH$_3$I clusters, we observe that the interaction energies are not matching as well. Indeed, we have a factor 2 between MP2 and
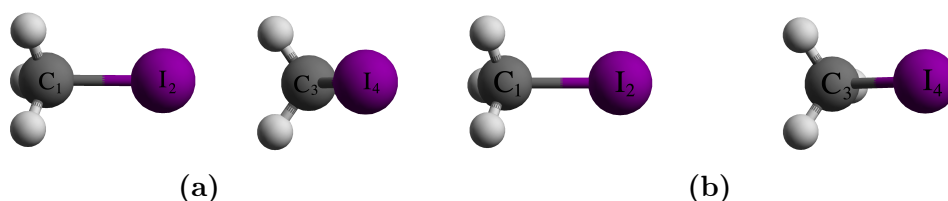
Figure 3.16: Geometry comparison of $2\,CH_3I$ head-to-head gas cluster from (a) MP2/aug-cc-pVTZ and (b) force field calculations.

Table 3.13: Geometric parameter of the $2\,CH_3I$ HtH geometrie optimized at different levels of theories.

	MP2/aug-cc-pVTZ(-PP)	Force field
$r(I_2 \cdots I_4)$ \Å	3.760	4.497
$r(I_2 \cdots C_1)$ \Å	3.696	3.937
$\measuredangle\ I_2I_4C_3$ \°	71.8	28.2
$\measuredangle\ C_1I_2I_4$ \°	169.2	170.1

force field values for the $2\,CH_3I$ HtH cluster, and we have a $20\,\%$ relative error for the $3\,CH_3I$ one. To further understand what is not well described in these configurations by our force field, we will look closer at the $2\,CH_3I$ HtH cluster. The structures obtained by MP2 and force field methods are shown in Fig. 3.16 and Table 3.13.

We observe that both structures are not identical. Indeed, the two methyl iodide molecules appear to be at a higher distance when computed using our force field compared to the MP2-optimized structure. Regarding the intermolecular bond distances, the $(I_2 \cdots I_4)$ intermolecular distance increases from $3.760\,\text{Å}$ for MP2 geometry to $4.497\,\text{Å}$ for the one obtained by the force field. Furthermore, the $(I_2 \cdots C_1)$ intermolecular distance increases from $3.696\,\text{Å}$ for MP2 to $3.937\,\text{Å}$ for the force field resulting geometry. Same observations can be done for the angles, were a high difference is observed for the $I_2I_4C_3$ one. These differences could have several causes. First, it can be due to the lack of polarization in our force field. It only describes inherent polarization by scaling the atomic charges and can miss key elements describing the intermolecular interaction. Then, our force field could have issues describing the halogen-halogen interaction. Indeed, in the structure obtained by MP2 calculations, the iodine from a molecule points toward the C−I covalent bond of the other. When computing the same structure with our force field, we observe a repulsion of the iodine of the second molecule. Another hypothesis is

that our force field does not describe these kinds of interactions well. In the 3 CH$_3$I cluster, we can isolate the 2 CH$_3$I HtH structure, which is poorly described by our force field, resulting in defective interaction energy for this cluster.

To conclude about these results, our force field describes well the interactions between CH$_3$I and H$_2$O molecules. However, it poorly describes CH$_3$I − CH$_3$I interactions when a iodine-iodine interaction occurs. This poor description makes us conclude that the force field can be used only when CH$_3$I molecules do not interact with another CH$_3$I molecule. The next step is benchmarking the density of liquid CH$_3$I to test if this identified deficiency has an importance in bulk where many interactions are present.

3.5.2   Liquid methyl iodide

The benchmark of the liquid CH$_3$I density at 298.15 K played a critical role in evaluating the accuracy of the updated force field with inherent polarization. The selection of this benchmark was based on several important factors. Firstly, the density of a liquid is a fundamental physical property widely used to characterize the state of matter. Secondly, the density of liquid methyl iodide at 298.15 K has been well-established through experiments and provides a reliable reference for our calculations. It allows us to compare our results to a known and well-established value [265–270] of 2280 kg m^{-3}, providing a criterion for the accuracy of the force field. It provides a rigorous test of the force field and allow us to assess its effectiveness in predicting molecular interactions in a bulk environment with multiple interactions.

We first prepare the system to compute the density of liquid methyl iodide. We define the edge lengths to obtain the experimental liquid density for a given number of molecules in a cubic simulation box. Then, we equilibrate the system to avoid starting with unphysical states. Equilibration is done by running MD calculations in the NVT ensemble at constant temperature and volume, using 3D periodic boundary conditions for 100 ps. The particle-mesh Ewald method [271] is used to compute long-range electrostatic interactions within a cut-off of 2.13 nm. The same cut-off is used for Van der Waals interactions. The velocity-rescaling scheme [272] within a target temperature of 298.15 K and a coupling constant of 0.1 ps has been used to control the temperature. We integrated the equations of motion using the leap-frog algorithm [226], with a 2 fs time-step. To obtain the computed liquid density, the NVT calculation is followed by a NPT equilibration using the Parrinello-Rahman barostat [273, 274] at 1 bar and a coupling constant of 1 ps during 400 ps. The value for CH$_3$I compressibility used in the equilibration is 6.7×10^{-5} bar^{-1} [275]. Measuring the simulation box average volume allows us to determine the calculated density of methyl iodide. The unaltered process is
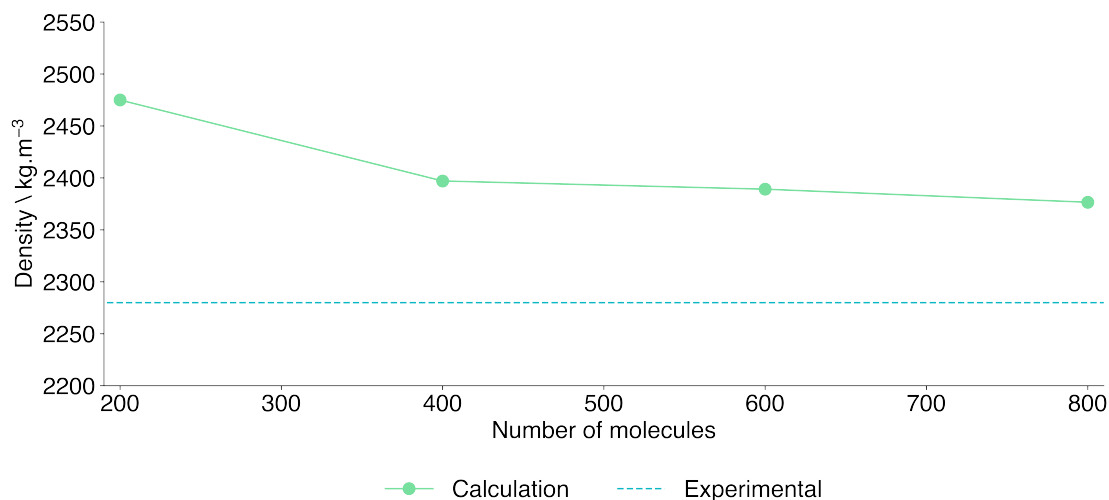
Figure 3.17: Computed liquid methyl iodide density according to the number of molecules present in the simulation box.

done for different numbers of molecules, namely 200, 400, 600 and 800. Results are shown in Fig. 3.17.

The calculated density decreases when the number of molecules inside the simulation box increases. Indeed, a too small simulation cell leads to an incorrect description of the bulk. Above 800 molecules, the density seems to be converged around $2380\,\mathrm{kg\,m^{-3}}$. The relative error between the calculated and the experimental values is $4.4\,\%$, leading to a computed value that agrees with the experimental ones. These results imply that our force field correctly reproduces the liquid density of methyl iodide and is an additional element in its ability to describe $CH_3I - CH_3I$ intermolecular interactions.

3.5.3 Adsorption on a NaCl(001) surface

Testing the adsorption of the CH_3I cluster on a NaCl(001) surface is a crucial step in evaluating the accuracy of our force field in the context of our study. It may also means that if our force field works well for the CH_3I/NaCl, it may be transferable to any other environment. Having a good description of the adsorption of methyl iodide on sea salt aerosols allows us to run extensive simulations to evaluate the effect of H_2O on CH_3I adsorption on the NaCl(001) surface. Clusters calculated in chapter 4 are taken as references for quantum calculations.

Concerning force field calculations, the NaCl(001) surface was built as done by Lovrić et al. [99]. Different force fields exist to describe the NaCl crystal, such as the one developed by Joung et al. [262] or Smith et al. [276]. The latter is
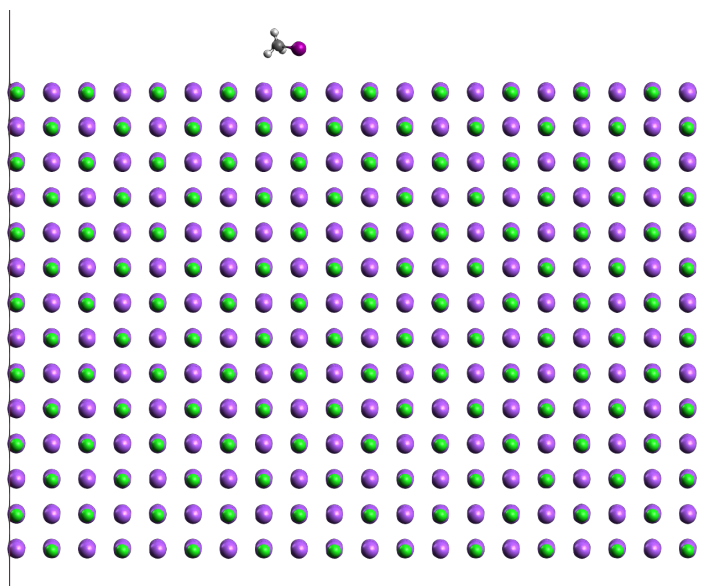
Figure 3.18: Representation of the periodic unit cell of CH$_3$I adsorbed on the NaCl(001) surface to benchmark adsorption energies obtained with parameter 4.

known to describe bulk NaCl well, as it reproduces the interaction with different water models as the lattice constant of bulk NaCl [99, 277]. In our system, the calculated lattice constant (0.54 nm) is in agreement with the experimental one (0.56 nm) [278–281]. Water molecules are described using the three-site SPC/E model [263, 264]. The NaCl crystal fully occupied a simulation box with dimensions of $5.5 \times 5.5 \times 39.0$ nm in the x, y, and z directions, respectively. A vacuum of 17 nm is set in the normal direction from the surface for each side of the slab. The latter is composed of fourteen layers all free to move, according the z-axis's direction. Each one is a filled square composed by 10 NaCl pairs in the x and y direction. The system is shown in Fig. 3.18

Classical force field and quantum calculations adsorption energies obtained from energy minimizations at 0 K are compared in Fig. 3.19. We observe that adsorption energy values from classical force field calculations agrees with quantum results, except for the 2 CH$_3$I HtH cluster. As in the previous section, classical calculations underestimate the interaction in this geometry due to a poor description of the halogen-halogen interaction. Excepting this configuration, we have shown that our force field tends to reproduce methyl iodide's adsorption energy on NaCl(001) correctly, with or without water molecules. This force field can be used to run MD calculations with CH$_3$I adsorbed on the sea-salt surface at different humidities.
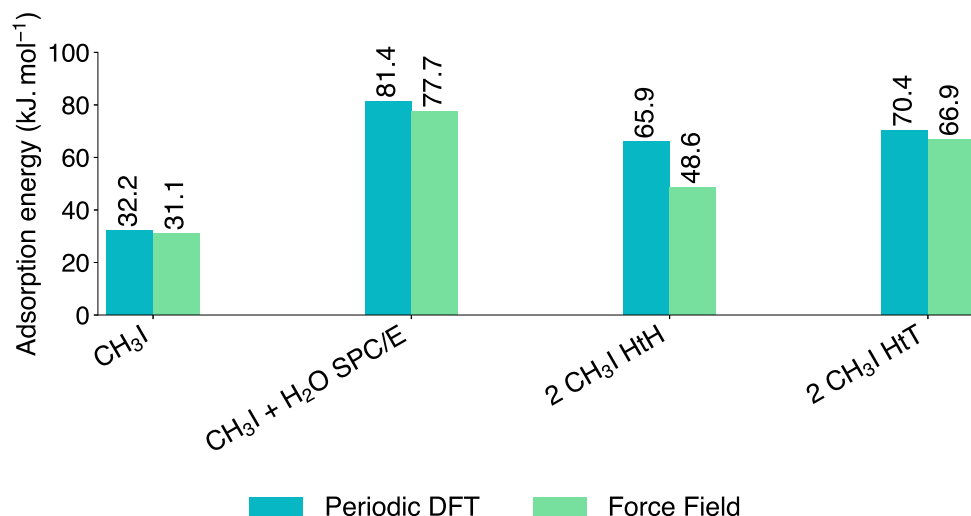
Figure 3.19: Comparison of the force field adsorption energies obtained with parameter 4 with periodic DFT results using the vdW-DF-cx exchange-correlation functional. Water is described using the SPC/E model.

3.6 Conclusion

Building a transferable classical non-polarizable force field for this molecule was a challenging task. Using the harmonic approximation, we have succeeded in describing intramolecular interactions, namely bond stretching and angle bending around the equilibrium values.

Regarding intermolecular interactions, we have used and scaled RESP charges to describe the molecule's inherent polarization. We have tested the performance of several LJ parameters by studying the structure and the interaction energy differences between CH_3I-containing clusters. It allowed us to pick an ensemble of parameters summarized in Table 3.14, that will be used in chapters 4 and 5.

The force field was benchmarked on gas-phase CH_3I-containing clusters. We have seen that our force field describes the majority of the interactions well, except the halogen-halogen interactions. It might be due to our model's need for a more explicit polarization description. Consequently, two clusters are poorly described by our force field, namely $2\,CH_3I$ HtH and $3\,CH_3I$. We have made the same observation concerning benchmarks on adsorbed species on the NaCl(001) surface. Our force field performed well for most structures but failed to describe as precisely $2\,CH_3I$ HtH adsorbed geometry. Nevertheless, the force field performs well in describing

Table 3.14:   Force field parameters for CH$_3$I with RESP charges fitted from MP2/aug-cc-pVTZ-(PP) *ab initio* calculations. The LJ parameters for C and H are taken from Habartová et al.[225], whereas the one for I is from Crone-Münzebrock et al.[236]. The fixed atomic point charges are scaled by a factor 1.7 to describe inherent polarization. Non-bonded terms are fitted using a non-linear least square method from MP2/aug-cc-pVTZ(-PP) calculations.

Non-bonded terms

	σ (nm)	ϵ (kJ/mol)	RESP
C	0.34[1]	0.46[1]	-1.07
H	0.41[1]	0.07[1]	0.41
I	0.41[2]	2.69[2]	-0.16

Bonded terms

	Parameters	Values
C$-$I	r_{eq} (Å)	2.125
	K_{b} (kJ/mol/Å^2)	814.2
C$-$H	r_{eq} (Å)	1.084
	K_{b} (kJ/mol/Å^2)	1691.0
$\measuredangle$ HCI	θ_{eq} (°)	107.8
	K_{a} (kJ/mol/°^{2})	0.0783
$\measuredangle$ HCH	θ_{eq} (°)	111.2
	K_{a} (kJ/mol/°^{2})	0.0771

[1] Habartová et al. [225]
[2] Crone-Münzebrock et al.[236]

the bulk density of liquid CH$_3$I indicating that the failure noticed previously does not alter the capacity of the model to account for CH$_3$I mutual interactions.

To conclude, our force field allows us to perform simulations of CH$_3$I on water or NaCl(001) surfaces in the presence of H$_2$O. Nevertheless, we must limit CH$_3$I $-$ CH$_3$I

interactions to describe all the interactions well. It implies simulating systems with few CH$_3$I molecules relative to the entire system.

Further work can be done to improve the force field. In order to improve the halogen-halogen intermolecular interaction description, we can work on the parametrization of a polarizable force field, even if the simulation time grows using these kinds of methods. In this case, the benchmark should be carried out on a more extended set of properties.This improvement would be relevant only for systems containing multiple CH$_3$I molecules or to improve its transferability.

CH$_3$I adsorption on the NaCl(001) surface

Outline of the current chapter

Methyl iodide is the most naturally emitted organic iodinated compound by oceans [11]. Because it is highly implied in the ozone cycle in the atmosphere [4, 5], improving our knowledge of the transport and the reactivity of CH$_3$I is essential. The transport can be done through sea-salt aerosols. Houjeij et al. [96] have performed DRIFT experiments, studying the interaction between methyl iodide and NaCl. They observed that methyl iodide remains bonded to the sea-salt surface. According to their DRIFT spectrum, they observed the apparition of two new and unassigned bands at 1024 and 1073 cm^{-1}. A representative spectrum of the CH$_3$ deformation region is shown in Fig. 4.1 [96]. These results suggest reactivity or chemisorption of methyl iodide on the NaCl surface.

This chapter aims to perform theoretical calculations of methyl iodide absorbed on the NaCl(001) surface. First, we present periodic DFT calculations of the system, allowing us to compute the infrared spectra of the adsorbed system. Then, we investigate through MD calculations the effect of water coverage on CH$_3$I absorption
.
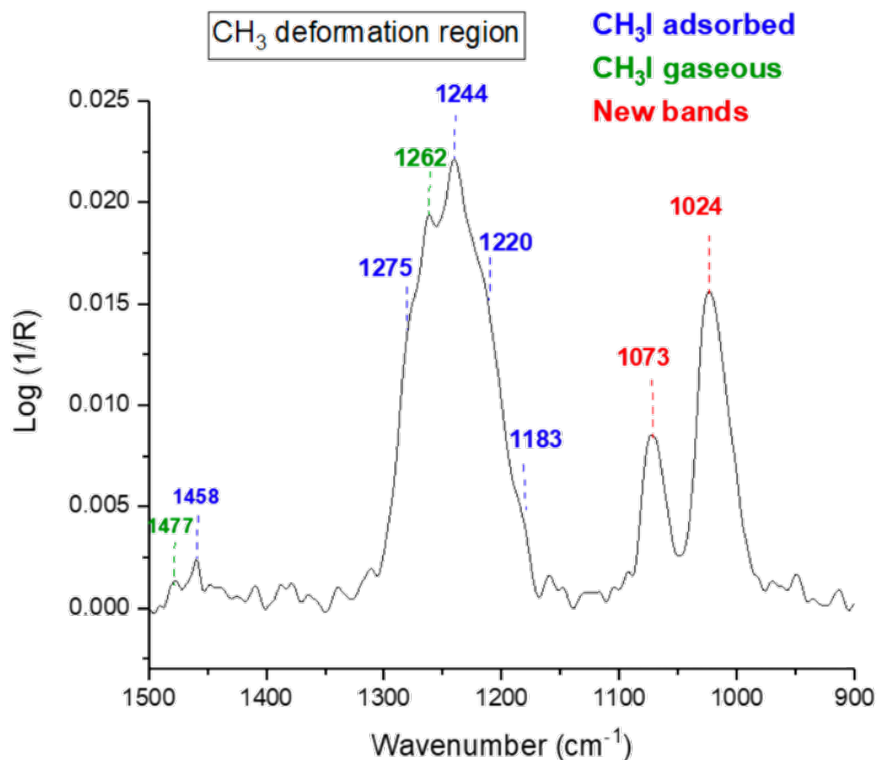
Figure 4.1: DRIFT spectra of NaCl exposed to 5 h of CH$_3$I (108 mL min^{-1}, 1000 ppm) continuous flow at 23 °C and 1 atm. Figure taken from Houjeij et al. [96].

4.1 Benchmarks

If not specified, all the periodic DFT calculations were done using the 3D periodic calculations package QUANTUM ESPRESSO version 6.5 [282, 283]. The projector augmented wave (PAW) [284, 285] scalar relativistic pseudopotentials from the PS Library [286] (version 1.0.0) generated with the Perdew-Burke-Ernzerhof (PBE) [287] exchange-correlation functional are used to describe valence-core electrons. Respectively, for Na, Cl, O, I, C, and H, the $2s^2\ 2p^6\ 3s^1$, $3s^2\ 3p^5$, $2s^2\ 2p^4$, $5s^2\ 5p^5$, $2s^2\ 2p^2$, and $1s^1$ electrons are treated as valence ones. Concerning sodium description, it has been shown that correlating only the valence electron orbitals may lead to non-negligible errors for alkali metals [288–291]. Then, correlating the $2s^2\ 2p^6$ orbitals with the $3s^1$ one is mandatory in describing Na.

4.1.1 Bulk NaCl

When using 3D periodic DFT calculations, we need to pay attention to the parameters of the simulations. In this section, we aim to find the optimal values of these parameters to be used in surface calculations. In addition to choosing the exchange-correlation functional, we must define the plane-wave kinetic energy cutoff and the number of k-points for bulk calculations.

A high number of calculations were done on NaCl in the literature. One of them was done by Kebede et al. [292] where they compared the efficiency of different van der Waals exchange-correlation functionals on bulk NaCl, as well as on the H_2O/NaCl(001) adsorbate-surface adsorption using the VASP package [293–297]. According to them, two exchange-correlation give excellent results for each studied system: vdW-DF-cx and optPBE-vdW. However, only the vdW-DF-cx exchange-correlation functional is available using the QUANTUM ESPRESSO version 6.5 package. In addition, using DFT, the choice of the exchange-correlation functional has to be judicious. Choosing a bad functional may lead to false results. Li et al. [298] have shown that including dispersion forces gives better results. The vdW-DF-cx [299] one treats the dispersion term as part of the exchange-correlation energy. To see its effect, we have also done simulations with an exchange-correlation functional with no dispersion term: PBE [287].

Ideally, an infinite number of plane-waves (i.e., no kinetic cutoff energy) associated with an infinite number of k-points leads to an accurate system description. However, it is numerically impossible to compute such systems. Nonetheless, observables such as the total potential energy or the lattice parameter tend to converge when increasing the cutoff kinetic energy and the number of k-points. The strategy consists in varying both parameters until convergence of the potential energy and the geometry (or indirectly computing lattice parameter).

The bulk NaCl is simulated using the primitive cell. We performed variable cell relaxation (vc-relax) calculations that optimizes the atomic position and the cell lengths simultaneously. We used two different exchange-correlation functionals: PBE [287] and vdW-DF-cx [299], using the PW module from QUANTUM ESPRESSO version 6.5 [282, 283]. For each exchange-correlation functional, a $4 \times 4 \times 4$ and $8 \times 8 \times 8$ Monkhorst-Pack k-points mesh is tested at many cutoff values. Results obtained using the PBE exchange-correlation functional are shown in Fig. 4.2 and 4.3. The system converges in both cases for a value of the kinetic cutoff energy of $628 \, \text{eV}$. We obtain a converged lattice parameter of $5.68 \, \text{Å}$ for both Monkhorst-Pack k-points mesh. This value is in excellent agreement with the experimental value of $5.64 \, \text{Å}$ [300]. These results also agree with the work of Kebede et al. [292], showing that the PBE exchange-correlation functional reproduces well bulk NaCl properties.
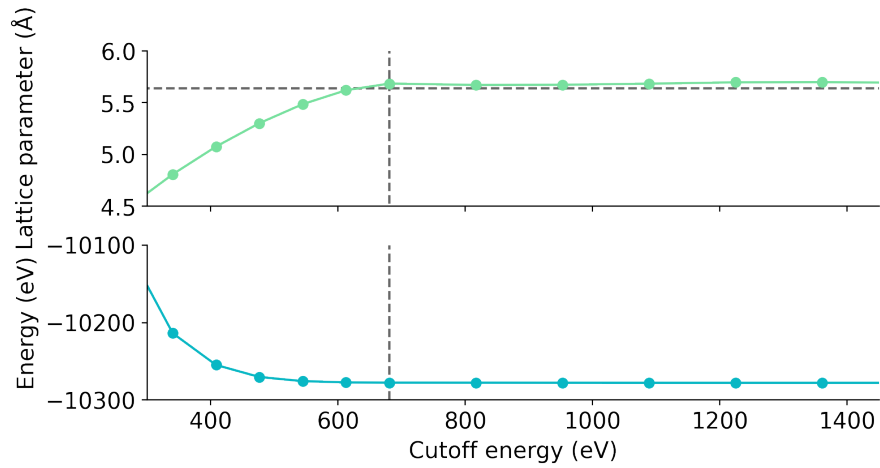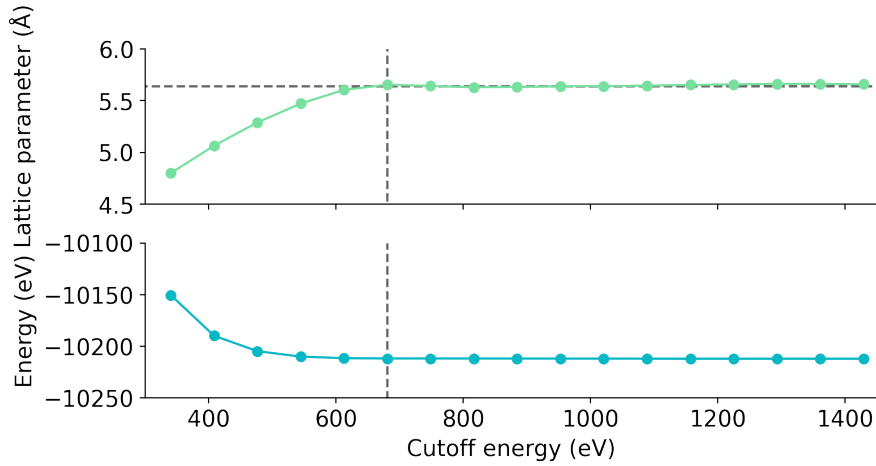
Figure 4.2: Evolution of the lattice parameter (top) and the total potential energy (bottom) according to the cutoff kinetic energy using the PBE exchange-correlation functional and a $4 \times 4 \times 4$ Monkhorst-Pack k-points mesh. The horizontal dashed line corresponds to the experimental value of the lattice parameter. The vertical dashed lines correspond to the minimum kinetic energy ($680\,\mathrm{eV}$) for which the system reaches convergence.
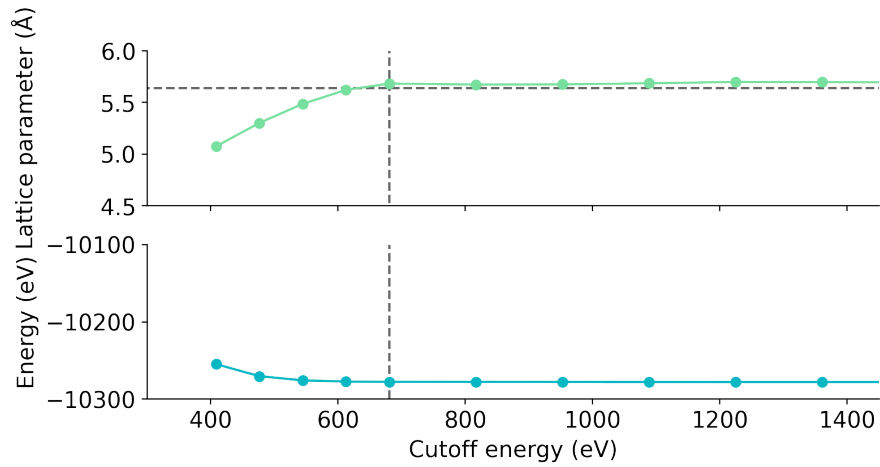
Figure 4.3: Evolution of the lattice parameter (top) and the total potential energy (bottom) according to the cutoff kinetic energy using the PBE exchange-correlation functional and an $8 \times 8 \times 8$ Monkhorst-Pack k-points mesh. Legend is the same as in Fig. 4.2.

The next exchange-correlation functional to benchmark is vdW-DF-cx using the same process. Results are shown in Fig. 4.4 and 4.5. The system converges

Figure 4.4: Evolution of the lattice parameter (top) and the total potential energy (bottom) according to the cutoff kinetic energy using the vdW-DF-cx exchange-correlation functional and a $4 \times 4 \times 4$ Monkhorst-Pack k-points mesh. Legend is the same as in Fig. 4.2.
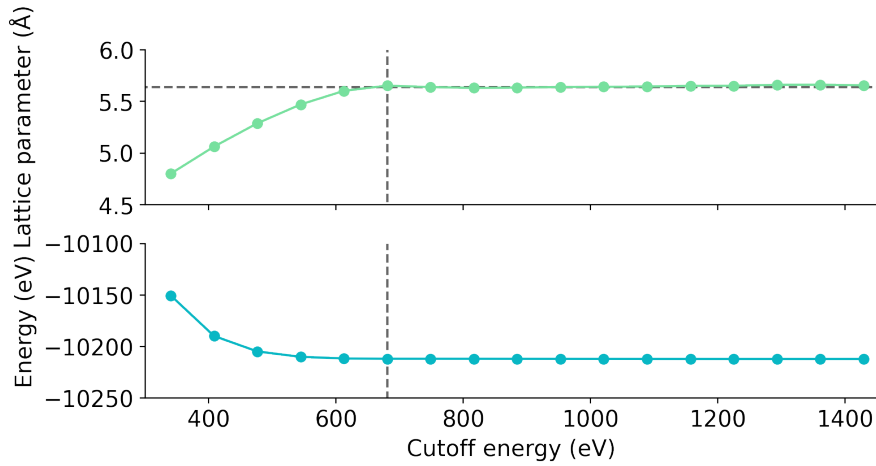

Figure 4.5: Evolution of the lattice parameter (top) and the total potential energy (bottom) according to the cutoff kinetic energy using the vdW-DF-cx exchange-correlation functional and an $8 \times 8 \times 8$ Monkhorst-Pack k-points mesh. Legend is the same as in Fig. 4.2.

at a kinetic cutoff energy of 680 eV, higher than for the PBE exchange-correlation functional. Both cutoff kinetic energy gives similar results. The converged lattice parameter is slightly better than the one given by PBE with a value of 5.65 Å (5.64 Å for the experimental value [300]) for both Monkhorst-Pack k-points mesh.

Both tested exchange-correlation functionals give excellent results of the optimized lattice parameter at a cutoff value of 680 eV. A $4 \times 4 \times 4$ Monkhorst-Pack k-points mesh is sufficient to describe bulk NaCl as the results are similar with a higher k-points number. Then, the $4 \times 4 \times 4$ Monkhorst-Pack k-points mesh will be adopted for the rest of the Thesis because it has a lower computational cost.

### 4.1.2   Gas phase methyl iodide and vibrational frequencies

The environment around a molecule influences its vibrational frequencies. We need to look at these changes for CH$_3$I adsorbed on a NaCl(001) surface and in presence of water molecules. However, we must benchmark vibrational frequency calculations from the QUANTUM ESPRESSO version 6.5 package for isolated CH$_3$I. We have calculated the molecule's minimum energy geometry and the vibrational frequencies. Usually, periodic plane-wave methods can do it correctly by setting a large simulation box. This box size represents the distance between molecules. In this part, we will describe the method, present the results, and discuss them.

Three steps are required to compute the vibrational frequencies. First, we have done a relaxation calculation (optimization) of the whole system, which leads to minimum energy geometries. Secondly, we made a single-point calculation on the resulting geometries using a tighter convergence threshold (10^{-13} eV). It gives an accurate electronic density of the system. Finally, we did a phonon calculation using the DFPT method, previously presented in chapter 2. Only the last step provides vibrational frequencies.

Dealing with gas phase molecules in a large simulation box, we performed calculations at the Γ point (i.e., one k-point). We used the conjugate gradient algorithm to diagonalize matrices. Both PBE and vdW-DF-cx exchange-correlation functionals are GGA functionals. Consequently, we set the kinetic energy cutoff for charge density up to six times the one for wavefunctions. This leads to better electronic convergence.

We should avoid mutual interaction between CH$_3$I and its periodic image. We can control it by setting the optimal cubic box length. Methyl iodide can interact with itself if this value is too low. However, a too-large value will increase the computational cost without any benefit. Then, we benchmarked the evolution of the CH$_3$I total energy according to the cubic box dimension. Results are shown in Fig. 4.6. The system's total energy converges to a normalized value of -0.265 eV when the box length is larger than 15 Å.

This section aims to study CH$_3$I adsorption on the NaCl(001) surface. Using the same simulation box for gas and adsorbed phase calculations is judicious. Then, we set the simulation box length to three times the NaCl computed lattice parameter (17.04 Å for PBE and 16.95 Å for vdW-DF-cx), assuming a 3×3 box, to avoid edge effects.
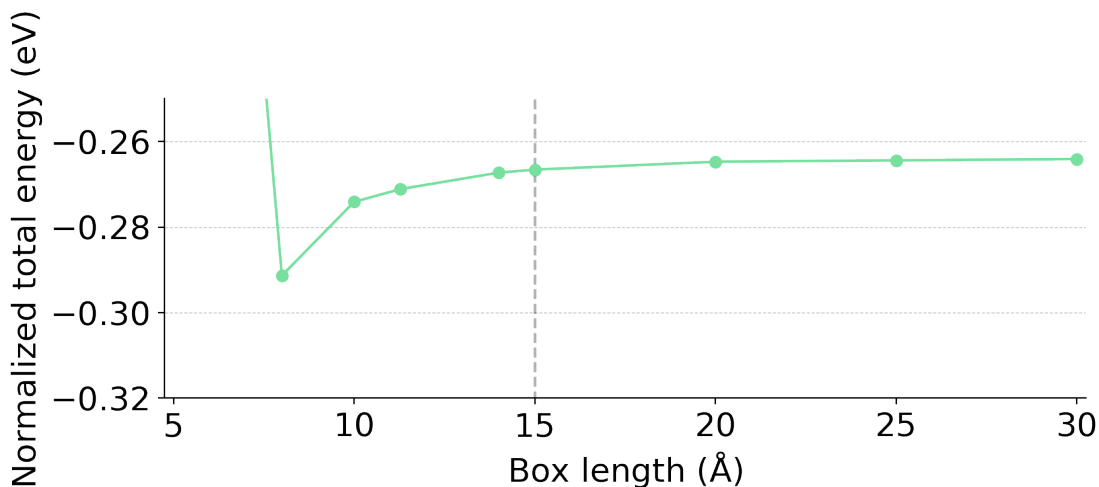
Figure 4.6: Evolution of the optimized CH_3I total energy according to the simulation box length. Calculations are done using the vdW-DF-cx exchange-correlation functional. The vertical dashed line corresponds to the minimum box length (15 Å) for which the system reaches convergence.

At the end of the relaxation calculation, we obtained the optimized geometry. Results are shown in Table 4.1. We observe slight differences between geometries obtained from periodic DFT calculations, DFT calculations, and experimental values. We see that PBE and vdW-DF-cx results are similar. The more significant

Table 4.1: CH_3I geometry derived from periodic DFT calculations compared to experimental values and non-periodic calculations. Distances are expressed in Å and angles in °.

	PBE	vdW-DF-cx	Exp[a]	M06-2X [b] 6-311(2df,2p)	MP2 [c] aug-cc-pVTZ(-PP)
r C−H	1.092	1.094	1.084	1.082	1.083
r C−I	2.158	2.153	2.136	2.136	2.123
∠ HCI	107.4	107.4	107.5	107.8	107.7
∠ HCH	111.5	111.5	111.4	111.1	111.2

[a] Graner [301]
[b] Using GAUSSIAN 16 / See chapter 6
[c] Using GAUSSIAN 16 / See chapter 3

Table 4.2: Harmonic normal mode frequencies of gas phase methyl iodide computed with periodic DFT compared to experimental values and non-periodic calculations. All frequencies are in cm^{-1}.

	Sym.	PBE	vdW-DF-cx	Exp.[a]	M062-X[b]
C−I str.	A$_1$	528	526	533	565
CH$_3$ rock	E	866	873	883	910
CH$_3$ sym. def.	A$_1$	1239	1235	1251	1293
CH$_3$ asym. def.	E	1416	1406	1438	1479
CH$_3$ sym. str.	A$_1$	3022	3008	2971	3122
CH$_3$ asym. str.	E	3134	3115	3060	3231

[a] McNaught [303] and references therein
[b] Using GAUSSIAN 16 at the M062-X/6-311+G(2df,2p) level of theory

difference occurs on the C−I bond length slightly overestimated by quantum periodic calculations. Nevertheless, this difference is small, as the maximum deviation from experimental values is 0.02 Å.

The next step is to perform a single-point calculation on optimized geometries. The aim is to obtain a better electronic description of the molecule. Compared to the previous step, only the convergence energy threshold is different, set to 10^{-13} eV.

In the last step, we computed the vibrational frequencies. We have used the PHonon package from QUANTUM ESPRESSO version 6.5. The convergence energy threshold is the same as for the single-point calculation. Regarding the electron-phonon coupling, we set a double-delta smearing value of 0.1 eV. When diagonalizing the dynamical matrix, the vibrational frequencies are corrected using the acoustics sum rules for translational and rotational corrections [282, 283]. The PBE and vdW-DF-cx exchange-correlation functionals are benchmarked and compared to those computed using the GAUSSIAN 16 code [244] package at different levels of theory and experimental results, as shown in Table 4.2. We observed that theoretical frequencies are similar and in agreement with experimental values. We observe that the two methods overestimate high frequencies corresponding to C−H stretching. Anharmonicity effects may explain such a difference [302].

Anharmonic effects can be computed using the GAUSSIAN 16 code [244] package. Then, we calculated the vibrational frequencies of methyl iodide at different levels of theory and compared them to experimental results. They are shown in Table 4.3.

We observe that anharmonic vibrational frequencies are in excellent agreement with experimental results.

We conclude that we reproduce well the vibrational frequencies of methyl iodide using a periodic DFT code. This observation is essential because it will enable us to compute frequencies on surfaces and adsorbate. Though frequency calculations with periodic DFT remain computationally expensive and are limited to small systems The following section will present benchmarks on surfaces.

Table 4.3: Theoretical and experimental frequencies of isolated $^{12}C^1H_3{}^{127}I$

	Sym.	Harm.[a]	Anharm.[a]	Harm.[b]	Anharm.[b]	Harm.[c]	Anharm.[c]	Exp.[d]	Exp.[e]	Harm.[e]	Harm.[f]
C−I str.	A$_1$	580.3	570.2	563.5	630.1	526.5	518.9	533.2	533.2	548.1	525.6
CH$_3$ rock	E	908.4	896.6	902.8	1055.5	861.0	835.6	882.9	882.7	895.6	872.9
CH$_3$ sym. def.	A$_1$	1300.7	1269.5	1297.0	1388.4	1221.3	1213.6	1250.8	1251.2	1286.1	1234.9
CH$_3$ asym. def.	E	1489.6	1440.2	1476.7	1535.2	1414.8	1378.1	1438.1	1410.3	1486.2	1405.6
CH$_3$ sym. str.	A$_1$	3116.3	3008.9	3101.0	2952.4	3020.4	2909.8	2971.3	3010.8	3096.1	3007.8
CH$_3$ asym. str.	E	3236.0	3035.3	3213.4	3012.8	3131.4	2929.6	3060.1	3060.1	3212.5	3115.4

[a] This work. MP2/aug-cc-PVTZ-(PP)
[b] This work. ωB97X-D/aug-cc-PVTZ-(PP)
[c] This work PBE-D3BJ/aug-cc-PVTZ-(PP)
[d] McNaught[303] and references therein
[e] Duncan et al.[304]
[f] This work. vdW-DF-cx using QUANTUM ESPRESSO version 6.5.

4.1.3 H_2O adsorption on the NaCl(001) surface

The adsorption of the water molecule on the NaCl(001) surface is well known, both theoretically and experimentally [96, 292, 305–320]. Thus, the H_2O/NaCl(001) system is a good candidate to benchmark our method.

Based on the calculations done by Kebede et al. [292], the H_2O/NaCl(001) system is modeled as a four layers slab, using 3D periodic boundary conditions. The two bottommost layers are kept frozen to mimic bulk NaCl and avoid system breaking. Introduction of a vacuum is mandatory to create a surface using 3D periodic boundary conditions. Then, a gap of 15 Å is created in the direction perpendicular to the surface to avoid border effects.

We used a $4\times4\times1$ Monkhorst-Pack k-points mesh and optimized the H_2O/NaCl(001) in a $11.28 \times 11.28 \times 26.28$ Å simulation box, taking the experimental NaCl lattice constant as a reference and setting the kinetic cutoff energy to 400 eV to reproduce Kebede et al. [292] calculations. Both PBE and vdW-DF-cx exchange-correlation functionals are benchmarked. The structure optimization used the conjugate-gradient algorithm with a convergence criterion of 10^{-6} eV. Gaussian smearing of 0.1 eV is employed. The same simulation box is used at the Γ point to compute isolated H_2O optimized geometry, energy, and vibrational frequencies. Only one minimum energy geometry was found. Then, the exact process of section 4.1.2 is done to obtain vibrational frequencies. Illustrations of the whole system are shown in Fig. 4.7.

Two parameters can be computed to benchmark the exchange-correlation functionals: the adsorption energy and the H_2O/NaCl(001) distance. The distance between H_2O and the surface (d) is slightly higher using PBE (2.581 Å) compared to the one obtained using vdW-DF-cx (2.566 Å). The adsorption energy results are shown in Table 4.4. Our calculations give slightly lower adsorption energies than

Table 4.4: Calculated adsorption energies (E_{ads}) of H_2O on the NaCl(001) surface. Energies are in meV.

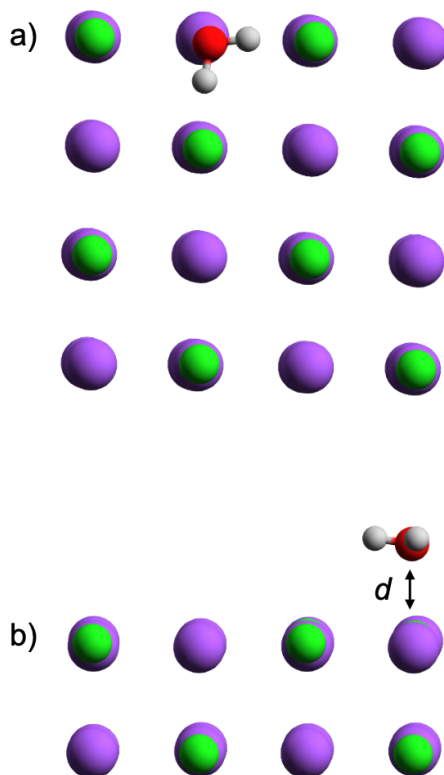|	PBE[a]	PBE[b]	vdW-DF-cx [a]	vdW-DF-cx [b]	CCSD(T)[c]	HAS[d]	LEEF[e]
E_{ads}	344	360	378	430	517	600	617

[a] This work
[b] Kebede et al. [292]
[c] Li et al. [298]
[d] Helium atom scattering experiment by Bruch et al. [321]
[e] Low-energy electron diffraction experiment by Fölsch et al. [309]

Figure 4.7: Top (a) and side (b) view of the minimal energy geometry of H$_2$O adsorbed on the NaCl(001) surface by periodic DFT calculations using the vdW-DF-cx exchange-correlation functional. Na atoms are represented in purple whereas Cl atoms are represented in green. The vertical distance between the oxygen and the surface is written d.

those computed by Kebede et al. [292]. Using a different periodic DFT software, it was challenging to use the same parameters and pseudopotentials to reproduce their calculations. In addition, we used a small core pseudopotential for Na with a higher number of valence electrons. However, our results highly underestimate experimental results. We computed a H$_2$O monomer adsorbed on the NaCl(001) surface. This simulation is not entirely representative of the experiment. Indeed, at higher coverage, water molecules tend to form clusters and monolayers on the surface, increasing the adsorption energy per water molecule.

Furthermore, we also computed the vibrational frequencies of an isolated and adsorbed H$_2$O molecule on the NaCl(001) surface using the method described in section 4.1.2. Results are shown in Table. 4.5. As for methyl iodide, we see that the calculated vibrational frequencies of an isolated H$_2$O molecule agree with

Table 4.5: Calculated harmonic vibrational frequencies using the PBE exchange-correlation functional of isolated and adsorbed H$_2$O on the NaCl(001) surface. The shift column represents the difference between the computed values (adsorbed and isolated). Frequencies are in cm^{-1}.

	Sym.	Exp. (Isolated)	Isolated	Adsorbed	Shift
Bend	A$_1$	1595[a]	1552	1563	−11
Sym. stretch	A$_1$	3657[a]	3629	3605	24
Asym. stretch	E	3756[b]	3728	3699	29

[a] Porezag et al. [322]
[b] Shimanouchi et al. [323]

experimental values. Regarding adsorbed vibrational frequencies, a red-shift occurs for both stretching modes. However, we observe a blue-shift regarding the bending mode of the water molecule. To our knowledge, no experimental data clearly gives the vibrational frequencies of adsorbed H$_2$O on a NaCl(001) surface. Nevertheless, Fajardo et al. [324] and Yamakawa et al. [325] have shown that the H$_2$O stretching mode frequencies are red-shifted when it is adsorbed on a NaCl(001) surface. Our results are then partially in agreement with experiments, with a blue-shift computed for the bending mode of the water molecule.

To conclude, we have succeeded in simulating the H$_2$O adsorption on the NaCl(001) surface. In addition, the harmonic vibrational frequencies were computed for the isolated and adsorbed H$_2$O molecule on the NaCl(001) surface. It validates our method to study the adsorption of CH$_3$I on the NaCl(001) surface in presence or not of water.

4.2 Adsorption of CH$_3$I on the NaCl(001) surface

The adsorption of CH$_3$I on the NaCl(001) surface is done using two different systems depending on the exchange-correlation functional. We set the lattice parameter to the theoretical one (17.04 Å for PBE and 16.95 Å for vdW-DF-cx) to have a bulk NaCl at its minimum. We use a cutoff kinetic energy of 680 meV. A 4 × 4 × 1 Monkhorst-Pack k-points mesh is used to compute the CH$_3$I/NaCl(001) system. Two minimum energy configurations were found for each exchange-correlation functional.

Minimum energy geometries using PBE are shown in Fig 4.8. We observe two configurations. The first (a,b) is defined by lying flat adsorption of methyl iodide
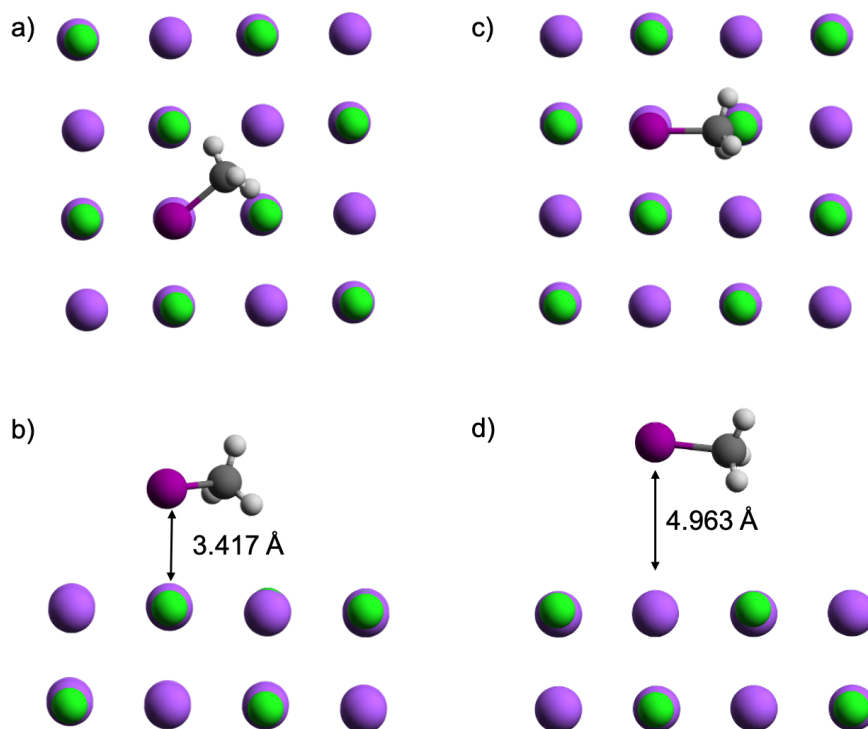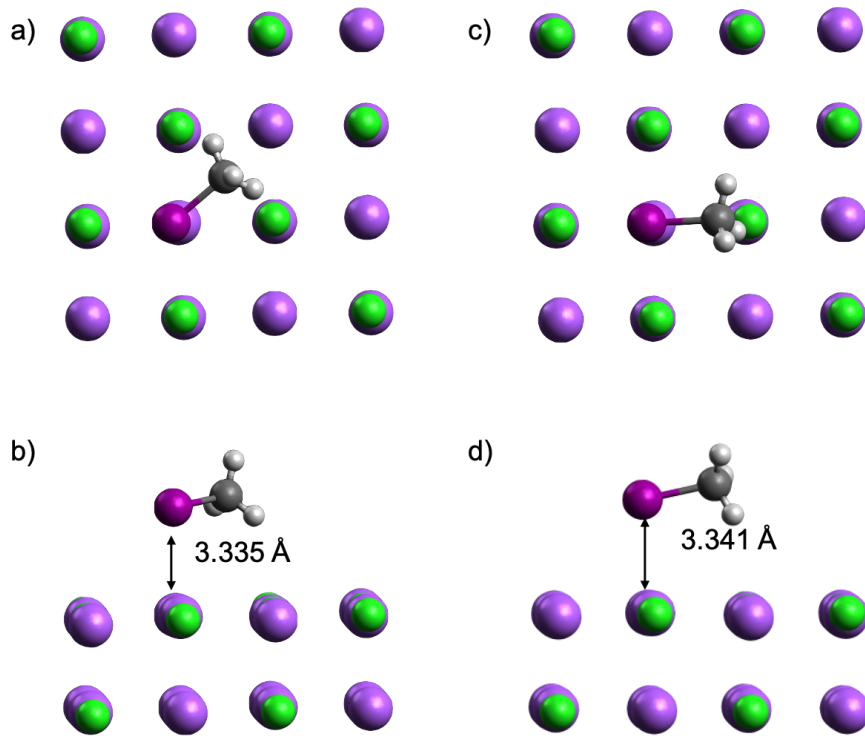
Figure 4.8: Top (a) and side (b) view of the global minimum energy geometry computed using PBE of CH$_3$I adsorbed on the NaCl(001) surface (configuration 1); Top (c) and side (d) view of the local minimum energy geometry of CH$_3$I adsorbed on the NaCl(001) surface (configuration 2). The distance between the iodine atom and the surface is noted with an arrow.

on the NaCl(001) surface, the C−I axis being oriented along the diagonal according to the surface lattice vectors. The distance between iodine and the surface highly differs between the two configurations, CH$_3$I being really closer to the surface in configuration (1). In the second orientation, the C−I bond is parallel to a Na−Na axis. In both cases, the I atom is adsorbed on top of a Na atom.

Minimum energy geometries using vdW-DF-cx are shown in Fig 4.9. Two configurations are observed. They are similar to the ones found using the PBE exchange-correlation functional. However, the distance between the iodine atom and the surface is smaller using the vdW-DF-cx exchange-correlation functional. It reduces this distance from 3.417 Å to 3.335 Å for the first configuration (a,b) and from 4.963 Å to 3.341 Å for the second one (c,d). The second configuration has a significant variation, with a difference of 1.546 Å.

The vdW-DF-cx exchange-correlation functional describes the system better when only considering minimum geometries. Nevertheless, an essential characteristic

Figure 4.9: Top (a) and side (b) view of the global minimum energy geometry computed using vdW-DF-cx of CH_3I adsorbed on the NaCl(001) surface (configuration 1); Top (c) and side (d) view of the local minimum energy geometry of CH_3I adsorbed on the NaCl(001) surface (configuration 2). The distance between the iodine atom and the surface is noted with an arrow.

Table 4.6: Computed adsorption energies of the CH_3I/NaCl(001) system. Energies are in meV.

	Configuration 1	Configuration 2
PBE	110	30
vdW-DF-cx	334	315

of an adsorption process is the adsorption energy, even if there are no reliable adsorption energies to our knowledge. Results are shown in Table 4.6. PBE and vdW-DF-cx adsorption energies highly differ from each other. This is however not surprising for configuration 2 since in configuration 2, at PBE level CH_3I is really more distant from the surface compared to the geometry obtained at vdW-DF-cx.
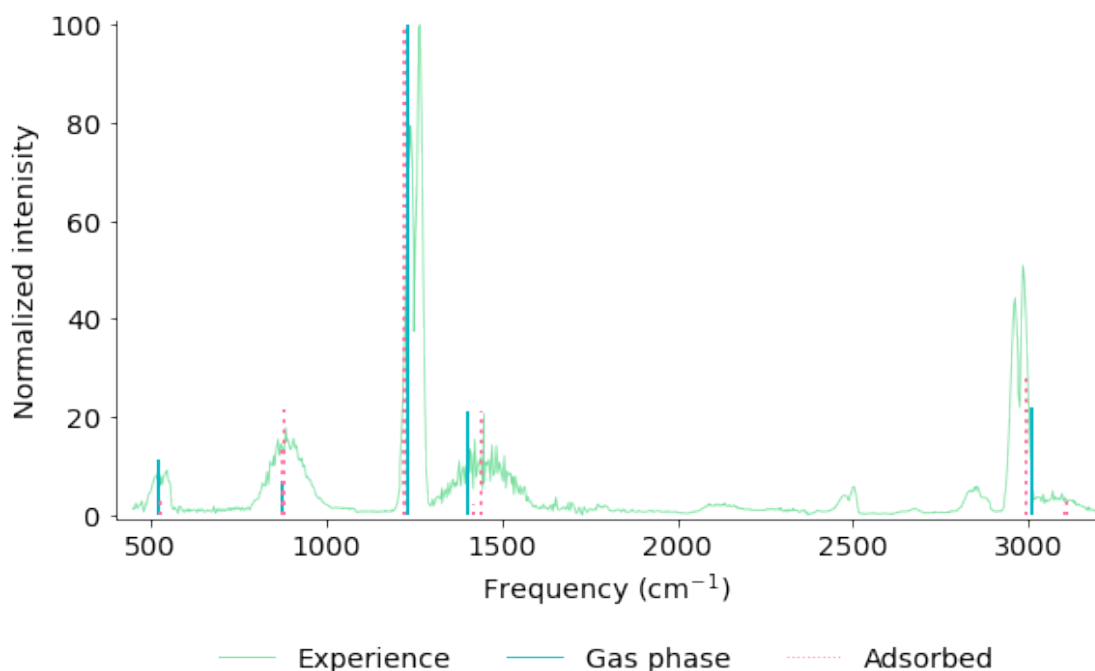
Figure 4.10: Gas phase experimental [336] and calculated harmonic infrared spectrum of CH₃I adsorbed on the NaCl(001) surface and in the gas phase.

Indeed, a difference of 224 meV is calculated for configuration 1 and 285 meV for configuration 2. It has been shown that adsorption processes involving non-covalent interactions between molecules and the surface are not accurately described using standard exchange-correlation functionals because they can not account for long-range van der Waals forces [326–329]. The problem can be overcome using DFT-D treatment (where the dispersion interaction is calculated semi-classically)[326, 330, 331]. This method improves the physisorption of molecules on surfaces [332–334]. However, van der Waals type density functionals can also overcome this problem, improving adsorption energies in physisorption processes [292, 335].

Indeed, long-range interactions play an essential role in the adsorption of CH₃I on the NaCl(001) surface. The vdW-DF-cx exchange-correlation functional gives more accurate results than the PBE one. Then, we will use only the vdW-DF-cx exchange-correlation functional from this point. The energy adsorption difference between configurations 1 and 2 is relatively small (14 meV). We can obtain configuration 2 by a rotation of 45° of configuration 1. The infrared spectra of the gas phase and adsorbed CH₃I (minimum energy configuration) are computed and shown in Fig. 4.10 and Table 4.7. We do not observe significant vibrational frequency shifts when methyl iodide is adsorbed on the NaCl(001) surface, as

suggested by the low value of the adsorption energy. Comparing our results with the work done by Houjeij et al. [96], we do not observe the same frequency shift or frequencies close to 1024 or 1073 cm^{-1}. Their results are shown in Table 4.8.

Their proposed geometry remains unstable at our level of theory on a bare perfect NaCl(001) surface. The latter is shown in Fig. 4.11.

Table 4.7: Gas phase experimental and calculated methyl iodide harmonic vibrational frequencies using periodic DFT in gas phase and adsorbed on the NaCl(001) surface. Frequencies are in cm^{-1}.

| Vibrational modes	Exp. (gas phase)[a]	Calc. (gas phase)[b]	Calc. (adsorbed)[b]
C−I stretching	533	526	528
CH$_3$ rocking	883	873	870
			878
CH$_3$ symmetric deformation	1251	1235	1221
CH$_3$ asymmetric deformation	1410	1406	1405
			1415
CH$_3$ symmetric stretching	3011	3008	2989
CH$_3$ asymmetric stretching	3060	3115	3102
			3107

[a] Duncan et al. [304]
[b] This work / 1 CH$_3$I adsorbed on the NaCl(001) surface

Table 4.8: Experimental methyl iodide vibrational frequencies in gas phase and adsorbed on the NaCl (001) surface. Data taken from Houjeij et al. [96]. Frequencies are in cm^{-1}.

Vibrational modes	CH$_3$I$_{(g)}$	CH$_3$I$_{(ads)}$	Shift
CH$_3$ symmetric deformation	1262	1024, 1073, 1183, 1220, 1244	−238, −189, −79, −42, −18
CH$_3$ asymmetric deformation	1477	1458	−19
CH$_3$ overtone	2847	2855	8
CH$_3$ symmetric stretching	2953	2961, 2993	8, 40
CH$_3$ asymmetric stretching	2981	3018	37

[a] Duncan et al. [304]
[b] This work
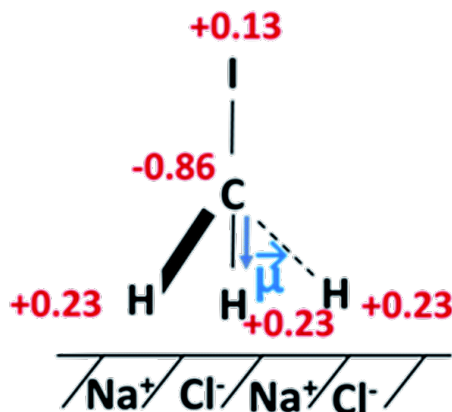
Figure 4.11: Scheme of CH$_3$I monomer adsorption on NaCl and Mulliken charge distribution calculated with DFT performed using the ωB97XD/aug-cc-pVTZ-PP level of theory. Figures taken from Houjeij et al. [96].

Nevertheless, we know that surface defects of formation of molecular clusters can highly modify methyl iodide behavior on the surface. In addition, even if the DRIFT infrared spectrum was recorded under dry conditions, some water molecules can remain on the surface. Thus, the effect of water on the adsorption of CH$_3$I has to be studied to see if it can be neglected for such calculations.

Periodic DFT methods can compute methyl iodide containing clusters adsorbed on the NaCl(001) surface. Thus, we simulated the adsorption of different dimers (see in Fig 3.2 of chapter 3) on the NaCl(001) surface. Adsorption energies are shown in Table 4.10. Moreover, associated vibrational frequencies are shown in Table 4.9.

We observe that the adsorption energy is increasing as we adsorb dimers on the NaCl(001) surface, as expected by the definition of the adsorption energy.

Nevertheless, the highest value of the adsorption energy is when methyl iodide is adsorbed in interaction with a water molecule. Concerning vibrational frequency shifts, we observe a systematic red-shift for the CH$_3$ symmetric deformation and symmetric stretching within all the dimers. Concerning the CH$_3$ asymmetric stretching, we observe a red shift for all dimers except for one vibrational frequency of the CH$_3$I + H$_2$O system.

We hypothesize that the remaining water molecules on the surface impact the adsorption of methyl iodide. Thus, we decided to study the effect of water molecules on the adsorption at different water coverages. Such simulations need a larger simulation box with a higher number of molecules to be representative. Larger systems can be computed using classical MD calculations, where the computational cost per atom is much lower than in periodic DFT calculations.

Table 4.9: Theoretical harmonic frequencies of isolated and adsorbed CH_3I containing dimers on the NaCl(001) surface. Frequencies are in cm^{-1}.

Mode	Sym	$CH_3I_{(g)}$	$CH_3I_{(ads)}$	$CH_3I + H_2O_{(ads)}$	$2\,CH_3I\ HtH_{(ads)}$	$2\,CH_3I\ HtT_{(ads)}$
C−I str.	A_1	528	528	574	506, 519	516, 525
CH_3 rock	E	873	870, 878	884, 893	876, 878, 882, 885	869, 870, 876, 882
CH_3 sym. def.	A_1	1235	1221	1231	1220, 1226	1210, 1214
CH_3 asym. def.	E	1406	1405, 1415	1404, 1423	1400, 1408, 1410, 1418	1405, 1412, 1423, 1439
CH_3 sym. str.	A_1	3008	2989	3002	2985, 3006	2979, 2984
CH_3 asym. str.	E	3115	3102, 3107	3113, 3119	3103, 3105, 3111, 3114	3093, 3097, 3100, 3104

Table 4.10: Computed adsorption energies using vdW-DF-cx of CH$_3$I containing molecular clusters adsorbed on the NaCl(001) surface. Adsorption energies are in meV.

Species	CH$_3$I	CH$_3$I + H$_2$O	2 CH$_3$I HtT	2 CH$_3$I HtH
E_{ads}	334	844	730	683

4.3 Classical molecular dynamics: effect of water coverage

MD calculations were performed to demonstrate the effect of H$_2$O on the CH$_3$I adsorption on NaCl(001) surfaces. We used the force field developed in chapter 3. The SPC/E force field is used to describe water molecules. It is optimized for interaction with organic molecules [337] and reproduces well the surface tension of liquid water [338], two essential criteria for our system. The NaCl(001) surface is described using the parameters of Smith et al. [276]. The latter force field was picked because it reproduces the experimental lattice constant well, as well as the interaction with different water models [339].

All the simulations are done in the NVT ensemble, with a thermalization of 2 ns and a simulation time of 3 ns. The Verlet algorithm cutoff scheme with a neighbor list updated at each step is used. For long-range Coulombic calculations, the particle-mesh Ewald [271] method is used with a cutoff of 0.9 nm. A plain cutoff of 0.9 nm is used for Van der Waals interactions. Both potentials are shifted by a constant such as it is zero at the cutoff. Standard periodic boundary conditions have been applied. The Berendsen thermostat [232] has been used at a temperature target of 300 K and a time constant of 0.5 ps.

Previous studies [99, 311, 340] have shown that H$_2$O molecules tend to be organized as a monolayer on sea salt surfaces. Thus, we firstly adsorbed water on the NaCl(001) surface and made a 5 ns thermalization at 300 K. The second step is to adsorb 1 CH$_3$I molecule on each surface, thermalized during 2 ns at 300 K. Finally, we computed a 3 ns MD run on the resulting system, where data are collected . To form a complete theoretical water monolayer on the NaCl(001) surface, one must have one H$_2$O molecule for each Na−Cl pair. Since we have 200 Na−Cl pairs per surface, we need 200 H$_2$O molecules on the substrate to form a complete monolayer. The latter will be defined as a full theoretical monolayer (TM). However, the initial water molecule positions are randomly distributed at a maximal distance of 0.6 nm from the upper surface plane.

Table 4.11: Adsorption energy of methyl iodide on the NaCl(001) surface at different H_2O TM fractions.

H_2O TM fraction	Mean ($kJ\,mol^{-1}$)	Standard deviation ($kJ\,mol^{-1}$)
0	-12.8	6.4
25	-21.6	9.4
50	-22.9	9.2
100	-24.3	9.4

The simulated system consists of $1\,CH_3I$ adsorbed on a NaCl(001) surface thermalized at $300\,K$ using a Berendsen thermostat [341] during $2\,ns$, centered in a $5.54 \times 5.54 \times 38.98$ nm supercell. The box is extended along the z axis to form vacuum on each side of the NaCl crystal. Both surfaces of the NaCl slab are used, giving a total of $1\,CH_3I$ per interface. Different water coverages[1] are calculated to study the evolution of the adsorption energy. The latter is expressed as a percentage of a complete H_2O TM on the NaCl(001) surface.
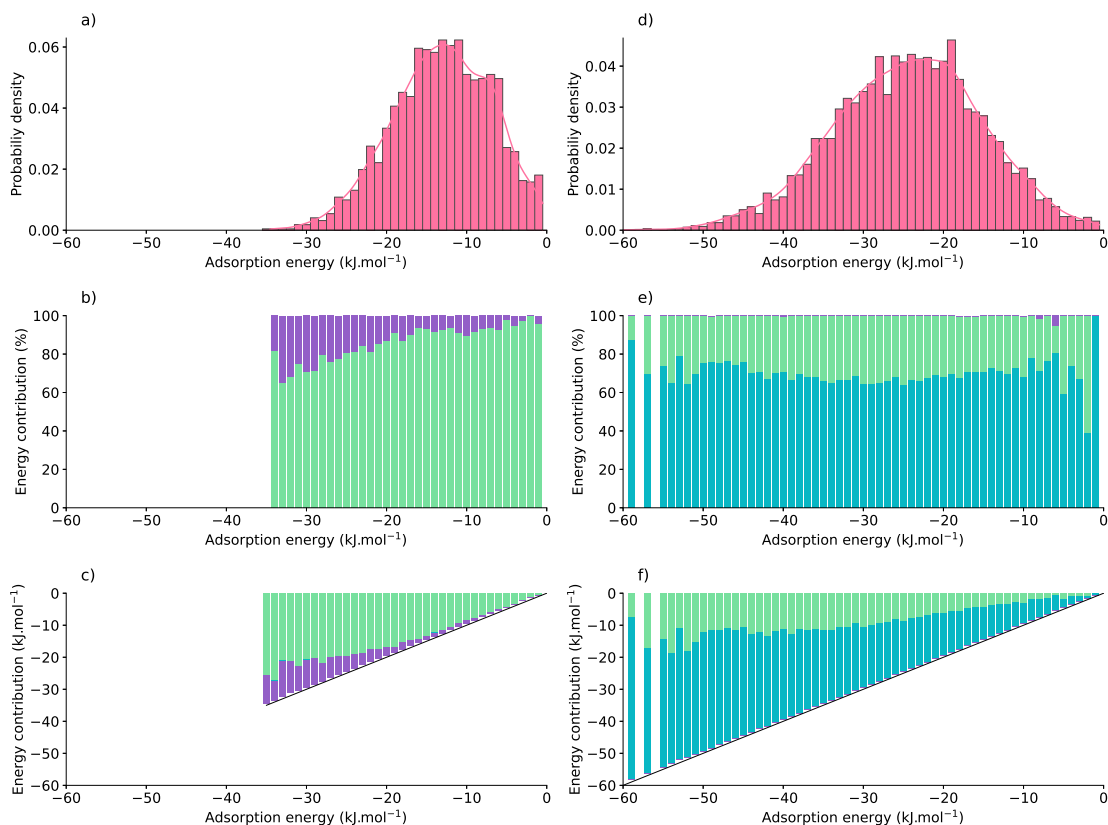
4.3.1 Adsorption energy

In order to better understand the effect of water on the CH_3I adsorption on the NaCl(001) surface, we studied the adsorption energy distributions for all the trajectories. Results are shown in Table 4.11. We can see a high modification of the mean adsorption energy from $0\,\%$ TM to 25 and $50\,\%$ TM, with average adsorption energies of $-12.8\,kJ\,mol^{-1}$, -21.6, and $-22.9\,kJ\,mol^{-1}$, respectively. Regarding the standard deviations, we see that they increase as well. Regarding the adsorption energy at $100\,\%$ TM, we see a slight drop compared to $50\,\%$ TM. The standard deviation remains unchanged. The behavior of adsorbed methyl iodide on the NaCl(001) surface is strongly modified by H_2O, even at low coverage.

To further understand the CH_3I behavior adsorbed with water, we have decomposed the adsorption energies of the system with $0\,\%$ and $100\,\%$ TM as shown in Fig. 4.12. Due to desorption events and system design, we observe some CH_3I-CH_3I interactions, mainly in the system without water molecules. The latter are minority interactions when water is present.

As previously discussed, the adsorption energy distribution is broader at higher water coverage than at $0\,\%$ TM. Regarding the system with water molecules, we can see that CH_3I-H_2O interactions dominate the adsorption energy. The latter

---

[1]0%, 25%, 50 %, and 100% of a complete H_2O monolayer

Figure 4.12: Adsorption energy of methyl iodide on the NaCl(001) surface: (a) at 0% ; (d) 100 % H$_2$O TM coverage. The CH$_3$I−NaCl interaction is represented in green, the CH$_3$I−H$_2$O in blue, and the CH$_3$I−CH$_3$I in purple. The relative energy contribution of the corresponding plots is respectively shown in (b) and (e), whereas the quantitative ones are presented in (c) and (f).

increases according to adsorption energy, whereas CH$_3$I−NaCl interactions remain constant after $30\,\text{kJ}\,\text{mol}^{-1}$. We observe that H$_2$O molecules increase adsorption energy, even at low coverage.

4.3.2   Angular distribution

Houjeij et al.[96] have proposed a CH$_3$I adsorption geometry with the CI vector normal to the surface, the methyl group being attached to the surface. We have analyzed the molecular axis orientation with respect to the surface normal for each H$_2$O coverage to check if we have a similar structure during our MD calculations. The results are shown in Figure 4.13.
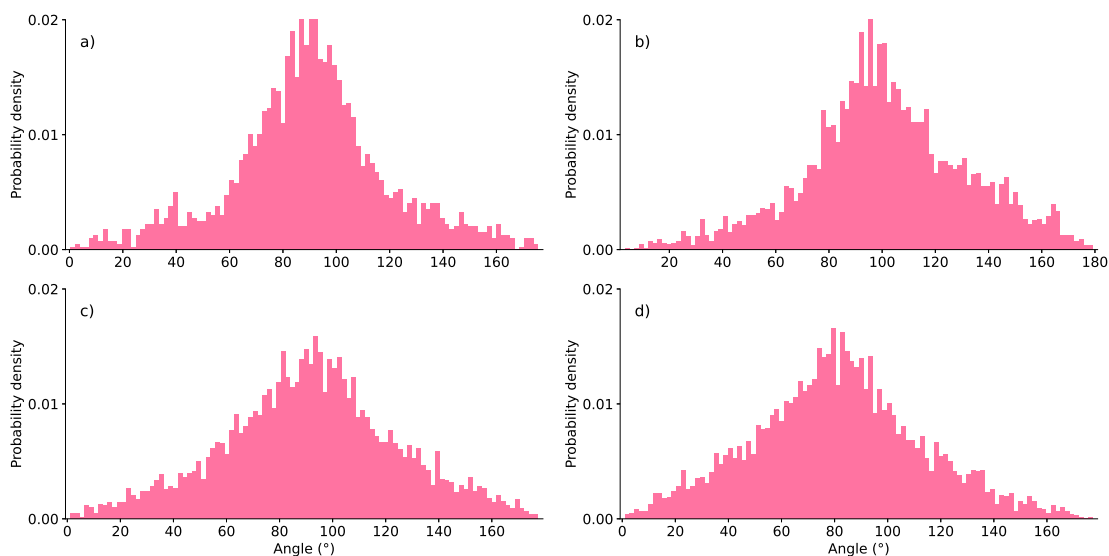
Figure 4.13: Angular distribution between the CI vector and the normal of the surface: (a) at 0%; (b) at 25%; (c) at 50%; (d) at 100% theoretical monolayer coverage.

For each water TM coverage, we see a peaked angular distribution around 90° between the CI vector and the normal to the surface. It suggests an orientation of methyl iodide parallel to the surface, similar to the static equilibrium geometries shown in Figure 4.9. The number of configurations close to 0 or 180° is negligible. This angle would correspond to the geometry inferred in the experiments. From our statistics, it is very unlikely to have it. The orientation distribution is not significantly modified when water covers the surface.

4.3.3 Effect of the temperature

Previous sections show broad adsorption energy and angle distributions of adsorbed CH_3I on the NaCl(001) surface. We hypothesize that it is due to temperature effects. Indeed, a temperature of 300 K can allow methyl iodide to explore all the possible configurations on the surface. It can be verified by measuring the adsorption energy and angle distribution by varying the temperature. Results are shown in Fig 4.14 and Table 4.12.

We observe that the adsorption energy distribution's mean decreases when temperature decreases. At 10 K, the mean adsorption energy is much lower than at 200 K ($-16.4\,\mathrm{kJ\,mol^{-1}}$). In addition, the associated standard deviation is linearly increasing with the temperature.
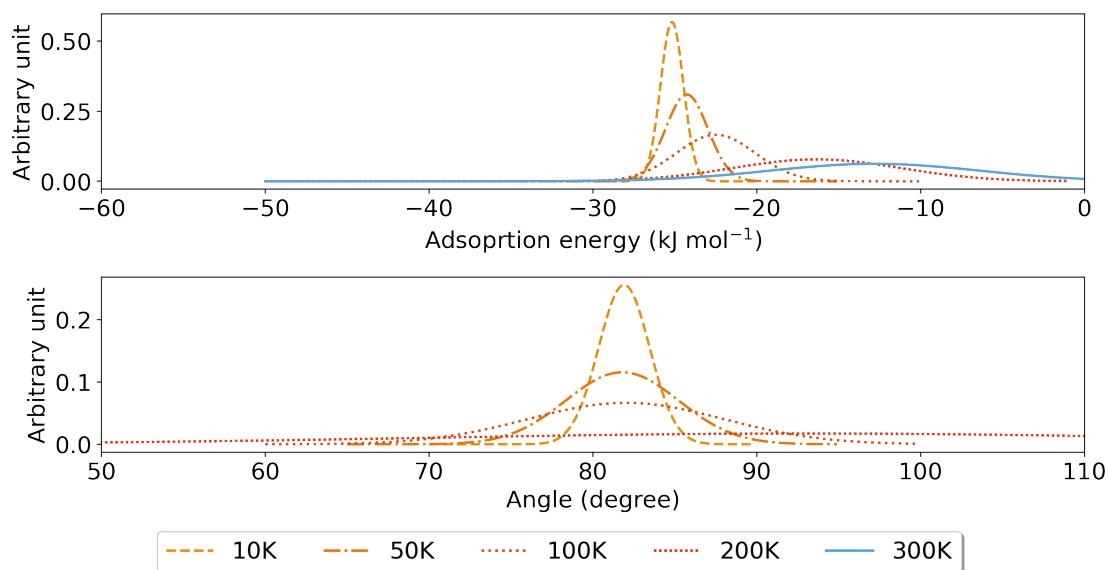
Figure 4.14: Evolution of the adsorption energy and angle distribution of CH$_3$I adsorbed on a bare NaCl(001) surface according to temperature.
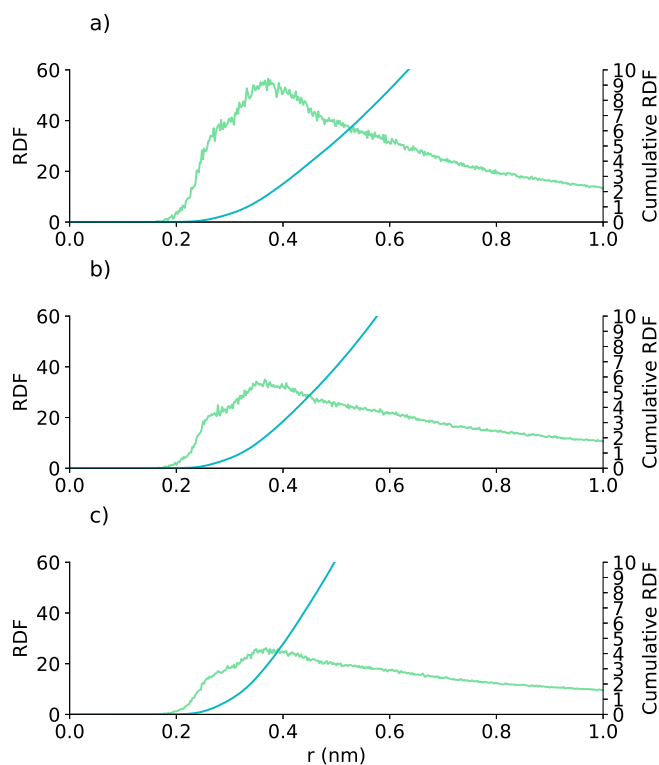
Table 4.12: Adsorption energy and angle distributions averages and standard deviations of the CH$_3$I/NaCl(001) system at different temperatures.

Temperature (K)	Adsorption energy (kJ mol^{-1})		Angle (°)	
	Mean	Standard dev.	Mean	Standard dev.
10	−25.2	0.7	81.9	1.6
50	−24.3	1.3	81.8	3.5
100	−22.5	2.4	82.0	6.0
200	−16.4	5.1	93.2	23.0

The mean angle distribution is not evolving for a temperature range of 10 to 100 K, with a constant mean angle at 82°. However, this value slightly increases at 200 K, with a mean value of 93.2°, closer to the value obtained at 300 K. As the temperature increases, the angle distribution standard deviation increases linearly for temperatures from 10 to 100 K. At 200 K, the latter value highly increases.

For the adsorption of methyl iodide on a bare NaCl(001) surface, we observe temperature effects on the adsorption energy and the angle distribution. We also see significant differences when the system is below 200 K. Methyl iodide can

Figure 4.15: Radial distribution function (green) and cumulative radial distribution function (blue) between CH_3I and H_2O: (a) at 25% TM ; (b) at 50% TM ; (c) at 100% TM.

explore all the NaCl(001) surface at 300 K, resulting in broad adsorption energy and angle distributions.

4.3.4 Radial distribution function

Radial distribution functions (RDFs) are commonly used to analyze MD simulations. The RDF is a probability distribution function that describes the distribution of particle pairs as a function of the distance between them. In other words, it describes the spatial arrangement of particles in a system. The cumulative RDF, which is the integral of the RDF, provides additional information about the system by quantifying the number of particles within a certain radius of a given particle. In this way, the cumulative RDF measures the coordination number around a particle.

The center-of-mass / center-of-mass RDFs between H_2O and methyl iodide are shown in Figure 4.15 for all water coverages. RDFs for all coverages are similar, with a maximum of around 0.38 nm. Regarding the cumulative RDFs, we observe an
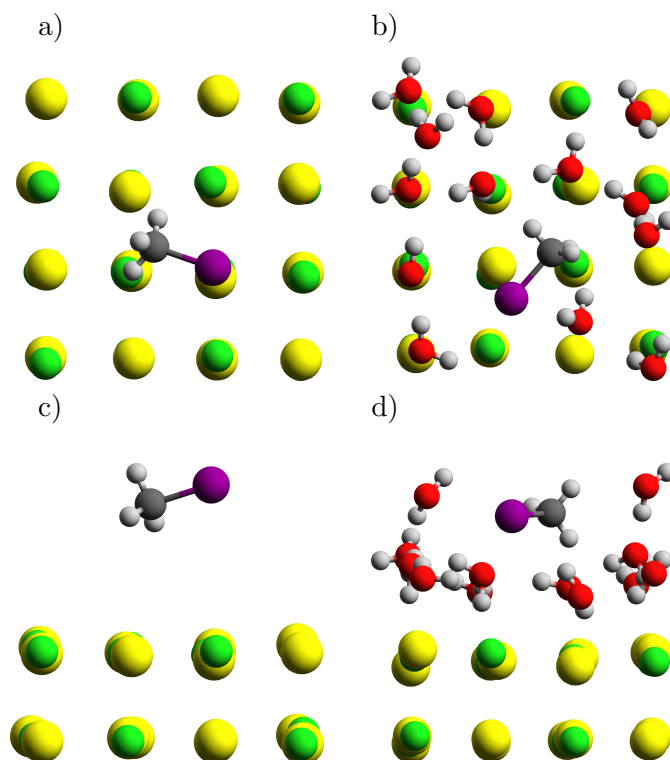
Figure 4.16: Top (a,c) and side (b,d) snapshot of the MD simulation at 300 K at 0 % and 100 % of a complete TM, respectively. Na atoms are represented in yellow whereas Cl atoms are represented in green.

average number of 2 H$_2$O molecules at the maximum at 25 and 50 % TM. However, the latter increased up to 3 molecules at 100 % TM. This increase in the number of water molecules around CH$_3$I agrees with the highest value of the adsorption energy at this coverage. As shown in Fig. 4.16, H$_2$O molecules surround methyl iodide. It increases the average adsorption energy of the latter and contributes to its stabilization at the surface.

4.4   Conclusion

The presence of water on a NaCl(001) surface has a non-negligible effect on the methyl iodide adsorption: the adsorption energy of the latter is increased by CH$_3$I−H$_2$O interactions. A 25 % TM H$_2$O can multiply the adsorption energy by a factor of 2.

   In contrast with previous results [96], our study found a horizontal orientation of methyl iodide on the NaCl surface with or without H$_2$O. In addition, we have

not observed significant vibrational frequency shifts upon adsorption of CH_3I on the surface, even for cluster adsorptions. This result agrees with the low value of the adsorption energy. Additional calculations on CH_3I-nH_2O or CH_3I-CH_3I adsorption dimers can be considered to give further information. Nevertheless, a high shift is usually linked to a massive change in the structure, like reactivity in the molecular system. The latter can be induced by surface defects and may not be observed on a perfect surface. The influence of surface defects was beyond the scope of the present work but would definitively need some specific investigations. Surface specific experiments could also be considered to better understand the methyl iodide adsorption on NaCl.

CH₃I adsorption on amorphous solid water

Outline of the current chapter

Amorphous solid water (ASW) is a solid form of ice different from the crystalline structure. This form can be found in space, in the interstellar medium at the surface of dust grains at low ($T <$120 K) temperatures [342, 343]. Nonetheless, its presence is also postulated in the Earth's upper atmosphere [111, 112]. Experimentally, ASW surfaces can also be used in low temperature experiments, as it was done by DeSimone et al. [134] among others [117, 118, 157–159]. These solid phases have the particularity to display free OH bonds dangling at the surface. In the literature, they are called dOH [114, 117, 118, 122, 123, 344, 345]. dOHs present a small adsorption peak around 3700 cm^{-1} on bare ASW surfaces.

Numerous experimental [114, 115] and theoretical [116, 123, 124] studies have shown that the presence of an adsorbate induces a red shift of the dOH vibrational frequencies. Indeed, measuring the vibrational shift gives indication on the strength of the interaction between the adsorbate and the surface. Determining the shift induced by a molecule is thus a crucial information to characterize adsorbed compounds, even if the shift is small (tens of cm^{-1}).

This chapter aims at determining the dOH vibrational frequency shifts induced by methyl iodide on ASW. It is a challenging task because of the nature of ASW surfaces, presenting a non-ordered molecular behavior. In addition, vibrational spectra are not accurately reproduced by force field methods. Thus, computing vibrational frequencies imply an explicit electronic description, with the concerned molecules at their minimum energy geometries. Therefore, a statistical analysis of all possible configurations is crucial to obtain an average spectrum as obtained experimentally.

The strategy employed in this part is inspired by previous work of Michoulier et al. [123, 133, 346] but using a different methodology for the QM treatment and extraction of the vibrational spectra. It starts with MD calculations of an ASW slab to probe statistically possible configurations of adsorbed CH$_3$I molecules on this surface. Then, a selection is made to find the most relevant configurations by regrouping them according to different criteria that will be detailed. Finally, the relevant configurations are extracted and computed using the multilevel ONIOM method to calculate the vibrational frequencies.

5.1 Generating adsorption geometries

As already stated before, classical MD simulations allow us to handle larger systems compared to quantum calculations. Moreover, to simulate the non-ordered ASW surface, we need to use a large simulation box (similar size as for the CH$_3$I/NaCl system done in chapter 4). This work was previously done by Michoulier et al.[123, 133, 346], when studying the effect of adsorption of polycyclic aromatic hydrocarbons on ASW surfaces, among others. We have used the same structures of the ASW slabs.

Using the TIP4P-2005 water model [338, 347], they started with a crystalline water system at 77 K and 1 bar during 10 ns, using the GROMACS package [246, 348–354]. The whole system contains 3360 water molecules. The next step was to gradually increase the pressure by incrementing it by 1.5 kbar every 5 ns until reaching 15 kbar. At this point, the crystal structure is broken, and the system is called a high-density amorphous solid water system. Then, the pressure is decreased to 1 bar by steps of 1.5 kbar. The final step in obtaining our ASW system is to heat the system at 200 K before cooling it down to 77 K and equilibrating it during 10 ns. The resulting ASW system is called low-density amorphous solid water within these conditions. After analyzing the final system, the comparison between the densities and the radial distribution functions showed a good agreement with experimental results.

Starting from bulk low-density ASW, we need to build a slab to adsorb methyl iodide. To do so, we have expanded the simulation box in the z-direction to create

two interfaces. Then, we have thermally equilibrated the system at 77 K during 5 ns.

We took the ASW slab generated following the method previously described. To model CH$_3$I adsorption, NVT trajectories were performed with the Berendsen thermostat at a target temperature of 77 K and a coupling constant of 0.5 ns. The system is equilibrated during 2 ns thermalization. The last 3 ns were used for the analysis. The Verlet algorithm cut-off scheme with a neighbor list updated each step is used. For long-range Coulombic calculations, the particle-mesh Ewald [271] method is used with a cut-off of 0.9 nm. A plain cut-off of 0.9 nm is used for Van der Waals interactions. The force field built as described previously and validated with the TIP4P/2005 model [338, 347] is used to describe methyl iodide interaction with ice.

The first aim is to generate adsorption geometries of CH$_3$I at the ice surface. Our ASW slab contains 1344 water molecules centered in a 2.65 × 3.07 × 9.24 nm simulation box. Using a slab allows us to run two simulations simultaneously, with one or two CH$_3$I molecules adsorbed on each interface. An illustration of the whole system is represented in Fig. 5.1. As the surface is amorphous and the studied temperature is very low, we need to have several trajectories with different initial conditions to sample the system correctly. We randomly selected 18 bare ASW surfaces from the previously described NVT equilibration at 77 K. Thus, we performed a total of 18 trajectories on the CH$_3$I/ASW system. Because the slab have two surfaces and because we have CH$_3$I adsorbed on each side, the number of generated trajectories is the double, with a total of 36 trajectories simulated.
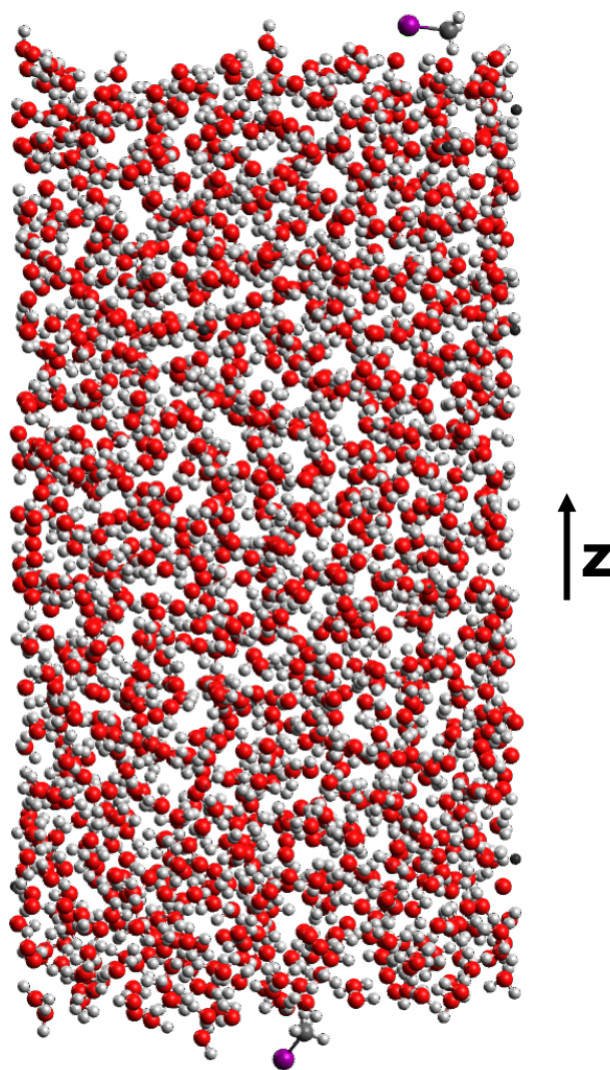
Figure 5.1: Illustration of adsorption geometry obtained by classical molecular dynamics calculation. One CH$_3$I molecule is adsorbed on each part of the slab.

5.1.1 Selecting configurations

The next step is to extract representative configurations of adsorbed methyl iodide on the ASW surface. First, we will analyze each trajectory to understand how CH$_3$I evolves on the surface.

One essential aspect of the adsorption process is the adsorption energy. The latter is not constant over time and may vary from one trajectory to the other. Then, we can look at its time evolution during the simulation or the probability distribution to find a configuration within a given adsorption energy. The second
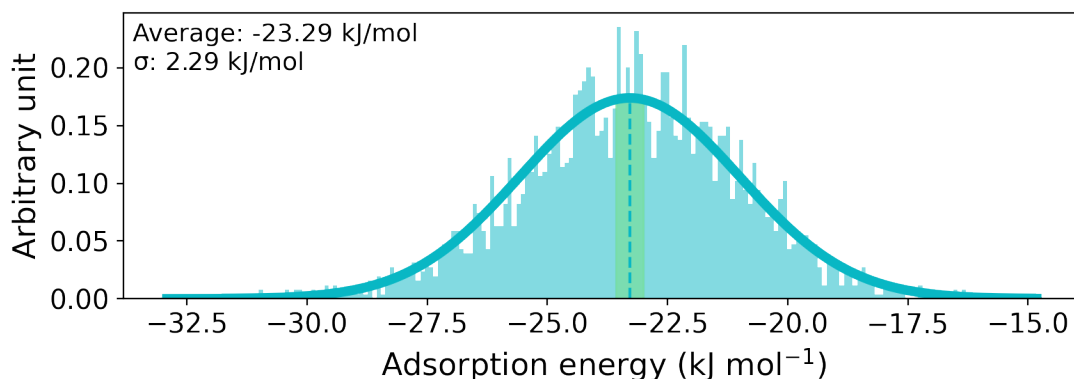
Figure 5.2: Distribution of the adsorption energy of CH_3I on the ASW surface. The blue line corresponds to the probability distribution fitted to a Gaussian function; the green dashed line to the mean, and the green region to be within 10 % around the mean. The standard deviation is indicated as σ.

option better suits our objectives by highlighting which configurations are most likely to occur, as shown in Fig. 5.2 for one trajectory.

In the present case, the adsorption energy distribution of the methyl iodide on the ASW surface (blue bars) follows a Gaussian distribution with an average of $23.29\,kJ\,mol^{-1}$ and a standard deviation of $2.29\,kJ\,mol^{-1}$. It suggests that only one relevant configuration has been found. It can be verified by studying the in-plane CH_3I trajectory on the ASW surface, shown in Fig. 5.3. It shows that CH_3I remains trapped in the adsorption site after $300\,ps$. Both figures suggest that this trajectory presents only one representative adsorption geometry, with oscillations in the potential well. An illustration of the corresponding adsorption geometry is presented in Fig 5.4.

Then, we can plot the corresponding Gaussian distribution (blue line in Fig. 5.2). The latter is also known as the probability function. Then, we can define an area around the mean adsorption energy corresponding to 10 % of the most probable configurations (green area). Finally, we decide to pick configurations within this area for further quantum calculations.

We can find more than one representative configuration among all our trajectories as represented in Fig. 5.5 for one trajectory. In the present case, we can define one Gaussian distribution of the adsorption energy per configuration. We can isolate the first configuration (blue) described by a Gaussian distribution with an average adsorption energy of $-23.74\,kJ\,mol^{-1}$ and a standard deviation of $2.21\,kJ\,mol^{-1}$. In addition, we define the second representative configuration with a Gaussian distribution of the adsorption energy with an average of $-30.86\,kJ\,mol^{-1}$ and a standard deviation of $2.50\,kJ\,mol^{-1}$. The corresponding in-plane trajectory
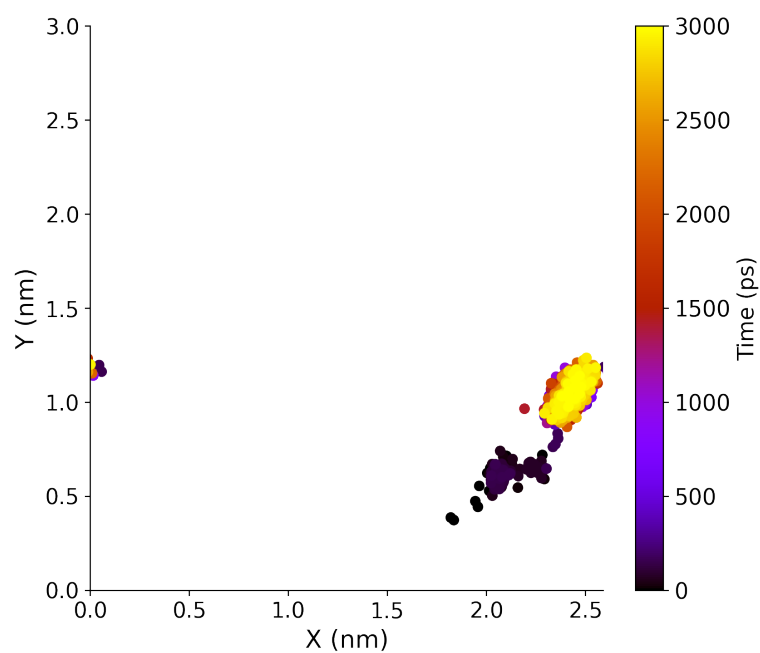
Figure 5.3: In-plane motion of CH$_3$I adsorbed on the ASW surface when finding one adsorption geometry in one trajectory. The colors and the dots are related to time along the trajectory. The X and Y axes correspond to the surface directions (a and b vectors).

(a)   (b)
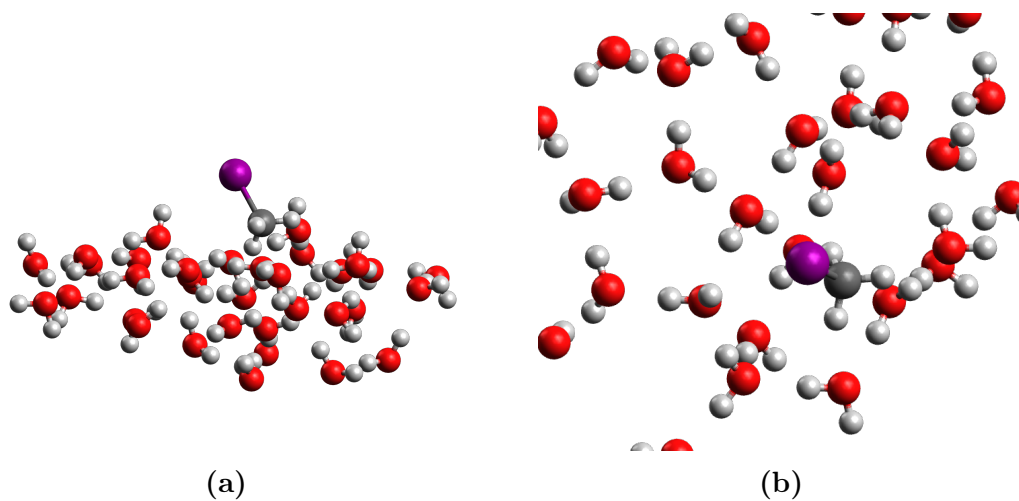
Figure 5.4: Snapshots of the adsorption geometry of CH$_3$I on the ASW surface after 300 ps: (a) Side view, (b) Top view.
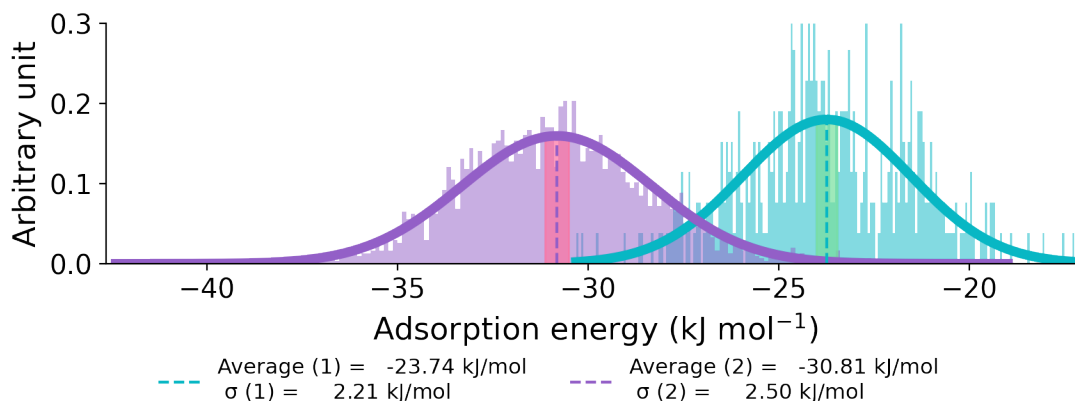
Figure 5.5: Density distributions of the adsorption energy of CH_3I on an ASW surface. The first configuration is blue (1), and the second is purple (2). The corresponding standard deviations are indicated as σ.
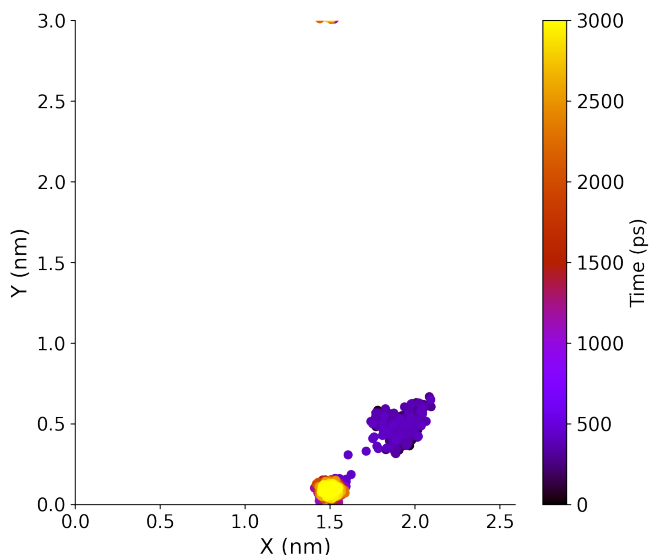
Figure 5.6: In-plane motion of CH_3I adsorbed on the ASW surface when finding two adsorption geometries in one trajectory. The colors and the dots are related to time along the trajectory. The X and Y axes correspond to the surface directions (a and b vectors).

is shown in Fig 5.6. We see that the CH_3I molecules is firstly trapped in a first potential well during the first 700 ps. Then, the molecule moves quickly to another potential well until the end of the simulation. This displacement agrees with finding two adsorption geometries in the present case. Illustrations of the different

Figure 5.7: Snapshots of the adsorption geometry of CH$_3$I on the ASW surface: before 700 ps (a) Side view, (b) Top view; after 700 ps (c) Side view, (d) Top view.

adsorption geometries found in this trajectory are presented in Fig. 5.7.

Among all the trajectories, we obtained one extreme case. For this trajectory, we found the adsorption energy of CH$_3$I on the ASW surface probability distribution presented in Fig. 5.8. In this extreme case, the adsorption energy distribution follows a Gaussian distribution with an average of $-41.86 \, \text{kJ} \, \text{mol}^{-1}$ and a standard dev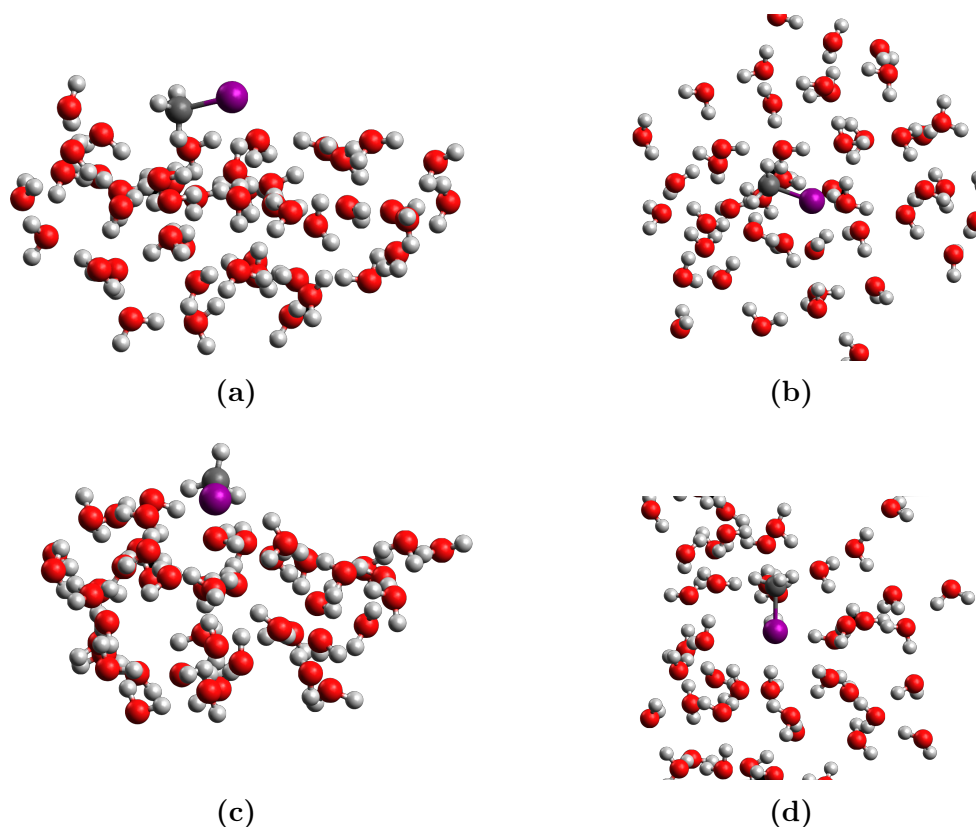iation of $2.53 \, \text{kJ} \, \text{mol}^{-1}$. Thus, there is a factor 2 between the adsorption energy found in this trajectory and the one previously studied and presented in Fig. 5.2. In addition, both distributions are not even overlapping, suggesting a totally different geometry. The latter is illustrated in Fig. 5.9. Compared to the other adsorption geometries, we see that methyl iodide is adsorbed in a cavity in the ASW surface. As a consequence, the amount of water molecule around CH$_3$I is much higher than for the other adsorption geometries. It leads to an increase of the adsorption energy. Nonetheless, this extreme case appends only once among all our trajectories. Therefore, the probability to have such adsorption geometry in our system must be lower than the ones previously found.
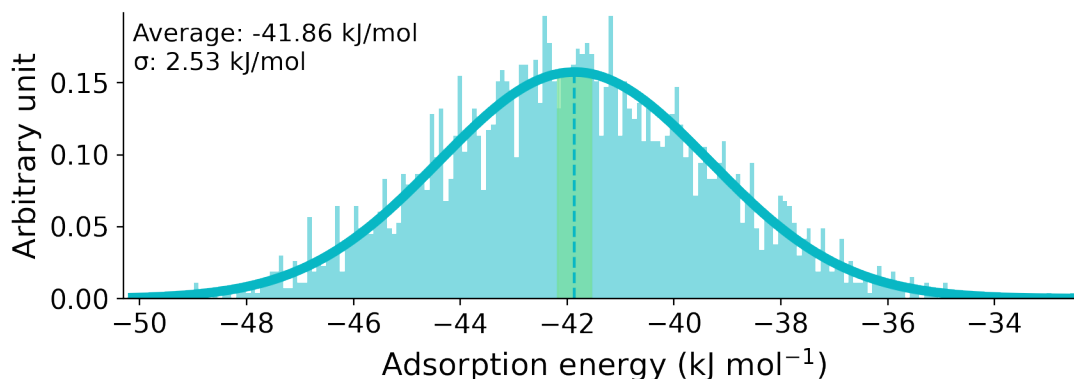
Figure 5.8: Distribution of the adsorption energy of CH₃I on the ASW surface for the extreme case. The blue line corresponds to the probability distribution fitted to a Gaussian function; the green dashed line to the mean, and the green region to be within 10 % around the mean. The standard deviation is indicated as σ.
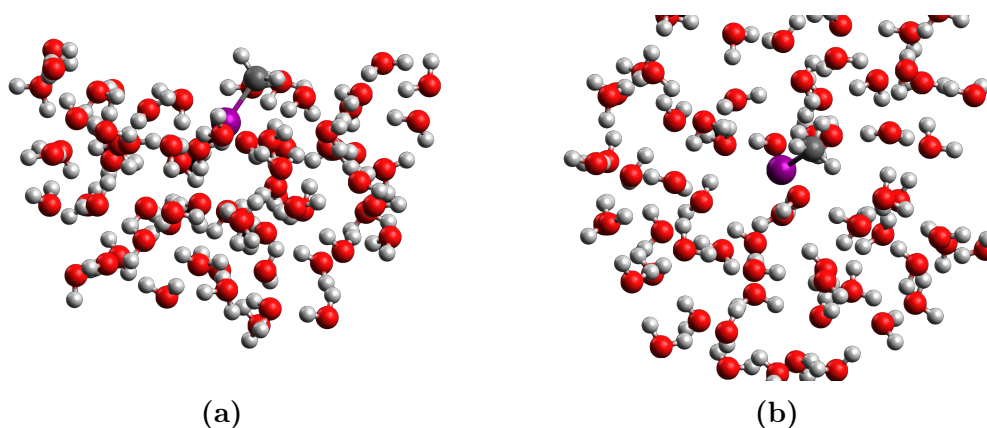
Figure 5.9: Snapshots of the adsorption geometry of CH₃I on the ASW surface for the extreme case: (a) Side view, (b) Top view.

The same methodology is applied to all the trajectories done in this chapter. In total, 53 configurations were found with this method. Even if this method does not ensure that all the configurations are found, it gives a representative picture of the most probable adsorption geometries.

By running 36 trajectories of CH₃I adsorbed on the ASW surface, we were able to collect in total 162 053 points with a total duration of 108 ns, including different adsorption geometries and energies. Using all these data, we can look at the probability distribution of all the adsorption energies. The latter is shown in Fig 5.10. We observe that the probability distribution does not follow a Gaussian
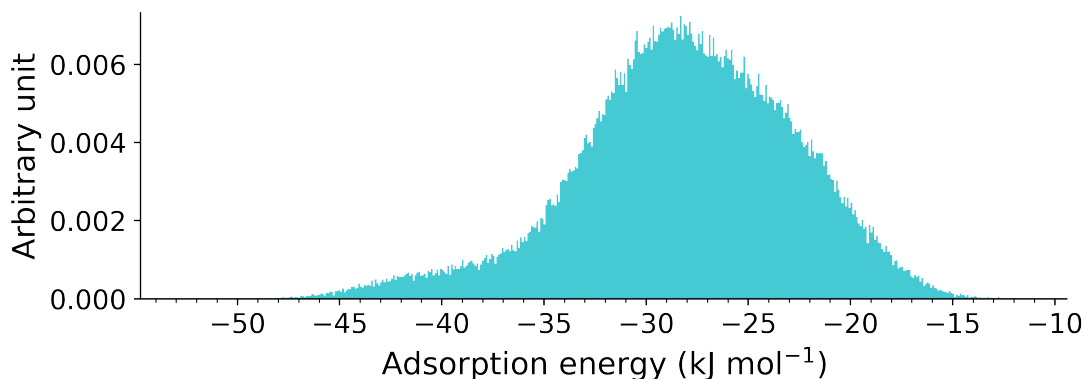
Figure 5.10: Distribution of the adsorption energy of CH$_3$I on the ASW surface for all the trajectories.

distribution. The highest probability is found for adsorption geometries with a corresponding adsorption energy around $-29\,\text{kJ}\,\text{mol}^{-1}$. Rare events (with low probabilities) are observed for highest adsorption energies. It corresponds to the extreme case previously described. Such events depending on the surface topology and the displacement of methyl iodide on the ASW surface, it is consistent to find low probabilities for an adsorption into a cavity present on the surface.

5.2   Clustering configurations

Using MD calculations, we have obtained 53 possible configurations of adsorbed methyl iodide on the ASW surface. Nevertheless, many configurations have similar adsorption energies and may be redundant. Treating all these configurations at the QM level is not possible due to the high computational cost. We observed that many configurations have similar adsorption energies. This section will further analyze these configurations and identifies the most relevant ones that will be used in the QM model.

We need to define parameters on which we can group and evaluate configurations. First, all the configurations found during the thermalization of the system (first 2 ns) of the simulation are removed. Because our force field fails to describe CH$_3$I$\cdots$CH$_3$I correctly, all configurations showing CH$_3$I$\cdots$CH$_3$I interactions are removed too. The latter is not a rare event, as it concerns around 40 % of the total number of configurations.

At ASW surfaces, two types of intermolecular interactions are driving the adsorption process: The number of I$\cdots$H H-bonds between the iodine of CH$_3$I (I-HW) and CH$\cdots$O H-bonds between the hydrogen of CH$_3$I and the oxygen of
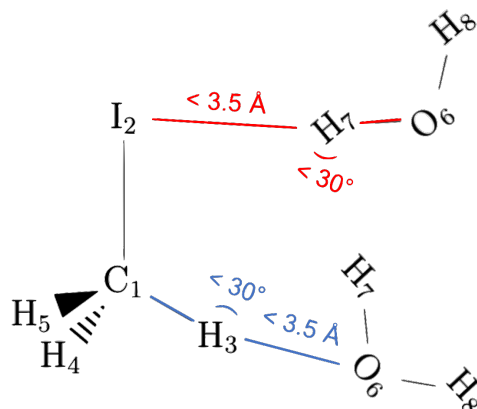
Figure 5.11: Schematic representations of the conditions to count a I-HW intermolecular hydrogen bond (blue) and a H-OW intermolecular hydrogen bond (red).

water molecules (H-OW). Based on the HBOND algorithm of the GROMACS package which calculates the number of hydrogen bonds between molecules, we assume formation of such bonds if we have:

- An interatomic distance lower than $3.5\,\text{Å}$.

- An angle between both three concerned atoms lower than 30°.

These conditions are summarized schematically in Fig. 5.11.

We can also count the number of water molecules close to the adsorbed methyl iodide (coordination number). Indeed, this number also influences the number of interactions that the adsorbate has, increasing its adsorption energy with the ASW surface. The water molecules are located into spheres around methyl iodide called *coordination sphere*. To compute the radius of these spheres, we compute the center-of-mass/center-of-mass RDF between methyl iodide and water. Results are displayed in Fig. 5.12. The first coordination sphere has a radius between $0.39\,\text{nm}$ to $0.41\,\text{nm}$ and the second one between $0.46\,\text{nm}$ to $0.48\,\text{nm}$. Then, all water molecules with their center of mass at a distance lower than $0.5\,\text{nm}$ from the methyl iodide molecule are considered close to CH_3I (counting both the first and second coordination spheres).

Applying these filters to our selected configurations drastically decreases the number of adsorption geometries from 53 to 13 with associated parameters: the number of H_2O molecules surrounding CH_3I, the number of I-HW and H-OW
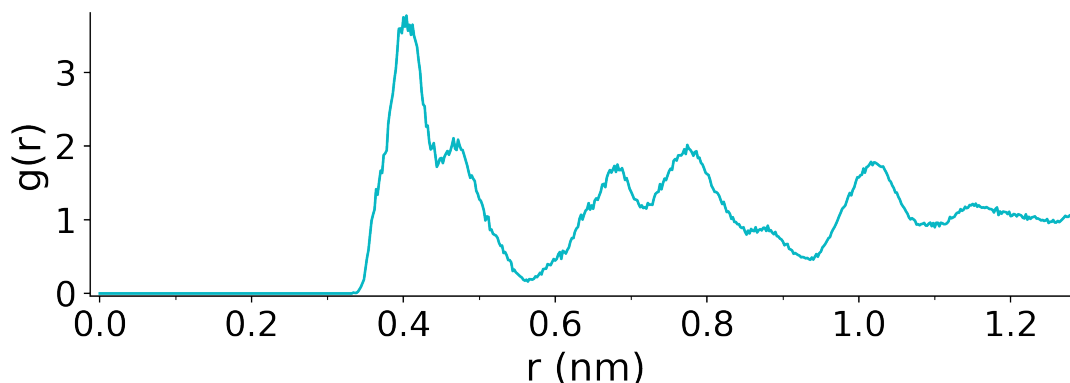
Figure 5.12: Center-of-mass center-of-mass radial diffusion functions between methyl iodide and water for one trajectory.

intermolecular bonds, and the corresponding adsorption energy[1]. All this information is gathered in Table 5.1. We observe that there is no direct correlation between the number of hydrogen bonds and the adsorption energy. As expected, the adsorption energy is larger when there are many water molecules around methyl iodide. Finally, having both water molecules and hydrogen bonds tend to favor adsorption. Adsorption energies ranged from $-23.3 \, \text{kJ} \, \text{mol}^{-1}$ to $-41.9 \, \text{kJ} \, \text{mol}^{-1}$. This large difference comes from the high differences between adsorption geometries, as discussed previously and present in Fig. 5.4 and 5.9. The highest adsorption energy corresponds to the adsorption of CH$_3$I in a cavity.

In order to better understand how the adsorption energy evolves according to the parameters, we can discriminate results according to the number of I-HW intermolecular bonds. We have 7, 5, and 1 configurations for 0, 1, and 2 I-HW bonds respectively. Starting with the configurations with 0 I-HW bond, we can visualize the results as shown in Fig. 5.13

We observe a clear correlation between the interaction energy and the number of water molecules and H-OW bonds. Indeed, as both parameters increase, the interaction energy increases. Regarding the geometries and values of the parameters, we can split them into three groups of similar configurations. We choose the vibrational frequencies of the most stable configuration for each group.

The process is repeated for configurations presenting one I-HW bond. The results are presented in Fig 5.14. The same observations can be made for configurations with one I-HW bond. One exception is the last configuration, presenting a high interaction energy without any H-OW bond and a lower number of water molecules

---

[1]These energies are taken from the MD trajectory. There is no geometry optimization and the resulting energies are computed using the force field.

Table 5.1: Representation of the 13 configurations found for the CH$_3$I adsorption on the ASW surface and their associated parameters

Index	Adsorption energy (kJ mol^{-1})	Number of I-HW bonds	Number of H-OW bonds	Number of H$_2$O molecules within 5 Å from COM.
0	−23.2	1	0	2
1 − G4	−25.0	1	0	2
2	−26.1	0	0	8
3 − G1	−26.4	0	1	9
4 − G3	−29.0	1	0	3
5 − G6	−29.7	1	1	8
6	−30.8	0	1	11
7 − G2	−30.5	0	1	10
8	−30.8	0	1	11
9	−30.6	0	1	10
10 − G7	−31.6	1	0	6
11 − G8	−35.0	2	0	3
12 − G3	−41.9	0	2	14

surrounding CH$_3$I than the previous configuration in terms of interaction energy. In this case, we can define four different groups of similar configurations. Only one configuration presents two I-HW bonds.

In this section, we have seen how we reduced the number of representative configurations by classifying the configurations according to various parameters. We have grouped similar configurations allowing us to compute only the lowest configuration for each group, reducing the number of calculations needed for the study. Overall, we have reduced the number of configurations from 53 to 8 (now labeled G1 to G8). The next section will discuss how we have computed the dOH vibrational frequencies with and without adsorbed methyl iodide on the ASW surface.
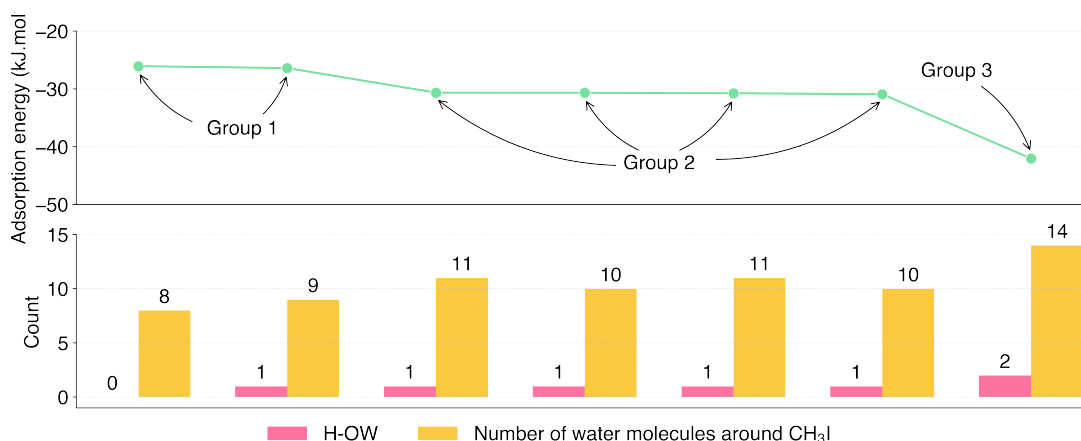
Figure 5.13: Adsorption energy variation for configurations without any I-HW bonds. The number of neighboring water molecules and of H-OW bonds is also reported. Some groups are defined based on these criteria as discussed in the text.
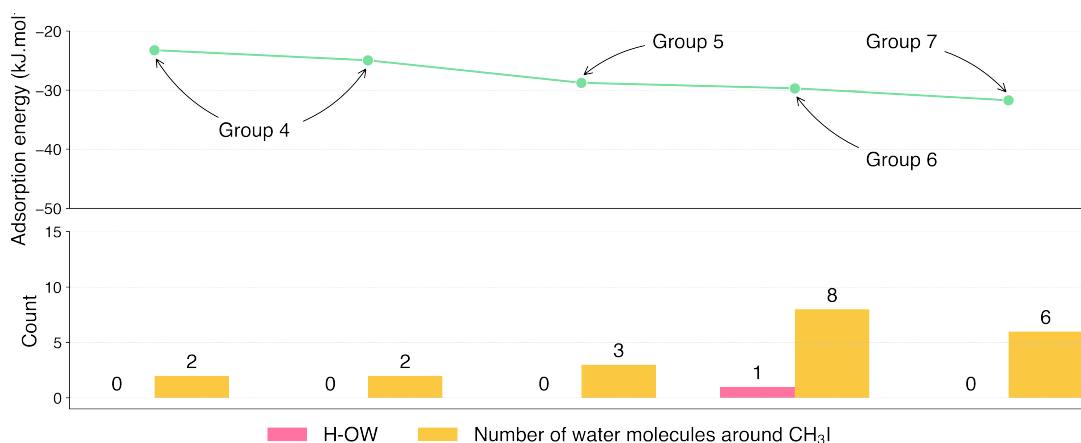
Figure 5.14: Adsorption energy variation for configurations with one I-HW bonds. The number of neighboring water molecules and of H-OW bonds is also reported. Some groups are defined based on these criteria as discussed in the text.

5.3 Vibrational frequencies

We have seen how we can generate and reduce the number of representative configurations of adsorbed methyl iodide on an ASW surface at 77 K. The last step of the whole process consists in computing the vibrational frequencies of the configurations with and without the CH$_3$I molecule.
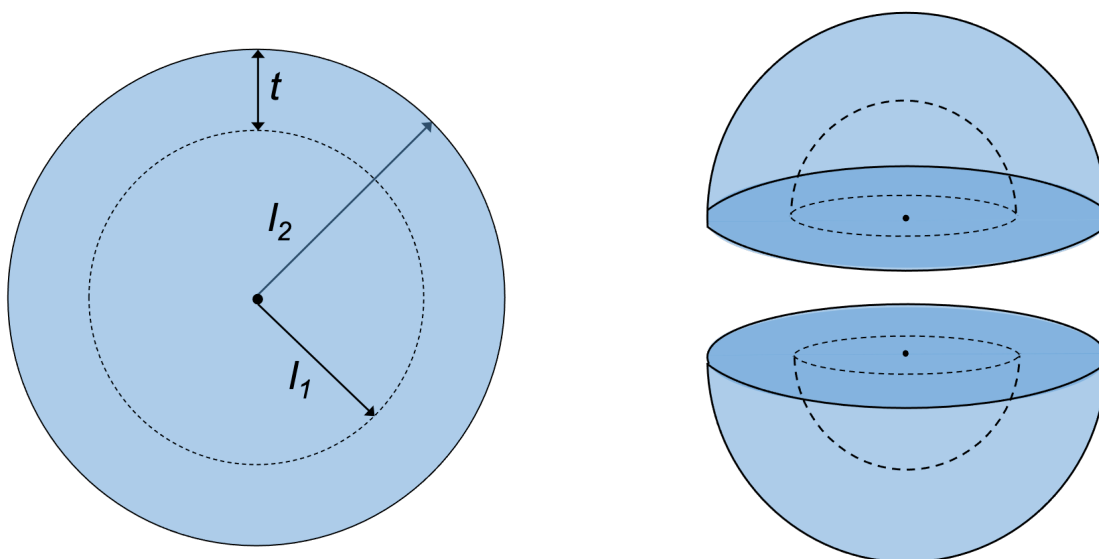
Figure 5.15: Schematic representation of the extraction of the system of interest. The total extracted system corresponds to a sphere of radius $I_2 = I_1 + t$. The inner sphere of radius I_1 contains the molecules that are minimized. The spherical shell of radius t represents the molecules kept frozen to maintain the system and account for long-range interactions.

The CH_3I + ASW molecular system has many atoms (4042 atoms for a system with one adsorbed CH_3I molecule). Then, we first need to reduce the number of molecules in the system before running quantum calculations. The area of interest is located around the CH_3I adsorption site. Indeed, there is no need to simulate the whole system to obtain reliable vibrational frequencies at the surface of the ASW. One solution is to draw a sphere around CH_3I to focus on the area of interest. Then, the water molecules in the periphery of the sphere are maintained to keep the structure of the system as it was in the classical MD calculations. Indeed, if we allow these molecules to move, the whole system will expand and will not represent methyl iodide adsorption on the ASW surface at 77 K. In addition, the methyl iodide molecule and few water molecules around the adsorbate have to be free to move during the optimization. Indeed, we can only compute vibrational frequencies when the system is at its minimum energy geometry. To summarize, we extract a sphere around CH_3I without freezing the molecules, and a spherical shell of frozen water molecules around the previous sphere, as shown in Fig. 5.15.

The next step is to compute the vibrational frequencies using quantum calculations. First, we need to pick a method which suits well with the system. ONIOM [355] (Own N-layered Integrated molecular Orbital Molecular Mechanics) is a computational method used in quantum chemistry to model large molecular
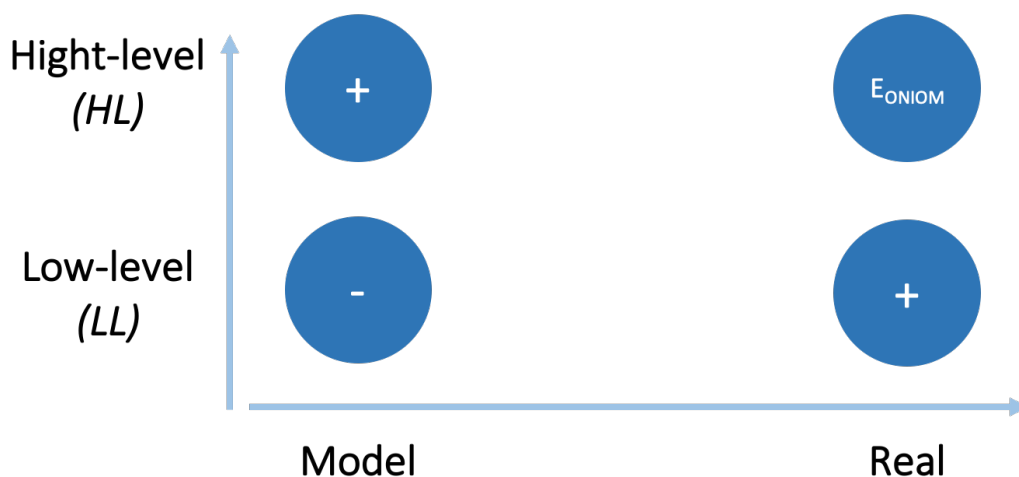
Figure 5.16: Subtractive high-level/low-level coupling as implemented in the ONIOM method.

systems at different levels. This method combines a high-level quantum mechanical method in small regions of the system with a lower level for the larger, less critical parts to achieve high accuracy. It enables the calculation of properties (such as vibrational frequencies) that would be otherwise unfeasible with purely quantum mechanical methods. The ONIOM method is a "subtractive" or "extrapolative" scheme. Writing the high-level region/method as HL and the low-level ones as LL, the energy is calculated as:

$$E_{\text{ONIOM}} = E_{\text{LL}}(\text{HL+LL}) + E_{\text{HL}}(\text{HL}) - E_{\text{LL}}(\text{HL}) . \tag{5.1}$$

Eq. 5.1 is illustrated in Fig. 5.16.

We used the hybrid ONIOM method [355] at the M062-X/6-311+G(2df,2p)//PM6 level of theory. In other words, the molecules around methyl iodide are computed at the M062-X/6-311+G(2df,2p) level of theory, whereas the other water molecules (the frozen ones) are computed at the PM6 semi-empirical level of theory [356]. This approach combines the accuracy of DFT calculations, the low computational cost of semi-empirical ones, and eliminate the mechanical/electrostatic embedding issues of QM/MM ONIOM methods [357]. To extract the system of interest, we set a sphere radii I_1 to 5.0 Å and I_2 to 9.0 Å according to the CH$_3$I center of mass. The total of water molecule inside each region (HL and LL) are given in Table 5.2.

We observe that all the calculations do not have the same number of water molecules in the HL and the LL regions. These numbers vary from 2 to 14 water molecule in the HL regions and 22 to 50 for the LL ones. To illustrate these calculations, one example of ONIOM calculation is displayed for G3 in Fig. 5.17.

Table 5.2: Number of H_2O molecules inside the high-level (N_{HL}) and the low-level (N_{LL}) region for each groups in ONIOM calculations.

	N_{HL}	N_{LL}	Total
G1	9	31	40
G2	10	31	41
G3	14	50	64
G4	2	22	24
G5	3	26	29
G6	8	26	34
G7	6	39	45
G8	3	26	29

Comparing the bare ASW surface with the one containing one adsorbed CH_3I, we see that some water molecules close to the adsorbate does not have the exact same position. We displayed the difference between both structures in Fig. 5.18.

Even if both structures are similar (with a corresponding RMSD value of 0.215 Å), we see that structures show small differences. Indeed, the water molecules having H-bonds with methyl iodide in the CH_3I/ASW system rotate in the bare ASW one, favoring H-bonds with other water molecules. These small rotations have an impact on the computed vibrational frequencies. Nevertheless, it is impossible to avoid this phenomena as it is mandatory to have optimized structures to compute harmonic vibrational frequencies. Table 5.3 shows the RMSD values for all the geometries between both systems.

These values range between 0.058 Å to 0.461 Å. Then, only a few amount of water molecules move from one system to the other. The highest RMSD value is found for G6 systems. They are represented in Fig. 5.19. We identify one water molecule which has a different position when CH_3I is adsorbed on the surface or when it is removed. This movement explains the high value of the RMSD for G6.

For some adsorption geometries, the optimization of the HL regions induces I-HW Hbond breaking. Then, it is necessary to compute the latter for the optimized geometries. Table 5.4 only shows the dOH vibrational frequencies identified with the visualization software MOLDEN [358]. In our system, it corresponds to the highest computed vibrational frequencies. We observe that dOH vibrational frequencies are red-shifted, going from the bare ASW surface to the one with one CH_3I
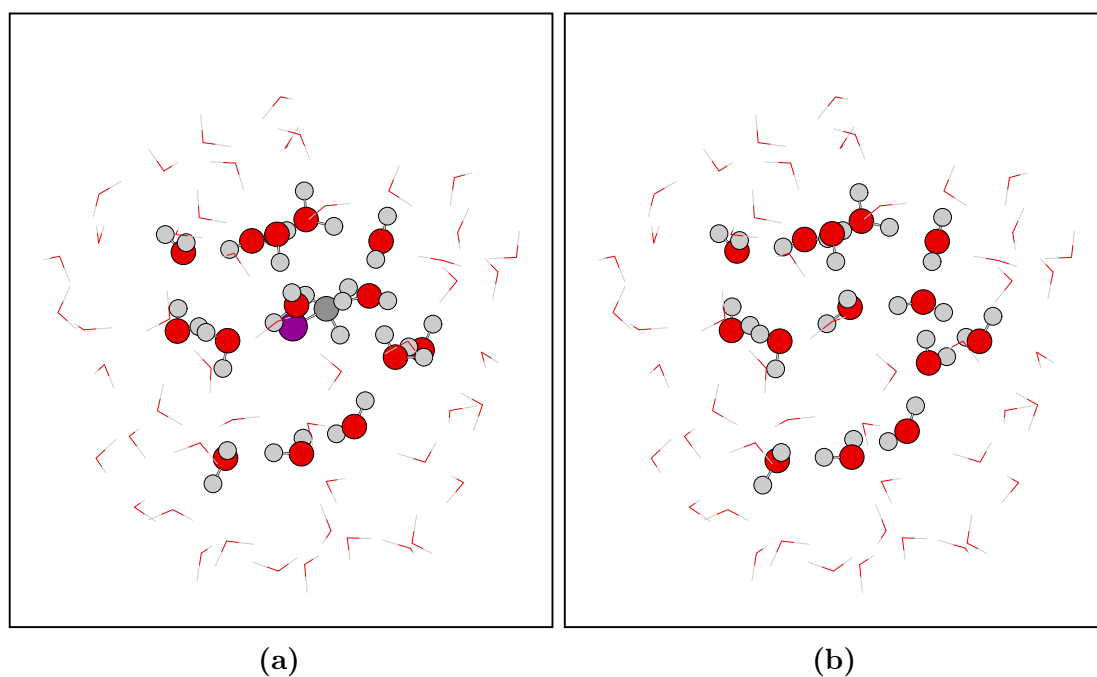
Figure 5.17: ONIOM optimized geometries of adsorbed CH$_3$I on the ASW surface for group G3. Water molecules in the HL region are represented with balls and sticks, whereas the ones in the LL region are represented with lines. (a) CH$_3$I + ASW; (b) bare ASW.
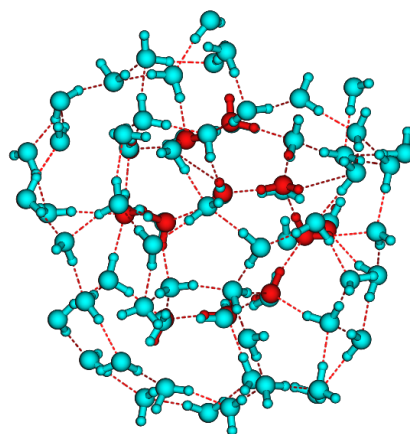
Figure 5.18: ONIOM superposition of optimized geometries of the system for G3 with (red) and without (blue) adsorbed CH$_3$I on the ASW surface. The corresponding RMSD value is 0.215 Å.

Table 5.3: ONION RMSD values comparing the CH_3I/ASW and bare ASW system for each calculated group.

	RMSD (Å)
G1	0.058
G2	0.039
G3	0.215
G4	0.103
G5	0.134
G6	0.461
G7	0.193
G8	0.235

molecule adsorbed on it. Shifts are varying between 1 to $-55\,cm^{-1}$. In section 5.1, more precisely in Fig 5.10, we have calculated the adsorption energy probability distribution. Using these probabilities, we can compute a weighted average for the vibrational frequency shifts. The corresponding weighted average red shift is $20\,cm^{-1}$. Furthermore, we observe a correlation between the presence of a I-HW Hbond and a high dOH red shift. For group G4 and G7, we observe a maximum dOH red shift of -55 and $-48\,cm^{-1}$, respectively. These values are higher than the one observed for G1 ($-29\,cm^{-1}$). It suggests that the adsorption geometry (particularly the presence of I-HW Hbonds) is an essential parameter that influences the value of dOH vibrational frequency shifts upon the adsorption of CH_3I. Nonetheless, having an adsorption geometry presenting I-HW bonds is not systematic, as CH_3I can be adsorbed without any of these particular Hbonds.

Another way to represent the results is by considering the dOH IR vibrational frequency intensities. In this statistical approach, we can simulate the IR absorption spectrum of each cluster by applying a Lorentzian smearing on each frequency of $10\,cm^{-1}$. Then, we can average all the obtained spectra by normalizing their intensities. The latter are weighted accordingly to the probability to observe the following configuration according to our MD trajectories. The resulting spectra are shown in Fig. 5.20. We observe the IR signature of methyl iodide with peaks at 800, 1250, 1400, and 3100 cm^{-1} comparing the CH_3I+ASW spectrum with the bare ASW one. To identify the IR band maximums, we computed the first-derivative of the IR intensity according to frequencies. When this derivate is zero, we can

(a)

(b)

(c)

Figure 5.19: ONIOM optimized geometries of adsorbed CH$_3$I on the ASW surface for group G6. Water molecules in the HL region are represented with balls and sticks, whereas the ones in the LL region are r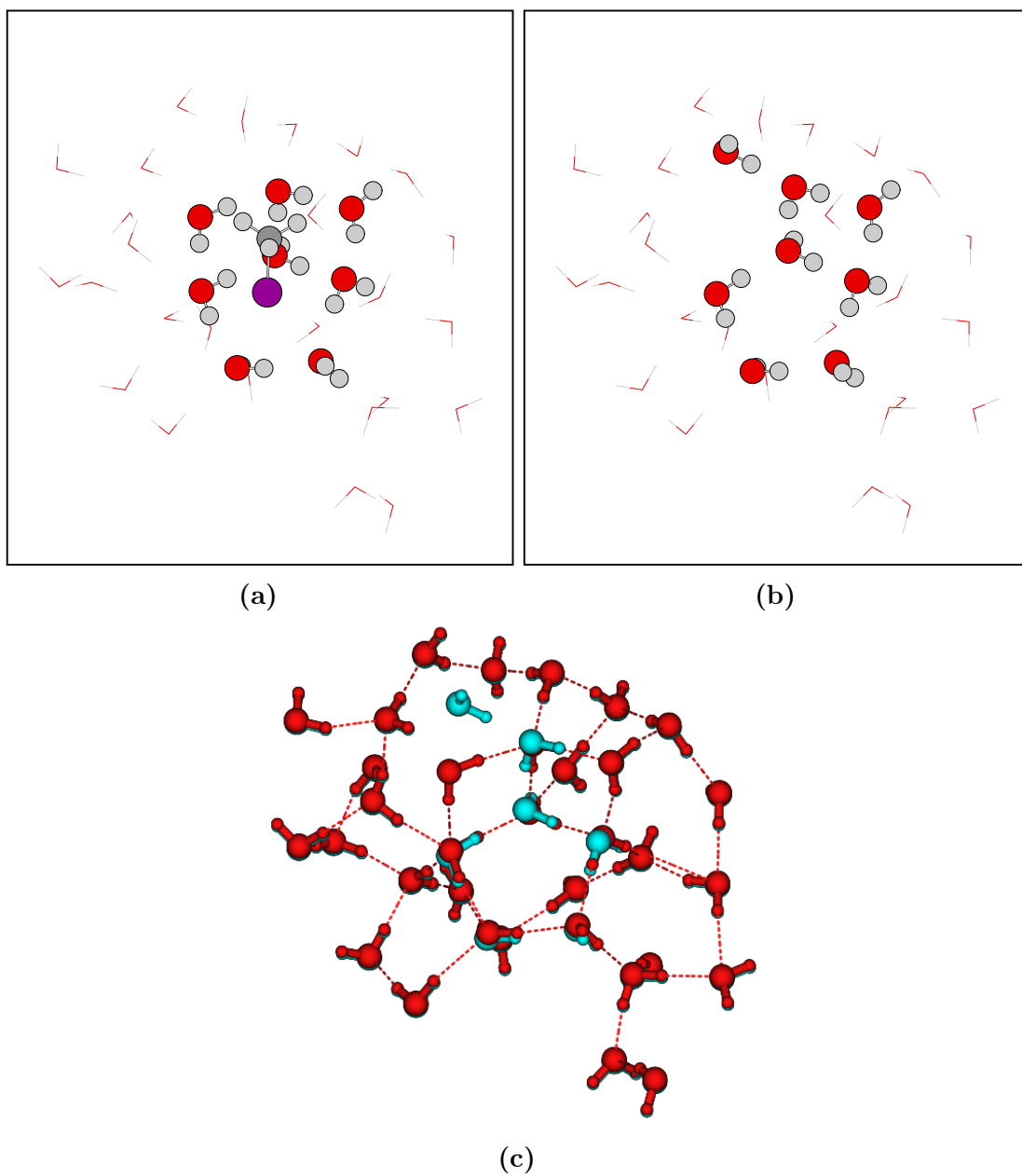epresented with lines. (a) CH$_3$I + ASW; (b) bare ASW; (c) superposition of CH$_3$I/ASW (red) and bare ASW (blue) with a corresponding RMSD value of 0.461 Å.

Table 5.4: ONIOM dOH calculated vibrational frequencies at the M062-X/6-311+G(2df,2p)//PM6 level of theory. All the frequencies are expressed in cm^{-1}.

Name	HW−I numbers	CH_3I+ASW	ASW	Shift
G1	0	3895	3911	−16
	0	3905	3934	−29
G2	0	3895	3899	−4
	0	3925	3924	1
G3	0	3873	3880	−2
G4	1	3765	3809	−55
	1	3824	3879	−55
G5	0	3838	3847	−9
G6	0	3917	3934	−17
G7	0	3904	3908	−4
G8	2	3833	3848	−15
	2	3917	3869	−48
WEIGHTED AVERAGE				−20

identify rather a maximum or a minimum. The first derivatives of both systems are shown in Fig. C.1. Regarding dOH vibrational frequencies, we observe a slight shift of $14\,cm^{-1}$, going from $3913\,cm^{-1}$ to $3899\,cm^{-1}$. This value is slightly lower than the one found with the previous method ($-20\,cm^{-1}$). In addition, we also observe a small vibrational frequency red-shift of water vibrational frequencies from $1648\,cm^{-1}$ to $1642\,cm^{-1}$, highlighted by the difference spectrum in red and the first derivatives previously introduced.
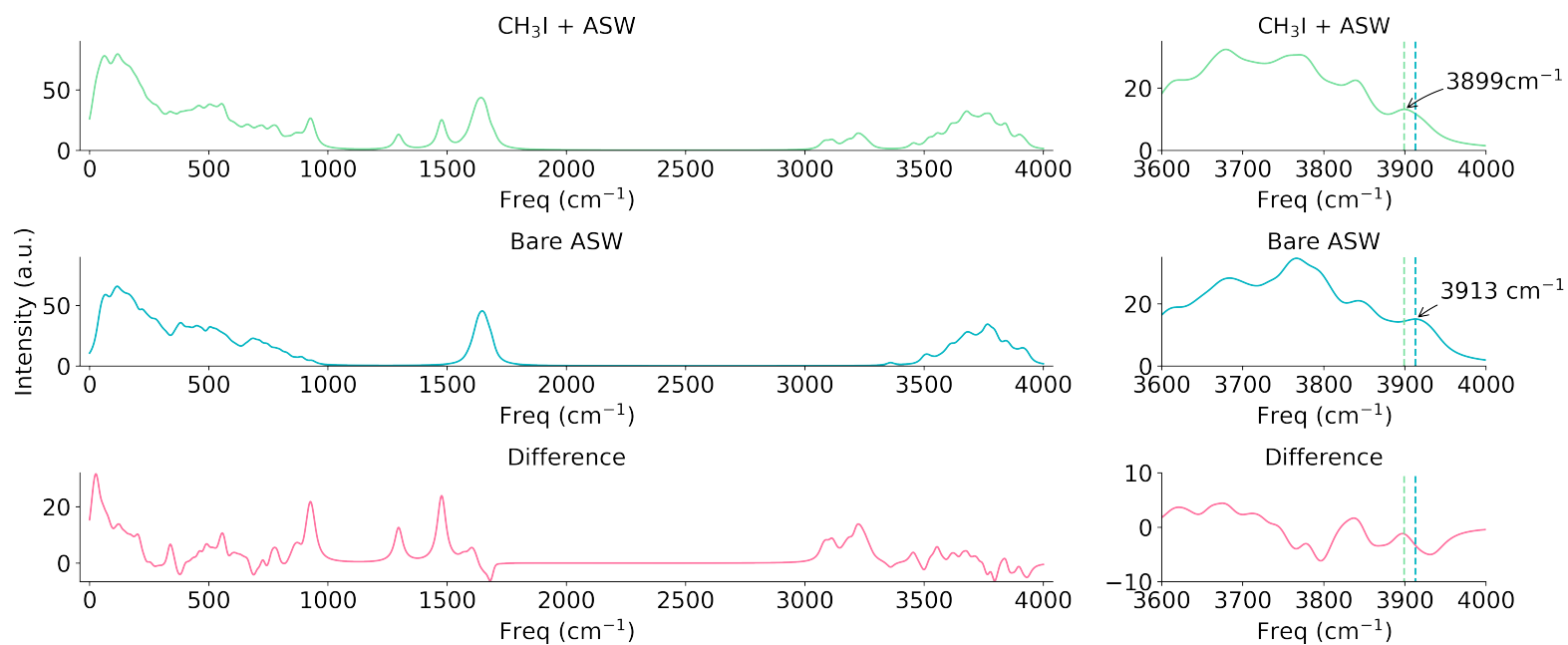
Figure 5.20: IR weighted spectra obtained after averaging over 8 configurations according to their respective probabilities of: (green) CH$_3$I adsorbed on ASW surface; (blue) Bare ASW; (red) Difference between both spectra. A Lorentzian smearing of $10\,\mathrm{cm^{-1}}$ has been applied.

5.4   Conclusion

In this chapter, we have established a strategy to compute the dOH vibrational frequency shifts when a CH_3I molecule is adsorbed on a ASW surface. We ran MD calculations at $77\,K$ to generate relevant and representative adsorption geometries. Then, we reduced the number of configurations based on interaction energies, intermolecular bonding and coordination numbers. Our calculations show that the adsorption energy is impacted by the number of surrounding water molecules around methyl iodide, stabilizing configurations located on surface cavities.

To account for the different possible configurations, we have averaged the theoretical IR spectra of the bare ASW surface and the CH_3I+ASW systems. We have shown that, in average, vibrational red shifts of $14\,cm^{-1}$ to $20\,cm^{-1}$ occur for the dOH when CH_3I is adsorbed on the surface. In addition, we observed small red shifts for H_2O vibrational modes from $1648\,cm^{-1}$ to $1642\,cm^{-1}$ (bending mode) induced by the adsorption of methyl iodide on the ASW surface.

Our results show the significance of the adsorption geometry sampling, wherein different geometries do not induce the same vibrational dOH shift. Associating them with their probability to occur and averaging their IR spectra allow us to reproduce IR band broadening, making possible comparisons with experiments possible. The IR band broadening is large, implying a low signal to noise ratio. In addition, several different molecules induce an equivalent red shift of the dOH vibrational frequencies upon adsorption. As a consequence, it might be challenging to identify molecules in interstellar medium based only on these dOH red shifts.

To improve our simulations, we can increase the number of adsorption geometries computed using the ONIOM method. This will increase the number of measured dOH vibrational frequencies and increase the accuracy of the calculated average weigthed IR spectra. In addition, the use of a polarizable and improved force field should improve the description of the CH_3I/ASW interaction and allow the simulation of CH_3I dimers or clusters adsorbed on the ASW surface by classical MD calculations.

Gas phase reaction of methyl iodide with hydroxyl radical without and with water: a theoretical investigation

Outline of the current chapter

The important role of methyl iodide (CH_3I) in the atmosphere was highlighted in the manuscript's introduction. The reactivity of CH_3I with OH has already been studied several times, both theoretically [83, 359] and experimentally [360–362]. Indeed, complete and accurate thermokinetic databases are required to perform global geophysical simulations properly [363, 364].

Recent studies [103, 108–110, 365, 366] show that a single water molecule may have important consequences on the gas phase chemistry. Indeed, H_2O is known to form stable molecular complexes (MCs) with polar molecules and radical
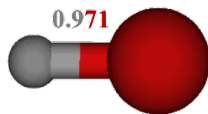
Figure 6.1: Schematic representation of OH optimized at the M06-2X/6-311+G(2df,2p) level of theory. The distance is expressed Angströms.

compounds. Picked as a catalyst for gas phase reactions, water molecules can modify the energetic barrier as well as the kinetic of chemical reactions through their intermolecular hydrogen bonds. This effect is likely to increase with the number of H$_2$O molecules inserted as catalysts until the formation of the first solvation shell.

In this chapter, we want to see the effect of adding one water molecule to the well-known CH$_3$I + OH reaction by measuring the energetic barrier differences and observing the modifications of MCs and transition states (TSs) structures. The two explored pathways are the following:

$$OH + CH_3I + H_2O \longrightarrow CH_2I + 2\,H_2O \qquad\qquad (R30)$$

$$OH + CH_3I + H_2O \longrightarrow HOI + CH_3I + H_2O \qquad\qquad (R31)$$
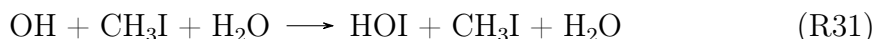
where the first reaction corresponds to the hydrogen abstraction (H$_{abs}$) and the second one to the iodine abstraction (I$_{abs}$) from CH$_3$I. Energetic profiles and all geometry optimizations are calculated at the M06-2X/6-311+G(2df,2p) level of theory using the GAUSSIAN 16 packages [244].

6.1 Structures of reactants and products

6.1.1 Structure of OH

We have represented the optimized geometry structure of the hydroxyl radical in Fig. 6.1. The calculated distance between O and H (0.971 Å) is in excellent agreement with the experimental one (0.970 Å) [367].

6.1.2 Structure of CH$_3$I

Similarly, we have optimized the methyl iodide molecule at the same level of theory. A visual representation of the optimized molecule can be found in Fig. 6.2. Table 6.1 presents the experimental and calculated geometric parameters at the same level
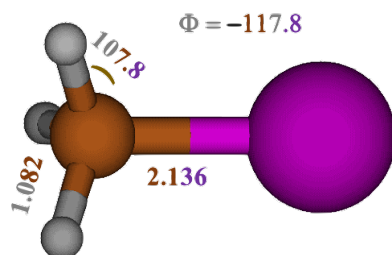
Figure 6.2: Schematic representation of the CH$_3$I optimized geometry at the M06-2X/6-311+G(2df,2p) level of theory. The distances are in Angströms; angles and dihedral angles are in degrees.

Table 6.1: Geometric parameters of CH$_3$I optimized at the M06-2X/6-311+G(2df,2p) level of theory in comparison with literature.

r C−I, Å	r H−C, Å	∠ ICH, °	∠ HCH, °	References
2.136	1.082	107.8	111.1	This work
2.136	1.084	107.5	111.4	Kuchitsu [368]

of theory. Experimental data [368] were obtained by Raman spectroscopy. Again, the calculated values are in excellent agreement with the experimental ones.

6.1.3   Structure of CH$_2$I

Then, we optimized one possible product, the CH$_2$I radical. A schematic representation of the latter is shown in Fig. 6.3. Table 6.2 compares the computed geometric parameters at the M06-2X/6-311+G(2df,2p) level of theory (this work) with ones at other levels of theories in the literature. Indeed, we have not found any experimental measurements of CH$_2$I in the literature. The calculated values are in excellent agreement with other theoretical studies.
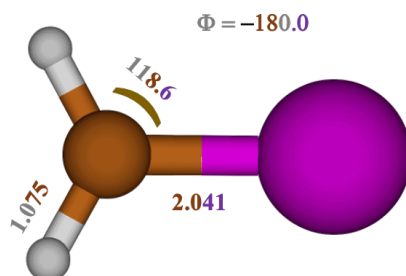
Figure 6.3: Schematic representation of the CH_2I optimized geometry at the M06-2X/6-311+G(2df,2p) level of theory. The distances are in Angströms; angles and dihedral angles are in degrees.

Table 6.2: Geometric parameters of CH_2I optimized at the M06-2X/6-311+G(2df,2p) level of theory in comparison with literature. The distance is in Angström; the angle is in degrees.

r C−I, Å	r H−C, Å	∡ ICH, °	∡ HCH, °	References
2.041	1.075	118.6	122.9	This work
2.030	1.074	118.2	–	Louis et al. [83][a]

[a] MP2/cc-pVTZ

Table 6.3:   Geometric parameters of H_2O optimized at the M06-2X/6-311+G(2df,2p) level of theory in comparison with literature.

r O−H, Å	∡ HOH, °	References
0.958	105.2	This work
0.958	104.5	Hoy et al. [369]
0.959	103.5	Louis et al. [83][a]

[a] MP2/cc-pVTZ

6.1.4   Structure of H_2O

Similarly, we have optimized the water molecule at the same level of theory. A visual representation of the optimized molecule can be found in Fig. 6.4. Table 6.3 shows the comparison between the computed geometry from our work and with ones found in the literature. Our computed values are in excellent agreement with the literature for the bond length, whereas the bond angle slightly differs according to different studies.
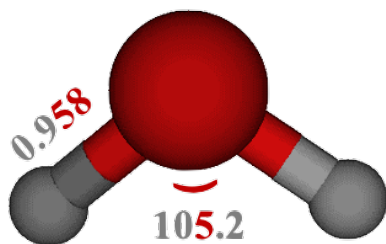
Figure 6.4: Schematic representation of the H_2O optimized geometry at the M06-2X/6-311+G(2df,2p) level of theory. The distance is in Angström; the angle is in degrees.

Table 6.4: Geometric parameters of CH$_3$ radical optimized at the M06-2X/6-311+G(2df,2p) level of theory in comparison with experimental parameters found in the literature.

r C−H, Å	$\measuredangle$ HCH, °	References
1.076	120.0	This work
1.079	120.0	Chase Jr et al. [370] (1998)
1.079	120.0	Herzberg [371] (1966)

6.1.5 Structure of CH$_3$

Then, we optimized one possible product, the CH$_3$ radical. A schematic representation of the latter is shown in Fig. 6.5. The radical is totally planar, i.e., has a dihedral angle Φ(HCHH) equal to 180.0°. Table 6.4 compares geometric parameters from calculations at the minimum energy geometry and experimental values. They are in good agreement with the resulting computed ones.
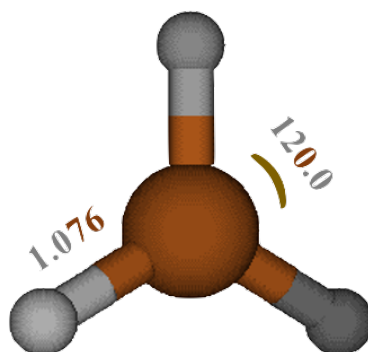
Figure 6.5: Schematic representation of the CH$_3$ radical optimized geometry at the M06-2X/6-311+G(2df,2p) level of theory. The distance is in Angström; the angle is in degrees.

Table 6.5: Geometric parameters of HOI molecule optimized at the M06-2X/6-311+G(2df,2p) level of theory in comparison with experimental parameters found in the literature.

| r O−H, Å	r O−I, Å	∡ HOI, °	References
0.962	1.979	106.7	This work
0.967	1.994	103.9	Ozeki et al. [372] (2004)

6.1.6 Structure of HOI

We have represented the optimized geometry structure of HOI in Fig. 6.6. Table 6.5 shows a comparison. The latter is in excellent agreement with the resulting computed ones. Experimental values were obtained by crossing FT-IR measurements with submillimeter-wave spectrometer ones [372]. Our values also agree very well with the experimental values.
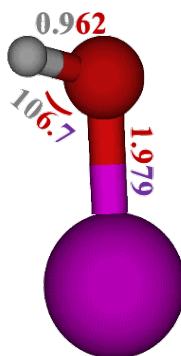
Figure 6.6: Schematic representation of the HOI radical optimized geometry at the M06-2X/6-311+G(2df,2p) level of theory. The distances are in Angströms; the angle is in degrees.

6.2 Study of the reactants and products vibrational frequencies

For each molecule and radical presented in the previous section, we have computed the harmonic molecular vibrational frequencies as defined in chapter 2, i.e., using the mass-weighted Hessian matrix. In addition, we introduce also a vibrational scaling factor. This factor is used to better match experimental vibrational frequencies. Indeed, *ab initio* and DFT computed frequencies are harmonic and slightly overestimate them.

Obtaining accurate vibrational frequencies are crucial. Indeed, as seen in chapter 2, they are used to compute the ZPE and, more globally, the vibrational contribution to the entropy and thermal internal energy. Because one objective of computational chemistry is to reach an accuracy of 1 kcal/mol, it is crucial to obtain an accurate result of the vibrational frequencies, the latter impacting the final enthalpy and Gibbs free energies. Nevertheless, the scaling factor depends on the method/DFT exchange-correlation functional and the basis set. More explanations can be found in the article written by Alecu et al. [373].

Table 6.6 presents the external symmetry number, electronic state, rotational constants, vibrational frequencies scaled by a factor 0.983, and scaled ZPE energies at the M06-2X/6-311+G(2df,2p) level of theory. Concerning the scaling factor, because it was not computed at our level of theory, we have approximated it to the one at the M06-2X/6-311++G(d,p) level of theory [373]. Our results are mostly in agreement with experimental frequencies, taking into account the confidence interval of harmonic vibrational frequency calculations at the M06-2X/6-311+G(2df,2p) level of theory.

Table 6.6: Reactants and products scaled vibrational frequencies, rotational constants, and ZPE energies for the reaction $CH_3I + OH + n(H_2O)$ computed at the M06-2X/6-311+G(2df,2p) level of theory. Comparisons with the literature are emphasized.

Specie	Symmetry number	Electronic state	Rotational constants (GHz)	Vibrational frequencies (cm^{-1})	ZPE ($kJ\,mol^{-1}$)
OH	1	$C_{\infty v} - {}^2\Pi$	565.46	3726 *3735*[a]	22.28
CH_3I	3	$C_{3v} - {}^1A_1$	157.34, 7.55	556, 895, 1271, 1454, 3069, 3176 *533, 882, 1252, 1437, 2933, 3060*[b]	95.38
CH_2I	2	$C_2 - {}^2B$	281.39, 8.88, 8.61	132, 629, 847, 1346, 3147, 3294 *375, 611, 1332, 3050*[c]	56.19
H_2O	2	$C_{2v} - {}^1A_1$	834.12, 432.38, 284.77	1602, 3822, 3925 *1595, 3651, 3756*[a]	55.92
CH_3	6	$D_{3h} - {}^2A_1$	288.56, 144.28	435, 1390, 3095, 3269 *606, 1396, 3004, 3161*[d]	76.85
HOI	1	$C_s - {}^1A'$	640.29, 8.45, 8.34	629, 1086, 3821 *575, 1068, 3625*[e]	33.11

[a] Chase Jr et al. [370] (1998)
[b] Kudchadker et al. [374] (1975)
[c] Baughcum et al. [375] (1980)
[d] Jacox [376] (1994)
[e] Klaassen et al. [377] (1996)

Table 6.7: Molar standard entropy at 298 K computed at the M06-2X/6-311+G(2df,2p) level of the reactants and products for the reaction CH$_3$I + OH + n(H$_2$O). Values from literature are emphasized.

Specie	S°_{298K} (J mol^{-1} K^{-1})	References
OH	183.52	This work
	183.74	Gurvich et al. [378] (1989)
CH$_3$I	253.52	This work
	254.53	Johnson [379] (2002)
CH$_2$I	269.98	This work
H$_2$O	188.65	This work
	188.83	Sugimura et al. [380] (2010), Robie et al. [381] (1978)
CH$_3$	195.59	This work
	195.29	Johnson [379] (2002)
HOI	254.50	This work

6.3   Reactants and products molar standard entropy at 298 K

The next step is to compute an important thermochemical property for each specie present in the reactions as reactants or products, namely the molar entropy at standard conditions ($P_0 = 10^5$ bar) at 298 K. All the calculations are done at the M06-2X/6-311+G(2df,2p) level of theory. Results are displayed and compared to experimental values, if possible, in Table 6.7. Calculated standard molar entropies are in excellent agreement with the ones found in the literature.
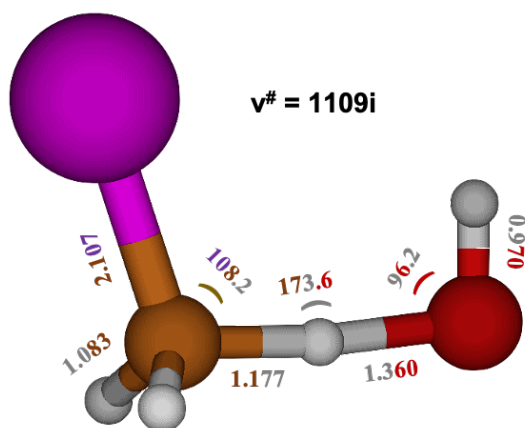
Figure 6.7: Schematic representation of TS_0 without additional H_2O molecule optimized at the M06-2X/6-311+G(2df,2p) level of theory. The distances are in Ångströms; the angles are in degrees; the imaginary vibrational frequency is given in cm^{-1}.

6.4 Hydrogen abstraction

6.4.1 Transition states

6.4.1.1 Without H_2O

H_{abs} channel for the reaction between CH_3I and the OH radical is characterized by the TS represented in Fig. 6.7. This reaction has already studied done by Louis et al. [83] at another level of theory (MP2/cc-pVTZ), and results can be compared.

The TS for the hydrogen abstraction channel without additional water molecule (TS_0) is characterized by the formation of a quasi-linear bond ($\theta = 173.6°$) between the hydrogen from CH_3I and the oxygen of the OH radical. Regarding these bond distances, the C−H bond from CH_3I is slightly increased according to its equilibrium value (from $1.075\,\text{Å}$ to $1.177\,\text{Å}$). On the opposite, the OH distance from this new bond ($1.360\,\text{Å}$) is much higher than in the H_2O molecule ($0.958\,\text{Å}$). The main change in the geometrical structure of the transition state can be characterized by the L parameter, defined as the ratio of the increase in the length of the bond being broken and the elongation of the bond being formed [382]. This parameter provides a reliable measure of the reactant- or product-like character of the concomitant transition state.

Within those characteristics, we define this transition state as reactant-like, i.e.; it has more common properties from reactants (CH_3I) than products (H_2O). The

imaginary TS vibrational frequency $v^{\#}$ is equal to 1109i cm^{-1}. Louis et al. [83] have also observed the same behavior at their level of theory, with a smaller OH bond distance (1.305 Å), bond angle (172.4°), and a much higher imaginary vibrational frequency (2003i cm^{-1}). Then, we are in agreement with their results.

6.4.1.2   With a single additional H_2O molecule

The influence of a single water molecule on the channel H_{abs} of the reaction CH_3I + OH + H_2O ⟶ CH_2I + 2 H_2O has been investigated by scanning the potential energy surface (PES) of the previous transition state with a supplementary water molecule. Four transition states have been found, namely TS_{1a}, TS_{1b}, TS_{1c}, and TS_{1d}. They are represented in Fig. 6.8. These four structures seem different with the position of the water molecule behind CH_3I (TS_{1a} and TS_{1c}) and below CH_3I (TS_{1b} and TS_{1d}).

In TS_{1a}, a hydrogen bond is formed between the hydrogen of the water molecule and the oxygen of the hydroxyl radical. The remaining transition state (TS_{1c}) induces more modifications to TS_0 than the three others. We observe that the hydroxyl radical creates a hydrogen bond with the oxygen of the additional water molecule, the latter generating another hydrogen bond with the iodine atom. We expect that these additional interactions between the species lower the resulting potential energy of TS_{1c} compared to the others.

The imaginary vibrational frequencies are modified, with a lower value for TS_{1a} (899i cm^{-1}) and TS_{1d} (1044i cm^{-1}) compared to the one from TS_0 (1109i cm^{-1}). On the opposite, the value concerning TS_{1b} (1122i cm^{-1}) and TS_{1c} (1393i cm^{-1}) are higher in energies within the same reference. We highlight that the highest value comes from TS_{1c}, which can be a consequence of its intermolecular interaction rearrangements.

Table 6.8 presents the L parameter values for all the TSs. The L parameter for TS_{1a} is lower in these complexes (L = 0.163) compared to the one found without an additional water molecule. It shows a more pronounced reactant-like character in this case. For others TSs, the L parameter is higher than the one for TS_0. In this case, the reactant-like character of the reaction is less pronounced.

6.4.2   Molecular complexes

Isolated reactants and products are linked to transition states via molecular complexes. Respectively, we name them molecular complex reactants (MCR) and molecular complex products (MCP). They are found by following the mass-weighted Hessian matrix displacement induced by the single imaginary vibrational frequency until finding a minimum energy MC. This pathway is called reaction coordinates
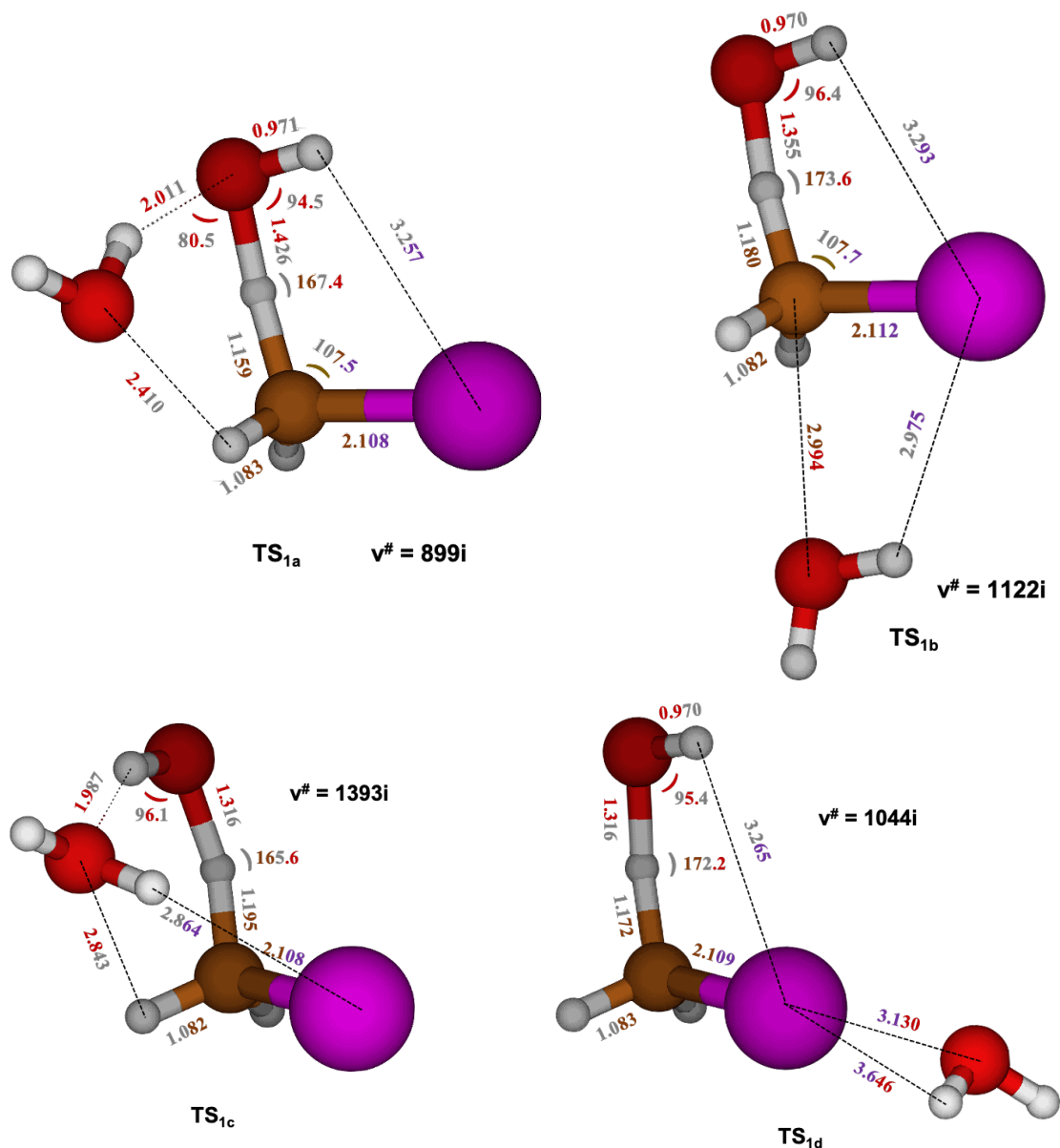
Figure 6.8: Schematic representation of TS_{1a} (top-left), TS_{1b} (top-right), TS_{1c} (bottom-left) and TS_{1d} (bottom-right) within a single additional H_2O molecule optimized at the M06-2X/6-311+G(2df,2p) level of theory. The distances are in Angströms; the angles are in degrees; the imaginary vibrational frequency is in cm^{-1}.

(RC), and the method is called intrinsic reaction coordinates (IRC) [383, 384]. Usually, each different TS leads to different MCs using the IRC method.

Table 6.8: L-parameter values for the different transition states for the hydrogen abstraction.

	TS$_0$	TS$_{1a}$	TS$_{1b}$	TS$_{1c}$	TS$_{1d}$
r (C$\cdots$H), Å	1.177	1.159	1.180	1.195	1.172
r (O$\cdots$H), Å	1.360	1.426	1.355	1.316	1.316
L	0.236	0.165	0.247	0.316	0.251
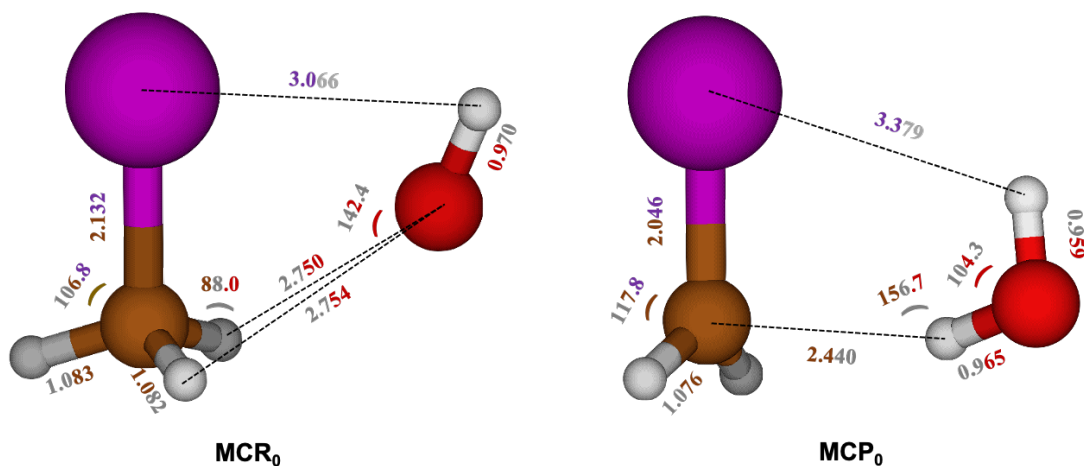
Figure 6.9: Schematic representation of MCR$_0$ (left) and MCP$_0$ (right) without any additional H$_2$O molecule optimized at the M06-2X/6-311+G(2df,2p) level of theory. The distances are in Angströms; the angles are in degrees.

In this section, we will discuss the differences between MCs for the reaction CH$_3$I + OH + H$_2$O $\longrightarrow$ CH$_2$I + 2 H$_2$O.

6.4.2.1   Without H$_2$O

The MCs resulting from TS$_0$ using the IRC method are shown in Fig. 6.9. They are respectively written as MCR$_0$ and MCP$_0$. As already observed by Louis et al. [83], the resulting molecular complexes are similar to TS$_0$. Nevertheless, there are notable differences. First, the linearity between atoms C, H, and O present in TS$_0$ is not present in MCR$_0$, with a corresponding angle of 88.0°. Then, the new OH bond formed during the reaction has a higher distance in MCR$_0$ (2.754 Å) than in TS$_0$ (1.360 Å). Regarding MCP$_0$, the previously discussed linearity between atoms C, H, and O is less perturbed, with a corresponding angle of 156.7° for MCP$_0$.
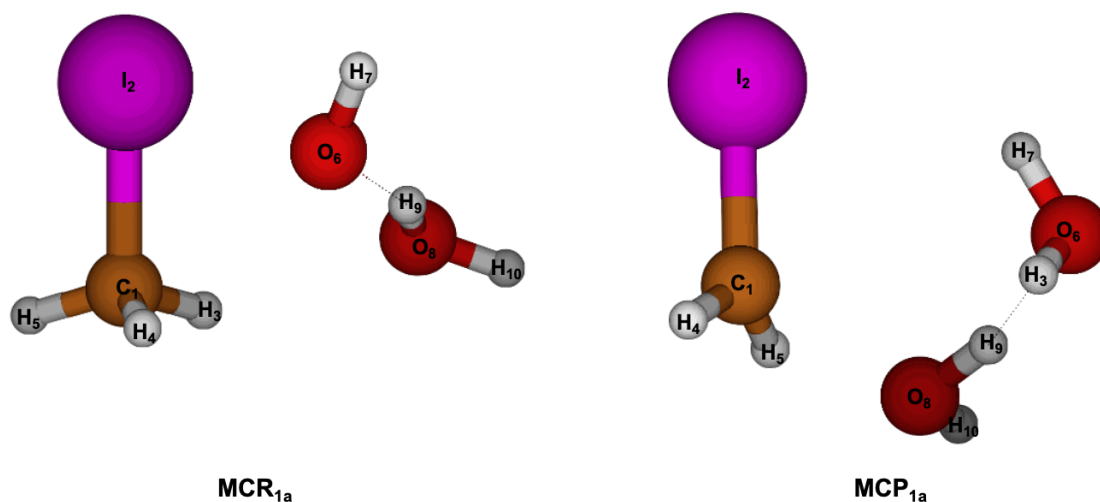
Figure 6.10: Schematic representation of MCR_{1a} (left) and MCP_{1a} (right) with an additional H_2O molecule optimized at the M06-2X/6-311+G(2df,2p) level of theory.

6.4.2.2   With a single additional H_2O molecule

This section will be divided into several parts, each one treating MCs from the four different TSs. First, the MCs resulting from TS_{1a} are respectively written as MCR_{1a} and MCP_{1a}. The same logic will be applied for write all other MCs. The two previously introduced MCs are shown in Fig. 6.10, where the geometric parameters are shown in Table 6.9.

As for MCR_0 and MCP_0, we can observe that both resulting MCs are similar to the corresponding TS. Nevertheless, we can see that the hydroxyl radical is closer to the abstracted H from CH_3I, with an O−H distance of 2.615 Å for MCR_{1a}, compared to 2.714 Å for MCR_0. Regarding the C−H distance with the hydrogen that will be abstracted, it is similar within and without additional H_2O molecules.

The MCPs present also small differences within and without an additional water molecule. We can see that the C−H distance with the hydrogen that has been abstracted is higher in MCP_{1a} (2.985 Å) than in MCP_0 (2.440 Å). The forming water molecule position is slightly modified, with an OHC angle going from 157.7° for MCP_0 to 105.8° for MCP_{1a}. The two H_2O molecules present strong similarities with the well-known $(H_2O)_2$ cluster [385–388], which the optimized geometry at the M06-2X/6-311+G(2df,2p) level of theory is shown in Fig. 6.11.

Comparing the $(H_2O)_2$ cluster with the two water molecules in MCP_{1a}, we see that the O−H bond distance (1.914 Å) is higher in MCP_{1a} than in the cluster (1.628 Å). In addition, the value of the angle formed by HOH is close for each

Table 6.9: Optimized geometric parameters of MCR_{1a} and MCP_{1a} calculated at the M06-2X/6-311+G(2df,2p) level of theory

Geometric parameters (Å, °)	MCR_{1a}	MCP_{1a}
r ($C_1 \cdots I_2$)	2.120	2.053
r ($C_1 \cdots H_4$)	1.083	1.076
r ($C_1 \cdots H_5$)	1.083	1.078
r ($I_2 \cdots H_7$)	2.388	2.926
r ($H_4 \cdots O_6$)	2.615	–
r ($H_5 \cdots O_6$)	–	2.192
r ($H_3 \cdots O_6$)	2.894	0.961
r ($H_3 \cdots O_8$)	2.283	–
r ($O_6 \cdots H_7$)	0.965	0.962
r ($O_6 \cdots H_9$)	1.830	1.914
r ($O_8 \cdots H_5$)	–	2.192
r ($H_9 \cdots O_3$)	–	2.312
θ ($I_2C_1H_5$)	107.6	117.1
θ ($I_2C_1H_3$)	106.0	89.7
θ ($H_7O_6H_3$)	151.9	104.5
θ ($H_4O_6H_9$)	88.4	–
θ ($O_6H_3C_1$)	–	105.8

configuration, with a corresponding angle of 101.9° for MCP_{1a} and 104.7° for the $(H_2O)_2$ cluster.

The next MCs are computed from TS_{1b}, and are written as MCR_{1b} and MCP_{1b}, respectively, for reactants and products. They are displayed in Fig. 6.12, where the geometric parameters are shown in Table 6.10.

Both MCR_{1b} and MCP_{1b} are similar to their corresponding TS. In addition, both MCs_{1b} show similarities with MCs_0. Indeed, in MCR_{1b}, the OH bond formed
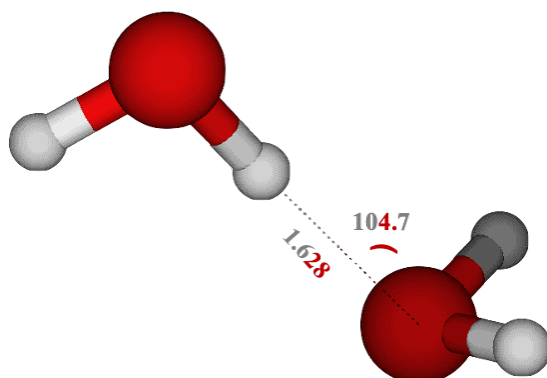
Figure 6.11: Schematic representation of the $(H_2O)_2$ cluster optimized geometry at the M06-2X/6-311+G(2df,2p) level of theory. The distance is in Angström; the angle is in degrees.
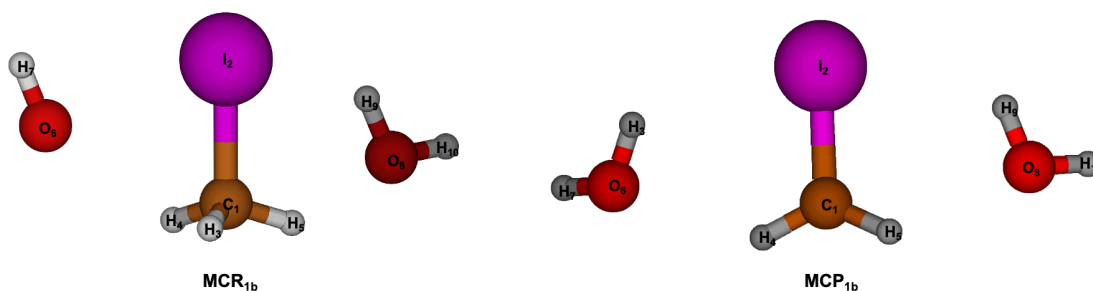
Figure 6.12: Schematic representation of MCR_{1b} (left) and MCP_{1b} (right) with an additional H_2O molecule optimized at the M06-2X/6-311+G(2df,2p) level of theory. The distances are in Angströms; the angles are in degrees

during the reaction has a higher interatomic distance in MCR_0 (2.750 Å) compared to MCR_{1b} (2.682 Å). However, the second stabilizing O−H interatomic distance is lower in MCR_0 (2.754 Å) than in MCR_{1b} (2.910 Å). Then, the stability of the latter complex is increased by the presence of a hydrogen bond between the hydrogen of the additional water molecule and the iodine atom from methyl iodide. Regarding MCP_{1b}, we do not observe a structure similar to MCP_0. Indeed, the newly formed H_2O molecule is not in the same direction in each MCPs. However, the hydrogen bond between the newly formed H_2O molecule and iodine has a larger distance in MCP_0 (3.379 Å) than in MCP_{1b} (2.957 Å). The additional water molecule remains in the same position for MCR_{1b} and MCP_{1b}, with a difference for the hydrogen bond with iodine lower than 0.5 Å between both complexes. The L parameter is equivalent to the one found for MCs_0.

Table 6.10: Optimized geometric parameters of MCR_{1b} and MCP_{1b} calculated at the M06-2X/6-311+G(2df,2p) level of theory

Geometric parameters (Å)	MCR_{1b}	MCP_{1b}
r $(C_1 \cdots I_2)$	2.137	2.055
r $(C_1 \cdots H_4)$	1.081	1.076
r $(C_1 \cdots H_5)$	1.083	1.076
r $(I_2 \cdots H_7)$	3.084	–
r $(I_2 \cdots H_3)$	–	2.957
r $(H_4 \cdots O_6)$	2.682	2.379
r $(H_3 \cdots O_6)$	2.910	0.961
r $(H_9 \cdots I_2)$	2.889	2.957
r $(H_5 \cdots O_8)$	2.390	2.379
r $(O_6 \cdots H_7)$	0.970	0.958
r $(O_8 \cdots H_9)$	0.961	0.961
r $(O_8 \cdots H_{10})$	0.958	0.958

Then, we need to compute the MCs from TS_{1c}, namely MCR_{1c}, and MCP_{1c}. Their optimized geometries are shown in Fig. 6.13.

We have already discussed that TS_{1c} is different from other TSs because of its hydroxyl radical bond orientation. In MCR_{1c}, we also see a difference in the OH radical, with the bond pointing to the additional H_2O molecule. This distance between H from the radical and O from the water molecule is higher in TS_{1c} (1.987 Å) than in MCR_{1c} (1.886 Å). In addition, the distance between the oxygen from the radical and the H atom of methyl group is much lower in TS_{1c} (1.316 Å) than in MCR_{1c} (2.432 Å).

Regarding MCP_{1c}, we do not observe the $(H_2O)_2$ cluster-like formation as in MCP_{1a}. Here, the hydrogen bond is formed firstly by the radical and not the water molecule. The L parameter value is higher for these complexes (L = 0.314) compared to the one found in MCs_0.

Focusing now on MCs from TS_{1d}, namely MCR_{1d}, and MCP_{1d}. Both MCs optimized geometries are shown in Fig. 6.14. Both reactants (CH_3I and OH) in
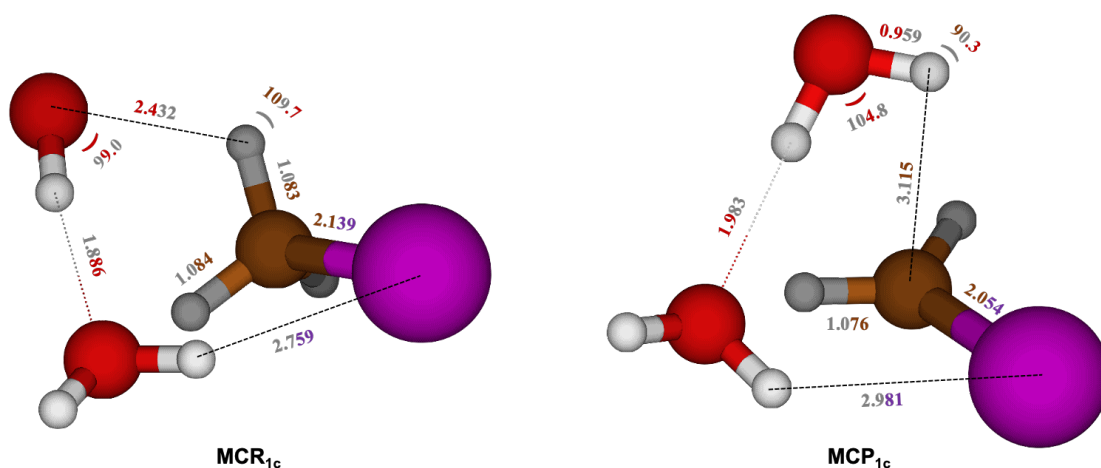
Figure 6.13: Schematic representation of MCR_{1c} (left) and MCP_{1c} (right) with an additional H_2O molecule optimized at the M06-2X/6-311+G(2df,2p) level of theory. The distances are in Angströms; the angles are in degrees.
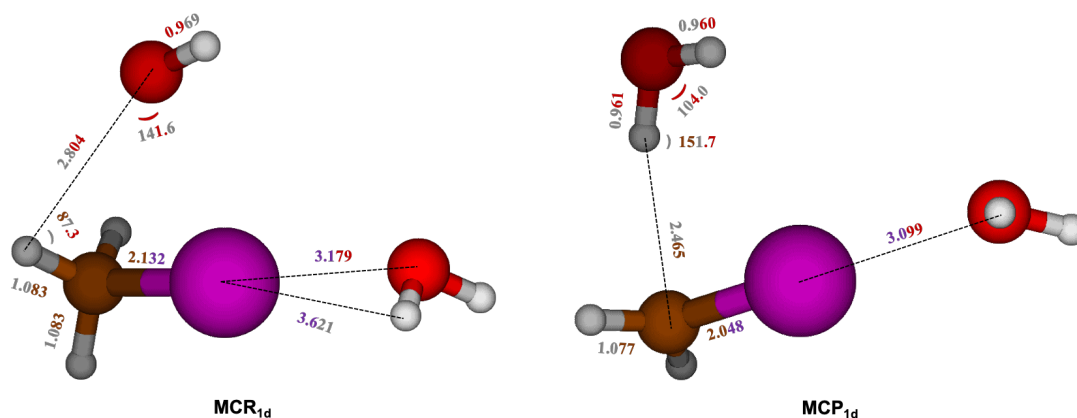
Figure 6.14: Schematic representation of MCR_{1d} (left) and MCP_{1d} (right) with an additional H_2O molecule optimized at the M06-2X/6-311+G(2df,2p) level of theory. The distances are in Angströms; the angles are in degrees.

MCR_{1d} have a structure similar to MCR_0. The distance and angle values are similar. The water molecule's role is only to interact with the iodine atom from CH_3I, and then stabilize it.

Observations on MCR_{1d} can be repeated for MCP_{1d}, when comparing it with MCP_0: both structures are similar if we take into account only the products and not the additional water molecule. From MCR_{1d} to MCP_{1d}, going through TS_{1d}, the water molecule remains at the same position with only a low variation of the

distance between itself and the CH_3I molecule during the reaction. Both halogen and hydrogen interactions are present in the aggregate structures.

All the information corresponding to the scaled vibrational frequencies, ZPE, and standard molar entropy at 298 K for the reaction without and within an additional water molecule are regrouped in Table 6.11.

Table 6.11: Rotational constants, scaled vibrational frequencies, zero-point energy (ZPE), and calculated molar stand entropy at 298 K of intermediates in the hydrogen abstraction pathway of the CH_3I + OH reaction at the M06-2X/6-311+G(2df,2p) level of theory.

Specie	Symmetry number	Electronic state	Rotational constants (GHz)	Vibrational frequencies (cm^{-1})	ZPE ($kJ\,mol^{-1}$)	$S^\circ_{298\,K}$ ($J\,mol^{-1}$)
MCR_0	1	$C_1 - {}^2A$	8.42, 3.90, 2.71	65, 95, 135, 175, 446, 556, 907, 908, 1272, 1441, 1449, 3072, 3183, 3185, 3746	123.42	347.10
TS_0	1	$C_s - {}^2A'$	17.06, 2.24, 2.01	**1109i**, 39, 91, 290, 572, 691, 889, 911, 1032, 1257, 1317, 1407, 3094, 3188, 3733	110.71	334.85
MCP_0	1	$C_1 - {}^2A$	10.86, 2.19, 1.85	43, 106, 117, 142, 170, 281, 436, 629, 855, 1348, 1605, 3135, 3279, 3799, 3896	118.65	371.23
MCR_{1a}	1	$C_1 - {}^2A$	4.84, 1.89, 1.71	55, 98, 122, 150, 192, 232, 237, 247, 423, 552, 678, 755, 914, 933, 1275, 1431, 1460, 1625, 3055, 3173, 3178, 3556, 3785, 3890	191.51	393.67
TS_{1a}	1	$C_1 - {}^2A$	5.49, 1.13, 1.03	**899i**, 21, 83, 112, 138, 177, 204, 294, 362, 525, 574, 686, 891, 969, 1139, 1302, 1365, 1439, 1608, 3093, 3190, 3714, 3742, 3897	176.59	403.36
MCP_{1a}	1	$C_1 - {}^2A$	4.60, 1.24, 1.10	29, 36, 66, 100, 151, 157, 196, 213, 218, 288, 414, 489, 623, 655, 874, 1342, 1607, 1611, 3119, 3276, 3687, 3782, 3871, 3894	183.62	442.20
MCR_{1b}	1	$C_1 - {}^2A$	4.75, 1.60, 1.27	9, 55, 86, 99, 104, 110, 125, 154, 190, 228, 433, 547, 912, 929, 1275, 1443, 1450, 1594, 3071, 3186, 3190, 3741, 3791, 3902	183.18	456.12
TS_{1b}	1	$C_1 - {}^2A$	2.79, 1.82, 0.983	**1122i**, 24, 60, 71, 92, 97, 126, 159, 227, 305, 560, 692, 896, 897, 1040, 1247, 1321, 1398, 1592, 3105, 3199, 3731, 3798, 3904	170.73	432.34
MCP_{1b}	1	$C_1 - {}^2A$	4.25, 1.36, 1.04	28, 54, 78, 89, 102, 119, 142, 160, 171, 236, 266, 276, 329, 619, 894, 1323, 1599, 1600, 3128, 3292, 3798, 3799, 3906, 3907	178.92	462.93
MCR_{1c}	1	$C_1 - {}^2A$	4.43, 1.37, 1.16	27, 79, 119, 139, 156, 192, 209, 251, 290, 501, 550, 601, 905, 909, 1273, 1450, 1465, 1586, 3063, 3169, 3176, 3569, 3755, 3889	187.35	413.97
TS_{1c}	1	$C_1 - {}^2A$	4.52, 1.49, 1.24	**1393i**, 67, 89, 106, 171, 188, 242, 260, 348, 512, 570, 705, 857, 935, 992, 1227, 1383, 1430, 1592, 3096, 3193, 3645, 3774, 3892	175.10	390.55
MCP_{1c}	1	$C_1 - {}^2A$	4.11, 1.41, 1.27	48, 69, 80, 114, 141, 148, 177, 181, 202, 237, 375, 391, 541, 622, 867, 1336, 1587, 1627, 3140, 3292, 3743, 3791, 3883, 3897	182.37	437.25
MCR_{1d}	1	$C_1 - {}^2A$	4.65, 1.79, 1.31	14, 28, 62, 84, 96, 107, 122, 125, 157, 176, 485, 560, 901, 901, 1269, 1443, 1451, 1598, 3067, 3175, 3177, 3749, 3814, 3917	182.30	466.71
TS_{1d}	1	$C_1 - {}^2A$	8.49, 1.21, 1.07	**1044i**, 33, 43, 65, 94, 110, 124, 133, 188, 289, 570, 687, 882, 939, 1064, 1263, 1312, 1409, 1598, 3091, 3181, 3727, 3814, 3917	170.66	170.66
MCP_{1d}	1	$C_1 - {}^2A$	4.09, 1.42, 1.07	28, 33, 47, 68, 99, 109, 117, 139, 153, 157, 186, 278, 407, 624, 848, 1350, 1598, 1608, 3130, 3270, 3796, 3814, 3889, 3918	177.44	482.25
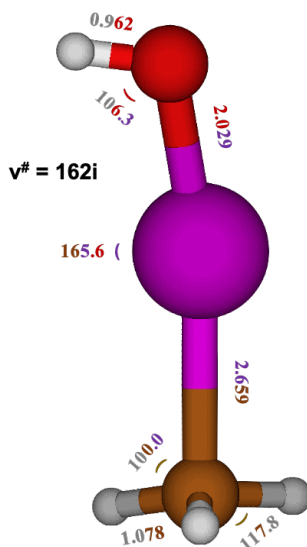
Figure 6.15: Schematic representation of TS$_{I0}$ without additional H$_2$O molecule optimized at the M06-2X/6-311+G(2df,2p) level of theory. The distances are in Angstroms; the angles are in degrees; the imaginary vibrational frequency is in cm^{-1}.

6.5   Iodine abstraction catalyzed by H$_2$O molecule

6.5.1   Transition states

6.5.1.1   Without H$_2$O

I$_{abs}$ channel for the reaction between CH$_3$I and the OH radical is characterized by the transition state represented in Fig. 6.15. As for H$_{abs}$, this reaction has already been studied by Louis et al. [83] at another level of theory (MP2/cc-pVTZ), and results can be compared.

The transition state, written TS$_{I0}$, is characterized by a nearly-linear CIO bond (165.6°), which is higher than the one computed by Louis et al. [83] (159.3°). Regarding the breaking bond C−I length, we computed a value of 2.659 Å, in agreement with the literature (2.538 Å) [83]. Then, looking at the forming O−I bond, we have calculated a length of 2.029 Å, also in agreement with previous calculations (1.989 Å) [83]. For TS$_{I0}$, we observe that our level of theory predicts a "late" transition state, i.e., with a structure that is closer to the product (CH$_3$ + HOI) than the reactants (CH$_3$I + OH). Indeed, the equilibrium distance for the O−I bond in HOI is 1.979 Å, and the one for the C−I bond in CH$_3$I is 2.136 Å. The imaginary

Table 6.12: L-parameter values for the different transition states for the iodine abstraction.

	TS$_{I0}$	TS$_{I1a}$	TS$_{I1b}$	TS$_{I1c}$
r (C$\cdots$H), Å	2.659	2.624	2.624	2.637
r (O$\cdots$H), Å	2.029	2.020	2.020	2.022
L	1.472	1.452	1.452	1.461

vibrational frequency is much lower than is TS$_0$, with a value of 162i cm^{-1} for TS$_{I0}$ and 1109i cm^{-1} for the former. This observation is also in agreement with the one done obtained Louis et al. [83], where they found an imaginary frequency of 232i cm^{-1} for their transition state.

6.5.1.2   With a single additional H$_2$O molecule

The influence of a single water molecule on the channel I$_{abs}$ of the reaction CH$_3$I + OH + H$_2$O $\longrightarrow$ CH$_3$ + HOI + H$_2$O has been investigated by scanning the PES of the previous transition state with a supplementary water molecule. This methodology has led to three different transition states, namely TS$_{I1a}$, TS$_{I1b}$, and TS$_{I1c}$. They are represented in Fig. 6.16.

All the transition states are found to be similar to TS$_{I0}$. The additional water molecule is at the same position, creating a hydrogen bond with the hydroxyl radical. Only the orientation of the former is changed. We have two transition states with hydrogen from the water molecule interacting with the iodine atom (TS$_{I1a}$ and TS$_{I1b}$). For symmetry reasons, we have two different structures. The last transition state (TS$_{I1c}$) presents a water molecule with two hydrogen atoms pointing in the opposite direction from the reaction. In this case, the water molecule interacts only with the hydroxyl radical.

The imaginary vibrational frequencies are higher when we have an additional water molecule. Indeed, we have a value of 162i cm^{-1} for TS$_{I0}$, and values of 239i, 235i, and 217i cm^{-1} respectively for TS$_{I1a}$, TS$_{I1b}$, and TS$_{I1c}$. We also highlight that the imaginary vibrational frequencies for TSs with an additional water molecule are similar.

Table 6.12 presents the L parameter values for this reaction. The latter is almost constant for all the TSs. With a value higher than 1, it characterizes a product-like reaction.
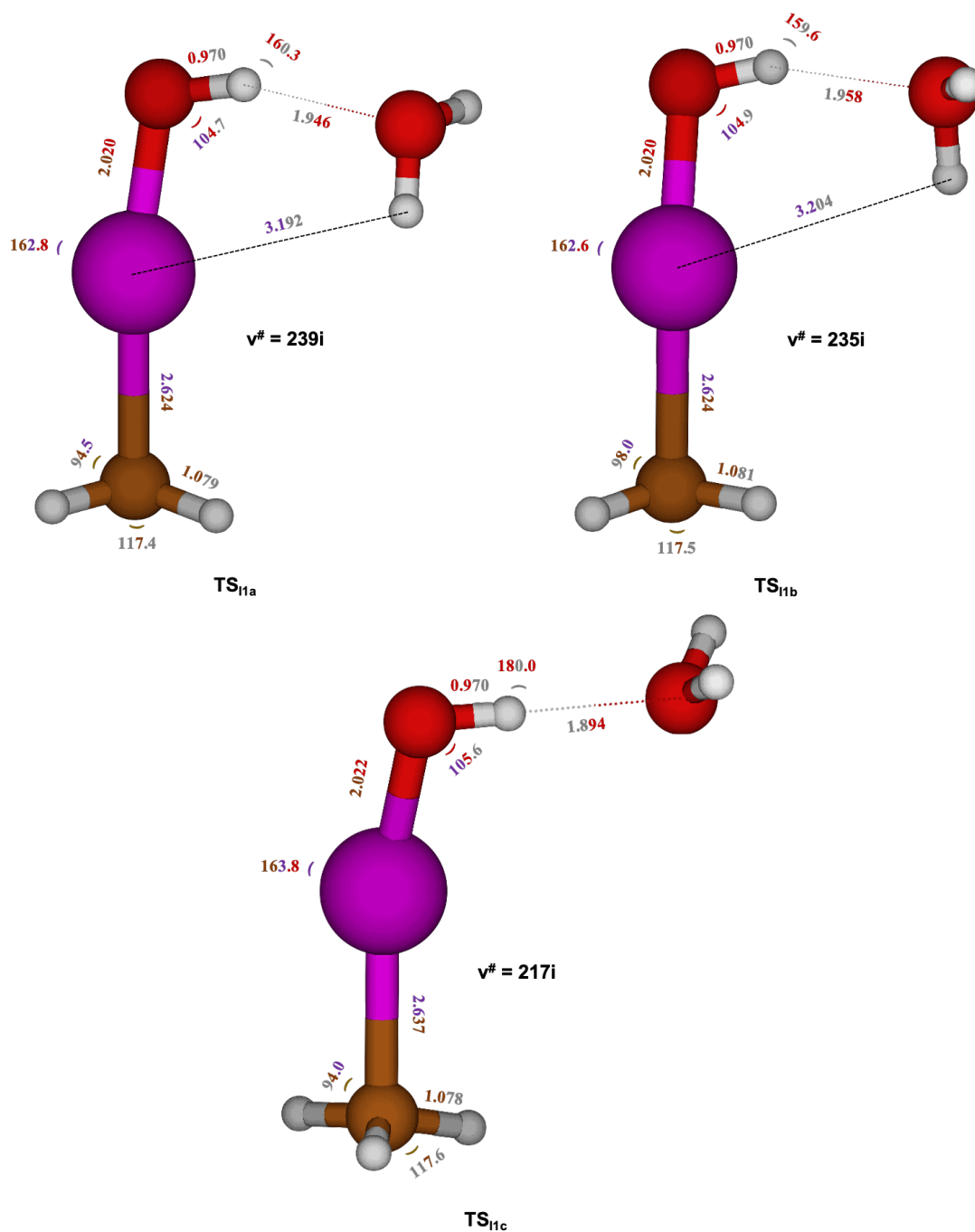
Figure 6.16: Schematic representation of TS$_{I1a}$ (top-left), TS$_{I1b}$ (top-right), and TS$_{I1c}$ (bottom) within a single additional H$_2$O molecule optimized at the M06-2X/6-311+G(2df,2p) level of theory. The distances are in Angströms; the angles are in degrees; the imaginary vibrational frequency is in cm^{-1}.
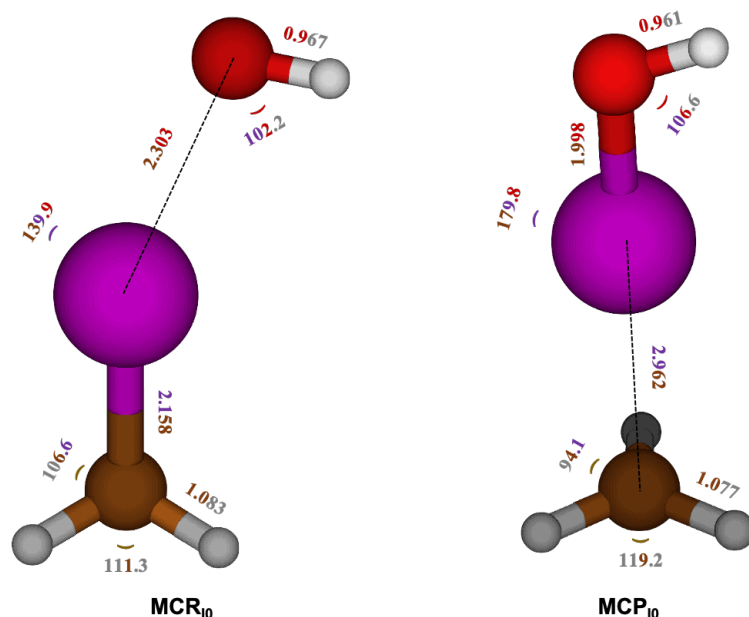
Figure 6.17: Schematic representation of MCR$_{I0}$ (left) and MCP$_{I0}$ (right) without any additional H$_2$O molecule optimized at the M06-2X/6-311+G(2df,2p) level of theory. The distances are in Angströms; the angles are in degrees.

6.5.2 Molecular complexes

6.5.2.1 Without H$_2$O

The MCs resulting from TS$_{I0}$ using the IRC method are shown in Fig. 6.17. They are respectively written as MCR$_{I0}$ and MCP$_{I0}$.

Both MCs have structures that are close to the corresponding TS. This was expected regarding the low value of the imaginary vibrational frequency from TS$_{I0}$. In MCR$_{I0}$, we observe that the linearity between the atoms O, I, and C is less pronounced, with a corresponding angle of 139.9°. Nonetheless, this linearity is totally present in MCP$_{I0}$, with a calculated angle of 179.8°. The forming O$-$I bond has a larger distance in MCR$_{I0}$ (2.303 Å) than in TS$_{I0}$ (2.029 Å). In MCP$_{I0}$, the latter is even lower, with a value of 1.998 Å, which is close to the one present in the HOI equilibrium geometry (1.979 Å). The resulting CH$_3$ radical in MCP$_{I0}$ has a structure close to the equilibrium one, with C$-$H bond distances of 1.077 Å (1.076 Å at the equilibrium). Only the HCH angles are slightly lower in MCP$_{I0}$ (111.3°) than at the equilibrium (120.0°). Indeed, in MCP$_{I0}$, the radical is not perfectly planar. This deformation induces a lower value for the HCH angles.

Figure 6.18: Schematic representation of MCR$_{I1a}$ (left) and MCP$_{I1a}$ (right) with an additional H$_2$O molecule optimized at the M06-2X/6-311+G(2df,2p) level of theory. The distances are in Ångströms; the angles are in degrees.

6.5.2.2   With a single additional H$_2$O molecule

As previously discussed, the presence of three different TSs implies three possible different MCRs and MCPs. Starting with MCs from TS$_{I1a}$, the corresponding MCs (namely MCR$_{I1a}$ and MCP$_{I1a}$) are presented in Fig. 6.18.

As for the reaction without an additional water molecule, the MCs have a similar structure as the corresponding transition state and other MCs without the additional water molecule. However, we note an elongation of the I−O forming bond in MCR$_{I1a}$ (3.130 Å) compared to MCR$_{I0}$ (2.303 Å). Due to the water molecule, the IOH angle is slightly modified, with a value of 89.2° for MCR$_{I1a}$ and 102.2° for MCR$_{I0}$. In addition, the linearity discussed for the transition state is more pronounced in MCR$_{I1a}$ compared to MCR$_{I0}$, with values for the CIO angle that are, respectively, 164.3° and 139.9°. We also highlight that the water forms a hydrogen bond with the oxygen of the hydroxyl radical and HOI, respectively, for the MCR$_{I1a}$ and MCP$_{I1a}$.

Then, we continue the analysis of the different MCs with the ones from TS$_{I1b}$, namely MCR$_{I1b}$ and MCP$_{I1b}$. They are represented in Fig. 6.19.
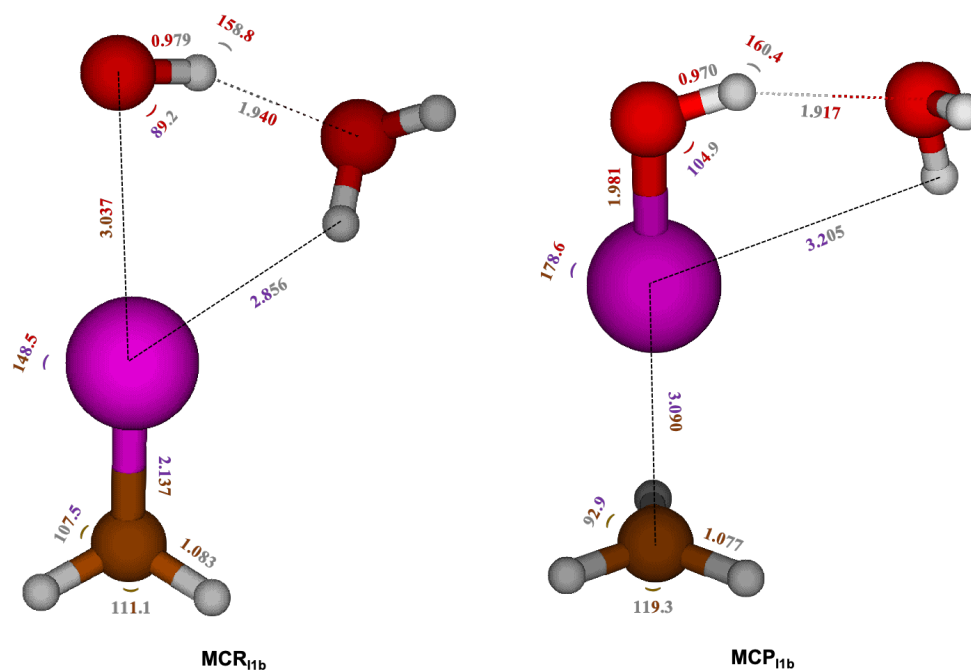
Figure 6.19: Schematic representation of MCR$_{I1b}$ (left) and MCP$_{I1b}$ (right) with an additional H$_2$O molecule optimized at the M06-2X/6-311+G(2df,2p) level of theory. The distances are in Angströms; the angles are in degrees.

For both MCs presented previously, we note the same observations as for MCR$_{I1a}$ and MCP$_{I1a}$. Indeed, the only difference remains in the orientation of the water molecule.

The last remaining MCs are the ones coming from TS$_{I1c}$, which are labelled MCR$_{I1c}$ and MCP$_{I1c}$. They are represented in Fig. 6.20. In this case, we observe that MCR$_{I1c}$ has a totally different structure from other MCRs. Indeed, with reference to the C−I bond, taken as the vertical direction, the hydroxyl radical and the additional water molecule are located next to the CH$_3$I in MCR$_{I1c}$, whereas they are located on the top of CH$_3$I in other MCRs. The linearity between atoms C, I, and O discussed before is non-existent in this MCR, with a corresponding CIO angle of 68.0°. Nevertheless, the distance between the oxygen of the hydroxyl radical and the iodine atom remains the same, with a calculated distance of 3.127 Å in MCR$_{I1c}$. Regarding MCP$_{I1c}$, it remains close to the other MCPs, with the water molecule hydrogens pointing in the opposite direction from the CH$_3$ radical.

All the information corresponding to the vibrational frequencies, ZPE, and standard molar entropy at 298 K are gathered in Table 6.13.
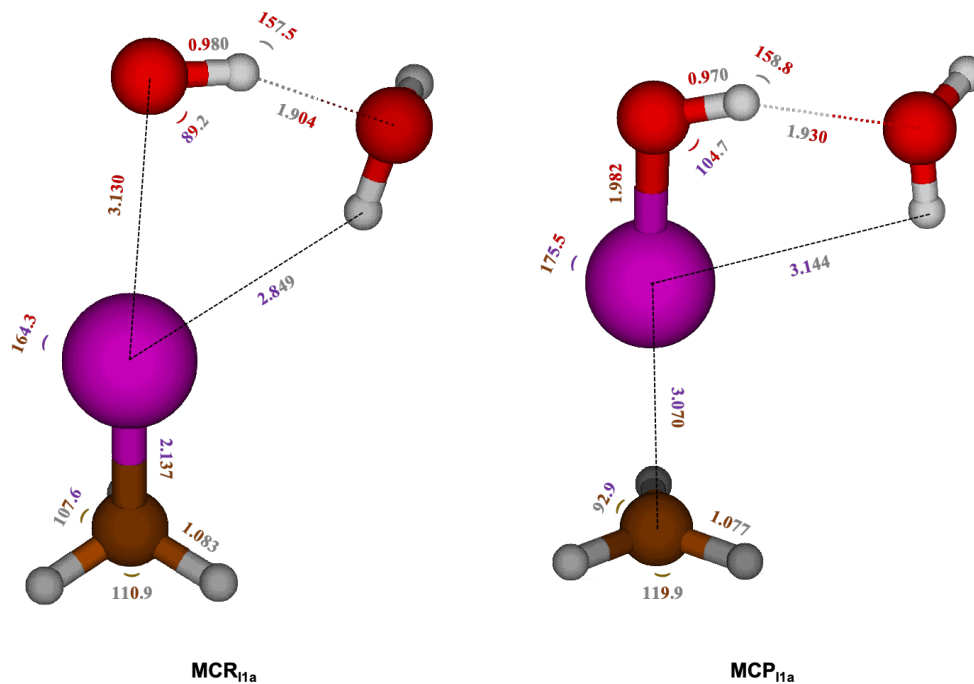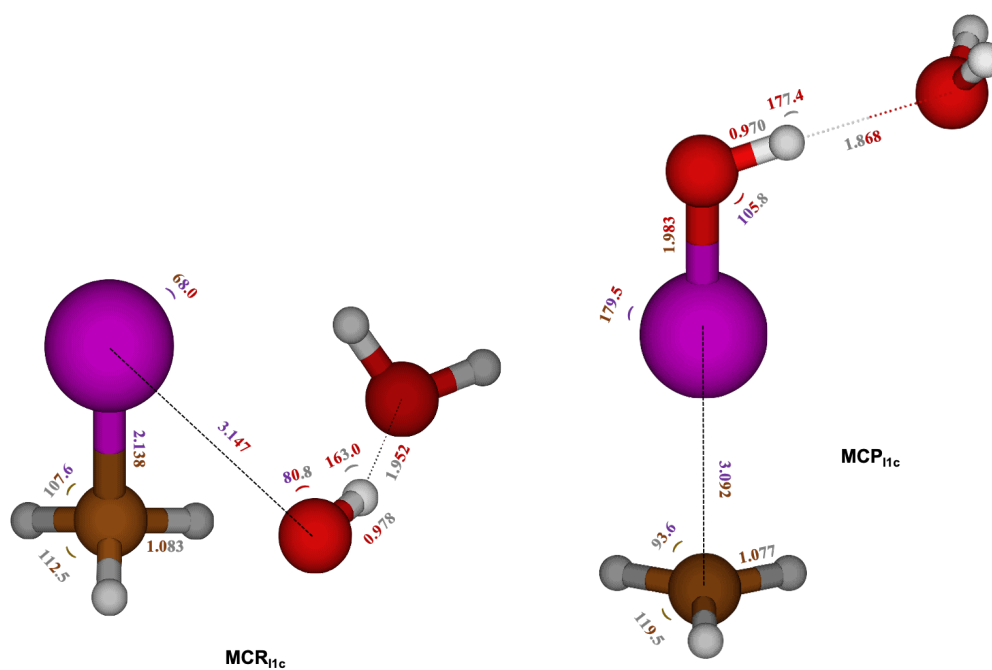
Figure 6.20: Schematic representation of MCR$_{I1c}$ (left) and MCP$_{I1c}$ (right) with an additional H$_2$O molecule optimized at the M06-2X/6-311+G(2df,2p) level of theory. The distances are in Angströms; the angles are in degrees.

Table 6.13: Rotational constants, scaled vibrational frequencies, zero-point energy (ZPE), and calculated molar stand entropy at $298\,K$ of intermediates in the iodine abstraction pathway of the $CH_3I + OH$ reaction at the M06-2X/6-311+G(2df,2p) level of theory.

Specie	Symmetry number	Electronic state	Rotational constants (GHz)	Vibrational frequencies (cm^{-1})	ZPE ($kJ\,mol^{-1}$)	$S^{\circ}{}_{298\,K}$ ($J\,mol^{-1}$)
MCR_{I0}	1	$C_1 - {}^2A$	25.65, 3.41, 3.09	25, 68, 161, 248, 515, 778, 849, 865, 1243, 1438, 1449, 3056, 3159, 3174, 3764	124.36	347.41
TS_{I0}	1	$C_1 - {}^2A$	75.32, 2.83, 2.79	**162i**, 28, 76, 123, 446, 461, 514, 873, 1013, 1393, 1404, 3076, 3237, 3250, 3818	117.91	342.37
MCP_{I0}	1	$C_1 - {}^2A$	117.12, 2.48, 2.47	61, 65, 95, 251, 261, 584, 707, 1055, 1393, 1394, 3080, 3252, 3255, 3824	115.30	345.90
MCR_{I1a}	1	$C_1 - {}^2A$	5.45, 1.44, 1.16	23, 48, 52, 89, 96, 134, 190, 207, 304, 488, 555, 653, 890, 893, 1271, 1453, 1454, 1598, 3065, 3171, 3171, 3562, 3763, 3886	185.59	436.93
TS_{I1a}	1	$C_1 - {}^2A$	5.45, 1.69, 1.33	**239i**, 43, 56, 65, 66, 120, 184, 207, 297, 471, 489, 520, 566, 885, 1154, 1395, 1404, 1598, 3072, 3229, 3244, 3677, 3800, 3902	182.17	419.91
MCP_{I1a}	1	$C_1 - {}^2A$	5.91, 1.48, 1.19	37, 40, 61, 82, 98, 99, 190, 202, 207, 218, 316, 564, 610, 644, 1210, 1392, 1393, 1601, 3083, 3256, 3257, 3662, 3800, 3900	179.04	450.14
MCR_{I1b}	1	$C_1 - {}^2A$	4.89, 1.51, 1.22	17, 41, 63, 86, 92, 135, 198, 211, 318, 542, 551, 600, 892, 895, 1271, 1453, 1454, 1597, 3066, 3172, 3173, 3574, 3767, 3886	185.81	438.37
TS_{I1b}	1	$C_1 - {}^2A$	5.90, 1.65, 1.32	**235i**, 6, 54, 56, 80, 122, 174, 197, 302, 466, 492, 522, 570, 879, 1142, 1397, 1403, 1601, 3071, 3226, 3249, 3681, 3798, 3900	181.82	436.61
MCP_{I1b}	1	$C_1 - {}^2A$	5.91, 1.48, 1.19	18, 39, 61, 81, 95, 98, 192, 203, 205, 222, 313, 566, 610, 644, 1210, 1391, 1392, 1601, 3083, 3255, 3258, 3662, 3800, 3901	178.91	456.65
MCR_{I1c}	1	$C_1 - {}^2A$	4.90, 1.51, 1.22	18, 42, 63, 87, 93, 135, 198, 212, 318, 543, 551, 600, 893, 896, 1271, 1454, 1455, 1597, 3066, 3173, 3174, 3574, 3767, 3887	185.81	438.58
TS_{I1c}	1	$C_1 - {}^2A$	6.44, 1.39, 1.17	**217i**, 27, 33, 53, 87, 115, 142, 183, 239, 466, 472, 522, 629, 871, 1136, 1393, 1405, 1599, 3075, 3233, 3248, 3672, 3810, 3911	181.43	432.76
MCP_{I1c}	1	$C_1 - {}^2A$	7.48, 1.24, 1.07	31, 43, 59, 63, 94, 98, 167, 170, 184, 211, 237, 605, 634, 646, 1191, 1392, 1392, 1598, 3086, 3259, 3259, 3654, 3812, 3914	178.24	459.71

6.6   Energetics

This section aims to compute the thermodynamic properties of the previous chemical reactions. In other words, we will compute the standard reaction enthalpy ($\Delta_r H^\circ_{298\,K}$) and the standard Gibbs free reaction energy ($\Delta_r G^\circ_{298\,K}$).

We performed single-point energy calculations at all the stationary points, including the isolated reactants and products. It has been shown that computing the overall equilibrium reaction implicating iodine at the CCSD(T)/aug-cc-pVTZ level of theory leads to an underestimation of the latter [83]. Thus, single-point energy calculations were done using the CCSD(T) method as implemented in the MOLCAS package [389] associated with the all-electron relativistic quadruple basis sets (ANO-RCC-VQZP) [390]. We used the second-order spin-free Douglas-Kroll-Hess Hamiltonian [391, 392] to compute scalar relativistic effects, essential when dealing with iodine [393, 394]. The Goodson continuous fraction formula [395] was applied to the DK-CCSD(T)/ANO-RCC-VQZP single-point energy calculations to estimate the contribution to the full CI extrapolation. In the following, it will be denoted as CCSD(T)-cf/ANO-RCC-VQZP.

Furthermore, the energy differences between TSs and MCRs (activation energies), the one between the isolated reactants and the MCRs (reactant binding energies), and the energy difference between the reactants and the TSs (energy barrier) are essential in describing a chemical reaction. Then, we show such differences to understand the energy profile better. The results are shown in Tables 6.14, 6.15, and 6.16.

Table 6.14: Calculated standard reaction enthalpies and standard Gibbs free reaction energies at $298\,\mathrm{K}$ at different levels of theory for the $\mathrm{H_{abs}}$ and $\mathrm{I_{abs}}$ channels in the $\mathrm{OH + CH_3I}$ reaction with one water molecule. Energies are in $(\mathrm{kJ\,mol^{-1}})$.

	M06-2X/6-311+G(2df,2p)		DK-CCSD(T)/ANO-RCC-VQZP		DK-CCSD(T)-cf/ANO-RCC-VQZP	
	$\Delta_\mathrm{r}H^\circ{}_{298\,\mathrm{K}}$	$\Delta_\mathrm{r}G^\circ{}_{298\,\mathrm{K}}$	$\Delta_\mathrm{r}H^\circ{}_{298\,\mathrm{K}}$	$\Delta_\mathrm{r}G^\circ{}_{298\,\mathrm{K}}$	$\Delta_\mathrm{r}H^\circ{}_{298\,\mathrm{K}}$	$\Delta_\mathrm{r}G^\circ{}_{298\,\mathrm{K}}$
$\mathrm{OH + CH_3I + H_2O} \longrightarrow$ $\mathrm{CH_2I + 2\,H_2O}$ (R30)	-67.95	-74.39	-70.71	-77.15	-71.96	-78.40
$\mathrm{OH + CH_3I + H_2O} \longrightarrow$ $\mathrm{CH_3 + HOI + H_2O}$ (R31)	42.52	38.66	40.17	36.31	39.25	35.39

Table 6.15: Calculated various standard enthalpies and standard Gibbs free energies at 298 K at different levels of theory in the OH + CH$_3$I reaction with one water molecule for the H$_{abs}$ channel. Energies are in (kJ mol^{-1}).

	M06-2X/6-311+G(2df,2p)		DK-CCSD(T)/ANO-RCC-VQZP		DK-CCSD(T)-cf/ANO-RCC-VQZP	
	$\Delta H^\circ_{298\,K}$	$\Delta G^\circ_{298\,K}$	$\Delta H^\circ_{298\,K}$	$\Delta G^\circ_{298\,K}$	$\Delta H^\circ_{298\,K}$	$\Delta G^\circ_{298\,K}$
H$_{abs}$: OH + CH$_3$I + H$_2$O $\longrightarrow$ CH$_2$I + 2 H$_2$O (R30)						
OH + CH$_3$I $\longrightarrow$ MCR$_0$	−19.03	7.79	−12.76	14.05	−11.24	15.57
MCR$_0$ $\longrightarrow$ TS$_0$	26.46	30.11	22.88	26.53	22.47	26.13
OH + CH$_3$I $\longrightarrow$ TS$_0$	7.44	37.90	10.11	40.58	11.23	41.70
OH + CH$_3$I + H$_2$O $\longrightarrow$ MCR$_{1a}$	−52.34	16.83	−44.29	24.89	−40.94	28.24
MCR$_{1a}$ $\longrightarrow$ TS$_{1a}$	40.75	37.86	36.28	33.39	36.68	33.79
OH + CH$_3$I + H$_2$O $\longrightarrow$ TS$_{1a}$	−11.59	54.69	−8.01	58.28	−4.25	62.04
OH + CH$_3$I + H$_2$O $\longrightarrow$ MCR$_{1b}$	−25.61	43.56	−19.25	49.92	−15.10	54.08
MCR$_{1b}$ $\longrightarrow$ TS$_{1b}$	25.85	22.97	23.53	20.64	23.08	20.20
OH + CH$_3$I + H$_2$O $\longrightarrow$ TS$_{1b}$	0.24	66.53	4.27	70.56	7.98	74.27
OH + CH$_3$I + H$_2$O $\longrightarrow$ MCR$_{1c}$	−37.72	31.46	−32.36	36.82	−28.06	41.12
MCR$_{1c}$ $\longrightarrow$ TS$_{1c}$	20.22	17.33	19.99	17.10	19.28	16.39
OH + CH$_3$I + H$_2$O $\longrightarrow$ TS$_{1c}$	−17.50	48.78	−12.37	53.92	−8.78	57.51
OH + CH$_3$I + H$_2$O $\longrightarrow$ MCR$_{1d}$	−20.76	48.42	−15.82	53.36	−11.69	57.49
MCR$_{1d}$ $\longrightarrow$ TS$_{1d}$	25.09	22.20	21.63	18.74	21.27	18.39
OH + CH$_3$I + H$_2$O $\longrightarrow$ TS$_{1d}$	4.34	70.62	5.81	72.10	9.59	75.87

Table 6.16: Calculated various standard enthalpies and standard Gibbs free energies at $298\,\mathrm{K}$ at different levels of theory in the OH + CH_3I reaction with one water molecule for the I_{abs} channel. Energies are in $(kJ\,mol^{-1})$.

	M06-2X/6-33+G(2df,2p)		DK-CCSD(T)/ANO-RCC-VQZP		DK-CCSD(T)-cf/ANO-RCC-VQZP	
	$\Delta H^{\circ}{}_{298\,K}$	$\Delta G^{\circ}{}_{298\,K}$	$\Delta H^{\circ}{}_{298\,K}$	$\Delta G^{\circ}{}_{298\,K}$	$\Delta H^{\circ}{}_{298\,K}$	$\Delta G^{\circ}{}_{298\,K}$
I_{abs}: OH + CH_3I + H_2O $\longrightarrow$ CH_3 + HOI + H_2O (R31)						
OH + CH_3I $\longrightarrow$ MCR_{I0}	−3.63	23.09	−2.73	23.99	−1.85	24.87
MCR_{I0} $\longrightarrow$ TS_{I0}	30.13	31.64	29.69	31.19	29.77	31.28
OH + CH_3I $\longrightarrow$ TS_{I0}	26.50	54.72	26.96	55.18	27.92	56.15
OH + CH_3I + H_2O $\longrightarrow$ MCR_{I1a}	−32.62	23.66	−31.14	25.14	−26.83	29.45
MCR_{I1a} $\longrightarrow$ TS_{I1a}	40.47	45.55	39.39	44.46	38.53	43.61
OH + CH_3I + H_2O $\longrightarrow$ TS_{I1a}	7.85	69.21	8.24	69.60	11.70	73.05
OH + CH_3I + H_2O $\longrightarrow$ MCR_{I1b}	−32.56	23.72	−29.32	26.96	−25.04	31.24
MCR_{I1b} $\longrightarrow$ TS_{I1b}	41.71	46.78	37.79	42.86	37.03	42.10
OH + CH_3I + H_2O $\longrightarrow$ TS_{I1b}	9.15	70.50	8.47	69.82	11.99	73.34
OH + CH_3I + H_2O $\longrightarrow$ MCR_{I1c}	−32.56	23.72	−22.14	34.14	−17.98	38.30
MCR_{I1c} $\longrightarrow$ TS_{I1c}	41.71	46.78	37.37	42.45	36.74	41.82
OH + CH_3I + H_2O $\longrightarrow$ TS_{I1c}	9.15	70.50	15.24	76.59	18.77	80.12

We observe that reaction R30 is exothermic and spontaneous at 298 K, whereas reaction R31 is endothermic and non-spontaneous at this temperature. The standard reaction enthalpy and the standard Gibbs free reaction energy decrease when the basis set is increased. We see that reaction R30 tends to be more favorable than reaction R31.

The addition of one water molecule affects the stationary point relative energies and not the whole overall equilibrium reaction. Increasing the basis set size destabilizes the binding energies for all the reaction pathways. In addition, the activation energies are mostly constant or lower when the basis set increases. The addition of one water molecule stabilizes the reactant binding energies for both reactions. Regarding reaction R30, the additional water molecule lowers the activation energy for all pathways except for reaction R30$_a$. Indeed, the reactant binding energy is high, leading to a more significant activation energy. For the same reasons, the additional water molecule induces an increase of the activation energy in reaction R31 for all the reaction pathways. For all the reactions, the reaction energy barrier increases when increasing the basis set.

For reaction R30, the additional water molecule reduces the energetic barrier and the activation energy. The most favorable pathway is reaction R30$_{1c}$, with the lowest energetic barriers and activation energies. For reaction R31, the additional water molecule highly stabilizes the molecular complexes. In addition, it reduces the energetic barrier for all the pathways. The most favorable pathway is reaction R31$_{I1a}$.

Energetic diagrams were done using the *PyEnergyDiagrams* package [396]. We present the energetic diagrams of the most favorable pathways. Fig. 6.21 shows the energetic profile of the H$_{abs}$ in the OH + CH$_3$I reaction with and without water molecule.

As usual in many atmospheric gas-phase reactions involving hydroxyl radicals, each elementary reaction begins with the formation of prereactive hydrogen bonded complexes (MCR$_0$ and MCR$_{1c}$) before the transition states and the formation of the products. Both prereactive complexes are held by a hydrogen bond interaction between the hydrogen atom of the CH$_3$I and the oxygen atom of the hydroxyl radical. MCPs are stabilized by Van der Waals interactions between the iodine atom of the CH$_2$I radical and one hydrogen atom of water.

Fig. 6.21 shows a binding energy of -10.09 and -27.34 kJ mol^{-1} for MCR$_0$ and MCR$_{1c}$, respectively. The reaction proceeds through transition states TS$_0$ and TS$_{1c}$ forming the postreactive complex MCP$_0$ and MCP$_{1c}$, before the release of the products, H$_2$O, CH$_2$I$_2$, and 2 H$_2$O. The analysis of the wave function at the two transition states indicates that the reaction with and without water molecule involves the concerted breaking and forming of the (C)O$-$H and H$-$O(H) bond.
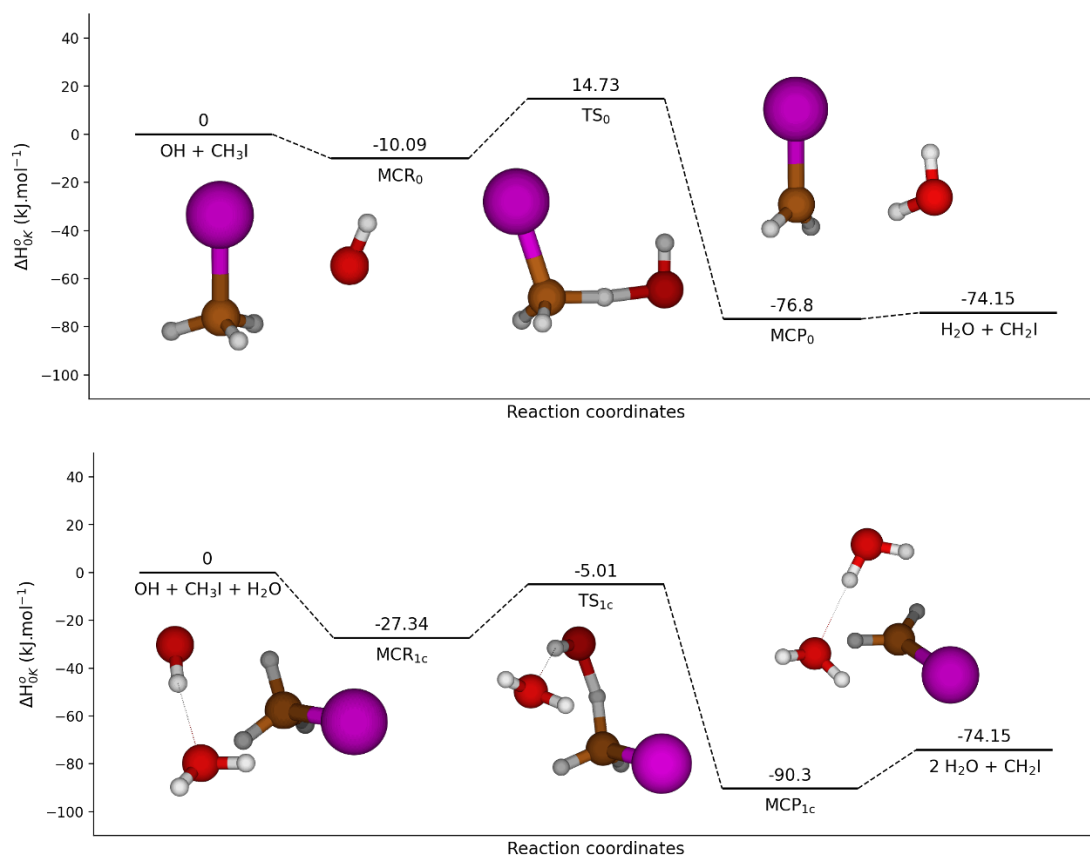
Figure 6.21: Energetic profile of the H_{abs} in $OH + CH_3I$ reaction with and without an additional water molecule calculated at the DK-CCSD(T)-cf/ANO-RCC-VQZP level of theory.

Focusing now on the water assisted reaction, beginning with the $CH_3I\cdots$ $H_2O + OH$ reactants, the first step of the reaction involves the formation of the MCR_{1c} hydrogen bond complex, in which the hydroxyl radical interacts with the lone pair of the water molecule of the $CH_3I\cdots H_2O$ reactant. Thus, the MCR_{1c} complex is formed by three entities, which are held together by two hydrogen bonds $(ICH_3\cdots H_2O\cdots HO)$. After the transition state, TS_{1c}, which has an energy barrier of only $22.33\,\text{kJ}\,\text{mol}^{-1}$, relative to MCR_{1c}, lying below the energy of the reactants, the six-member ring TS_{1c} hydrogen bonded complex is formed, with a binding energy of $-5.01\,\text{kJ}\,\text{mol}^{-1}$. The latter has two hydrogen bonds, the first between the hydrogen atom of the CH_3I moiety and the oxygen atom of the hydroxyl radical moiety; the second one between the hydrogen atom of the OH moiety and the oxygen atom of water. The influence of a single water molecule on the $CH_3I + OH$ reaction lowered the energy barrier of the TS.
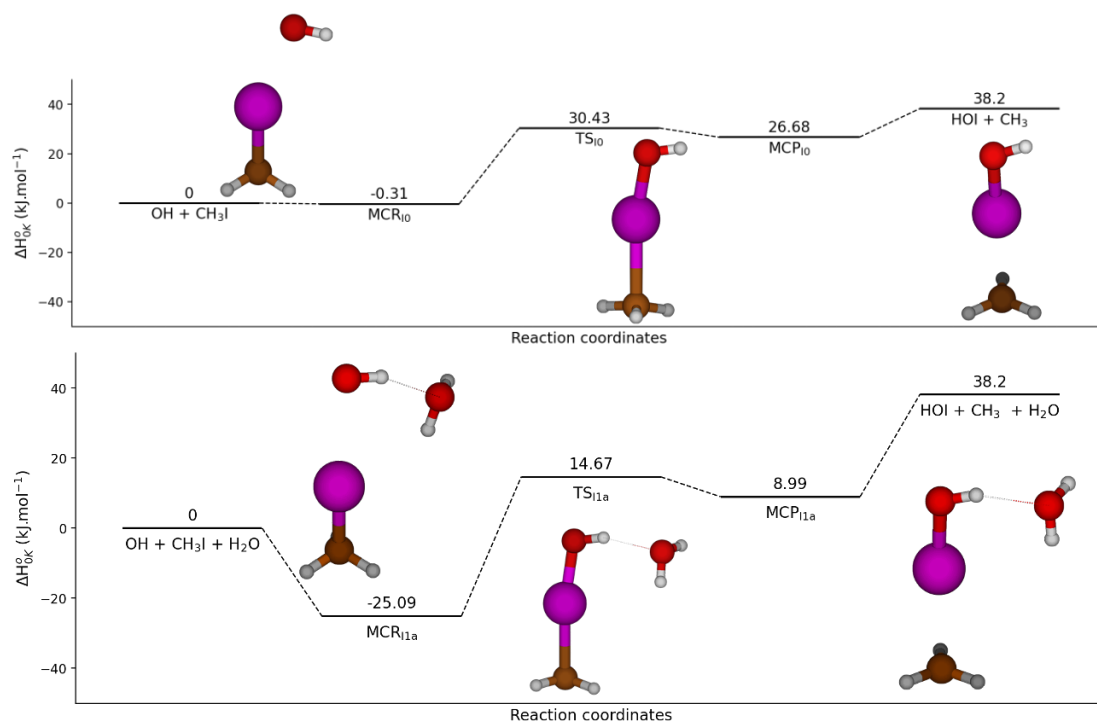
Figure 6.22: Energetic profile of the I$_{abs}$ in OH + CH$_3$I reaction with and without an additional water molecule calculated at the DK-CCSD(T)-cf/ANO-RCC-VQZP level of theory.

Then, the energetic diagram of the I-abstraction in OH + CH$_3$I reaction within and without water molecule is presented in Fig. 6.22. Similar to the H$_{abs}$ reaction described above, each reaction begins with the formation of a prereactive hydrogen bond complex, but now the prereactive MCR$_{I0}$ is located at the same level of energy as separate reactants whereas MCR$_{I1a}$ is located at $-25.09\,\mathrm{kJ\,mol^{-1}}$ below the energy of the separate reactants.

From an energetic point of view, Fig. 6.22 and Table 6.16 show that TS$_{I0}$ (without water) and TS$_{I1a}$ (with water) are predicted to lie at 30.40 and 14.67 kJ mol^{-1} at 0 K respectively above the energy of the separate reactants. The addition of a water molecule has lowered the energy barrier of the TS, certainly, but due to the high barrier this pathway of abstraction is not feasible from the energetic point of view.

6.7 Conclusion

We have studied gas-phase chemical reactivity of OH towards CH_3I with and without water, using high-level *ab initio* methods. The stationary points on the energy profiles were determined at M06-2X/6-311+G(2df,2p) level of theory. The energetics was calculated at two different levels of theory: DK-CCSD(T)/ANO-RCC-VQZP, and DK-CCSD(T)-cf/ANO-RCC-VQZP. These single-point energy calculations revealed, in both cases, that the H_{abs} are exothermic while the I_{abs} are endothermic.

Studying the effect that a single water molecule can have on the potential energy surface of the OH + CH_3I reaction has revealed some interesting findings, particularly in the context of the OH + CH_3I reaction assisted by water. When water is added to the reaction, the resulting products do not change from that of the naked reaction forming CH_2I, H_2O for H_{abs} and HOI, CH_3 for I_{abs}. However, the water molecule does impact the reaction. It can begin by collision of either $CH_3I \cdots H_2O$ with OH or $HO \cdots H_2O$ with CH_3I.

CHAPTER 7

Conclusions and perspectives

In the present work, some examples of the effects of the environing molecules/aerosols on CH$_3$I behavior have been presented. The interactions with sea-salt aerosols (NaCl) and the effect of water coverage on its behavior have been investigated. To perform large-scale calculations, we successfully parametrized a flexible non-polarizable force field that reproduces the CH$_3$I/H$_2$O and CH$_3$I/NaCl interactions well. In addition, theoretical harmonic vibrational frequencies of CH$_3$I and CH$_3$I-containing dimers adsorbed on the NaCl(001) surface have been computed, making the comparison with experiments possible. Through cooperation with the laboratory "Physics of the Interactions of Ions and Molecules (PIIM)", we have performed multi-level theoretical simulations on the adsorption of methyl iodide on ASW surfaces. Thus, theoretical IR spectra were computed, and the dOH vibrational shifts were calculated. Finally, we investigated the effect of a surrounding water molecule on the CH$_3$I + OH reaction. We have shown that the water molecule acts as a catalyst by lowering the activation barrier of the hydrogen abstraction by the hydroxyl radical.

The force field developed in this Thesis was built by mixing existing parameters found in the literature with ones fitted on quantum calculations at the MP2/aug-cc-pVTZ(-PP) level of theory. This force field has shown promising performances in describing interactions with water and sea-salt surfaces. However, despite its good performance in computing the bulk CH$_3$I liquid density at 300 K, it showed limitations regarding the interactions between methyl iodide dimers and trimers. We hypothesize that the lack of polarization induces an approximative description of the I$\cdots$I interactions. Nonetheless, this force field was effective in describing large systems where no CH$_3$I$\cdots$CH$_3$I interactions occur.

During this Thesis, we were interested in the interactions of methyl iodide with the model sea-salt aerosol, NaCl. Based on previous studies done by Houjeij et al. [96], we have investigated the adsorption of CH_3I on the NaCl(001) surface using periodic DFT calculations. We computed the harmonic vibrational frequencies of the adsorbed and gas phase CH_3I using the DFPT method. At our level of theory, we show that the minimum energy geometry of adsorbed methyl iodide on the NaCl(001) surface is when the C−I axis is being oriented along the diagonal according to the surface lattice vectors. This geometry is associated with a low adsorption energy value. Harmonic vibrational frequencies of methyl iodide were computed in the gas phase and adsorbed on the NaCl(001) surface. We did not observe significant vibrational shifts upon adsorption at our level of theory. Finally, the effects of water coverage were investigated. We showed that, even at low coverage, water highly modifies the average adsorption energy of CH_3I on the sea-salt surface.

The study of the adsorption of CH_3I on ASW surfaces was challenging. Using the force field developed in this Thesis, we first performed classical MD sampling to generate adsorption geometries. During this step, we could compute the probability of finding an adsorption geometry for a given adsorption energy. Instead of randomly picking adsorption geometries, we performed a selection of the most relevant adsorption geometries. The latter was done by introducing parameters to group and evaluate configurations. Therefore, we performed ONIOM calculations and computed a dOH vibrational red shift of $20\,cm^{-1}$. In addition, we have also calculated theoretical IR spectra by averaging the ones from each selected adsorption geometry.

The last study of this Thesis consisted of studying the effect of an additional water molecule on the CH_3I + OH reaction. When adding a water molecule, we found four different TSs for the hydrogen abstraction pathway and three different TSs for the iodine abstraction. We showed that water acts as a catalyst by lowering the activation energy of the reaction. Performing quantum calculations at the M06-2X/6-311+G(2df,2p) level of theory, we have identified all possible pathways, namely the hydrogen and iodine abstraction.

The work presented in this Thesis can be expanded in various directions. The first one is the use of a polarizable force field. Even if the computational cost is higher, describing the polarization may improve the description of CH_3I clusters. On the NaCl(001) surface, it should be possible to observe if methyl iodide tends to form clusters with itself or if it mixes with water molecules homogeneously. When CH_3I is adsorbed on ASW surfaces, we could be able to investigate the effect of adsorbed CH_3I clusters and how it impacts the dOH vibrational shifts, as well as the adsorption energy. The adsorption energy of CH_3I on ASW being quite

small, the proposed methodology could be extended to adsorbates having a stronger affinity for ice and consequently leading to larger shifts.

The adsorption of molecules is drastically different on perfect surfaces compared to those presenting defaults. Thus, another direction could be to study the effect of several defaults on the adsorption of CH_3I on the NaCl(001) surface. Furthermore, results obtained by Houjeij et al. [96] highly suggest surface reactivity on the sea-salt surface. Therefore, after picking relevant candidates, we could perform reactivity calculations of CH_3I when adsorbed on a defective NaCl(001) surface. To this end, quantum calculations seems to be mandatory, using for example the ONIOM approach, such as the one used for ASW.

Several improvements can be made regarding the study of the adsorption of CH_3I on the ASW surface. Generating and selecting a more significant number of configurations will improve the results. In addition, the methodology used in this work to group and evaluate adsorption geometries can be improved by machine-learning algorithms. Indeed, we can use neural network algorithms or clustering ones to better discriminate configurations according to their parameters. Finally, adding parameter others than the ones present in this Thesis could be an excellent manner to improve the selection of the adsorption geometries further.

We have several possibilities concerning the effect of one additional water molecule on the CH_3I + OH reaction. The next step should be to compute the reaction rates with and without the additional water molecule. In addition, we can increase the number of additional water molecules and quantify the corresponding impacts on kinetic rates and activation barriers.

Born-Oppenheimer mathematical development

The starting point of this appendix is equation (2.2) but for the ground state. For simplicity, the "{ ... }" symbols are dropped. In this mathematical development, all the results from section (2.1) are used.

$$
\begin{aligned}
E_0\Psi_0(\mathbf{r}, \mathbf{R}) &= H\Psi_0(\mathbf{r}, \mathbf{R}) & \text{(A.1)} \\
&= \left[T_e + V_{ee} + V_{ne} + T_n + V_{nn}\right]\Psi_0(\mathbf{r}, \mathbf{R}) & \text{(A.2)} \\
&= \left[H_e + T_n\right]\Psi_0(\mathbf{r}, \mathbf{R}) & \text{(A.3)} \\
&= \left[H_e + \sum_i^{N_n} \frac{-\hbar^2}{2M_i} \nabla^2_{\mathbf{R}_i}\right] \sum_\nu \Lambda_\nu(\mathbf{R})\Phi_\nu(\mathbf{r}, \mathbf{R}) & \text{(A.4)} \\
&= \sum_\nu \Lambda_\nu(\mathbf{R})H_e\Phi_\nu(\mathbf{r}, \mathbf{R}) & \text{(A.5)} \\
&\quad + \sum_\nu \left[\sum_i^{N_n} \frac{-\hbar^2}{2M_i} \nabla^2_{\mathbf{R}_i}\right]\Lambda_\nu(\mathbf{R}_i)\Phi_\nu(\mathbf{r}, \mathbf{R}) \\
&= \sum_\nu \Lambda_\nu(\mathbf{R})E^e_\nu\Phi_\nu(\mathbf{r}, \mathbf{R}) & \text{(A.6)} \\
&\quad + \sum_\nu \sum_i^{N_n} \frac{-\hbar^2}{2M_i} \nabla^2_{\mathbf{R}_i} \Lambda_\nu(\mathbf{R})\Phi_\nu(\mathbf{r}, \mathbf{R})
\end{aligned}
$$

A part of the equation (A.7) is treated separately for simplicity and the following symbols will be written as $\Lambda_\nu(\mathbf{R}) = \Lambda_\nu$ and $\Phi_\nu(\mathbf{r}, \mathbf{R}) = \Phi_\nu$.

$$\nabla^2_{\mathbf{R}_i}\Lambda_\nu\Phi_\nu \quad = \quad \nabla_{\mathbf{R}_i}[\nabla_{\mathbf{R}_i}(\Lambda_\nu\Phi_\nu)] \tag{A.7}$$

$$\nabla_{\mathbf{R}_i}(\Lambda_\nu\Phi_\nu) \quad = \quad \Lambda_\nu(\nabla_{\mathbf{R}_i}\Phi_\nu) + \Phi_\nu(\nabla_{\mathbf{R}_i}\Lambda_\nu) \tag{A.8}$$

$$\nabla^2_{\mathbf{R}_i}\Lambda_\nu\Phi_\nu \quad = \quad \nabla_{\mathbf{R}_i}[\Lambda_\nu(\nabla_{\mathbf{R}_i}\Phi_\nu) + \Phi_\nu(\nabla_{\mathbf{R}_i}\Lambda_\nu)] \tag{A.9}$$

$$\nabla^2_{\mathbf{R}_i}\Lambda_\nu\Phi_\nu \quad = \quad \Lambda_\nu(\nabla^2_{\mathbf{R}_i}\Phi_\nu) + 2(\nabla_{\mathbf{R}_i}\Lambda_\nu)(\nabla_{\mathbf{R}_i}\Phi_\nu) + (\nabla^2_{\mathbf{R}_i}\Lambda_\nu)\Phi_\nu \tag{A.10}$$

Equation (A.10) is injected in equation (A.7):

$$E_0\Psi_0(\mathbf{r}, \mathbf{R}) = \sum_\nu \Lambda_\nu E^e_\nu \Phi_\nu \qquad + \sum_v \sum_i^{N_n} \frac{-\hbar^2}{2M_i}\Lambda_\nu(\nabla^2_{\mathbf{R}_i}\Phi_\nu) \tag{A.11}$$

$$+2(\nabla_{\mathbf{R}_i}\Lambda_\nu)(\nabla_{\mathbf{R}_i}\Phi_\nu) + (\nabla^2_{\mathbf{R}_i}\Lambda_\nu)\Phi_\nu$$

Multiplying equation (A.12) by Φ^*_μ and integrating over all the ionic coordinates gives:

$$\langle\Phi_\mu|H|\Psi_0\rangle \quad = \quad E_0\langle\Phi_\mu|\Psi_0\rangle = E_0\langle\Phi_\mu|\Lambda_\mu\Phi_\mu\rangle = E_0\Lambda_\mu \tag{A.12}$$

$$E_0\Lambda_\mu \quad = \quad E^e_\mu\Lambda_\mu + \sum_\nu\sum_i^{N_n}\frac{-\hbar^2}{2M_i}[\langle\Phi_\mu|\nabla^2_{\mathbf{R}_i}|\Phi_\nu\rangle\Lambda_\mu +$$

$$2\langle\Phi_\mu|\nabla_{\mathbf{R}_i}|\Phi_\nu\rangle(\nabla_{\mathbf{R}_i}\Lambda_\mu) + \nabla^2_{\mathbf{R}_i}\Lambda_\mu] \tag{A.13}$$

$$= \quad \left[E^e_\mu + T_n\right]\Lambda_\mu$$

$$+ \quad \sum_\nu\sum_i^{N_n}\frac{-\hbar^2}{2M_i}[\langle\Phi_\mu|\nabla^2_{\mathbf{R}_i}|\Phi_\nu\rangle\Lambda_\mu$$

$$+ \quad 2\langle\Phi_\mu|\nabla_{\mathbf{R}_i}|\Phi_\nu\rangle(\nabla_{\mathbf{R}_i}\Lambda_\mu)] \tag{A.14}$$

$$\mathcal{A}_{\mu\nu} \quad = \quad \sum_i^{N_n}\frac{-\hbar^2}{2M_i}\langle\Phi_\mu|\nabla^2_{\mathbf{R}_i}|\Phi_\nu\rangle \tag{A.15}$$

$$\mathcal{B}_{\mu\nu} \quad = \quad \sum_i^{N_n}\frac{-\hbar^2}{M_i}\langle\Phi_\mu|\nabla_{\mathbf{R}_i}|\Phi_\nu\rangle\nabla_{\mathbf{R}_i} \tag{A.16}$$

$$E_0\Lambda_\mu \quad = \quad \left[E^e_\mu + T_n\right]\Lambda_\mu + \sum_\nu(\mathcal{A}_{\mu\nu} + \mathcal{B}_{\mu\nu})\Lambda_\mu \tag{A.17}$$

Equation (A.17) is the one which is used in section (2.1).

Mathematical development for the vibrational entropic contribution to the energy

This Appendix contains the details from the mathematical development concerning the vibrational contribution from section 2.8. We start our development with the vibrational partition function (q_v) as it is written in Eq. (2.139):

$$q_v = e^{-E_{ZPE}/k_B T} \prod_{N_v} \frac{1}{1 - e^{-\Theta_{v,N_v}/T}} \ , \tag{B.1}$$

$$\ln(q_v) = \frac{-E_{ZPE}}{k_B T} \sum_{N_v} \ln \left(\frac{1}{1 - e^{-\Theta_{v,N_v}/T}} \right) \ , \tag{B.2}$$

$$= \frac{-E_{ZPE}}{k_B T} \sum_{N_v} \ln(1) - \ln \left(1 - e^{-\Theta_{v,N_v}/T} \right) \ , \tag{B.3}$$

$$= \frac{-E_{ZPE}}{k_B T} \sum_{N_v} - \ln \left(1 - e^{-\Theta_{v,N_v}/T} \right) \ . \tag{B.4}$$

197

The next step is to compute the first derivative of $\ln(q_v)$ according to the temperature at constant volume:

$$\left(\frac{\partial \ln q_v}{\partial T}\right)_V = \frac{E_{ZPE}}{k_B T^2} + \sum_{N_v} - \left[\frac{-\Theta_{v,N_v}/T^2 \ e^{-\Theta_{v,N_v}/T}}{1 - e^{-\Theta_{v,N_v}/T}}\right] , \tag{B.5}$$

$$= \frac{E_{ZPE}}{k_B T^2} + \sum_{N_v} \frac{\Theta_{v,N_v}/T^2 \ e^{-\Theta_{v,N_v}/T}}{1 - e^{-\Theta_{v,N_v}/T}} , \tag{B.6}$$

$$= \frac{E_{ZPE}}{k_B T^2} + \sum_{N_v} \frac{e^{\Theta_{v,N_v}/T}}{e^{\Theta_{v,N_v}/T}} \frac{\Theta_{v,N_v}/T^2 \ e^{-\Theta_{v,N_v}/T}}{1 - e^{-\Theta_{v,N_v}/T}} , \tag{B.7}$$

$$= \frac{E_{ZPE}}{k_B T^2} + \sum_{N_v} \frac{\Theta_{v,N_v}}{T^2} \frac{1}{e^{\Theta_{v,N_v}/T} - 1} . \tag{B.8}$$

Now, we are able to write the vibrational internal energy contribution from Eq. (2.125) as:

$$E_T^v = RT^2 \left(\frac{\partial \ln q_v}{\partial T}\right)_V , \tag{B.9}$$

$$= RT^2 \left[\frac{E_{ZPE}}{k_B T^2} + \sum_{N_v} \frac{\Theta_{v,N_v}}{T^2} \frac{1}{e^{\Theta_{v,N_v}/T} - 1}\right] , \tag{B.10}$$

$$= R \left[\frac{E_{ZPE}}{k_B} + \sum_{N_v} \frac{\Theta_{v,N_v}}{e^{\Theta_{v,N_v}/T} - 1}\right] . \tag{B.11}$$

Within the same scheme, we can also compute the vibrational entropic contribution from Eq. (2.127) as:

$$S_v = R \left[\ln(q_v) + T \left(\frac{\partial \ln q_v}{\partial T}\right)_V\right] , \tag{B.12}$$

$$= R \left[\frac{-E_{ZPE}}{k_B T} \sum_{N_v} - \ln\left(1 - e^{-\Theta_{v,N_v}/T}\right) + T \left(\frac{E_{ZPE}}{k_B T^2} + \sum_{N_v} \frac{\Theta_{v,N_v}/T^2}{e^{\Theta_{v,N_v}/T} - 1}\right)\right] , \tag{B.13}$$

$$= R \left[\frac{-E_{ZPE}}{k_B T} + \frac{E_{ZPE}}{k_B T} \sum_{N_v} \frac{\Theta_{v,N_v}/T}{e^{\Theta_{v,N_v}/T} - 1} - \ln\left(1 - e^{-\Theta_{v,N_v}/T}\right)\right] , \tag{B.14}$$

$$= R \sum_{N_v} \frac{\Theta_{v,N_v}/T}{e^{\Theta_{v,N_v}/T} - 1} - \ln\left(1 - e^{-\Theta_{v,N_v}/T}\right) . \tag{B.15}$$

APPENDIX C

CH$_3$I adsorption on amorphous solid water
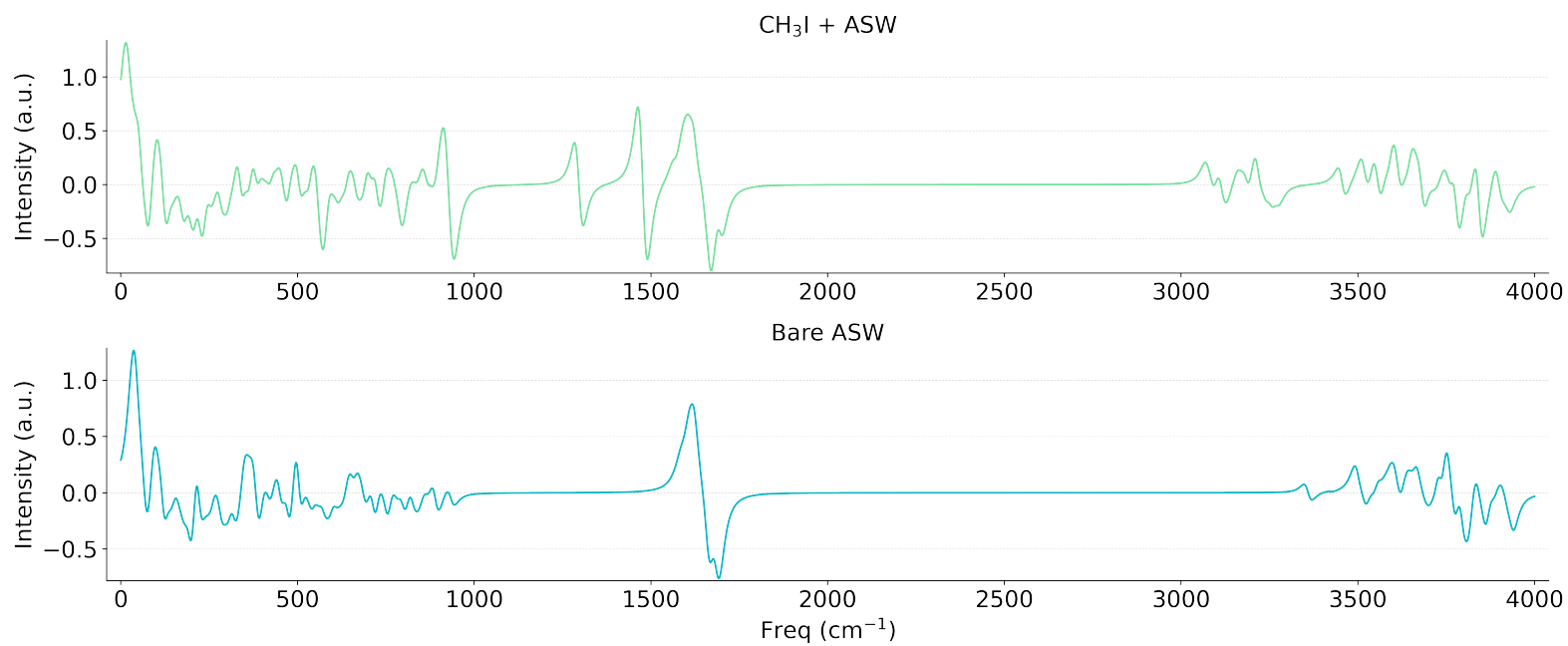
Figure C.1: First derivative according to frequencies of the IR weighted spectra obtained after averaging over 8 configurations according to their respective probabilities of: (green) CH$_3$I adsorbed on ASW surface; (blue) Bare ASW; A Lorentzian smearing of $10\,\mathrm{cm}^{-1}$ has been applied in the IR original spectrum.

Bibliography

[1] Brown M. Dobyns et al. "Malignant and Benign Neoplasms of the Thyroid in Patients Treated for Hyperthyroidism: A Report of the Cooperative Thyrotoxicosis Therapy Follow-up Study". In: *The Journal of Clinical Endocrinology & Metabolism* 38.6 (June 1974), pp. 976–998. ISSN: 0021-972X, 1945-7197. DOI: 10.1210/jcem-38-6-976.

[2] D.C. Whitehead. "The Distribution and Transformations of Iodine in the Environment". In: *Environment International* 10.4 (Jan. 1984), pp. 321–339. ISSN: 01604120. DOI: 10.1016/0160-4120(84)90139-9.

[3] Eric J. Underwood. *Trace Elements in Human and Animal Nutrition.* 4th ed. New York: Academic Press, 1977. ISBN: 978-0-12-709065-8.

[4] Alfonso Saiz-Lopez et al. "Atmospheric Chemistry of Iodine". In: *Chemical Reviews* 112.3 (Mar. 2012), pp. 1773–1804. ISSN: 0009-2665, 1520-6890. DOI: 10.1021/cr200029u.

[5] Jack G. Calvert and Steve E. Lindberg. "Potential Influence of Iodine-Containing Compounds on the Chemistry of the Troposphere in the Polar Spring. I. Ozone Depletion". In: *Atmospheric Environment* 38.30 (Sept. 2004), pp. 5087–5104. ISSN: 13522310. DOI: 10.1016/j.atmosenv.2004.05.049.

[6] N. Bell et al. "Methyl Iodide: Atmospheric Budget and Use as a Tracer of Marine Convection in Global Models: GLOBAL ATMOSPHERIC METHYL IODIDE". In: *Journal of Geophysical Research: Atmospheres* 107.D17 (Sept. 2002), ACH 8-1-ACH 8–12. ISSN: 01480227. DOI: 10.1029/2001JD001151.

[7] M. Waggoner et al. "Methyl Iodide: An Alternative to Methyl Bromide for Insectary Fumigation". In: *Journal of Applied Entomology* 124.2 (May 2000), pp. 113–117. ISSN: 0931-2048, 1439-0418. DOI: 10.1046/j.1439-0418.2000.00437.x.

[8]   W. L. Chameides and D. D. Davis. "Iodine: Its Possible Role in Tropospheric Photochemistry". In: *Journal of Geophysical Research: Oceans* 85.C12 (Dec. 1980), pp. 7383–7398. ISSN: 01480227. DOI: `10.1029/JC085iC12p07383`.

[9]   Rainer Vogt et al. "Iodine Chemistry and Its Role in Halogen Activation and Ozone Loss in the Marine Boundary Layer: A Model Study". In: (), p. 21.

[10] Lucy J. Carpenter. "Iodine in the Marine Boundary Layer". In: *Chemical Reviews* 103.12 (Dec. 2003), pp. 4953–4962. ISSN: 0009-2665, 1520-6890. DOI: `10.1021/cr0206465`.

[11] J.E. Lovelock, R. J. Maggs, and J. Wade. "Halogenated Hydrocarbons in and over the Atlantic". In: *Nature* 241.5386 (1973), pp. 194–196. DOI: `10.1038/241194a0`.

[12] Jarvis L. Moyers and Robert A. Duce. "Gaseous and Particulate Bromine in the Marine Atmosphere". In: *Journal of Geophysical Research* 77.27 (Sept. 1972), pp. 5330–5338. ISSN: 01480227. DOI: `10.1029/JC077i027p05330`.

[13] Mark A. Kritz and Jacques Rancher. "Circulation of Na, Cl, and Br in the Tropical Marine Atmosphere". In: *Journal of Geophysical Research* 85.C3 (1980), p. 1633. ISSN: 0148-0227. DOI: `10.1029/JC085iC03p01633`.

[14] James H. Butler et al. "Oceanic Distributions and Emissions of Short-Lived Halocarbons: Oceanic Emissions of Short-Lived Halocarbons". In: *Global Biogeochemical Cycles* 21.1 (Mar. 2007). ISSN: 08866236. DOI: `10.1029/2006GB002732`.

[15] Adele L. Chuck. "Oceanic Distributions and Air-Sea Fluxes of Biogenic Halocarbons in the Open Ocean". In: *Journal of Geophysical Research* 110.C10 (2005), p. C10022. ISSN: 0148-0227. DOI: `10.1029/2004JC002741`.

[16] Yoko Yokouchi et al. "Global Distribution and Seasonal Concentration Change of Methyl Iodide in the Atmosphere". In: *Journal of Geophysical Research* 113.D18 (Sept. 2008), p. D18311. ISSN: 0148-0227. DOI: `10.1029/2008JD009861`.

[17] Brett Kuyper et al. "Volatile Halocarbon Measurements in the Marine Boundary Layer at Cape Point, South Africa". In: *Atmospheric Environment* 214 (Oct. 2019), p. 116833. ISSN: 13522310. DOI: `10.1016/j.atmosenv.2019.116833`.

[18] Ronald Fuge and Christopher C. Johnson. "The Geochemistry of Iodine — a Review". In: *Environmental Geochemistry and Health* 8.2 (June 1986), pp. 31–54. ISSN: 0269-4042, 1573-2983. DOI: `10.1007/BF02311063`.

[19] L. J. Carpenter et al. "Short-Lived Alkyl Iodides and Bromides at Mace Head, Ireland: Links to Biogenic Sources and Halogen Oxide Production". In: *Journal of Geophysical Research: Atmospheres* 104.D1 (1999), pp. 1679–1689. DOI: `10.1029/98JD02746`. eprint: `https://agupubs.onlinelibrary.wiley.com/doi/pdf/10.1029/98JD02746`.

[20] L. J. Carpenter et al. "Novel Biogenic Iodine-Containing Trihalomethanes and Other Short-Lived Halocarbons in the Coastal East Atlantic". In: *Global Biogeochemical Cycles* 14.4 (Dec. 2000), pp. 1191–1204. ISSN: 08866236. DOI: `10.1029/2000GB001257`.

[21] Y-K. Lim et al. "Halocarbon Emissions from Marine Phytoplankton and Climate Change". In: *International Journal of Environmental Science and Technology* 14.6 (June 2017), pp. 1355–1370. ISSN: 1735-2630. DOI: `10.1007/s13762-016-1219-5`.

[22] Gordon W. Gribble. *Naturally Occurring Organohalogen Compounds: A Comprehensive Update.* Wien : New York: Springer-Verlag ; SpringerWien-NewYork, 2010. ISBN: 978-3-211-99322-4 978-3-211-99323-1.

[23] Seigo Amachi et al. "Bacteria Mediate Methylation of Iodine in Marine and Terrestrial Environments". In: *Applied and Environmental Microbiology* 67.6 (June 2001), pp. 2718–2722. ISSN: 1098-5336, 0099-2240. DOI: `10.1128/AEM.67.6.2718-2722.2001`.

[24] Martina Landini et al. "Metabolic Engineering of the Iodine Content in Arabidopsis". In: *SCIENTIFIC REPORTS* (), p. 6.

[25] H. S. SAINI, J. M. ATTIEH, and A. D. HANSON. "Biosynthesis of Halomethanes and Methanethiol by Higher Plants via a Novel Methyltransferase Reaction". In: *Plant, Cell & Environment* 18.9 (1995), pp. 1027–1033. DOI: `10.1111/j.1365-3040.1995.tb00613.x`. eprint: `https://onlinelibrary.wiley.com/doi/pdf/10.1111/j.1365-3040.1995.tb00613.x`.

[26] Y. Muramatsu et al. "Iodine Desorption from Rice Paddy Soil". In: *Water, Air, and Soil Pollution* 86.1 (Jan. 1996), pp. 359–371. ISSN: 1573-2932. DOI: `10.1007/BF00279167`.

[27] K. R. Redeker et al. "Emissions of Methyl Halides and Methane from Rice Paddies". In: *Science* 290.5493 (2000), pp. 966–969. ISSN: 00368075, 10959203.

[28] S. Yoshida and Y. Muramatsu. "Determination of Organic, Inorganic and Particulate Iodine in the Coastal Atmosphere of Japan". In: *Journal of Radioanalytical and Nuclear Chemistry* 196.2 (Oct. 1995), pp. 295–302. ISSN: 1588-2780. DOI: `10.1007/BF02038047`.

[29] K. R. Redeker and R. J. Cicerone. "Environmental Controls over Methyl Halide Emissions from Rice Paddies: ENVIRONMENTAL CONTROLS OVER MeX FLUXES FROM RICE". In: *Global Biogeochemical Cycles* 18.1 (Mar. 2004), n/a–n/a. ISSN: 08866236. DOI: 10.1029/2003GB002092.

[30] Eva Duborská, Martin Urík, and Marek Bujdoš. "Comparison of Iodide and Iodate Accumulation and Volatilization by Filamentous Fungi during Static Cultivation". In: *Water, Air, & Soil Pollution* 228.6 (June 2017), p. 225. ISSN: 0049-6979, 1573-2932. DOI: 10.1007/s11270-017-3407-4.

[31] D. B. Harper and J. T. Kennedy. "Effect of Growth Conditions on Halomethane Production by Phellinus Species: Biological and Environmental Implications". In: *Microbiology* 132.5 (May 1986), pp. 1231–1246. ISSN: 1350-0872, 1465-2080. DOI: 10.1099/00221287-132-5-1231.

[32] Tadaaki Ban-nai, Yasuyuki Muramatsu, and Seigo Amachi. "Rate of Iodine Volatilization and Accumulation by Filamentous Fungi through Laboratory Cultures". In: *Chemosphere* 65.11 (Dec. 2006), pp. 2216–2222. ISSN: 00456535. DOI: 10.1016/j.chemosphere.2006.05.047.

[33] I. Stemmler et al. "Methyl Iodide Production in the Open Ocean". In: *Biogeosciences* 11.16 (Aug. 2014), pp. 4459–4476. ISSN: 1726-4189. DOI: 10.5194/bg-11-4459-2014.

[34] Robert M. Moore and Oliver C. Zafiriou. "Photochemical Production of Methyl Iodide in Seawater". In: *Journal of Geophysical Research* 99.D8 (1994), p. 16415. ISSN: 0148-0227. DOI: 10.1029/94JD00786.

[35] James D. Happell and Douglas W. R. Wallace. "Methyl Iodide in the Greenland/Norwegian Seas and the Tropical Atlantic Ocean: Evidence for Photochemical Production". In: *Geophysical Research Letters* 23.16 (Aug. 1996), pp. 2105–2108. ISSN: 0094-8276, 1944-8007. DOI: 10.1029/96GL01764.

[36] Jean E. Moran et al. "Atmospheric Dispersal of [129] Iodine from Nuclear Fuel Reprocessing Facilities". In: *Environmental Science & Technology* 33.15 (Aug. 1999), pp. 2536–2542. ISSN: 0013-936X, 1520-5851. DOI: 10.1021/es9900050.

[37] Nadia Buraglio et al. "[129] I from the Nuclear Reprocessing Facilities Traced in Precipitation and Runoff in Northern Europe". In: *Environmental Science & Technology* 35.8 (Apr. 2001), pp. 1579–1586. ISSN: 0013-936X, 1520-5851. DOI: 10.1021/es001375n.

[38] Usha Rao et al. "Tracing the History of Nuclear Releases: Determination of [129] I in Tree Rings". In: *Environmental Science & Technology* 36.6 (Mar. 2002), pp. 1271–1275. ISSN: 0013-936X, 1520-5851. DOI: 10.1021/es011045i.

[39] Yasuyuki Muramatsu et al. "Studies with Natural and Anthropogenic Iodine Isotopes: Iodine Distribution and Cycling in the Global Environment". In: *Journal of Environmental Radioactivity* 74.1-3 (Jan. 2004), pp. 221–232. ISSN: 0265931X. DOI: `10.1016/j.jenvrad.2004.01.011`.

[40] J. Handl et al. "Biospheric 129I Concentrations in the Pre-nuclear and Nuclear Age:" in: *Health Physics* 65.3 (Sept. 1993), pp. 265–271. ISSN: 0017-9078. DOI: `10.1097/00004032-199309000-00003`.

[41] X.L. Hou et al. "Level and Origin of Iodine-129 in the Baltic Sea". In: *Journal of Environmental Radioactivity* 61.3 (Jan. 2002), pp. 331–343. ISSN: 0265931X. DOI: `10.1016/S0265-931X(01)00143-6`.

[42] Seigo Amachi et al. "Microbial Participation in Iodine Volatilization from Soils". In: *Environmental Science & Technology* 37.17 (Sept. 2003), pp. 3885–3890. ISSN: 0013-936X, 1520-5851. DOI: `10.1021/es0210751`.

[43] Bernard L. Cohen. "The Origin of I in Soil and the 129I Problem:" in: *Health Physics* 49.2 (Aug. 1985), pp. 279–285. ISSN: 0017-9078. DOI: `10.1097/00004032-198508000-00008`.

[44] Radiation UNSCotEoA. *Sources and Effects of Ionizing Radiation: Sources.* United Nations Publications, 2000.

[45] Christian Schall and Klaus G. Heumann. "GC Determination of Volatile Organoiodine and Organobromine Compounds in Arctic Seawater and Air Samples". In: *Fresenius' Journal of Analytical Chemistry* 346.6 (June 1993), pp. 717–722. ISSN: 1432-1130. DOI: `10.1007/BF00321279`.

[46] Matthew R. Bassford et al. "The Concurrent Observation of Methyl Iodide and Dimethyl Sulphide in Marine Air; Implications for Sources of Atmospheric Methyl Iodide". In: *Atmospheric Environment* 33.15 (July 1999), pp. 2373–2383. ISSN: 1352-2310. DOI: `10.1016/S1352-2310(98)00403-8`.

[47] J. M. Cainey, N. Derek, and P. B. Krummel. *Baseline Atmospheric Program Australia 2005-2006.* Melbourne, Australian Bureau of Meteorology and CSIRO Marine and Atmospheric . . ., 2007. ISBN: 1-921424-10-9.

[48] Hong-Jun Li, Yoko Yokouchi, and Hajime Akimoto. "Measurement of Methyl Halides in the Marine Atmosphere". In: *Atmospheric Environment* 33.12 (June 1999), pp. 1881–1887. ISSN: 13522310. DOI: `10.1016/S1352-2310(98)00303-3`.

[49] Barkley C. Sive et al. "A Large Terrestrial Source of Methyl Iodide". In: *Geophysical Research Letters* 34.17 (Sept. 2007). ISSN: 0094-8276. DOI: `10.1029/2007GL030528`.

[50] Werner Reifenhäuser and Klaus G. Heumann. "Determinations of Methyl Io-
      dide in the Antarctic Atmosphere and the South Polar Sea". In: *Atmospheric
      Environment. Part A. General Topics* 26.16 (Nov. 1992), pp. 2905–2912.
      ISSN: 0960-1686. DOI: 10.1016/0960-1686(92)90282-P.

[51] Yan Li et al. "Volatile Halocarbons in the Marine Atmosphere and Surface
      Seawater: Diurnal and Spatial Variations and Influences of Environmental
      Factors". In: *Atmospheric Environment* 214 (Oct. 2019), p. 116820. ISSN:
      13522310. DOI: 10.1016/j.atmosenv.2019.116820.

[52] E. Atlas et al. "Alkyl Nitrates, Nonmethane Hydrocarbons, and Halocarbon
      Gases over the Equatorial Pacific Ocean during SAGA 3". In: *Journal of
      Geophysical Research: Atmospheres* 98.D9 (Sept. 1993), pp. 16933–16947.
      ISSN: 0148-0227. DOI: 10.1029/93JD01005.

[53] Nicola J. Blake et al. "Distribution and Seasonality of Selected Hydrocarbons
      and Halocarbons over the Western Pacific Basin during PEM-West A and
      PEM-West B". In: *Journal of Geophysical Research: Atmospheres* 102.D23
      (Dec. 1997), pp. 28315–28331. ISSN: 0148-0227. DOI: 10.1029/97JD02538.

[54] Y. Yokouchi et al. "Distribution of Methyl Iodide, Ethyl Iodide, Bromoform,
      and Dibromomethane over the Ocean (East and Southeast Asian Seas and the
      Western Pacific)". In: *Journal of Geophysical Research: Atmospheres* 102.D7
      (Apr. 1997), pp. 8805–8809. ISSN: 0148-0227. DOI: 10.1029/96JD03384.

[55] Hong-Jun Li et al. "Distribution of Methyl Chloride, Methyl Bromide, and
      Methyl Iodide in the Marine Boundary Air over the Western Pacific and
      Southeastern Indian Ocean." In: *GEOCHEMICAL JOURNAL* 35.2 (2001),
      pp. 137–144. ISSN: 0016-7002. DOI: 10.2343/geochemj.35.137.

[56] Stephen D. Archer et al. "Marked Seasonality in the Concentrations and
      Sea-to-Air Flux of Volatile Iodocarbon Compounds in the Western English
      Channel". In: *Journal of Geophysical Research* 112.C8 (Aug. 2007), p. C08009.
      ISSN: 0148-0227. DOI: 10.1029/2006JC003963.

[57] D. S. Cohan et al. "Atmospheric Methyl Iodide at Cape Grim, Tasmania,
      from AGAGE Observations". In: *Journal of Atmospheric Chemistry* 44.2
      (Feb. 2003), pp. 131–150. ISSN: 1573-0662. DOI: 10.1023/A:1022481516151.

[58] C. E. Jones et al. "Coastal Measurements of Short-Lived Reactive Iodocar-
      bons and Bromocarbons at Roscoff, Brittany during the RHaMBLe Cam-
      paign". In: *Atmos. Chem. Phys.* 9.22 (Nov. 2009), pp. 8757–8769. ISSN:
      1680-7324. DOI: 10.5194/acp-9-8757-2009.

[59] Charlotte E. Jones et al. "Quantifying the Contribution of Marine Organic
      Gases to Atmospheric Iodine". In: *Geophysical Research Letters* 37.18 (Sept.
      2010). ISSN: 0094-8276. DOI: 10.1029/2010GL043990.

[60] M. K. W. Ko et al. "Very Short-Lived Halogen and Sulfur Substances". In: *Scientific Assessment of Ozone Depletion: 2002, Global Ozone Res. Monit. Proj. Rep* 47 (2003), pp. 2.1–2.57.

[61] Robert M. Moore and Wayne Groszko. "Methyl Iodide Distribution in the Ocean and Fluxes to the Atmosphere". In: *Journal of Geophysical Research: Oceans* 104.C5 (May 1999), pp. 11163–11171. ISSN: 01480227. DOI: `10.1029/1998JC900073`.

[62] Juliane C. Mössinger, Dudley E. Shallcross, and R. Anthony Cox. "UV–VIS Absorption Cross-Sections and Atmospheric Lifetimes of CH2Br2, CH2I2 and CH2BrI". In: *Journal of the Chemical Society, Faraday Transactions* 94.10 (1998), pp. 1391–1396. ISSN: 09565000, 13645455. DOI: `10.1039/a709160e`.

[63] Sébastien Allard et al. "Formation of Methyl Iodide on a Natural Manganese Oxide". In: *Water Research* 44.15 (Aug. 2010), pp. 4623–4629. ISSN: 0043-1354. DOI: `10.1016/j.watres.2010.06.008`.

[64] Frank Keppler et al. "Formation of Volatile Iodinated Alkanes in Soil: Results from Laboratory Studies". In: *Naturally Produced Organohalogens* 52.2 (July 2003), pp. 477–483. ISSN: 0045-6535. DOI: `10.1016/S0045-6535(03)00198-X`.

[65] Eva Duborská et al. "Production of Methyl-Iodide in the Environment". In: *Frontiers in Microbiology* 12 (2021). ISSN: 1664-302X.

[66] Yasuyuki Muramatsu and Satoshi Yoshida. "Volatilization of Methyl Iodide from the Soil-Plant System". In: *Atmospheric Environment* 29.1 (Jan. 1995), pp. 21–25. ISSN: 1352-2310. DOI: `10.1016/1352-2310(94)00220-F`.

[67] Martina Landini et al. "Metabolic Engineering of the Iodine Content in Arabidopsis". In: *Scientific Reports* 2.1 (Mar. 2012), p. 338. ISSN: 2045-2322. DOI: `10.1038/srep00338`.

[68] Robert C. Rhew et al. "Genetic Control of Methyl Halide Production in Arabidopsis". In: *Current Biology* 13.20 (Oct. 2003), pp. 1809–1813. ISSN: 0960-9822. DOI: `10.1016/j.cub.2003.09.055`.

[69] Fariborz Taghipour and Greg J. Evans. "Radioiodine Volatilization in the Presence of Organic Compounds". In: *Nuclear Technology* 134.2 (2001), pp. 208–220. ISSN: 0029-5450.

[70] Christopher E. Bagwell et al. "Microbial Methylation of Iodide in Unconfined Aquifer Sediments at the Hanford Site, USA". In: *Frontiers in Microbiology* 10 (2019). ISSN: 1664-302X.

[71] J. P. D. Abbatt et al. "Halogen Activation via Interactions with Environmental Ice and Snow in the Polar Lower Troposphere and Other Regions". In: *Atmospheric Chemistry and Physics* 12.14 (2012), pp. 6237–6271. DOI: `10.5194/acp-12-6237-2012`.

[72] W. R. Simpson et al. "Halogens and Their Role in Polar Boundary-Layer Ozone Depletion". In: *Atmospheric Chemistry and Physics* 7.16 (2007), pp. 4375–4418. DOI: `10.5194/acp-7-4375-2007`.

[73] B. J. Finlayson-Pitts. "The Tropospheric Chemistry of Sea Salt: A Molecular-Level View of the Chemistry of NaCl and NaBr". In: *Chemical Reviews* 103.12 (Dec. 2003), pp. 4801–4822. ISSN: 0009-2665. DOI: `10.1021/cr020653t`.

[74] U. Platt and G. Hönninger. "The Role of Halogen Species in the Troposphere". In: *Naturally Produced Organohalogens* 52.2 (July 2003), pp. 325–338. ISSN: 0045-6535. DOI: `10.1016/S0045-6535(03)00216-9`.

[75] Alfonso Saiz-Lopez and Roland von Glasow. "Reactive Halogen Chemistry in the Troposphere". In: *Chemical Society Reviews* 41.19 (2012), pp. 6448–6472. ISSN: 0306-0012. DOI: `10.1039/C2CS35208G`.

[76] R. von Glasow and P.J. Crutzen. "4.02 - Tropospheric Halogen Chemistry". In: *Treatise on Geochemistry*. Ed. by Heinrich D. Holland and Karl K. Turekian. Oxford: Pergamon, Jan. 2003, pp. 1–67. ISBN: 978-0-08-043751-4. DOI: `10.1016/B0-08-043751-6/04141-4`.

[77] William R. Simpson et al. "Tropospheric Halogen Chemistry: Sources, Cycling, and Impacts". In: *Chemical Reviews* 115.10 (May 2015), pp. 4035–4062. ISSN: 0009-2665. DOI: `10.1021/cr5006638`.

[78] R. Atkinson et al. "Evaluated Kinetic and Photochemical Data for Atmospheric Chemistry: Volume III – Gas Phase Reactions of Inorganic Halogens". In: *Atmospheric Chemistry and Physics* 7.4 (2007), pp. 981–1191. DOI: `10.5194/acp-7-981-2007`.

[79] Alfonso Saiz-Lopez and Roland von Glasow. "Reactive Halogen Chemistry in the Troposphere". In: *Chemical Society Reviews* 41.19 (2012), pp. 6448–6472. ISSN: 0306-0012. DOI: `10.1039/C2CS35208G`.

[80] Juan Carlos Gómez Martín, Peter Spietz, and John P. Burrows. "Kinetic and Mechanistic Studies of the I2/O3 Photochemistry". In: *The Journal of Physical Chemistry A* 111.2 (Jan. 2007), pp. 306–320. ISSN: 1089-5639. DOI: `10.1021/jp061186c`.

[81] J. C. Gómez Martín et al. "On the Mechanism of Iodine Oxide Particle Formation". In: *Physical Chemistry Chemical Physics* 15.37 (2013), pp. 15612–15622. ISSN: 1463-9076. DOI: `10.1039/C3CP51217G`.

[82] R. Sommariva, W.J. Bloss, and R. von Glasow. "Uncertainties in Gas-Phase Atmospheric Iodine Chemistry". In: *Atmospheric Environment* 57 (Sept. 2012), pp. 219–232. ISSN: 1352-2310. DOI: 10.1016/j.atmosenv.2012.04.032.

[83] Florent Louis et al. "Atmospheric Reactivity of CH3I and CH2I2 with OH Radicals: A Comparative Study of the H- versus I-abstraction". In: *Theoretical chemistry of atmospheric processes* 965.2 (May 2011), pp. 275–284. ISSN: 2210-271X. DOI: 10.1016/j.theochem.2010.09.022.

[84] Igor Agranovski, ed. *Aerosols - Science and Technology.* Weinheim: Wiley-VCH, 2010. ISBN: 978-3-527-32660-0.

[85] Hans R. Pruppacher, James D. Klett, and Pao K. Wang. "Microphysics of Clouds and Precipitation". In: *Aerosol Science and Technology* 28.4 (Jan. 1998), pp. 381–382. ISSN: 0278-6826. DOI: 10.1080/02786829808965531.

[86] William C. Hinds. *Aerosol Technology: Properties, Behavior, and Measurement of Airborne Particles.* 2nd ed. New York: Wiley, 1999. ISBN: 978-0-471-19410-1.

[87] Ulrich Pöschl. "Atmospheric Aerosols: Composition, Transformation, Climate and Health Effects". In: *Angewandte Chemie International Edition* 44.46 (Nov. 2005), pp. 7520–7540. ISSN: 1433-7851. DOI: 10.1002/anie.200501122.

[88] Sokan Adeaga Adewale Allen et al. "Secondary Inorganic Aerosols: Impacts on the Global Climate System and Human Health". In: *Biodiversity International Journal* 3.6 (Nov. 2019), pp. 249–259. ISSN: 2575906X. DOI: 10.15406/bij.2019.03.00152.

[89] Deepchandra Srivastava et al. "Formation of Secondary Organic Aerosols from Anthropogenic Precursors in Laboratory Studies". In: *npj Climate and Atmospheric Science* 5.1 (Mar. 2022), p. 22. ISSN: 2397-3722. DOI: 10.1038/s41612-022-00238-6.

[90] Paolo Laj and Karine Sellegri. "Les Aérosols Atmosphéeriques: Impacts Locaux, Effete g Lobaux". In: *Revue Française des Laboratoires* 2003.349 (Jan. 2003), pp. 23–34. ISSN: 0338-9898. DOI: 10.1016/S0338-9898(03)80466-3.

[91] J. W. Chi et al. "Sea Salt Aerosols as a Reactive Surface for Inorganic and Organic Acidic Gases in the Arctic Troposphere". In: *Atmos. Chem. Phys.* 15.19 (Oct. 2015), pp. 11341–11353. ISSN: 1680-7324. DOI: 10.5194/acp-15-11341-2015.

[92]   David D. Weis and George E. Ewing. "The Reaction of Nitrogen Dioxide
         with Sea Salt Aerosol". In: *The Journal of Physical Chemistry A* 103.25
         (June 1999), pp. 4865–4873. ISSN: 1089-5639. DOI: `10.1021/jp984488q`.

[93]   I. J. George and J. P. D. Abbatt. "Heterogeneous Oxidation of Atmospheric
         Aerosol Particles by Gas-Phase Radicals". In: *Nature Chemistry* 2.9 (Sept.
         2010), pp. 713–722. ISSN: 1755-4349. DOI: `10.1038/nchem.806`.

[94]   E. James Davis. "Interpretation of Uptake Coefficient Data Obtained with
         Flow Tubes". In: *The Journal of Physical Chemistry A* 112.9 (Mar. 2008),
         pp. 1922–1932. ISSN: 1089-5639. DOI: `10.1021/jp074939j`.

[95]   G. M. Underwood et al. "A Knudsen Cell Study of the Heterogeneous
         Reactivity of Nitric Acid on Oxide and Mineral Dust Particles". In: *The
         Journal of Physical Chemistry A* 105.27 (July 2001), pp. 6609–6620. ISSN:
         1089-5639. DOI: `10.1021/jp002223h`.

[96]   Hanaa Houjeij et al. "Interaction Process between Gaseous CH$_3$I and
         NaCl Particles: Implication for Iodine Dispersion in the Atmosphere". In:
         Environmental Science: Processes & Impacts 23.11 (2021), pp. 1771–1781.
         ISSN: 2050-7887, 2050-7895. DOI: `10.1039/D1EM00266J`.

[97]   Abdelwahid Mellouki et al. "The Outdoor Atmospheric Simulation Chamber
         of Orleans-France (HELIOS)". In: *AGU Fall Meeting Abstracts*. Vol. 2016.
         2016, A33E–0290.

[98]   Antoine Roose et al. "Classical Molecular Dynamics Study of Small-Chain
         Carboxylic Acid Aerosol Particles". In: *ACS Earth and Space Chemistry* 3.3
         (Mar. 2019), pp. 380–389. DOI: `10.1021/acsearthspacechem.8b00172`.

[99]   Josip Lovrić et al. "Water-Induced Organization of Palmitic Acid at the
         Surface of a Model Sea Salt Particle: A Molecular Dynamics Study". In: *The
         Journal of Physical Chemistry A* 120.51 (Dec. 2016), pp. 10141–10149. ISSN:
         1089-5639, 1520-5215. DOI: `10.1021/acs.jpca.6b07792`.

[100]   M. Stock et al. "Hygroscopic Properties of Atmospheric Aerosol Particles
         over the Eastern Mediterranean: Implications for Regional Direct Radiative
         Forcing under Clean and Polluted Conditions". In: *Atmos. Chem. Phys.* 11.9
         (May 2011), pp. 4251–4271. ISSN: 1680-7324. DOI: `10.5194/acp-11-4251-2011`.

[101]   E. Swietlicki et al. "Hygroscopic Properties of Submicrometer Atmospheric
         Aerosol Particles Measured with H-TDMA Instruments in Various Environ-
         ments—a Review". In: *Tellus B: Chemical and Physical Meteorology* 60.3
         (Jan. 2008), pp. 432–469. ISSN: null. DOI: `10.1111/j.1600-0889.2008.00350.x`.

[102]   Michael L. Chabinyc et al. "Gas-Phase Ionic Reactions: Dynamics and Mechanism of Nucleophilic Displacements". In: *Science* 279.5358 (Mar. 1998), pp. 1882–1886. DOI: `10.1126/science.279.5358.1882`.

[103]   E. Vöhringer-Martinez et al. "Water Catalysis of a Radical-Molecule Gas-Phase Reaction". In: *Science* 315.5811 (Jan. 2007), pp. 497–501. DOI: `10.1126/science.1134494`.

[104]   Simone Aloisio and Joseph S. Francisco. "Radical-Water Complexes in Earth's Atmosphere". In: *Accounts of Chemical Research* 33.12 (Dec. 2000), pp. 825–830. ISSN: 0001-4842. DOI: `10.1021/ar000097u`.

[105]   Robert J. Buszek, Joseph S. Francisco, and Josep M. Anglada. "Water Effects on Atmospheric Reactions". In: *International Reviews in Physical Chemistry* 30.3 (July 2011), pp. 335–369. ISSN: 0144-235X. DOI: `10.1080/0144235X.2011.634128`.

[106]   Sonia Taamalli et al. "Unraveling the Tropospheric Microhydration Processes of Iodous Acid HOIO". In: *ACS Earth and Space Chemistry* 4.1 (Jan. 2020), pp. 92–100. DOI: `10.1021/acsearthspacechem.9b00257`.

[107]   Sophie Sobanska et al. "Infrared Matrix-Isolation and Theoretical Studies of Interactions between CH3I and Water". In: *Journal of Molecular Structure* 1236 (July 2021), p. 130342. ISSN: 0022-2860. DOI: `10.1016/j.molstruc.2021.130342`.

[108]   Josep M. Anglada et al. "The Atmospheric Oxidation of CH3OOH by the OH Radical: The Effect of Water Vapor". In: *Physical Chemistry Chemical Physics* 19.19 (2017), pp. 12331–12342. ISSN: 1463-9076. DOI: `10.1039/C7CP01976A`.

[109]   Javier Gonzalez et al. "Impact of Water on the OH + HOCl Reaction". In: *Journal of the American Chemical Society* 133.10 (Mar. 2011), pp. 3345–3353. ISSN: 0002-7863. DOI: `10.1021/ja100976b`.

[110]   Mohamad A. Ali and Balaganesh Muthiah. "Effect of Water and Formic Acid on ·OH + CH4 Reaction: An Ab Initio/DFT Study". In: *Catalysts* 12.2 (2022). ISSN: 2073-4344. DOI: `10.3390/catal12020133`.

[111]   James E. Boulter, Christopher G. Morgan, and Jochen Marschall. "Ice Surfaces in the Mesosphere: Absence of Dangling Bonds in the Presence of Atomic Oxygen". In: *Geophysical Research Letters* 32.14 (July 2005). ISSN: 0094-8276. DOI: `10.1029/2005GL022560`.

[112]   Benjamin J. Murray and Eric J. Jensen. "Homogeneous Nucleation of Amorphous Solid Water Particles in the Upper Mesosphere". In: *Journal of Atmospheric and Solar-Terrestrial Physics* 72.1 (Jan. 2010), pp. 51–61. ISSN: 1364-6826. DOI: `10.1016/j.jastp.2009.10.007`.

[113] C. Austen Angell. "Amorphous Water". In: *Annual Review of Physical Chemistry* 55.1 (June 2004), pp. 559–583. ISSN: 0066-426X. DOI: 10.1146/annurev.physchem.55.091602.094156.

[114] J. Paul Devlin and V. Buch. "Surface of Ice as Viewed from Combined Spectroscopic and Computer Modeling Studies". In: *The Journal of Physical Chemistry* 99.45 (Nov. 1995), pp. 16534–16548. ISSN: 0022-3654. DOI: 10.1021/j100045a010.

[115] C. Martin, C. Manca, and P. Roubin. "Adsorption of Small Molecules on Amorphous Ice: Volumetric and FT-IR Isotherm Co-Measurements: Part II. The Case of CO". In: *Surface Science* 502–503 (Apr. 2002), pp. 280–284. ISSN: 0039-6028. DOI: 10.1016/S0039-6028(01)01964-1.

[116] Antoine Patt et al. "Adsorption of CO and N2 Molecules at the Surface of Solid Water. A Grand Canonical Monte Carlo Study". In: *The Journal of Chemical Physics* 153.20 (Nov. 2020), p. 204502. ISSN: 0021-9606. DOI: 10.1063/5.0031254.

[117] J. A. Noble et al. "Unveiling the Surface Structure of Amorphous Solid Water via Selective Infrared Irradiation of OH Stretching Modes". In: *The Journal of Physical Chemistry Letters* 5.5 (Mar. 2014), pp. 826–829. DOI: 10.1021/jz5000066.

[118] J. A. Noble et al. "IR Selective Irradiations of Amorphous Solid Water Dangling Modes: Irradiation vs Annealing Effects". In: *The Journal of Physical Chemistry C* 118.35 (Sept. 2014), pp. 20488–20495. ISSN: 1932-7447. DOI: 10.1021/jp506943k.

[119] O. Mishima, L. D. Calvert, and E. Whalley. "'Melting Ice' I at 77 K and 10 Kbar: A New Method of Making Amorphous Solids". In: *Nature* 310.5976 (Aug. 1984), pp. 393–395. ISSN: 1476-4687. DOI: 10.1038/310393a0.

[120] Osamu Mishima. "Reversible First-order Transition between Two H2O Amorphs at ∼0.2 GPa and ∼135 K". In: *The Journal of Chemical Physics* 100.8 (Apr. 1994), pp. 5910–5912. ISSN: 0021-9606. DOI: 10.1063/1.467103.

[121] Osamu Mishima, K. Takemura, and K. Aoki. "Visual Observations of the Amorphous-Amorphous Transition in H2O Under Pressure". In: *Science* 254.5030 (Oct. 1991), pp. 406–408. DOI: 10.1126/science.254.5030.406.

[122] V. Buch and J. P. Devlin. "Spectra of Dangling OH Bonds in Amorphous Ice: Assignment to 2- and 3-coordinated Surface Molecules". In: *The Journal of Chemical Physics* 94.5 (Mar. 1991), pp. 4091–4092. ISSN: 0021-9606. DOI: 10.1063/1.460638.

[123]   Eric Michoulier et al. "Perturbation of the Surface of Amorphous Solid
        Water by the Adsorption of Polycyclic Aromatic Hydrocarbons". In: *The
        Journal of Physical Chemistry C* 124.5 (Feb. 2020), pp. 2994–3001. ISSN:
        1932-7447, 1932-7455. DOI: 10.1021/acs.jpcc.9b09499.

[124]   C. Manca and A. Allouche. "Quantum Study of the Adsorption of Small
        Molecules on Ice: The Infrared Frequency of the Surface Hydroxyl Group
        and the Vibrational Stark Effect". In: *The Journal of Chemical Physics* 114.9
        (Mar. 2001), pp. 4226–4234. ISSN: 0021-9606. DOI: 10.1063/1.1331106.

[125]   David Hollenbach and E. E. Salpeter. "Surface Recombination of Hydrogen
        Molecules". In: *The Astrophysical Journal* 163 (Jan. 1971), p. 155. ISSN:
        0004-637X. DOI: 10.1086/150754.

[126]   G. Manicò et al. "Laboratory Measurements of Molecular Hydrogen Forma-
        tion on Amorphous Water Ice". In: *The Astrophysical Journal* 548.2 (Feb.
        2001), p. L253. ISSN: 0004-637X. DOI: 10.1086/319116.

[127]   M. Minissale et al. "Quantum Tunneling of Oxygen Atoms on Very Cold
        Surfaces". In: *Physical Review Letters* 111.5 (July 2013), p. 053201. DOI:
        10.1103/PhysRevLett.111.053201.

[128]   A. G. G. M. Tielens and W. Hagen. "Model Calculations of the Molecular
        Composition of Interstellar Grain Mantles". In: *Astronomy and Astrophysics*
        114 (Oct. 1982), pp. 245–260. ISSN: 0004-6361.

[129]   J. A. Noble et al. "CO2 FORMATION IN QUIESCENT CLOUDS: AN
        EXPERIMENTAL STUDY OF THE CO + OH PATHWAY". In: *The
        Astrophysical Journal* 735.2 (June 2011), p. 121. ISSN: 0004-637X. DOI:
        10.1088/0004-637X/735/2/121.

[130]   Yasuhiro Oba et al. "EXPERIMENTAL STUDY OF CO2 FORMATION BY
        SURFACE REACTIONS OF NON-ENERGETIC OH RADICALS WITH
        CO MOLECULES". In: *The Astrophysical Journal Letters* 712.2 (Mar. 2010),
        p. L174. ISSN: 2041-8205. DOI: 10.1088/2041-8205/712/2/L174.

[131]   M. Tafalla et al. "Systematic Molecular Differentiation in Starless Cores".
        In: *The Astrophysical Journal* 569.2 (Apr. 2002), p. 815. ISSN: 0004-637X.
        DOI: 10.1086/339321.

[132]   Naoki Watanabe and Akira Kouchi. "Efficient Formation of Formaldehyde
        and Methanol by the Addition of Hydrogen Atoms to CO in H2O-CO Ice
        at 10 K". In: *The Astrophysical Journal* 571.2 (May 2002), p. L173. ISSN:
        0004-637X. DOI: 10.1086/341412.

[133]   Eric Michoulier et al. "Adsorption of PAHs on Interstellar Ice Viewed by
        Classical Molecular Dynamics". In: *Physical Chemistry Chemical Physics*
        20.13 (2018), pp. 8753–8764. ISSN: 1463-9076. DOI: 10.1039/C8CP00593A.

[134] Alice J. DeSimone et al. "Photodissociation of Methyl Iodide Adsorbed on Low-Temperature Amorphous Ice Surfaces". In: *The Journal of Chemical Physics* 138.8 (Feb. 2013), p. 084703. ISSN: 0021-9606. DOI: 10.1063/1.4790585.

[135] V. Sadtchenko et al. "Interactions of CCl4 with Thin D2O Amorphous Ice Films, Part I: A Nanoscale Probe of Ice Morphology". In: *The Journal of Physical Chemistry B* 104.11 (Mar. 2000), pp. 2511–2521. ISSN: 1520-6106. DOI: 10.1021/jp9926185.

[136] Aleksey B. Alekseyev et al. "An Ab Initio Study of the CH3I Photodissociation. I. Potential Energy Surfaces". In: *The Journal of Chemical Physics* 126.23 (June 2007), p. 234102. ISSN: 0021-9606. DOI: 10.1063/1.2736695.

[137] Aleksey B. Alekseyev, Heinz-Peter Liebermann, and Robert J. Buenker. "An Ab Initio Study of the CH3I Photodissociation. II. Transition Moments and Vibrational State Control of the I* Quantum Yields". In: *The Journal of Chemical Physics* 126.23 (June 2007), p. 234103. ISSN: 0021-9606. DOI: 10.1063/1.2736696.

[138] John F. Black and Ivan Powis. "Competing Ionization and Dissociation of Methyl Iodide in the One-Photon A-band Region". In: *Chemical Physics Letters* 148.6 (July 1988), pp. 479–485. ISSN: 0009-2614. DOI: 10.1016/0009-2614(88)80317-8.

[139] John F. Black and Ivan Powis. "Photofragment Investigations of the 280 Nm Photodissociation of Methyl Iodide Using Rempii Atom Detection". In: *Chemical Physics* 125.2 (Oct. 1988), pp. 375–388. ISSN: 0301-0104. DOI: 10.1016/0301-0104(88)87090-3.

[140] Yifeng Jiang, Maria R. Giorgi-Arnazzi, and Richard B. Bernstein. "Concurrent Photodissociation and Multiphoton Ionization Processes in CH3I from 266–307 Nm". In: *Chemical Physics* 106.1 (July 1986), pp. 171–178. ISSN: 0301-0104. DOI: 10.1016/0301-0104(86)87048-3.

[141] Guosheng Li and Hyun Jin Hwang. "State-to-State Correlated Study of CD3I Photodissociation at 266 and 304nm". In: *The Journal of Chemical Physics* 124.24 (June 2006), p. 244306. ISSN: 0021-9606. DOI: 10.1063/1.2212938.

[142] Guosheng Li, Yun Kyung Shin, and Hyun Jin Hwang. "State-to-State Reaction Dynamics of CH3I Photodissociation at 304 Nm". In: *The Journal of Physical Chemistry A* 109.41 (Oct. 2005), pp. 9226–9231. ISSN: 1089-5639. DOI: 10.1021/jp054421k.

[143]   Diane M. Szaflarski and M. A. El-Sayed. "Kinetic Energy and Formation Mechanisms of Iodine(1+) and Methyl(1+) from 266-Nm Picosecond versus Nanosecond Laser Multiphoton Absorption". In: *The Journal of Physical Chemistry* 92.8 (Apr. 1988), pp. 2234–2239. ISSN: 0022-3654. DOI: 10.1021/j100319a030.

[144]   G.N.A. Van Veen et al. "The Excitation of the Umbrella Mode of CH3 and CD3 Formed from Photodissociation of CH3I and CD3I at 248 Nm". In: *Chemical Physics* 87.3 (July 1984), pp. 405–417. ISSN: 0301-0104. DOI: 10.1016/0301-0104(84)85121-6.

[145]   Anne M. Woodward et al. "Vibrational Analysis of the ~A-~X Photodissociation Spectrum of Methyl Iodide". In: *The Journal of Physical Chemistry* 90.2 (Jan. 1986), pp. 274–278. ISSN: 0022-3654. DOI: 10.1021/j100274a014.

[146]   S. R. Coon, K. B. Myli, and V. H. Grassian. "Photoproduct Characterization and Dynamics in the 248 Nm Photolysis of CH3I Thin Films on Ag(111)". In: *The Journal of Physical Chemistry* 99.44 (Nov. 1995), pp. 16416–16424. ISSN: 0022-3654. DOI: 10.1021/j100044a032.

[147]   D. Howard Fairbrother et al. "Molecular Orientation and Surface Morphology in Methyl Iodide Films Grown on MgO(100) Probed by Photodissociation". In: *The Journal of Physical Chemistry* 98.49 (Dec. 1994), pp. 13042–13049. ISSN: 0022-3654. DOI: 10.1021/j100100a037.

[148]   D. Howard Fairbrother et al. "The Role of Adsorbate Structure in the Photodissociation Dynamics of Adsorbed Species: Methyl Iodide/MgO(100)". In: *The Journal of Chemical Physics* 102.18 (May 1995), pp. 7267–7276. ISSN: 0021-9606. DOI: 10.1063/1.469038.

[149]   Simon J. Garrett et al. "The Adsorption and Photochemistry of CD3I on TiO2(110)". In: *The Journal of Chemical Physics* 100.6 (Mar. 1994), pp. 4615–4625. ISSN: 0021-9606. DOI: 10.1063/1.466294.

[150]   Simon J. Garrett et al. "Wavelength Dependence of the Photodissociation and Photodesorption of CD3I Adsorbed on the TiO2(110) Surface". In: *The Journal of Chemical Physics* 100.6 (Mar. 1994), pp. 4626–4636. ISSN: 0021-9606. DOI: 10.1063/1.466295.

[151]   Victor P Holbert et al. "The Photochemistry of CD3I Adsorbed on the TiO2(110) Surface". In: *Surface Science* 346.1 (Feb. 1996), pp. 189–205. ISSN: 0039-6028. DOI: 10.1016/0039-6028(95)00899-3.

[152]   E. T. Jensen. "Near-UV Photodissociation of Oriented CH3I Adsorbed on Cu(110)–I". In: *The Journal of Chemical Physics* 123.20 (Nov. 2005), p. 204709. ISSN: 0021-9606. DOI: 10.1063/1.2126593.

[153]   Seong Han Kim et al. "Photoreactions of Methyl Iodide Multilayers on the
        TiO2(110) Surface". In: *Journal of Vacuum Science & Technology A* 14.3
        (May 1996), pp. 1557–1561. ISSN: 0734-2101. DOI: `10.1116/1.580295`.

[154]   Seong Han Kim, Peter C. Stair, and Eric Weitz. "UV-induced Desorption
        of CH3X (X=I and Br)/TiO2(110)". In: *The Journal of Chemical Physics*
        108.12 (Mar. 1998), pp. 5080–5088. ISSN: 0021-9606. DOI: `10.1063/1.475914`.

[155]   Abneesh Srivastava and Richard M. Osgood. "State-Resolved Dynamics of
        248 Nm Methyl-Iodide Fragmentation on GaAs(110)". In: *The Journal of
        Chemical Physics* 119.19 (Nov. 2003), pp. 10298–10306. ISSN: 0021-9606.
        DOI: `10.1063/1.1619944`.

[156]   X.-L Zhou and J.M White. "Alkyl Halide Photochemistry on Ag(111): III.
        Methyl Iodide". In: *Surface Science* 241.3 (Jan. 1991), pp. 270–278. ISSN:
        0039-6028. DOI: `10.1016/0039-6028(91)90087-9`.

[157]   A. Allanic and M. J. Rossi. "Heterogeneous Reactions of HOI on Substrates of
        Atmospheric Importance". In: *Journal of Geophysical Research: Atmospheres*
        104.D15 (Aug. 1999), pp. 18689–18696. ISSN: 0148-0227. DOI: `10.1029/1999JD900285`.

[158]   Stephen B. Barone, Mark A. Zondlo, and Margaret A. Tolbert. "Investigation
        of the Heterogeneous Reactivity of HCl, HBr, and HI on Ice Surfaces". In:
        The Journal of Physical Chemistry A 103.48 (Dec. 1999), pp. 9717–9730.
        ISSN: 1089-5639. DOI: `10.1021/jp990400c`.

[159]   Carl J. Percival, Juliane C. Mössinger, and R. Anthony Cox. "The Uptake
        of HI and HBr on Ice". In: *Physical Chemistry Chemical Physics* 1.19 (1999),
        pp. 4565–4570. ISSN: 1463-9076. DOI: `10.1039/A904651H`.

[160]   A. Allanic et al. "The Heterogeneous Kinetics of the Reactions ClONO2 +
        HX/Ice (X = Br, I), BrONO2 + HI/Ice and the Reactivity of the Interhalo-
        gens BrCl, ICl and IBr with HX/Ice (X = Cl, Br, I) in the Temperature
        Range 180 to 205 K". In: 214.11 (2000), p. 1479. DOI: `10.1524/zpch.2000.214.11.1479`.

[161]   E. R. Miller, G. D. Muirhead, and E. T. Jensen. "Mechanisms for the
        Near-UV Photodissociation of CH3I on D2O/Cu(110)". In: *The Journal
        of Chemical Physics* 138.8 (Feb. 2013), p. 084702. ISSN: 0021-9606. DOI:
        `10.1063/1.4770225`.

[162]   Youngku Sohn. "Thermal and Photochemistry of Methyl Iodide on Ice Film
        Grown on Cu(111)". In: *Bulletin of the Korean Chemical Society* 30.7 (July
        2009), pp. 1470–1474. ISSN: 0253-2964/1229-5949. DOI: `10.5012/BKCS.2009.30.7.1470`.

[163] B. H. Bransden and C. J. Joachain. *Physics of Atoms and Molecules*. London ; New York: Longman, 1986. ISBN: 978-0-582-44401-0.

[164] B. T. Geilikman. "The Adiabatic Approximation and Frohlich Model in the Theory of Metals". In: *Journal of Low Temperature Physics* 4.2 (Feb. 1971), pp. 189–208. ISSN: 0022-2291, 1573-7357. DOI: 10.1007/BF00628391.

[165] E. G. Brovman and Yu. Kagan. "The Phonon Spectrum of Metals". In: *Soviet Journal of Experimental and Theoretical Physics* 25 (Aug. 1967), p. 365. ISSN: 1063-7761.

[166] Göran Grimvall. *The Electron-Phonon Interaction in Metals*. Selected Topics in Solid State Physics 16. Amsterdam ; New York: North-Holland Pub. Co. : sole distributors for the U.S.A. and Canada, Elsevier North-Holland, 1981. ISBN: 978-0-444-86105-4.

[167] Douglas Rayner Hartree and Haverford College William Pyle Philips Fund. *The Calculation of Atomic Structures*. J. Wiley, 1957.

[168] J. C. Slater. "The Theory of Complex Spectra". In: *Physical Review* 34.10 (Nov. 1929), pp. 1293–1322. DOI: 10.1103/PhysRev.34.1293.

[169] L.D. Landau and E.M. Lifshitz. *Quantum Mechanics: Non-relativistic Theory*. Teoreticheskaiafizika. Elsevier Science, 2013. ISBN: 978-1-4831-4912-7.

[170] J. Callaway. *Quantum Theory of the Solid State*. Elsevier Science, 2013. ISBN: 978-1-4832-8828-4.

[171] C. C. J. Roothaan. "New Developments in Molecular Orbital Theory". In: *Reviews of Modern Physics* 23.2 (Apr. 1951), pp. 69–89. DOI: 10.1103/RevModPhys.23.69.

[172] G. G. Hall and John Edward Lennard-Jones. "The Molecular Orbital Theory of Chemical Valency VIII. A Method of Calculating Ionization Potentials". In: *Proceedings of the Royal Society of London. Series A. Mathematical and Physical Sciences* 205.1083 (1951), pp. 541–552. DOI: 10.1098/rspa.1951.0048. eprint: https://royalsocietypublishing.org/doi/pdf/10.1098/rspa.1951.0048.

[173] C.J. Cramer. *Essentials of Computational Chemistry: Theories and Models*. Wiley, 2005. ISBN: 978-0-470-09183-8.

[174] E. Perlt. *Basis Sets in Computational Chemistry*. Lecture Notes in Chemistry. Springer International Publishing, 2021. ISBN: 978-3-030-67262-1.

[175] J. C. Slater. "Atomic Shielding Constants". In: *Physical Review* 36.1 (July 1930), pp. 57–64. DOI: 10.1103/PhysRev.36.57.

[176] Peter M.W. Gill. "Molecular Integrals Over Gaussian Basis Functions". In: *Advances in Quantum Chemistry*. Ed. by John R. Sabin and Michael C. Zerner. Vol. 25. Academic Press, Jan. 1994, pp. 141–205. ISBN: 0065-3276. DOI: `10.1016/S0065-3276(08)60019-2`.

[177] R McWeeny. "Gaussian Approximations, to Wave Functions". In: *Nature* 166.4209 (1950), pp. 21–22. ISSN: 0028-0836.

[178] W. J. Hehre, R. F. Stewart, and J. A. Pople. "Self-Consistent Molecular-Orbital Methods. I. Use of Gaussian Expansions of Slater-Type Atomic Orbitals". In: *The Journal of Chemical Physics* 51.6 (Sept. 1969), pp. 2657–2664. ISSN: 0021-9606. DOI: `10.1063/1.1672392`.

[179] R. Ditchfield, W. J. Hehre, and J. A. Pople. "Self-Consistent Molecular-Orbital Methods. IX. An Extended Gaussian-Type Basis for Molecular-Orbital Studies of Organic Molecules". In: *The Journal of Chemical Physics* 54.2 (Jan. 1971), pp. 724–728. ISSN: 0021-9606. DOI: `10.1063/1.1674902`.

[180] Thom H. Dunning. "Gaussian Basis Sets for Use in Correlated Molecular Calculations. I. The Atoms Boron through Neon and Hydrogen". In: *The Journal of Chemical Physics* 90.2 (Jan. 1989), pp. 1007–1023. ISSN: 0021-9606, 1089-7690. DOI: `10.1063/1.456153`.

[181] Felix Bloch. "Über Die Quantenmechanik Der Elektronen in Kristallgittern". In: *Zeitschrift für Physik* 52.7 (July 1929), pp. 555–600. ISSN: 0044-3328. DOI: `10.1007/BF01339455`.

[182] S.F. Boys and F. Bernardi. "The Calculation of Small Molecular Interactions by the Differences of Separate Total Energies. Some Procedures with Reduced Errors". In: *Molecular Physics* 19.4 (Oct. 1970), pp. 553–566. ISSN: 0026-8976. DOI: `10.1080/00268977000101561`.

[183] Chr. Møller and M. S. Plesset. "Note on an Approximation Treatment for Many-Electron Systems". In: *Physical Review* 46.7 (Oct. 1934), pp. 618–622. DOI: `10.1103/PhysRev.46.618`.

[184] JWS Rayleigh. "The Theory of Sound, Article 88, Vol. 1". In: *2nd revised edn. New York: Dover (reprint 1945)* (1894), pp. 110–111.

[185] E. Schrödinger. "Quantisierung Als Eigenwertproblem". In: *Annalen der Physik* 385.13 (Jan. 1926), pp. 437–490. ISSN: 0003-3804. DOI: `10.1002/andp.19263851302`.

[186] Attila Szabo and Neil S. Ostlund. *Modern Quantum Chemistry: Introduction to Advanced Electronic Structure Theory*. Mineola, N.Y: Dover Publications, 1996. ISBN: 978-0-486-69186-2.

[187] Dieter Cremer. "Møller-Plesset Perturbation Theory: From Small Molecule Methods to Methods for Thousands of Atoms: Møller-Plesset Perturbation Theory". In: *Wiley Interdisciplinary Reviews: Computational Molecular Science* 1.4 (July 2011), pp. 509–530. ISSN: 17590876. DOI: `10.1002/wcms.58`.

[188] Ira N. Levine. *Quantum Chemistry*. Seventh edition. Boston: Pearson, 2014. ISBN: 978-0-321-80345-0.

[189] Krishnan Raghavachari et al. "A Fifth-Order Perturbation Comparison of Electron Correlation Theories". In: *Chemical Physics Letters* 157.6 (May 1989), pp. 479–483. ISSN: 0009-2614. DOI: `10.1016/S0009-2614(89)87395-6`.

[190] P. Hohenberg and W. Kohn. "Inhomogeneous Electron Gas". In: *Physical Review* 136.3B (Nov. 1964), B864–B871. ISSN: 0031-899X. DOI: `10.1103/PhysRev.136.B864`.

[191] W. Kohn and L. J. Sham. "Self-Consistent Equations Including Exchange and Correlation Effects". In: *Physical Review* 140.4A (Nov. 1965), A1133–A1138. ISSN: 0031-899X. DOI: `10.1103/PhysRev.140.A1133`.

[192] John Michael Wills. *Full-Potential Electronic Structure Method: Energy and Force Calculations with Density Functional and Dynamical Mean Field Theory*. Springer Series in Solid-State Sciences 167. Berlin Heidelberg New York: Springer, 2010. ISBN: 978-3-642-15144-6.

[193] Stefano Baroni et al. "Phonons and Related Crystal Properties from Density-Functional Perturbation Theory". In: *Reviews of Modern Physics* 73.2 (July 2001), pp. 515–562. DOI: `10.1103/RevModPhys.73.515`.

[194] Hans Hellmann. "Einfuhrung in Die Quantenchemie". In: (1937).

[195] R. P. Feynman. "Forces in Molecules". In: *Physical Review* 56.4 (Aug. 1939), pp. 340–343. DOI: `10.1103/PhysRev.56.340`.

[196] H. Goldstein, C.P. Poole, and J.L. Safko. *Classical Mechanics*. Addison Wesley, 2002. ISBN: 978-0-201-65702-9.

[197] Ricardo A. Broglia et al. "Phonons: Harmonic Approximation". In: *Solid State Physics of Finite Systems: Metal Clusters, Fullerenes, Atomic Wires*. Ed. by Ricardo A. Broglia et al. Berlin, Heidelberg: Springer Berlin Heidelberg, 2004, pp. 105–130. ISBN: 978-3-662-09938-4. DOI: `10.1007/978-3-662-09938-4_6`.

[198] P. D. DeCicco, F. A. Johnson, and Robert Allan Smith. "The Quantum Theory of Lattice Dynamics. IV". In: *Proceedings of the Royal Society of London. A. Mathematical and Physical Sciences* 310.1500 (Apr. 1969), pp. 111–119. DOI: 10.1098/rspa.1969.0066.

[199] Robert M. Pick, Morrel H. Cohen, and Richard M. Martin. "Microscopic Theory of Force Constants in the Adiabatic Approximation". In: *Physical Review B* 1.2 (Jan. 1970), pp. 910–920. DOI: 10.1103/PhysRevB.1.910.

[200] R. Shankar. *Principles of Quantum Mechanics.* New York, NY: Springer US, 1994. ISBN: 978-1-4757-0578-2 978-1-4757-0576-8. DOI: 10.1007/978-1-4757-0576-8.

[201] Donald A. McQuarrie and John D. Simon. *Molecular Thermodynamics.* Sausalito, Calif: University Science Books, 1999. ISBN: 978-1-891389-05-4.

[202] Harold C. Urey and Charles A. Bradley. "The Vibrations of Pentatonic Tetrahedral Molecules". In: *Physical Review* 38.11 (Dec. 1931), pp. 1969–1978. DOI: 10.1103/PhysRev.38.1969.

[203] C.J. Cramer. *Essentials of Computational Chemistry: Theories and Models.* Wiley, 2013. ISBN: 978-1-118-71227-6.

[204] Johann Gasteiger and Mario Marsili. "Iterative Partial Equalization of Orbital Electronegativity—a Rapid Access to Atomic Charges". In: *Tetrahedron* 36.22 (Jan. 1980), pp. 3219–3228. ISSN: 0040-4020. DOI: 10.1016/0040-4020(80)80168-2.

[205] R. S. Mulliken. "Electronic Population Analysis on LCAO–MO Molecular Wave Functions. I". In: *The Journal of Chemical Physics* 23.10 (Oct. 1955), pp. 1833–1840. ISSN: 0021-9606. DOI: 10.1063/1.1740588.

[206] Frank A. Momany. "Determination of Partial Atomic Charges from Ab Initio Molecular Electrostatic Potentials. Application to Formamide, Methanol, and Formic Acid". In: *The Journal of Physical Chemistry* 82.5 (Mar. 1978), pp. 592–601. ISSN: 0022-3654, 1541-5740. DOI: 10.1021/j100494a019.

[207] S. R. Cox and D. E. Williams. "Representation of the Molecular Electrostatic Potential by a Net Atomic Charge Model". In: *Journal of Computational Chemistry* 2.3 (1981), pp. 304–323. ISSN: 0192-8651, 1096-987X. DOI: 10.1002/jcc.540020312.

[208] U. Chandra Singh and Peter A. Kollman. "An Approach to Computing Electrostatic Charges for Molecules". In: *Journal of Computational Chemistry* 5.2 (Apr. 1984), pp. 129–145. ISSN: 0192-8651, 1096-987X. DOI: 10.1002/jcc.540050204.

[209]   Scott J. Weiner et al. "A New Force Field for Molecular Mechanical Simulation of Nucleic Acids and Proteins". In: *Journal of the American Chemical Society* 106.3 (Feb. 1984), pp. 765–784. ISSN: 0002-7863, 1520-5126. DOI: `10.1021/ja00315a051`.

[210]   Scott J. Weiner et al. "An All Atom Force Field for Simulations of Proteins and Nucleic Acids: An All Atom Force Field". In: *Journal of Computational Chemistry* 7.2 (Apr. 1986), pp. 230–252. ISSN: 01928651. DOI: `10.1002/jcc.540070216`.

[211]   Joey W. Storer et al. "Class IV Charge Models: A New Semiempirical Approach in Quantum Chemistry". In: *Journal of Computer-Aided Molecular Design* 9.1 (Feb. 1995), pp. 87–110. ISSN: 1573-4951. DOI: `10.1007/BF00117280`.

[212]   William L. Jorgensen et al. "Comparison of Simple Potential Functions for Simulating Liquid Water". In: *The Journal of Chemical Physics* 79.2 (July 1983), pp. 926–935. ISSN: 0021-9606. DOI: `10.1063/1.445869`.

[213]   Brent H. Besler, Kenneth M. Merz Jr., and Peter A. Kollman. "Atomic Charges Derived from Semiempirical Methods". In: *Journal of Computational Chemistry* 11.4 (May 1990), pp. 431–439. ISSN: 0192-8651. DOI: `10.1002/jcc.540110404`.

[214]   Christopher I. Bayly et al. "A Well-Behaved Electrostatic Potential Based Method Using Charge Restraints for Deriving Atomic Charges: The RESP Model". In: *The Journal of Physical Chemistry* 97.40 (Oct. 1993), pp. 10269–10280. ISSN: 0022-3654, 1541-5740. DOI: `10.1021/j100142a004`.

[215]   Zhifeng Jing et al. "Polarizable Force Fields for Biomolecular Simulations: Recent Advances and Applications". In: *Annual Review of Biophysics, Vol 40* 48.1 (May 2019), pp. 371–394. ISSN: 1936-122X, 1936-1238. DOI: `10.1146/annurev-biophys-070317-033349`.

[216]   Justin A. Lemkul et al. "An Empirical Polarizable Force Field Based on the Classical Drude Oscillator Model: Development History and Recent Applications". In: *Chemical Reviews* 116.9 (May 2016), pp. 4983–5013. ISSN: 0009-2665, 1520-6890. DOI: `10.1021/acs.chemrev.5b00505`.

[217]   Garland R. Marshall. "Limiting Assumptions in Molecular Modeling: Electrostatics". In: *Journal of computer-aided molecular design* 27.2 (Feb. 2013), pp. 107–114. ISSN: 0920-654X, 1573-4951. DOI: `10.1007/s10822-013-9634-x`.

[218]   Omar Demerdash, Lee-Ping Wang, and Teresa Head-Gordon. "Advanced Models for Water Simulations". In: *Wiley Interdisciplinary Reviews: Computational Molecular Science* 8.1 (Jan. 2018). ISSN: 1759-0876, 1759-0884.

[219]   Steven W. Rick and B. J. Berne. "Dynamical Fluctuating Charge Force
        Fields: The Aqueous Solvation of Amides". In: *Journal of the American
        Chemical Society* 118.3 (Jan. 1996), pp. 672–679. ISSN: 0002-7863. DOI:
        `10.1021/ja952535b`.

[220]   P. Drude. "Zur Elektronentheorie Der Metalle". In: *Annalen der Physik*
        306.3 (Jan. 1900), pp. 566–613. ISSN: 0003-3804. DOI: `10.1002/andp.`
        `19003060312`.

[221]   James Caldwell, Liem X. Dang, and Peter A. Kollman. "Implementation
        of Nonadditive Intermolecular Potentials by Use of Molecular Dynamics:
        Development of a Water-Water Potential and Water-Ion Cluster Interactions".
        In: *Journal of the American Chemical Society* 112.25 (Dec. 1990), pp. 9144–
        9147. ISSN: 0002-7863. DOI: `10.1021/ja00181a017`.

[222]   Christian J. Burnham et al. "The Parametrization of a Thole-type All-Atom
        Polarizable Water Model from First Principles and Its Application to the
        Study of Water Clusters (N=2–21) and the Phonon Spectrum of Ice Ih". In:
        The Journal of Chemical Physics 110.9 (Mar. 1999), pp. 4566–4581. ISSN:
        0021-9606. DOI: `10.1063/1.478797`.

[223]   Pengyu Ren and Jay W. Ponder. "Polarizable Atomic Multipole Water
        Model for Molecular Mechanics Simulation". In: *The Journal of Physical
        Chemistry B* 107.24 (June 2003), pp. 5933–5947. ISSN: 1520-6106. DOI:
        `10.1021/jp027815+`.

[224]   Igor V. Leontyev and Alexei A. Stuchebrukhov. "Polarizable Molecular
        Interactions in Condensed Phase and Their Equivalent Nonpolarizable
        Models". In: *The Journal of Chemical Physics* 141.1 (July 2014), p. 014103.
        ISSN: 0021-9606, 1089-7690. DOI: `10.1063/1.4884276`.

[225]   Alena Habartová, Kalliat T. Valsaraj, and Martina Roeselová. "Molecular
        Dynamics Simulations of Small Halogenated Organics at the Air–Water
        Interface: Implications in Water Treatment and Atmospheric Chemistry".
        In: *Journal of Physical Chemistry A* 117.38 (Sept. 2013), pp. 9205–9215.
        ISSN: 1089-5639, 1520-5215. DOI: `10.1021/jp405292k`.

[226]   R.W Hockney, S.P Goel, and J.W Eastwood. "Quiet High-Resolution Com-
        puter Models of a Plasma". In: *Journal of Computational Physics* 14.2 (Feb.
        1974), pp. 148–158. ISSN: 0021-9991. DOI: `10.1016/0021-9991(74)90010-`
        `2`.

[227]   Ernst Hairer et al. "Geometric Numerical Integration". In: *Oberwolfach
        Reports* (2006), pp. 805–882. ISSN: 1660-8933. DOI: `10.4171/OWR/2006/14`.

[228]   Jean-Paul Ryckaert, Giovanni Ciccotti, and Herman J.C Berendsen. "Numerical Integration of the Cartesian Equations of Motion of a System with Constraints: Molecular Dynamics of n-Alkanes". In: *Journal of Computational Physics* 23.3 (Mar. 1977), pp. 327–341. ISSN: 0021-9991. DOI: `10.1016/0021-9991(77)90098-5`.

[229]   P. P. Ewald. "Die Berechnung Optischer Und Elektrostatischer Gitterpotentiale". In: *Annalen der Physik* 369.3 (Jan. 1921), pp. 253–287. ISSN: 0003-3804. DOI: `10.1002/andp.19213690304`.

[230]   J.C. Maxwell and W.D. Niven. *The Scientific Papers of James Clerk Maxwell ...* The Scientific Papers of James Clerk Maxwell. University Press, 1890.

[231]   R. J. Dimelow and A. J. Masters. "Deriving the Distribution of N-particle Kinetic Energies in a Classical System". In: *Molecular Simulation* 33.14 (Dec. 2007), pp. 1165–1166. ISSN: 0892-7022. DOI: `10.1080/08927020701613649`.

[232]   H. J. C. Berendsen et al. "Molecular Dynamics with Coupling to an External Bath". In: *The Journal of Chemical Physics* 81.8 (Oct. 1984), pp. 3684–3690. ISSN: 0021-9606, 1089-7690. DOI: `10.1063/1.448118`.

[233]   William G. Hoover. "Canonical Dynamics: Equilibrium Phase-Space Distributions". In: *Physical Review A* 31.3 (Mar. 1985), pp. 1695–1697. DOI: `10.1103/PhysRevA.31.1695`.

[234]   Shūichi Nosé. "A Molecular Dynamics Method for Simulations in the Canonical Ensemble". In: *Molecular Physics* 52.2 (June 1984), pp. 255–268. ISSN: 0026-8976. DOI: `10.1080/00268978400101201`.

[235]   Shuichi Nosé. "A Unified Formulation of the Constant Temperature Molecular Dynamics Methods". In: *The Journal of Chemical Physics* 81.1 (July 1984), pp. 511–519. ISSN: 0021-9606. DOI: `10.1063/1.447334`.

[236]   H. Crone-Münzebrock and G. Döge. "Computer Simulation of Liquid Methyl Iodide". In: *Berichte der Bunsengesellschaft für physikalische Chemie* 94.3 (Mar. 1990), pp. 297–300. ISSN: 00059021. DOI: `10.1002/bbpc.19900940320`.

[237]   Yoshisuke Futami et al. "Structures of Methyl Halide Dimers in Supersonic Jets by Matrix-Isolation Infrared Spectroscopy and Quantum Chemical Calculations". In: *Journal of Molecular Structure* 690.1 (Mar. 2004), pp. 9–16. ISSN: 0022-2860. DOI: `10.1016/j.molstruc.2003.10.037`.

[238]   Fumiyuki Ito. "Infrared Studies of the CH3I–H2O Complex and Large CH3I Clusters in Ar Matrices". In: *Journal of Molecular Structure* 1035 (Mar. 2013), pp. 54–60. ISSN: 0022-2860. DOI: `10.1016/j.molstruc.2012.09.027`.

[239] Ponnadurai Ramasami and Thomas A. Ford. "The Structures and Vibrational Spectra of the Methyl Halide Dimers. An Ab Initio Study". In: *From Molecules to Molecular Materials, Biological Molecular Systems and Nanostructures* 1126 (Dec. 2016), pp. 2–10. ISSN: 0022-2860. DOI: 10.1016/j.molstruc.2016.03.003.

[240] Fumiyuki Ito et al. "Isomeric Structures of CH3I Dimers in a Supersonic Jet Studied by Matrix-Isolation Infrared Spectroscopy and Ab Initio Calculation". In: *Chemical Physics Letters* 343.1 (July 2001), pp. 185–191. ISSN: 0009-2614. DOI: 10.1016/S0009-2614(01)00688-1.

[241] Alena Habartová et al. "Partial Hydration of N-Alkyl Halides at the Water–Vapor Interface: A Molecular Simulation Study with Atmospheric Implications". In: *Theoretical Chemistry Accounts* 133.3 (Feb. 2014), p. 1455. ISSN: 1432-2234. DOI: 10.1007/s00214-014-1455-z.

[242] Alena Habartová, Kalliat T. Valsaraj, and Martina Roeselová. "Molecular Dynamics Simulations of Small Halogenated Organics at the Air–Water Interface: Implications in Water Treatment and Atmospheric Chemistry". In: *The Journal of Physical Chemistry A* 117.38 (Sept. 2013), pp. 9205–9215. ISSN: 1089-5639, 1520-5215. DOI: 10.1021/jp405292k.

[243] F. F. Martins Freitas, Fernando M. S. Silva Fernandes, and B. J. Costa Cabral. "Vapor-Liquid Equilibrium and Structure of Methyl Iodide Liquid". In: *The Journal of Physical Chemistry* 99.14 (Apr. 1995), pp. 5180–5186. ISSN: 0022-3654, 1541-5740. DOI: 10.1021/j100014a045.

[244] M. J. Frisch et al. *Gaussian~16 Revision C.01*. 2016.

[245] Junmei Wang et al. "Antechamber: An Accessory Software Package for Molecular Mechanical Calculations". In: *J. Am. Chem. Soc* 222.1 (2001).

[246] David Van Der Spoel et al. "GROMACS: Fast, Flexible, and Free". In: *Journal of Computational Chemistry* 26.16 (Dec. 2005), pp. 1701–1718. ISSN: 0192-8651, 1096-987X. DOI: 10.1002/jcc.20291.

[247] Chr. Møller and M. S. Plesset. "Note on an Approximation Treatment for Many-Electron Systems". In: *Physical Review* 46.7 (Oct. 1934), pp. 618–622. DOI: 10.1103/PhysRev.46.618.

[248] J. Grant Hill. "Gaussian Basis Sets for Molecular Applications". In: *International Journal of Quantum Chemistry* 113.1 (Jan. 2013), pp. 21–34. ISSN: 00207608. DOI: 10.1002/qua.24355.

[249] Kirk A. Peterson et al. "Systematically Convergent Basis Sets with Relativistic Pseudopotentials. II. Small-core Pseudopotentials and Correlation Consistent Basis Sets for the Post-d Group 16–18 Elements". In: *The Journal of Chemical Physics* 119.21 (Dec. 2003), pp. 11113–11123. ISSN: 0021-9606. DOI: 10.1063/1.1622924.

[250] P.D. Mallinson. "The Microwave Spectrum of CH2DI". In: *Journal of Molecular Spectroscopy* 55.1 (Mar. 1975), pp. 94–107. ISSN: 0022-2852. DOI: 10.1016/0022-2852(75)90255-6.

[251] W. O'Reilly. "Numerical Data and Functional Relationships in Science and Technology". In: *Physics of the Earth and Planetary Interiors* 45.3 (Apr. 1987), pp. 304–305. ISSN: 00319201. DOI: 10.1016/0031-9201(87)90019-7.

[252] Richard M. Ibberson and Michael Prager. "Temperature-Dependent Crystal Structure Analysis of Methyl Iodide by High-Resolution Neutron Powder Diffraction". In: Zeitschrift Für Kristallographie 222.8 (2007), pp. 416–419. DOI: 10.1524/zkri.2007.222.8.416.

[253] Fumiyuki Ito. "Infrared Studies of the CH3I–H2O Complex and Large CH3I Clusters in Ar Matrices". In: *Journal of Molecular Structure* 1035 (Mar. 2013), pp. 54–60. ISSN: 00222860. DOI: 10.1016/j.molstruc.2012.09.027.

[254] Pauli Virtanen et al. "SciPy 1.0: Fundamental Algorithms for Scientific Computing in Python". In: *Nature Methods* 17.3 (Mar. 2020), pp. 261–272. ISSN: 1548-7105. DOI: 10.1038/s41592-019-0686-2.

[255] Andrew R. Conn, Katya Scheinberg, and Luis N. Vicente. *Introduction to Derivative-Free Optimization*. SIAM, 2009. ISBN: 0-89871-668-3.

[256] Brian Doherty et al. "Revisiting OPLS Force Field Parameters for Ionic Liquid Simulations". In: *Journal of Chemical Theory and Computation* 13.12 (Dec. 2017), pp. 6131–6145. ISSN: 1549-9618. DOI: 10.1021/acs.jctc.7b00520.

[257] Junmei Wang et al. "Development and Testing of a General Amber Force Field". In: *Journal of Computational Chemistry* 25.9 (July 2004), pp. 1157–1174. ISSN: 0192-8651. DOI: 10.1002/jcc.20035.

[258] Junmei Wang et al. "Development and Testing of a General Amber Force Field". In: *Journal of Computational Chemistry* 25.9 (July 2004), pp. 1157–1174. ISSN: 0192-8651. DOI: 10.1002/jcc.20035.

[259] Guillaume Lamoureux and Benoît Roux. "Absolute Hydration Free Energy Scale for Alkali and Halide Ions Established from Simulations with a Polarizable Force Field". In: *The Journal of Physical Chemistry B* 110.7 (Feb. 2006), pp. 3308–3322. ISSN: 1520-6106, 1520-5207. DOI: 10.1021/jp056043p.

[260] Kasper P. Jensen and William L. Jorgensen. "Halide, Ammonium, and Alkali Metal Ion Parameters for Modeling Aqueous Solutions". In: *Journal of Chemical Theory and Computation* 2.6 (Nov. 2006), pp. 1499–1509. ISSN: 1549-9618, 1549-9626. DOI: 10.1021/ct600252r.

[261] Sowmianarayanan Rajamani, Tuhin Ghosh, and Shekhar Garde. "Size Dependent Ion Hydration, Its Asymmetry, and Convergence to Macroscopic Behavior". In: *The Journal of Chemical Physics* 120.9 (Mar. 2004), pp. 4457–4466. ISSN: 0021-9606, 1089-7690. DOI: 10.1063/1.1644536.

[262] In Suk Joung and Thomas E. Cheatham. "Determination of Alkali and Halide Monovalent Ion Parameters for Use in Explicitly Solvated Biomolecular Simulations". In: *The Journal of Physical Chemistry B* 112.30 (July 2008), pp. 9020–9041. ISSN: 1520-6106, 1520-5207. DOI: 10.1021/jp8001614.

[263] H. J. C. Berendsen, J. R. Grigera, and T. P. Straatsma. "The Missing Term in Effective Pair Potentials". In: *Journal of Physical Chemistry* 91.24 (Nov. 1987), pp. 6269–6271. ISSN: 0022-3654, 1541-5740. DOI: 10.1021/j100308a038.

[264] Swaroop Chatterjee et al. "A Computational Investigation of Thermodynamics, Structure, Dynamics and Solvation Behavior in Modified Water Models". In: *The Journal of chemical physics* 128.12 (2008), p. 124511.

[265] Arnold Audsley and Frank R. Goss. "154. The Magnitude of the Solvent Effect in Dipole-Moment Measurements. Part IV. Determination of Distortion Polarisation and Its Additivity in the Alkyl and Aryl Halides". In: *Journal of the Chemical Society (Resumed)* 0 (1941), pp. 864–873. ISSN: 0368-1769. DOI: 10.1039/JR9410000864.

[266] Juraj Kizlink. "Improved Preparation of Methyl Iodide". In: *Chemicke Listy* 74.1 (1980), pp. 91–2. ISSN: 0009-2770.

[267] I. A. Korshunov. "Synthesis of Trimethylcarbinol and Isobutylene Labeled with C14". In: *Trudy po Khimii i Khimicheskoi Tekhnologii* 1.No. 1 (1958), pp. 192–5. ISSN: 0564-3457.

[268] Richard W. Niemeier and Isaac Obadia. "International Chemical Safety Cards and Global Harmonization". In: *Safety Science* 39.1 (Oct. 2001), pp. 107–115. ISSN: 0925-7535. DOI: 10.1016/S0925-7535(01)00030-3.

[269] J. Timmermans. "Work of the International Bureau of Physico-Chemical Standards. VI. Physical Constants of Twenty Organic Compounds". In: *Journal de chimie physique et de physico-chimie biologique.* 31 (1934), pp. 85–124. ISSN: 0021-7689.

[270] Arthur I. Vogel. "169. Physical Properties and Chemical Constitution. Part VIII. Alkyl Chlorides, Bromides, and Iodides". In: *Journal of the Chemical Society (Resumed)* 0 (1943), pp. 636–647. ISSN: 0368-1769. DOI: 10.1039/JR9430000636.

[271] Tom Darden, Darrin York, and Lee Pedersen. "Particle Mesh Ewald: An N Log(N) Method for Ewald Sums in Large Systems". In: *The Journal of Chemical Physics* 98.12 (June 1993), pp. 10089–10092. ISSN: 0021-9606, 1089-7690. DOI: 10.1063/1.464397.

[272] Giovanni Bussi, Davide Donadio, and Michele Parrinello. "Canonical Sampling through Velocity Rescaling". In: *The Journal of Chemical Physics* 126.1 (Jan. 2007), p. 014101. ISSN: 0021-9606. DOI: 10.1063/1.2408420.

[273] Shuichi Nosé and M.L. Klein. "Constant Pressure Molecular Dynamics for Molecular Systems". In: *Molecular Physics* 50.5 (Dec. 1983), pp. 1055–1076. ISSN: 0026-8976. DOI: 10.1080/00268978300102851.

[274] M. Parrinello and A. Rahman. "Polymorphic Transitions in Single Crystals: A New Molecular Dynamics Method". In: *Journal of Applied Physics* 52.12 (Dec. 1981), pp. 7182–7190. ISSN: 0021-8979. DOI: 10.1063/1.328693.

[275] D. I. R. Low and E. A. Moelwyn-Hughes. "The Heat Capacities of Acetone, Methyl Iodide and Mixtures Thereof in the Liquid State". In: *Proceedings of the Royal Society of London. Series A, Mathematical and Physical Sciences* 267.1330 (1962), pp. 384–394. ISSN: 00804630. JSTOR: 2414262.

[276] David E. Smith and Liem X. Dang. "Computer Simulations of NaCl Association in Polarizable Water". In: *The Journal of Chemical Physics* 100.5 (Mar. 1994), pp. 3757–3766. ISSN: 0021-9606, 1089-7690. DOI: 10.1063/1.466363.

[277] Michael Patra and Mikko Karttunen. "Systematic Comparison of Force Fields for Microscopic Simulations of NaCl in Aqueous Solutions: Diffusion, Free Energy of Hydration, and Structural Properties". In: *Journal of Computational Chemistry* 25.5 (Apr. 2004), pp. 678–689. ISSN: 01928651, 1096987X. DOI: 10.1002/jcc.10417.

[278] Bo Chen, Xiuling Jiao, and Dairong Chen. "Fabrication of Hollow Cubic Ag Microboxes with Net-like Nanofiber Structures and Their Surface Plasmon Resonance". In: *CrystEngComm* 13.1 (2011), pp. 204–211. DOI: 10.1039/C0CE00132E.

[279] G. Selvarajan and C. K. Mahadevan. "Studies on (NaCl)x(KBr)y-x(KI)1-Ysolid Solutions: 1. Lattice and Thermal Parameters". In: *Journal of Materials Science* 41.24 (Dec. 2006), pp. 8211–8217. ISSN: 1573-4803. DOI: 10.1007/s10853-006-0999-2.

[280] Kiyotaka Shiba et al. "Distinct Macroscopic Structures Developed from Solutions of Chemical Compounds and Periodic Proteins". In: *EMBO reports* 4.2 (Feb. 2003), pp. 148–153. ISSN: 1469-221X. DOI: 10.1038/sj.embor.embor737.

[281] Vitali E. Gruzdev and Vladimir L. Komolov. "Possible Physical Mechanisms of Large-Scale Heating of Nonmetal Crystals by Femtosecond Laser Pulses". In: *Proc.SPIE*. Vol. 5506. July 2004, pp. 176–183. DOI: 10.1117/12.579987.

[282] Paolo Giannozzi et al. "QUANTUM ESPRESSO: A Modular and Open-Source Software Project for Quantum Simulations of Materials". In: *Journal of Physics: Condensed Matter* 21.39 (Sept. 2009), p. 395502. DOI: 10.1088/0953-8984/21/39/395502.

[283] Paolo Giannozzi et al. "Advanced Capabilities for Materials Modelling with Quantum ESPRESSO". In: *Journal of physics: Condensed matter* 29.46 (2017), p. 465901.

[284] Peter E Blöchl. "Projector Augmented-Wave Method". In: *Physical review B* 50.24 (1994), p. 17953.

[285] Georg Kresse and Daniel Joubert. "From Ultrasoft Pseudopotentials to the Projector Augmented-Wave Method". In: *Physical review b* 59.3 (1999), p. 1758.

[286] Andrea Dal Corso. "Pseudopotentials Periodic Table: From H to Pu". In: *Computational Materials Science* (2014), p. 14.

[287] John P. Perdew, Kieron Burke, and Matthias Ernzerhof. "Generalized Gradient Approximation Made Simple". In: *Physical Review Letters* 77.18 (Oct. 1996), pp. 3865–3868. ISSN: 0031-9007, 1079-7114. DOI: 10.1103/PhysRevLett.77.3865.

[288] Charles W. Bauschlicher et al. "A Theoretical Study of Na(H2O)+n (N=1–4)". In: *The Journal of Chemical Physics* 95.7 (1991), pp. 5142–5148. DOI: 10.1063/1.461682. eprint: https://doi.org/10.1063/1.461682.

[289] David Feller et al. "An Extended Basis Set Ab Initio Study of Alkali Metal Cation–Water Clusters". In: *The Journal of Chemical Physics* 103.9 (1995), pp. 3526–3542. DOI: 10.1063/1.470237. eprint: https://doi.org/10.1063/1.470237.

[290] Axel Schulz, Brian J. Smith, and Leo Radom. "Heats of Formation of Alkali and Alkaline Earth Oxides and Hydroxides: Some Dramatic Failures of the G2 Method". In: *The Journal of Physical Chemistry A* 103.37 (1999), pp. 7522–7527. DOI: 10.1021/jp991577+. eprint: https://doi.org/10.1021/jp991577+.

[291]   MARK A. IRON, MIKHAL OREN, and JAN M. L. MARTIN. "Alkali and
        Alkaline Earth Metal Compounds: Core—Valence Basis Sets and Importance
        of Subvalence Correlation". In: *Molecular Physics* 101.9 (2003), pp. 1345–
        1361. DOI: 10.1080/0026897031000094498. eprint: https://doi.org/10.
        1080/0026897031000094498.

[292]   Getachew G. Kebede et al. "Comparing van Der Waals DFT Methods
        for Water on NaCl(001) and MgO(001)". In: *The Journal of Chemical
        Physics* 146.6 (Feb. 2017), p. 064703. ISSN: 0021-9606, 1089-7690. DOI:
        10.1063/1.4971790.

[293]   G. Kresse and J. Furthmüller. "Efficiency of Ab-Initio Total Energy Calcu-
        lations for Metals and Semiconductors Using a Plane-Wave Basis Set". In:
        Computational Materials Science 6.1 (July 1996), pp. 15–50. ISSN: 0927-0256.
        DOI: 10.1016/0927-0256(96)00008-0.

[294]   G. Kresse and J. Furthmüller. "Efficient Iterative Schemes for Ab Initio Total-
        Energy Calculations Using a Plane-Wave Basis Set". In: *Physical Review B*
        54.16 (Oct. 1996), pp. 11169–11186. DOI: 10.1103/PhysRevB.54.11169.

[295]   G. Kresse and J. Hafner. "Ab Initio Molecular Dynamics for Liquid Met-
        als". In: *Physical Review B* 47.1 (Jan. 1993), pp. 558–561. DOI: 10.1103/
        PhysRevB.47.558.

[296]   G. Kresse and J. Hafner. "Ab Initio Molecular-Dynamics Simulation of
        the Liquid-Metal–Amorphous-Semiconductor Transition in Germanium".
        In: *Physical Review B* 49.20 (May 1994), pp. 14251–14269. DOI: 10.1103/
        PhysRevB.49.14251.

[297]   G. Kresse and D. Joubert. "From Ultrasoft Pseudopotentials to the Projector
        Augmented-Wave Method". In: *Physical Review B* 59.3 (Jan. 1999), pp. 1758–
        1775. DOI: 10.1103/PhysRevB.59.1758.

[298]   Bo Li, Angelos Michaelides, and Matthias Scheffler. "How Strong Is the
        Bond between Water and Salt?" In: *Surface Science* 602.23 (Dec. 2008),
        pp. L135–L138. ISSN: 00396028. DOI: 10.1016/j.susc.2008.09.039.

[299]   Kristian Berland et al. "Assessment of Two Hybrid van Der Waals Density
        Functionals for Covalent and Non-Covalent Binding of Molecules". In: *The
        Journal of Chemical Physics* 146.23 (June 2017), p. 234106. ISSN: 0021-9606,
        1089-7690. DOI: 10.1063/1.4986522.

[300]   David Walker et al. "Halite-Sylvite Thermoelasticity". In: *American Miner-
        alogist* 89.1 (2004), pp. 204–210.

[301]   G. Graner. *Structure of Free Polyatomic Molecules: Basic Data*. Springer,
        1998. ISBN: 3-540-60766-8.

[302]   Swapnil Singh and Mirosław Antoni Czarnecki. "How Much Anharmonicity Is in Vibrational Spectra of CH3I and CD3I?" In: *Spectrochimica Acta Part A: Molecular and Biomolecular Spectroscopy* 248 (Mar. 2021), p. 119176. ISSN: 1386-1425. DOI: 10.1016/j.saa.2020.119176.

[303]   Ian J. McNaught. "Structural Parameters of Methyl Iodide by Infrared Spectroscopy". In: *Journal of Chemical Education* 59.10 (Oct. 1982), p. 879. ISSN: 0021-9584, 1938-1328. DOI: 10.1021/ed059p879.

[304]   J. L. Duncan, A. M. Ferguson, and S. Mathews. "Vibrational Anharmonicity in CH_3I: A Joint Local and Normal Mode Study". In: *The Journal of Chemical Physics* 91.2 (July 1989), pp. 783–790. ISSN: 0021-9606, 1089-7690. DOI: 10.1063/1.457131.

[305]   D. Alfè and M. J. Gillan. "*Ab Initio* Statistical Mechanics of Surface Adsorption and Desorption. I. H2O on MgO (001) at Low Coverage". In: *The Journal of Chemical Physics* 127.11 (Sept. 2007), p. 114709. ISSN: 0021-9606, 1089-7690. DOI: 10.1063/1.2772258.

[306]   A. Allouche. "Water Dissociation on Defective Sites on the NaCl(100) Surface. A Quantum Ab Initio Study". In: *The Journal of Physical Chemistry B* 102.50 (Dec. 1998), pp. 10223–10228. ISSN: 1520-6106, 1520-5207. DOI: 10.1021/jp9814496.

[307]   Pepa Cabrera-Sanfelix et al. "On the Structure of the First Hydration Layer on NaCl(100): Role of Hydrogen Bonding". In: *The Journal of Chemical Physics* 126.21 (June 2007), p. 214707. ISSN: 0021-9606, 1089-7690. DOI: 10.1063/1.2743411.

[308]   Ola Engkvist and Anthony J. Stone. "Adsorption of Water on NaCl(001). I. Intermolecular Potentials and Low Temperature Structures". In: *The Journal of Chemical Physics* 110.24 (June 1999), pp. 12089–12096. ISSN: 0021-9606, 1089-7690. DOI: 10.1063/1.479144.

[309]   S. Fölsch, A. Stock, and M. Henzler. "Two-Dimensional Water Condensation on the NaCl(100) Surface". In: *Surface Science* 264.1-2 (Mar. 1992), pp. 65–72. ISSN: 00396028. DOI: 10.1016/0039-6028(92)90165-3.

[310]   Michelle C. Foster and George E. Ewing. "Adsorption of Water on the NaCl(001) Surface. II. An Infrared Study at Ambient Temperatures". In: *The Journal of Chemical Physics* 112.15 (Apr. 2000), pp. 6817–6826. ISSN: 0021-9606, 1089-7690. DOI: 10.1063/1.481256.

[311]   Michelle Foster and George E. Ewing. "An Infrared Spectroscopic Study of Water Thin Films on NaCl (100)". In: *Surface Science* 427–428 (June 1999), pp. 102–106. ISSN: 00396028. DOI: 10.1016/S0039-6028(99)00242-3.

[312]   Sutapa Ghosal and John C. Hemminger. "Surface Adsorbed Water on NaCl
        and Its Effect on Nitric Acid Reactivity with NaCl Powders". In: *The
        Journal of Physical Chemistry B* 108.37 (Sept. 2004), pp. 14102–14108. ISSN:
        1520-6106, 1520-5207. DOI: 10.1021/jp047774c.

[313]   M Henzler and A Stock. "Adsorption .of Water Vapor on NaCI(lOO) and
        KCI(lOO) without and with Defects". In: (), p. 9.

[314]   Hendrik Meyer, Peter Entel, and Jürgen Hafner. "Physisorption of Water on
        Salt Surfaces". In: *Surface Science* 488.1-2 (Aug. 2001), pp. 177–192. ISSN:
        00396028. DOI: 10.1016/S0039-6028(01)01136-0.

[315]   Jung Mee Park, Jun-Hyung Cho, and Kwang S. Kim. "Atomic Structure
        and Energetics of Adsorbed Water on the NaCl(001) Surface". In: *Physical
        Review B* 69.23 (June 2004), p. 233403. ISSN: 1098-0121, 1550-235X. DOI:
        10.1103/PhysRevB.69.233403.

[316]   Steven J. Peters and George E. Ewing. "Water on Salt: An Infrared Study
        of Adsorbed H_2O on NaCl(100) under Ambient Conditions". In: *The
        Journal of Physical Chemistry B* 101.50 (Dec. 1997), pp. 10880–10886. ISSN:
        1520-6106, 1520-5207. DOI: 10.1021/jp972810b.

[317]   Amitava Pramanik et al. "Adsorption of Water on Sodium Chloride Sur-
        faces: Electrostatics – Guided Ab Initio Studies". In: *Theoretical Chemistry
        Accounts* 114.1-3 (Sept. 2005), pp. 129–136. ISSN: 1432-881X, 1432-2234.
        DOI: 10.1007/s00214-005-0653-0.

[318]   J. P. Toennies et al. "Low-Energy Electron Induced Restructuring of Water
        Monolayers on NaCl(100)". In: *The Journal of Chemical Physics* 120.24
        (June 2004), pp. 11347–11350. ISSN: 0021-9606, 1089-7690. DOI: 10.1063/1.
        1763837.

[319]   Albert Verdaguer et al. "Initial Stages of Water Adsorption on NaCl (100)
        Studied by Scanning Polarization Force Microscopy". In: *The Journal of
        Chemical Physics* 123.12 (Sept. 2005), p. 124703. ISSN: 0021-9606, 1089-7690.
        DOI: 10.1063/1.1996568.

[320]   Yong Yang, Sheng Meng, and E. G. Wang. "Water Adsorption on a NaCl
        (001) Surface: A Density Functional Theory Study". In: *Physical Review B*
        74.24 (Dec. 2006), p. 245409. ISSN: 1098-0121, 1550-235X. DOI: 10.1103/
        PhysRevB.74.245409.

[321]   L. W. Bruch et al. "A Helium Atom Scattering Study of Water Adsorption
        on the NaCl(100) Single Crystal Surface". In: *The Journal of Chemical
        Physics* 103.12 (Sept. 1995), pp. 5109–5120. ISSN: 0021-9606, 1089-7690.
        DOI: 10.1063/1.470598.

[322]   Dirk Porezag and Mark R. Pederson. "Density Functional Based Studies of Transition States and Barriers for Hydrogen Exchange and Abstraction Reactions". In: *The Journal of Chemical Physics* 102.23 (June 1995), pp. 9345–9349. ISSN: 0021-9606. DOI: 10.1063/1.468801.

[323]   Takehiko Shimanouchi et al. "Tables of Molecular Vibrational Frequencies". In: *Journal of Physical and Chemical Reference Data* 7.4 (Oct. 1978), pp. 1323–1444. ISSN: 0047-2689. DOI: 10.1063/1.555587.

[324]   Mario E Fajardo and Simon Tam. "Observation of the Cyclic Water Hexamer in Solid Parahydrogen". In: (), p. 5.

[325]   Koichiro Yamakawa and Katsuyuki Fukutani. "Infrared Spectroscopy of Water Clusters Co-Adsorbed with Hydrogen Molecules on a Sodium Chloride Film". In: *Chemical Physics* 472 (June 2016), pp. 89–94. ISSN: 03010104. DOI: 10.1016/j.chemphys.2016.02.023.

[326]   Stephan Ehrlich et al. "System-Dependent Dispersion Coefficients for the DFT-D3 Treatment of Adsorption Processes on Ionic Surfaces". In: *ChemPhysChem* 12.17 (Dec. 2011), pp. 3414–3420. ISSN: 1439-4235. DOI: 10.1002/cphc.201100521.

[327]   Pavel Hobza, Jiří šponer, and Tomáš Reschel. "Density Functional Theory and Molecular Clusters". In: *Journal of Computational Chemistry* 16.11 (Nov. 1995), pp. 1315–1325. ISSN: 0192-8651. DOI: 10.1002/jcc.540161102.

[328]   Sándor Kristyán and Péter Pulay. "Can (Semi)Local Density Functional Theory Account for the London Dispersion Forces?" In: *Chemical Physics Letters* 229.3 (Oct. 1994), pp. 175–180. ISSN: 0009-2614. DOI: 10.1016/0009-2614(94)01027-7.

[329]   JoséM. Pérez-Jordá and A.D. Becke. "A Density-Functional Study of van Der Waals Forces: Rare Gas Diatomics". In: *Chemical Physics Letters* 233.1 (Feb. 1995), pp. 134–137. ISSN: 0009-2614. DOI: 10.1016/0009-2614(94)01402-H.

[330]   Stefan Grimme. "Accurate Description of van Der Waals Complexes by Density Functional Theory Including Empirical Corrections". In: *Journal of Computational Chemistry* 25.12 (Sept. 2004), pp. 1463–1473. ISSN: 0192-8651. DOI: 10.1002/jcc.20078.

[331]   Stefan Grimme. "Semiempirical GGA-type Density Functional Constructed with a Long-Range Dispersion Correction". In: *Journal of Computational Chemistry* 27.15 (Nov. 2006), pp. 1787–1799. ISSN: 0192-8651. DOI: 10.1002/jcc.20495.

[332]   Tomáš Bučko et al. "Improved Description of the Structure of Molecular and Layered Crystals: Ab Initio DFT Calculations with van Der Waals Corrections". In: *The Journal of Physical Chemistry A* 114.43 (Nov. 2010), pp. 11814–11824. ISSN: 1089-5639. DOI: 10.1021/jp106469x.

[333]   Torsten Kerber, Marek Sierka, and Joachim Sauer. "Application of Semiempirical Long-Range Dispersion Corrections to Periodic Systems in Density Functional Theory". In: *Journal of Computational Chemistry* 29.13 (Oct. 2008), pp. 2088–2097. ISSN: 0192-8651. DOI: 10.1002/jcc.21069.

[334]   Marcus A. Neumann and Marc-Antoine Perrin. "Energy Ranking of Molecular Crystals Using Density Functional Theory Calculations and an Empirical van Der Waals Correction". In: *The Journal of Physical Chemistry B* 109.32 (Aug. 2005), pp. 15531–15541. ISSN: 1520-6106. DOI: 10.1021/jp050121r.

[335]   Guo-Xu Zhang et al. "Van Der Waals Interactions in Ionic and Semiconductor Solids". In: *Physical Review Letters* 107.24 (Dec. 2011), p. 245501. DOI: 10.1103/PhysRevLett.107.245501.

[336]   P.J. Linstrom and W.G. Mallard. *Inc., "Evaluated Infrared Reference Spectra" in NIST Chemistry WebBook, NIST Standard Reference Database Number 69, Eds.* National Institute of Standards and Technology, Gaithersburg MD, 20899: Coblentz Society.

[337]   H. J. C. Berendsen, J. R. Grigera, and T. P. Straatsma. "The Missing Term in Effective Pair Potentials". In: *The Journal of Physical Chemistry* 91.24 (Nov. 1987), pp. 6269–6271. ISSN: 0022-3654, 1541-5740. DOI: 10.1021/j100308a038.

[338]   Carlos Vega and Jose L. F. Abascal. "Simulating Water with Rigid Non-Polarizable Models: A General Perspective". In: *Physical Chemistry Chemical Physics* 13.44 (2011), p. 19663. ISSN: 1463-9076, 1463-9084. DOI: 10.1039/c1cp22168j.

[339]   Michael Patra and Mikko Karttunen. "Systematic Comparison of Force Fields for Microscopic Simulations of NaCl in Aqueous Solutions: Diffusion, Free Energy of Hydration, and Structural Properties". In: *Journal of computational chemistry* 25.5 (2004), pp. 678–689.

[340]   George E. Ewing. "Ambient Thin Film Water on Insulator Surfaces". In: *Chemical Reviews* 106.4 (Apr. 2006), pp. 1511–1526. ISSN: 0009-2665, 1520-6890. DOI: 10.1021/cr040369x.

[341]   H. J. C. Berendsen et al. "Molecular Dynamics with Coupling to an External Bath". In: *The Journal of Chemical Physics* 81.8 (Oct. 1984), pp. 3684–3690. ISSN: 0021-9606, 1089-7690. DOI: 10.1063/1.448118.

[342] D. C. B. Whittet et al. "Interstellar Ice Grains in the Taurus Molecular Clouds". In: *Nature* 303.5914 (May 1983), pp. 218–221. ISSN: 1476-4687. DOI: `10.1038/303218a0`.

[343] F Salama et al. "Polycyclic Aromatic Hydrocarbons and the Diffuse Interstellar Bands: A Survey". In: *The Astrophysical journal* 728.2 (2011), 154–jQuery1323911069801='48'. ISSN: 0004-637X. DOI: `10.1088/0004-637X/728/2/154`.

[344] B. Rowland et al. "Infrared Spectra of Ice Surfaces and Assignment of Surface-localized Modes from Simulated Spectra of Cubic Ice". In: *The Journal of Chemical Physics* 102.21 (June 1995), pp. 8328–8341. ISSN: 0021-9606. DOI: `10.1063/1.468825`.

[345] Brad Rowland, Mark Fisher, and J. Paul Devlin. "Probing Icy Surfaces with the dangling-OH-mode Absorption: Large Ice Clusters and Microporous Amorphous Ice". In: *The Journal of Chemical Physics* 95.2 (July 1991), pp. 1378–1384. ISSN: 0021-9606. DOI: `10.1063/1.461119`.

[346] Eric Michoulier et al. "Theoretical Determination of Adsorption and Ionisation Energies of Polycyclic Aromatic Hydrocarbons on Water Ice". In: *Physical Chemistry Chemical Physics* 20.17 (2018), pp. 11941–11953. ISSN: 1463-9076. DOI: `10.1039/C8CP01175C`.

[347] J. L. F. Abascal and C. Vega. "A General Purpose Model for the Condensed Phases of Water: TIP4P/2005". In: *The Journal of Chemical Physics* 123.23 (Dec. 2005), p. 234505. ISSN: 0021-9606, 1089-7690. DOI: `10.1063/1.2121687`.

[348] Mark James Abraham et al. "GROMACS: High Performance Molecular Simulations through Multi-Level Parallelism from Laptops to Supercomputers". In: *SoftwareX* 1–2 (Sept. 2015), pp. 19–25. ISSN: 23527110. DOI: `10.1016/j.softx.2015.06.001`.

[349] H Bekker et al. "GROMACS - A PARALLEL COMPUTER FOR MOLECULAR-DYNAMICS SIMULATIONS". In: *Physics Computing '92: Proceedings of the 4th International Conference, Prague, Czechoslovakia, August 24-28, 1992*. RA DeGroot and J Nadrchal. World Scientific Publishing, 1993, pp. 252–256. ISBN: 981-02-1245-3.

[350] H.J.C. Berendsen, D. van der Spoel, and R. van Drunen. "GROMACS: A Message-Passing Parallel Molecular Dynamics Implementation". In: *Computer Physics Communications* 91.1-3 (Sept. 1995), pp. 43–56. ISSN: 00104655. DOI: `10.1016/0010-4655(95)00042-E`.

[351] Berk Hess et al. "GROMACS 4: Algorithms for Highly Efficient, Load-Balanced, and Scalable Molecular Simulation". In: *Journal of Chemical Theory and Computation* 4.3 (Mar. 2008), pp. 435–447. ISSN: 1549-9618, 1549-9626. DOI: 10.1021/ct700301q.

[352] Erik Lindahl, Berk Hess, and David van der Spoel. "GROMACS 3.0: A Package for Molecular Simulation and Trajectory Analysis". In: *Journal of Molecular Modeling* 7.8 (Aug. 2001), pp. 306–317. ISSN: 1610-2940, 0948-5023. DOI: 10.1007/s008940100045.

[353] Szilárd Páll et al. "Tackling Exascale Software Challenges in Molecular Dynamics Simulations with GROMACS". In: *Solving Software Challenges for Exascale*. Ed. by Stefano Markidis and Erwin Laure. Vol. 8759. Cham: Springer International Publishing, 2015, pp. 3–27. ISBN: 978-3-319-15975-1 978-3-319-15976-8. DOI: 10.1007/978-3-319-15976-8_1.

[354] Sander Pronk et al. "GROMACS 4.5: A High-Throughput and Highly Parallel Open Source Molecular Simulation Toolkit". In: *Bioinformatics* 29.7 (Apr. 2013), pp. 845–854. ISSN: 1460-2059, 1367-4803. DOI: 10.1093/bioinformatics/btt055.

[355] Lung Wa Chung et al. "The ONIOM Method and Its Applications". In: *Chemical Reviews* 115.12 (June 2015), pp. 5678–5796. ISSN: 0009-2665. DOI: 10.1021/cr5004419.

[356] James J. P. Stewart. "Optimization of Parameters for Semiempirical Methods VI: More Modifications to the NDDO Approximations and Re-Optimization of Parameters". In: *Journal of Molecular Modeling* 19.1 (Jan. 2013), pp. 1–32. ISSN: 0948-5023. DOI: 10.1007/s00894-012-1667-x.

[357] Denis Duflot, Céline Toubin, and Maurice Monnerville. "Theoretical Determination of Binding Energies of Small Molecules on Interstellar Ice Surfaces". In: *Frontiers in Astronomy and Space Sciences* 8 (2021). ISSN: 2296-987X.

[358] G. Schaftenaar and J.H. Noordik. "Molden: A Pre- and Post-Processing Program for Molecular and Electronic Structures*". In: *Journal of Computer-Aided Molecular Design* 14.2 (Feb. 2000), pp. 123–134. ISSN: 1573-4951. DOI: 10.1023/A:1008193805436.

[359] Paul Marshall, Ashutosh Misra, and R.J. Berry. "Computational Studies of the Reactions of CH3I with H and OH". In: *Chemical Physics Letters* 265.1 (Jan. 1997), pp. 48–54. ISSN: 0009-2614. DOI: 10.1016/S0009-2614(96)01400-5.

[360]   Anne C. Brown, Carlos E. Canosa-Mas, and Richard P. Wayne. "A Kinetic Study of the Reactions of OH with CH3I and CF3I". In: *Atmospheric Environment. Part A. General Topics* 24.2 (Jan. 1990), pp. 361–367. ISSN: 0960-1686. DOI: `10.1016/0960-1686(90)90115-4`.

[361]   Eimear S.N. Cotter et al. "Kinetic Study of the Reactions of OH with the Simple Alkyl Iodides: CH3I, C2H5I, 1-C3H7I and 2-C3H7I". In: *Atmospheric Environment* 37.8 (Mar. 2003), pp. 1125–1133. ISSN: 1352-2310. DOI: `10.1016/S1352-2310(02)00928-7`.

[362]   Mary K. Gilles et al. "Reactions of O(3P) with Alkyl Iodides: Rate Coefficients and Reaction Products". In: *The Journal of Physical Chemistry* 100.33 (Jan. 1996), pp. 14005–14015. ISSN: 0022-3654. DOI: `10.1021/jp960688v`.

[363]   R. Vogt. "Iodine Compounds in the Atmosphere". In: *Reactive Halogen Compounds in the Atmosphere*. Ed. by P. Fabian and Onkar N. Singh. Vol. 4E. Berlin/Heidelberg: Springer-Verlag, 1999, pp. 113–128. ISBN: 978-3-540-64090-5. DOI: `10.1007/10628761_4`.

[364]   Paul Marshall, G. N. Srinivas, and M. Schwartz. "A Computational Study of the Thermochemistry of Bromine- and Iodine-Containing Methanes and Methyl Radicals". In: *The Journal of Physical Chemistry A* 109.28 (July 2005), pp. 6371–6379. ISSN: 1089-5639. DOI: `10.1021/jp0518052`.

[365]   Mária Sudolská, Laurent Cantrel, and Ivan Černušák. "Microhydration of Caesium Compounds: Cs, CsOH, CsI and Cs2I2 Complexes with One to Three H2O Molecules of Nuclear Safety Interest". In: *Journal of Molecular Modeling* 20.4 (Apr. 2014), p. 2218. ISSN: 0948-5023. DOI: `10.1007/s00894-014-2218-4`.

[366]   Mária Sudolská et al. "Molecular Structures and Thermodynamic Properties of Monohydrated Gaseous Iodine Compounds: Modelling for Severe Accident Simulation". In: *Journal of Nuclear Materials* 446.1 (Mar. 2014), pp. 73–80. ISSN: 0022-3115. DOI: `10.1016/j.jnucmat.2013.11.029`.

[367]   K. P. Huber and G. Herzberg. *Molecular Spectra and Molecular Structure*. Boston, MA: Springer US, 1979. ISBN: 978-1-4757-0963-6 978-1-4757-0961-2. DOI: `10.1007/978-1-4757-0961-2`.

[368]   K. Kuchitsu, ed. *Structure of Free Polyatomic Molecules: Basic Data*. Berlin, Heidelberg: Springer Berlin Heidelberg, 1998. ISBN: 978-3-540-60766-3 978-3-642-45748-7. DOI: `10.1007/978-3-642-45748-7`.

[369]   A.R. Hoy and P.R. Bunker. "A Precise Solution of the Rotation Bending Schrödinger Equation for a Triatomic Molecule with Application to the Water Molecule". In: *Journal of Molecular Spectroscopy* 74.1 (Jan. 1979), pp. 1–8. ISSN: 0022-2852. DOI: `10.1016/0022-2852(79)90019-5`.

[370] Malcom W Chase Jr and NIST-JANAF Thermochemical Tables. "Data Reported in NIST Standard Reference Database 69, June 2005 Release: NIST Chemistry WebBook". In: *J. Phys. Chem. Ref. Data, Monograph* 9 (1998), pp. 1–1951.

[371] Gerhard Herzberg. *Electronic Spectra and Electronic Structure of Polyatomic Molecules.* Vol. 3. van Nostrand, 1966. ISBN: 0-442-03387-7.

[372] Hiroyuki Ozeki and Shuji Saito. "Submillimeter-Wave Spectra of Hypoiodous Acid". In: *The Journal of Chemical Physics* 120.11 (Mar. 2004), pp. 5110–5116. ISSN: 0021-9606. DOI: 10.1063/1.1647053.

[373] I. M. Alecu et al. "Computational Thermochemistry: Scale Factor Databases and Scale Factors for Vibrational Frequencies Obtained from Electronic Model Chemistries". In: *Journal of Chemical Theory and Computation* 6.9 (Sept. 2010), pp. 2872–2887. ISSN: 1549-9618. DOI: 10.1021/ct100326h.

[374] S. A. Kudchadker and A. P. Kudchadker. "Ideal Gas Thermodynamic Properties of the Eight Bromo- and Lodomethanes". In: *Journal of Physical and Chemical Reference Data* 4.2 (Apr. 1975), pp. 457–470. ISSN: 0047-2689. DOI: 10.1063/1.555522.

[375] Steven L. Baughcum and Stephen R. Leone. "Photofragmentation Infrared Emission Studies of Vibrationally Excited Free Radicals CH3 and CH2I". In: *The Journal of Chemical Physics* 72.12 (June 1980), pp. 6531–6545. ISSN: 0021-9606. DOI: 10.1063/1.439111.

[376] Marilyn E. Jacox. "Vibrational and Electronic Energy Levels of Polyatomic Transient Molecules". In: *Journal of Physical and Chemical Reference Data, Monograph* 3 (1994), pp. 1–461. ISSN: 1063-0651.

[377] Jody J. Klaassen, Jörg Lindner, and Stephen R. Leone. "Observation of the $N1$ OH(OD) Stretch of HOI and DOI by Fourier Transform Infrared Emission Spectroscopy". In: *The Journal of Chemical Physics* 104.19 (May 1996), pp. 7403–7411. ISSN: 0021-9606. DOI: 10.1063/1.471456.

[378] Lev Veniaminovich Gurvich, IV Veyts, and Ch B Alcock. *Thermodynamic Properties of Individual Substances: Elements O, H (D, T), F, Cl, Br, I, He, Ne, Ar, Kr, Xe, Rn, S, N, P, and Their Compounds.* Vol. 1. Hemisphere, 1989. ISBN: 0-89116-761-7.

[379] R D Johnson. *Computational Chemistry Comparison and Benchmark Database, NIST Standard Reference Database 101.* 2002. DOI: 10.18434/T47C7Z.

[380] Emiko Sugimura et al. "Simultaneous High-Pressure and High-Temperature Volume Measurements of Ice VII and Its Thermal Equation of State". In: *Physical Review B* 82.13 (Oct. 2010), p. 134103. DOI: 10.1103/PhysRevB.82.134103.

[381] Richard A. Robie, Bruch S. Hemingway, and James R. Fisher. *Thermodynamic Properties of Minerals and Related Substances at 298.15 K and 1 Bar (105 Pascals) Pressure and at Higher Temperatures*. Report 1452. 1978. DOI: `10.3133/b1452`.

[382] Marie-Therese Rayez, Jean-Claude Rayez, and Jean-Pierre Sawerysyn. "Ab Initio Studies of the Reactions of Chlorine Atoms with Fluoro- and Chloro-Substituted Methanes". In: *The Journal of Physical Chemistry* 98.44 (Nov. 1994), pp. 11342–11352. ISSN: 0022-3654. DOI: `10.1021/j100095a017`.

[383] Liqun Deng, Tom Ziegler, and Liangyou Fan. "A Combined Density Functional and Intrinsic Reaction Coordinate Study on the Ground State Energy Surface of H2CO". In: *The Journal of Chemical Physics* 99.5 (Sept. 1993), pp. 3823–3835. ISSN: 0021-9606. DOI: `10.1063/1.466129`.

[384] Liqun Deng and Tom Ziegler. "The Determination of Intrinsic Reaction Coordinates by Density Functional Theory". In: *International Journal of Quantum Chemistry* 52.4 (Nov. 1994), pp. 731–765. ISSN: 0020-7608. DOI: `10.1002/qua.560520406`.

[385] Thomas R. Dyke, Kenneth M. Mack, and J. S. Muenter. "The Structure of Water Dimer from Molecular Beam Electric Resonance Spectroscopy". In: *The Journal of Chemical Physics* 66.2 (Jan. 1977), pp. 498–510. ISSN: 0021-9606. DOI: `10.1063/1.433969`.

[386] K. Morokuma and L. Pedersen. "Molecular-Orbital Studies of Hydrogen Bonds. An Ab Initio Calculation for Dimeric H2O". In: *The Journal of Chemical Physics* 48.7 (Apr. 1968), pp. 3275–3282. ISSN: 0021-9606. DOI: `10.1063/1.1669604`.

[387] Sotiris S. Xantheas, Christian J. Burnham, and Robert J. Harrison. "Development of Transferable Interaction Models for Water. II. Accurate Energetics of the First Few Water Clusters from First Principles". In: *The Journal of Chemical Physics* 116.4 (Jan. 2002), pp. 1493–1499. ISSN: 0021-9606. DOI: `10.1063/1.1423941`.

[388] Ryan M. Olson et al. "A Novel Approach to Parallel Coupled Cluster Calculations: Combining Distributed and Shared Memory Techniques for Modern Cluster Based Systems". In: *Journal of Chemical Theory and Computation* 3.4 (July 2007), pp. 1312–1328. ISSN: 1549-9618. DOI: `10.1021/ct600366k`.

[389] Francesco Aquilante et al. "MOLCAS 7: The Next Generation". In: *Journal of Computational Chemistry* 31.1 (Jan. 2010), pp. 224–247. ISSN: 0192-8651. DOI: `10.1002/jcc.21318`.

[390] Björn O. Roos et al. "Main Group Atoms and Dimers Studied with a New Relativistic ANO Basis Set". In: *The Journal of Physical Chemistry A* 108.15 (Apr. 2004), pp. 2851–2858. ISSN: 1089-5639. DOI: `10.1021/jp031064+`.

[391] Bernd A. Hess. "Relativistic Electronic-Structure Calculations Employing a Two-Component No-Pair Formalism with External-Field Projection Operators". In: *Physical Review A* 33.6 (June 1986), pp. 3742–3748. DOI: `10.1103/PhysRevA.33.3742`.

[392] Marvin Douglas and Norman M Kroll. "Quantum Electrodynamical Corrections to the Fine Structure of Helium". In: *Annals of Physics* 82.1 (Jan. 1974), pp. 89–155. ISSN: 0003-4916. DOI: `10.1016/0003-4916(74)90333-9`.

[393] Miroslav Iliaš, Vladimır Kellö, and Miroslav Urban. "Relativistic Effects in Atomic and Molecular Properties". In: *Acta Phys. Slovaca* 60.3 (2010), pp. 259–391.

[394] M. Urban and V. Kellö. "Some Trends in Relativistic and Electron Correlation Effects in Electric Properties of Small Molecules". In: *Advances in Quantum Chemistry*. Ed. by H.J.Å. Jensen. Vol. 50. Academic Press, Jan. 2005, pp. 249–269. ISBN: 0065-3276. DOI: `10.1016/S0065-3276(05)50012-1`.

[395] David Z. Goodson. "Extrapolating the Coupled-Cluster Sequence toward the Full Configuration-Interaction Limit". In: *The Journal of Chemical Physics* 116.16 (Apr. 2002), pp. 6948–6956. ISSN: 0021-9606. DOI: `10.1063/1.1462620`.

[396] Giacomo Marchioro et al. *Giacomomarchioro/PyEnergyDiagrams: New Features and Pypi*. Zenodo. Sept. 2022. DOI: `10.5281/ZENODO.7081045`.

UNRAVELLING THE ATMOSPHERIC IODINE CHEMISTRY USING MOLECULAR SIMULATIONS

Abstract

Oceans, through algae and phytoplankton activities, are the main source of iodine, including organic compounds as CH_3I. In the recent past, iodine has played a critical role in health issues through historical events such as the Fukushima nuclear crisis or open-air bomb testing. Iodine, among other halogens, also participates in the catalytic destruction of ozone. The details of the interactions between iodinated compounds and aerosols in the troposphere remain largely unknown. In particular, the modification of the chemical speciation or effects of the environing molecules/aerosols on the iodine chemistry have consequences on its reactivity. Therefore, the knowledge of iodine atmospheric chemistry is essential to better understand general atmospheric phenomena. In this context, this thesis aims to improve the iodine atmospheric chemistry state of knowledge using theoretical simulations, focusing on interactions/chemical reactions between methyl iodide (CH_3I) and its surrounding.

In a first part, the adsorption of gaseous iodomethane (CH_3I) on model sea-salt aerosols (NaCl) at various humidities is investigated. We performed periodic density functional theory (DFT) as well as classical molecular dynamics (MD) calculations to investigate the influence of water coverage. To this aim, we parametrized a flexible non-polarizable force field for iodomethane. This force field shows good performances in describing the interactions with water and sea-salt surfaces. Simulations show that the presence of water tends to stabilize CH_3I at the salt surface. The lifetime of CH_3I in the atmosphere (in gas phase or adsorbed on aerosols) may also be altered by its reaction with gas phase radicals. The reaction of CH_3I with OH is thus investigated both in gas phase and in presence of water by means of quantum mechanical calculations. The presence of an additional water molecule favors the hydrogen abstraction by OH radical under atmospheric conditions. In other words, H_2O plays the role of a catalyst in this atmospheric chemical reaction. Finally, through cooperation with the laboratory "Physics of the Interactions of Ions and Molecules (PIIM)", we investigated the adsorption of methyl iodide on amorphous solid water (ASW) surfaces. In agreement with previous studies, we highlighted the importance of configuration sampling when dealing with amorphous interfaces. Using classical MD and quantum mechanical calculations, we have computed theoretical spectra for ASW surfaces with and without adsorbed CH_3I, which could be directly compared with experimental ones. Adsorption of CH_3I induces a redshift of about $20\,cm^{-1}$ of the dangling OH stretching mode.

This thesis combines several theoretical methods to study the reactivity and capture of molecules by surfaces of atmospheric interest. The approaches applied in this work can be extended to other systems providing valuable interpretation of the spectra and experimental data.

Keywords: iodine, methyl iodide, sea-atmosphere interactions, atmospheric chemistry, marine aerosols, amorphous solid water, molecular dynamics, density functional theory

Étude de la chimie atmosphérique de l'iode avec des aérosols par simulations moléculaires

Résumé

Les océans, par le biais de l'activité des algues et du phytoplancton, sont la principale source d'iode, y compris de composés organiques tels que l'iodométhane (CH_3I). Dans un passé récent, l'iode a joué un rôle essentiel dans les questions de santé, en raison d'événements historiques tels que la crise nucléaire de Fukushima ou les essais de bombes en plein air. L'iode, parmi d'autres halogènes, participe également à la destruction catalytique de l'ozone. Les détails des interactions entre les composés iodés et les aérosols dans la troposphère restent encore peu connus. En particulier, la modification de la spéciation chimique ou les effets des molécules/aérosols environnants sur la chimie de l'iode ont des conséquences sur sa réactivité. Par conséquent, la connaissance de la chimie atmosphérique de l'iode est essentielle pour mieux comprendre les phénomènes atmosphériques généraux. Dans ce contexte, cette thèse vise à améliorer l'état des connaissances sur la chimie atmosphérique de l'iode par le biais de simulations théoriques, en se concentrant sur les interactions/réactions chimiques entre l'iodométhane (CH_3I) et son environnement.

Dans une première partie, l'adsorption de l'iodométhane gazeux (CH_3I) sur des aérosols modèles de sel marin (NaCl) à différentes humidités est étudiée. Nous avons effectué des calculs périodiques de théorie fonctionnelle de la densité (DFT) ainsi que des calculs classiques de dynamique moléculaire (MD) pour étudier l'influence de la couverture d'eau. À cette fin, nous avons paramétré un champ de force flexible non polarisable pour l'iodométhane. Ce champ de force montre de bonnes performances dans la description des interactions avec l'eau et les surfaces de sel marin. Les simulations montrent que la présence d'eau tend à stabiliser CH_3I à la surface du sel.

La durée de vie du CH_3I dans l'atmosphère (en phase gazeuse ou adsorbé sur des aérosols) peut également être modifiée par sa réaction avec des radicaux en phase gazeuse. La réaction de CH_3I avec OH est donc étudiée à la fois en phase gazeuse et en présence d'eau au moyen de calculs de mécanique quantique. La présence d'une molécule d'eau supplémentaire favorise l'abstraction d'hydrogène par le radical OH dans les conditions atmosphériques. En d'autres termes, H_2O joue le rôle de catalyseur dans cette réaction chimique atmosphérique.

Enfin, en collaboration avec le laboratoire "Physics of the Interactions of Ions and Molecules (PIIM)", nous avons étudié l'adsorption de l'iodure de méthyle sur des surfaces d'eau solide amorphe (ASW). En accord avec des études antérieures, nous avons mis en évidence l'importance de l'échantillonnage de configuration dans le cas d'interfaces amorphes. En utilisant des calculs classiques de MD et de structure électronique, nous avons calculé des spectres théoriques pour les surfaces ASW avec et sans CH_3I adsorbé, qui peuvent être directement comparés aux spectres expérimentaux. L'adsorption de CH_3I induit un décalage d'environ $20\,cm^{-1}$ du mode d'étirement des OH pendants de la surface.

Cette thèse combine plusieurs méthodes théoriques pour étudier la réactivité et la capture de molécules par des surfaces d'intérêt atmosphérique. Les approches suivies dans ces travaux peuvent être étendues à d'autres systèmes dans le but d'interpréter des spectres ou mieux comprendre des données expérimentales.

Mots clés : iode, iodométhane, interactions mer-atmosphère, chimie de l'atmosphère, aérosols marins, eau solide amorphe, dynamique moléculaire, théorie de la fonctionnelle de densité